School of Physics and Astronomy

On the Origin of the Stellar Initial Mass Function and Multiple Stellar Systems

Katy H. M. Nelson

Submitted for the degree of Doctor of Philosophy
School of Physics and Astronomy
Cardiff University

October 2014

Acknowledgements

Foremost, I would like to express my sincere gratitude to my advisor Professor Anthony Whitworth for the continuous support of my Ph.D study and research, for his patience and guidance.

I am indebted to David Hubber for making SEREN_VIEW available, and providing guidance on its use. I would like to thank my fellow Ph.D students and Postdocs in the office, Olly, Scott and Saemus, for the entertaining and informative discussions.

I would like to acknowledge the support of Allistair and Selina, who provided me with a home away from home during my Ph.D, my sister Carrie, who stuck by me, and my Mum and Dad, who have encouraged and supported me throughout my life.

Finally, I would like to acknowledge the support of my husband, Kieron, who makes my life all the sweeter for being a part of it.

Summary of Thesis

I first perform a statistical analysis on a distribution of pre-stellar core masses. Each core is split into a small number of stars, and two stars are chosen using a prescription based on stellar masses to form a binary system. The rest of the stars are taken to be singles. From this sample of binaries and singles, I compute the stellar initial mass function, the binary frequency and mass ratio distribution as a function of primary mass. I then test if the observed binary frequencies and mass ratios are compatible with this self-similar mapping of cores into stars. I show that self-similar mapping can reproduce the observed binary frequencies and mass ratios well, so long as the efficiency is rather high ($\approx 100\%$), and each core fragments into about 4 or 5 stars.

Using the code SEREN_VIEW, I then perform N-body simulations with core-clusters. I investigate the formation of multiple systems, and qualify the dependence of their parameters and longevity on certain initial conditions, including (i) the number of stars in a core-cluster, (ii) the variance of masses in those stars, (iii) the virial ratio and (iv) radial dependence of stellar density. I expand on those results by including (a) a prescription for the influence of disks during stellar flybys, (b) different initial spatial configurations of the stars (i.e. line and ring clusters) and (c) a background potential due to residual gas in the core-cluster. The full range of periods observed in the field cannot be explained by the distribution of periods of pure binaries alone, which is too narrow. However, the wide range can be explained either by combining the periods of pair-wise orbits of all multiple systems, i.e. the widest periods observed are in fact pair-wise orbits of higher-order multiples with unresolved companions, or by considering a distribution of pre-stellar cores that have a range of virial ratios.

Declaration of authorship

- Declaration:
  This work has not previously been accepted in substance for any degree or award at this or any other university or place of learning, nor is it being submitted concurrently in candidature for any degree or other award.

  Signed: ..... (candidate) Date: .....

- Statement 1:
  This thesis is being submitted in partial fulfillment of the requirements for the degree of Doctor of Philosophy (PhD).

  Signed: ..... (candidate) Date: .....

- Statement 2:
  This thesis is the result of my own independent work/investigation, except where otherwise stated. Other sources are acknowledged by explicit references. The views expressed are my own.

  Signed: ..... (candidate) Date: .....

- Statement 3
  I hereby give consent for my thesis, if accepted, to be available for photocopying and for inter-library loan, and for the title and summary to be made available to outside organisations.

  Signed: ..... (candidate) Date: .....

Contents

List of Figures

List of Tables

Chapter 1

Observations of Star Formation

This chapter is an overview of the processes involved in star formation, and observational techniques used to probe the various stages. I start with the material needed to form stars, called the interstellar medium, and identify regions of high density believed to be the precursors of stars; pre-stellar cores. I discuss their mass distribution and observational techniques used to identify them. These cores collapse to form a star, or a small cluster of stars. The distribution of masses of these stars is the Stellar Initial mass Function, whilst the distribution of the mass of stellar systems is the System Initial Mass Function. Stellar clusters are discussed, and how they often dissipate with time. Finally, an outline for the thesis is presented in Section 1.3.3.

1.1 The Interstellar Medium

Very fine dust grains and atoms, collectively called the interstellar medium, fill the space between the stars in a galaxy. In some regions this interstellar medium clumps together to form features that are denser than their surroundings, the largest of these features being called giant molecular clouds. These giant molecular clouds have masses of 10^3 to 10^7 $M_\odot$, densities of 10^2 to 10^3 cm^{-3} and scales of between 5 and 200 pc. The dust within these giant molecular clouds plays two roles in increasing the concentration of molecules such as H_2. Firstly, the dust acts as a catalyst for the formation of molecules, and secondly, if the giant molecular cloud is large enough, the dust acts as a shield against ultra violet radiation, which dissociates molecules. As a result, the gas within giant molecular clouds is primarily molecular hydrogen. The dust also keeps the gas temperature down by radiating the energy imparted to the dust grains from collisions with hydrogen molecules, making it easier for the gas to collapse and form stars. Molecular hydrogen has a very small moment of inertia, and doesn't have a dipole moment (meaning that certain transitions are forbidden in the gas phase), and so the energy levels are widely spaced. The temperatures found in giant molecular clouds (about 10 K) are not high enough to excite the molecular hydrogen from its ground states, meaning that molecular

hydrogen is very difficult to observe in these environments (van der Tak 2012). So less common molecules have to be observed, which are hoped to trace, or lie in the same distribution as molecular hydrogen, for example, $C^{18}O$, $H^{13}CO^+$ (which are tracers of dense gas), and NH_3, and look for their emission lines. Giant molecular clouds are generally gravitationally bound and may contain several sites of star formation.

Within these giant molecular clouds, turbulent motion leads to smaller features, that are again, denser than their surroundings, which are called clumps. Clumps are gravitationally unbound and are thought to be the precursors of stellar clusters. Dense features are also seen within these clumps, some of which are massive and dense enough to be gravitationally bound. These are generally called cores. It is believed that these cores will eventually collapse to form a star, or a small sub-cluster of stars (see Padoan & Nordlund 2002; Li et al. 2004), and so they are called pre-protostellar cores, or pre-stellar cores for short (Ward-Thompson et al. 1994). These cores are often aligned along filaments (Myers 2013).

1.2 Core Mass Function

Determining the masses of these pre-stellar cores is no easy problem, because of the difficulties in observing molecular hydrogen, as discussed on the previous section. The most common method of measuring the mass of a core is to process the millimetre or sub-millimetre thermal dust emission. The distribution of these core masses is called the Core Mass Function, or CMF.

Observers believe the CMF to have either a log normal distribution, or a three part power law in the star formation regions studied, which include Aquilla (Könyves et al. 2010), the Pipe Nebula (Alves et al. 2007; Rathborne et al. 2009), Ophiuchus (Motte et al. 1998; Johnstone et al. 2000; Stanke et al. 2006; Young et al. 2006; Simpson et al. 2008; Enoch et al. 2008), Orion (Johnstone et al. 2001; Johnstone & Bally 2006; Nutter & Ward-Thompson 2007; Motte et al. 2001), Serpens (Testi & Sargent 1998; Enoch et al. 2008) and Perseus (Enoch et al. 2006, 2008). The average CMF over all star formation regions peaks at about 1 $M_\odot$, with a logarithmic standard deviation of about 0.45±0.15. These results agree with theoretical models by Padoan & Nordlund (2002), Padoan et al. (2007) and Hennebelle & Chabrier (2009) which also show that the CMF can be approximated by a log normal merging into a power law at high masses. However, it should be noted that the cores as found by Padoan & Nordlund (2002), Padoan et al. (2007) and Hennebelle & Chabrier (2009) are gravitationally bound structures. Most surveys of CMFs define cores using column density, meaning that the cores they find are not guaranteed to be gravitationally bound, and may not go on to form stars. Typically, a pre-stellar core before collapse will have a radius of the scale 0.01 to 0.1 pc, a density of $\sim 10^{-18}$ g/cm^3 and a temperature of $\sim$ 10 K. A typical radius after collapse will be $\sim$ 100's of AU.

The shape of the CMF is constant from region to region. But the position of the peak shifts

from $\sim$0.1 $M_\odot$ in nearby low-mass regions (ρ-Ophiuchus Motte et al. 1998), to $\sim$1 $M_\odot$ in more distant high mass regions (Orion, Nutter & Ward-Thompson 2007).

Others are more sceptical about the shape of the observationally derived CMF. For example, Reid et al. (2010) use simulated images of star forming regions to test their observational techniques, and argue that the noise, source blending and spacial filtering all perturb the core masses to the point where a log normal distribution is found - simply as a result of the central limit theorem (see Section 3.1). They also show that the characteristic mass of the cores is related to the angular resolution of the map from which the core mass function is derived. Hence star formation regions further away would appear to have a higher characteristic mass than regions closer to the Sun. They conclude that existing measurements of the CMF are highly compromised by limitations such as sensitivity, angular resolution, distance uncertainty, and spatial filtering of larger scale emission.

Unlike stars, which appear as points, cores are extended objects with no clear boundaries. Hence a core boundary has to be defined, which may either include too much of the background radiation or not capture the entire core. Features on the map are divided into cores or filaments either by eye (Tothill et al. 2002; Ward-Thompson et al. 2000; Nutter & Ward-Thompson 2007) or a clump finding algorithm such as GAUSSCLUMP (Stutzki & Guesten 1990) or CLUMPFIND (Williams et al. 1994). However, the properties of cores found by these different techniques do not always correlate with each other. Also, cores do not have trivial shapes, which makes identifying a core more difficult (see Lomax et al. 2013, for a discussion on the 3-D shape and orientation of the clumps).

The use of grey-body fits to estimate the mean dust temperatures, the mass opacity coefficients needed to convert fluxes into masses, and the distances assumed for the star formation regions all also introduce their own errors when using dust continuum emission maps.

1.2.1 Pre-stellar Stages and Classes

A protostar is a condensed object which will eventually become a star, but has not yet reached the main sequence stage. Lada (1987) formulates a theoretical class system for protostars, as follows:

Stage 0 Most of the mass of the core is still in the envelope as opposed to the protostar. This phase lasts about 10^4 to 10^5 yr.

Stage 1 Most of the mass is now in the central star and its disk, but there is still a substantial envelope. This stage lasts about 10^5 yr.

Stage 2 The protostar no longer has an envelope, but it still has a massive disk. These protostars move along the Hayashi track, shrinking and becoming less luminous with an

approximately constant surface temperature and colour. Then the temperature increases with increasing luminosity along a Henyey track. This stages lasts about 10^6 yr.

Stage 3 The disk has mostly been accreted onto the protostar, and is in an active phase of planet building. The protostar slowly contracts, until hydrogen burning starts at the zero age main sequence. This stage lasts about 10^7 yr.

The process of core collapse to form a star is divided up into the following observational classes. Note that the numbering of classes usually correspond to the same numbering for the theoretical stages, but that orientation effects (the angle at which we view the protostar) can cause overlap.

Class 0 Andre et al. (1993) introduces this class. The protostar can be observed in the millimetre and sub-millimetre wavelengths, but is not detectable in the infra-red ($T \leq 30$ K). The protstar tends to drive very powerful outflows. As the protostar ages, its outflows become less dense, but have faster speeds.

Class I The peak of the Spectral Energy Distribution (or SED) is caused by warm circumstellar dust shells. The SED is broader than black body, rising for wavelengths greater than 2 microns. It has a spectral index $a = \frac{d\log(\lambda F_\lambda)}{d\log(\lambda)}$ of $0 < a \leq 3$. The protostar is still embedded, but can now be best detected at infra-red wavelengths.

Class II The star has emerged from its parent cloud, and become a T-Tauri star, or a class II object. This is referred to as the birth line, and corresponds to a point at which the envelope around the protostar becomes optically thin to optical radiation. The SED is broader than black body, and flat or decreasing for wavelengths greater than 2 microns. H^α emission is detected. The SED agrees well with models of pre-main sequence stars having circumstellar disks. This class has a spectral index of $-2 < a \leq -0$.

Class III Weak-line T-Tauri stars, or Class III objects have reddened black body SEDs, with little or no excess near infrared emission. They are more X-ray luminous than Class II on average. This class has a spectral index of $-3 < a \leq -2$

Examples of proposed characteristic SEDs for Classes I, II and III can be found in Figure 2 of Lada (1987).

A variety of detection methods are used for young low mass stars, including:

- Radio and X-rays for non-thermal and transient events.
- Millimetre continuum surveys to determine the mass and structure of the dust.
- Far-infrared for providing luminosity information for the embedded stages.

- Mid-infrared for probing the disk.
- Near-infrared for probing the inner disk and star.
- Visible and ultraviolet for probing the star and ongoing accretion.
- Lithium is an indicator of a young, low mass star. The temperature needed for Lithium to be destroyed (it interacts with a proton to form Helium) is just below the temperature needed for hydrogen burning at $4 * 10^6$ K. As a young star is convective, once this temperature is reached in the core, most of the Lithium is quickly destroyed. Therefore, as a general rule, if lithium is present, the star is likely not hydrogen burning.

Figure 1.1 is a copy of Figure 2 of Tohline (2002). It shows the evolutionary track of the central region of a pre-stellar core in the temperature-density plane. The track from A to B is the core's initial isothermal core collapse. At point B, the centre of the core becomes opaque to its cooling radiation. This inner core is called the first core, or the first hydrostatic core. It has a temperature of about 170 K, and is very short-lived, with a lifetime of 10^2 to 10^3 yrs (Bate 2011). Pezzuto et al 2012 have observed hydrostatic core candidates, and found them to have separations of $\approx 10^3$ AU, and sizes of 48 to 130 AU. Saigo and Tomisaka 2011 predict a smaller size of 20 AU for the first cores, and a size of 100 AU for the surrounding disk. The discrepancy may be due to Pezzuto et al observing the hybrid disk and core.

The first core collapses adiabatically between points B and C, accreting from the outer envelope as it does so. At 300 K, molecular hydrogen can be rotationally excited. At point C, the temperature is high enough to dissociate molecular hydrogen (2000 K). The energy released from collapse is used to dissociate the molecular hydrogen, keeping the temperature roughly constant, and so the collapse is approximately isothermal between points C and D. At point D, the inner part of the first core collapses, the is called the second collapse, forming the second core. The Class 0 stage of a protostar starts here. Between points D and E we have pre-main sequence contraction.

When a core fragments into a small stellar cluster, there are several stages along this evolutionary path at which it can do so (Chen et al. 2013).

- Initial clump/filament fragmentation: This occurs when the large scale clump or filament fragments before the collapse of the individual cores. The cores will typically have separations of $\sim 10^3$ to 10^4 AU (Kauffmann et al. 2008; Launhardt et al. 2010).
- Prompt/isothermal fragmentation: This occurs at the end of the core's isothermal collapse phase. The fragments will have separations of 10^2 to 10^3 AU (Tohline 2002).
- Adiabatic fragmentation: This occurs when the collapse enters the adiabatic accretion phase. The fragments will have separations of 3 to 300 AU (Machida et al. 2005, 2008; Goodwin & Kroupa 2005).

- Secondary fragmentation: This occurs during the core's secondary collapse phase. The fragments will have separations of 0.01 to 0.1 AU (Machida et al. 2008).

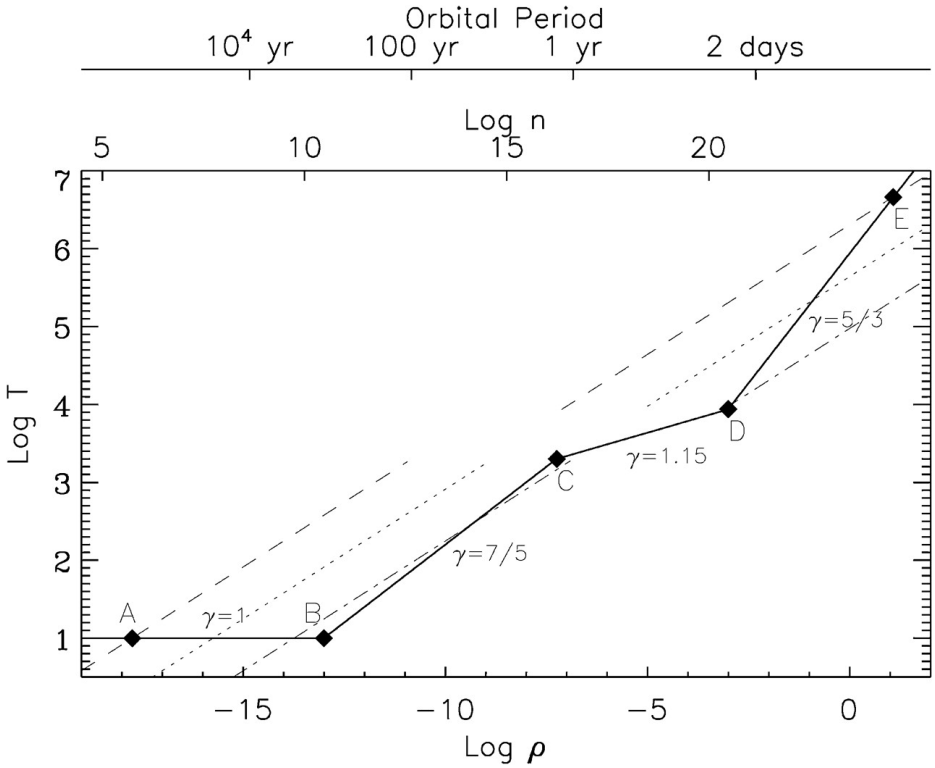

Figure 1.1: This figure is a copy of Figure 2 from Tohline (2002).
The evolutionary trajectory (solid curve) of the central region of a protostellar gas cloud is shown in the temperature-density plane, (patterned after Figure 3 of Tohline 1982.) The slope of each segment of the curve is indicated by the value of the effective adiabatic exponent γ. The density is shown both in g cm^3 (bottom horizontal axis) and in cm^3 (top horizontal axis); the temperature is given in degrees Kelvin. Also shown along the top of the plot is the orbital period of a binary system that has the equivalent mean density.

Chen et al. (2013) have observed multiple sources in prestellar cores, and have found them to have typical separations of a few 100s to a few 1000s of AU.

1.3 Stellar Initial Mass Function

At the end of the Class III stage, a protostar becomes hot enough to start burning hydrogen. It is at this point that it becomes a star, and starts its life on the main sequence. The Stellar Initial Mass function (StIMF) is given by $\xi(\log M) = \frac{\mathrm{d}N}{\mathrm{d}\log[M]}$ where M is the mass of a star when it reaches the main sequence, N is the number of stars in a logarithmic mass range $\log[M]$ and $\log[M] + \mathrm{d}\log[M]$.

The properties of a star, its evolution, and its effect on its environment is largely determined by its mass. Therefore, in order to understand the process of star formation, and predict its effect on galaxies, clusters, and on the cosmos, we need to have a good knowledge and understanding of the StIMF.

In order to measure the StIMF, we cannot simply look up in the sky, determine the masses of all the stars we see and plot their relative abundances on a graph. This would be the present day mass function (PDMF). Stars of different masses have different lifespans, and so we would expect to see a greater number of long-lived stars than their short-lived counterparts. High-mass stars are short-lived, they exhaust their fuel much quicker than low-mass stars, and so are rare in the galaxy. Low-mass stars live for a long time, and so are abundant. But even if we correct for these lifetimes, we still make the assumption that the StIMF doesn't change with time. Clusters of stars can be good places to observe the StIMF as all the stars are roughly the same age and have the same metallicity. In order to be useful laboratories, the clusters need to be (i) old enough to be open, i.e. all the enshrouding dust surrounding the protostars needs to have been cleared so that all its members can be detected, but (ii) not be so old that they have lost their low-mass members to ejection and high-mass members to death.

The three main approximations for the StIMF are due to Salpeter (1955), Kroupa (2001) and Chabrier (2005). Chabrier proposes that for field stars near the sun, the number of stars per logarithmic bin of masses, $\mathrm{d}N/\,\mathrm{d}\log M$, can be described by a log normal function below one solar mass $M_\odot$, which peaks at about a fifth of a solar mass. Above $M_\odot$, he proposes that the StIMF can be described by a power law with slope -1.3, i.e. a Salpeter slope (Salpeter 1955). Kroupa (2001) uses a three part power law to describe the StIMF. Above 10 $M_\odot$, the StIMF is extremely poorly known.

Chabrier (2005) StIMF

$$\xi(\log M) = \begin{cases} 0.093 \exp\left(-\frac{(\log M - \log 0.2)^2}{2*0.55^2}\right), & M \leq M_\odot \\ 0.041 M^{-1.35\pm0.3}, & M \geq M_\odot. \end{cases} \tag{1.1}$$

Kroupa (2001) StIMF

$$\xi(M) \propto M^{\alpha_i} \tag{1.2}$$

$$\begin{aligned}
\alpha_0 &= +0.3 \pm 0.7 \qquad 0.01 \leq M/M_\odot < 0.08, \\
\alpha_1 &= +1.3 \pm 0.5 \qquad 0.08 \leq M/M_\odot < 0.50, \\
\alpha_2 &= +2.3 \pm 0.3 \qquad 0.05 \leq M/M_\odot < 1.00, \\
\alpha_3 &= +2.3 \pm 0.7 \qquad 1.00 \leq M/M_\odot
\end{aligned} \tag{1.3}$$

The StIMF is quite well constrained, and uniform. Studies in various locations find very little, or no variation with either environment or metallicity.

The Malmquist bias affects magnitude limited samples. It states that brighter objects are easier to see, and so bright stars further away will be seen, but faint stars at the same distance will not be seen. It can be difficult to know if a star is close and faint, or bright and far away. More bright objects will be included in the sample, as the volume over which they can be detected is much larger, even if they are not truly more abundant.

1.3.1 System Initial Mass Function

Many stars (>53% for solar type stars, Raghavan et al. 2010) are in multiple systems. A multiple system consists of two or more stars that are mutual nearest neighbours, are gravitationally bound, and are likely to remain so for a significant amount of time. Multiple systems which consist of just two stars are called binaries, while those that consist of three stars are called triples, and those which consist of four stars are called quadruples. Any system with three or more members may be referred to as a higher-order multiple. I define hierarchical quadruples to be a multiple system of four stars where the stars are arranged hierarchically, i.e. a binary is orbited by a single star. This triple system is orbited by a fourth star (usually) much further out. Double quadruples are defined to be two sets of close binaries orbiting a common centre of mass. A multiple system can be split (sometimes in various ways) into two subsystems, each of which either satisfies the definition above, or is a single star. The orbit of two centres of mass around each other constitutes the pairwise orbit.

Note that when a core collapses, it will produce several stars. This collection of stars, whilst not stable, may initially be bound. To distinguish this state from more long-lived and stable multiple systems, it will be referred to as a core-cluster.

The StIMF is the initial mass function of stars regardless of what role they play in a multiple system, whether primary, secondary or even single. The System Mass Function (SysIMF) is the distribution of the masses of systems, where the mass of a system is the sum of the masses of its components.

In the early 2000s, there was a disagreement between the StIMF inferred from (i) the photometric Hubble Space Telescope (HST) luminosity function Gould et al. (1997) (ii) and

the nearby 5.2 pc luminosity function as evaluated by Henry & McCarthy (1990). Even after corrections for metallicity and a larger sample, the two mass functions did not agree.[1]

Chabrier (2003) realises that the HST survey, because it 'sees' much further, would not be able to resolve binaries, unlike the 5.2 pc survey. Therefore the luminosity function as determined by the HST is the luminosity function of systems, and not of single stars. To determine the StIMF, Chabrier performs monte carlo simulations. He takes the 5.2 pc mass function, and draws either 1 or 2 masses in an equal ratio (50% binary fraction). Assuming that the total magnitude of the unresolved binary systems is

$$\mathcal{M}_{sys} = -2.5 \log \left[10^{-0.4\mathcal{M}(M_1)} + 10^{-0.4\mathcal{M}(M_2)}\right] \tag{1.4}$$

where $\mathcal{M}$ is the magnitude, he finds a luminosity function. He compares his results to those found by the HST, and shows that the two are compatible. He finds that the system mass function has the form

$$\xi(\log M) = 0.076 \exp\left(-\frac{(\log M - \log 0.25)^2}{2 * 0.55^2}\right) \qquad M \leq M_\odot. \tag{1.5}$$

1.3.2 Cores and Clusters

When the protostars first form, the core has not yet used up all its gas by either converting it into stars (the protostars can still accrete matter at this stage) or expelling it out of the core-cluster with stellar winds. This residual gas causes a gravitational potential well, and it is thought that this potential may help to form stable multiple systems by keeping the stars from escaping too early, giving them a bit more time to establish themselves in a stable configuration before the gas is accreted or dispersed.

Another effect due to the residual gas is the formation of protostellar disks. As material in the core falls towards the protostar, it flattens into a disk which surrounds the protostar. The stars within a single core will interact gravitationally, and the presence of disks will affect those interactions by providing a means of dissipation of energy, making it more likely that the stars involved will form a long-lived multiple system. The energy lost by the stars involved is, to within an order of magnitude, the binding energy of the material stripped from the disk during the encounter (Clarke & Pringle 1993; Heller 1993).

Collections of pre-stellar cores, sometimes known as clumps, are believed to be the precursors of stellar clusters. The stars in a cluster will have a range of velocities. The fastest of the stars will generally have a velocity greater than the escape velocity of the cluster, and so will leave.

[1] $M < M_\odot$ for both StIMFs

The total energy of the cluster has now decreased, and the cluster contracts, becoming denser. As a result, there are more interactions between the remaining stars. These interactions allow the exchange of kinetic energy between the stars, and if a star's kinetic energy is increased enough, it becomes unbound and escapes. The cluster can then continue to collapse. This collapse can be halted by the energy released by multiple systems as they interact with other systems, and their internal binding energy increases. (See Vesperini 2010; Goodwin 2010).

Brown dwarfs are objects with masses between the opacity limit at 0.003 $M_{\odot}$ and the hydrogen burning limit at 0.075 $M_{\odot}$ (80 M_J). (This includes the boundary at the deuterium burning limit at 0.013 $M_{\odot}$ or 13 M_J). Because brown dwarfs fade with age, they are most easily spotted when young and at their brightest.

There is some debate regarding whether brown dwarfs are formed in the same way as stars, or if they are formed via a different mechanism. Standard cloud fragmentation models seem to have difficulty in making brown dwarfs, but other more successful proposed mechanisms include embryo ejection (Reipurth & Clarke 2001; Kroupa & Bouvier 2003) and disk fragmentation (Whitworth et al. 2010). If the binary statistics for brown dwarfs show the same trends as higher mass stars, then it can be inferred that brown dwarfs form in the same way as their higher mass counterparts. If not, then they are likely to have formed via a different mechanism.

High mass stars ($M > 10\ M_{\odot}$) have very short lifetimes of the order of a few million years, whereas the average lifetime of a cluster is a few Gyr. As a result, high mass stars will have typically used up all their fuel before the cluster is dissolved, and its stars become a part of the field population.

1.3.3 Thesis Plan

In Chapter 2 I will review present some of the properties of multiple systems, and summarise the observational data relating to them. I will also discuss some of the techniques used in observing multiple systems, and different classification models. This will give a basis to which simulations can be compared.

In Chapter 3 I will discuss the possibility that the shape of the StIMF is inherited directly from the CMF, i.e. self-similar mapping. I will also discuss some of the objections to this model. I will set up a model to investigate whether the binary frequency and mass ratios are compatible with self-similar mapping of core masses into the StIMF.

In Chapter 4 I will present the results of the mapping model. I will show that both the binary frequency for solar and sub-solar-mass stars, and the mass ratios for G and M-dwarfs can be reproduced assuming a self-similar mapping from cores to stars. The tightest constraints are found for the average number of stars formed in a core, and the average efficiency of a core.

In Chapter 5 I will set up a suite of small-N body simulations. These simulations will follow the N-body dynamics of core-clusters and investigate the production of stable, long-lived

multiple systems. The aim will be to investigate if N-body dynamics are compatible with the results of the self-similar mapping model.

In Chapter 6 I will present the code SEREN_VIEW, in particular the Hermite integrator, which is used to follow the N-body dynamics of the core-clusters. I will then present the results of testing the recovery of properties of eccentric binaries, and circular triple systems.

In Chapter 7 I will discuss the properties of multiple systems, and how they can be computed in simulations. I will also discuss how to identify multiple systems, and introduce a parameter to quantify the stability and longevity of multiple systems.

In Chapter 8 I will present the first half of the results of the N-body simulations of core-clusters, focussing on uniform, spherical distributions of stars. I will discuss the properties, of binaries, triples, hierarchical quadruples and double quadruples formed with the fiducial model, varying the average number of stars formed in a core, varying the virial number of the cores, and the standard deviation of stellar masses produced by a single core.

In Chapter 9 I will discuss the second half of the results of the N-body simulations of core-clusters. This half includes non-uniform and non-spherical configurations of the stars, as well as forms of dissipation between the stars. I will discuss the properties, of binaries, triples, hierarchical quadruples and double quadruples formed with varying the density gradient of stars, adding dissipation effects due to disks and a background potential due to residual gas, a line cluster and a ring cluster.

In Chapter 10 I will summarize the conclusions of both the self-similar mapping model and the N-body simulations of core-clusters. The structure of higher-order multiples are found to give the best indication of the initial conditions of core-clusters. I finish my thesis with suggestions for future work that could further constrain the parameters of star formation.

Chapter 2

Multiple Stellar Systems

The capture of a passing star is very difficult and many, if not most, stars are in multiple systems. Hence the stars within a multiple system must usually have been bound together gravitationally from the time of formation (Goodman & Hut 1993). Any star formation theory must be able to predict not only the existence of these multiples systems, but also their properties, including the wide range of periods and separations observed. In this Chapter, I introduce statistics that describe the properties of a collection of multiple systems. I then go on to describing different classification methods for binary systems, and typical observational methods for detecting, and determining properties of multiple systems. I summarise the observational data regarding multiple systems, including distributions of fractions of multiplicity, mass ratios, periods, eccentricities and higher-order multiples. This will allow me in later chapters to set a standard to which the results of theoretical models and simulations can be compared.

There isn't a single number that can fully describe the statistics of a collection of multiple systems. The most complete statistic would be $S : B : T : Q$, where

$$\begin{aligned} S &= \text{the number of single stars} \\ B &= \text{the number of binary systems} \\ T &= \text{the number of tertiary systems, and} \\ Q &= \text{the number of quadruples,} \end{aligned}$$

but even that doesn't give the structure of higher order multiples. A variety of statistics are commonly used in the literature, and are defined by Reipurth & Zinnecker (1993).

The probability that a given system is multiple,

$$\text{Multiplicity Frequency} = \frac{B + T + Q + ...}{S + B + T + Q + ...}. \tag{2.1}$$

If only binary systems are being considered, this is sometimes referred to as the binary frequency, $B/(S+B)$.

The companion probability is the probability of a given star being a part of a multiple system,

$$\text{Companion Probability} = \frac{2B + 3T + 4Q + ...}{S + 2B + 3T + 4Q + ...}. \tag{2.2}$$

The average number of pairwise orbits per multiple system,

$$\text{Pairing Factor} = \frac{B + 2T + 3Q + ...}{B + T + Q + ...}. \tag{2.3}$$

Each of the above can also be expressed as a function of primary mass.

Each pairwise orbit in a multiple system can be described by (among other things) its eccentricity e (shape), period P, semi-major axis a and mass ratio q, where

$$q = \frac{M_s}{M_p}. \tag{2.4}$$

For pairwise orbits involving two stars, M_s is the mass of the smaller star and M_p is the mass of the larger star. For the outer orbit of triple systems, M_s is the mass of the outer star, and M_p is the mass of the inner binary, $M_1 + M_2$.

These multiple system properties can help us constrain stellar formation models. For example, the average semi-major axis corresponds to the characteristic size of the core at the time of fragmentation (see Sterzik et al. 2003), the overall multiplicity frequency and mass ratio distributions are determined by the physics of fragmentation (Delgado-Donate et al. 2004), and an individual system mass ratio will depend on the accretion history after the protostars have been formed (Bate & Bonnell 1997).

2.1 Types of Binaries

For the rest of the chapter, I refer to classifications and observations of binaries. However, the statements made can usually be applied to any pairwise orbit in a multiple system.

Binaries can be grouped in a number of different ways. For example, one method groups the binaries according to the state of their Roche Lobes, the region of space around a star in a binary system within which matter is gravitationally bound to that star. The groups include

- Detached binaries: Both stars are wholly within their Roche lobe, and evolve independently. This group includes the majority of binaries.

- Semi-detached binaries: Also known as accreting binaries. One star fills its Roche lobe and transfers material to its companion via an accretion disk.
- Contact binaries: Both stars fill their Roche lobes, and have a common envelope. They may eventually merge.

A second method groups the binaries according to their stability.

- Soft binaries: These are binaries with typically wide orbits and lower-mass primaries. These systems are easily disrupted.
- Hard binaries: These are binaries with typically narrow orbits and higher-mass primaries. Theses systems are difficult to disrupt.

The final method groups binaries into the mode by which they can be identified and observed; visually, spectroscopically, photometrically and astrometrically. These observational classifications of binaries are not directly related to their intrinsic properties, but are indicative of the detection method(s) sensitive to its components. As a result, a binary may be simultaneously in more than one of these classifications. These methods for detecting binaries are generally complementary, e.g. visual and spectroscopic methods are useful for detecting binaries, whereas astrometric and photometric methods are useful for determining the parameters of the binary system. These same methods can also be used to detect extra-solar planets.

2.1.1 Visual Binaries

Visual binaries are those binaries whose components can be resolved visually.

Visual binaries are usually detected at either optical or infrared wavelengths using ground based telescopes, and so are subject to atmospheric affects which can shift or blur images of a source, and so reduce the precision and resolution of astrometric observations. Adaptive optics are used to overcome the atmospheric effects, and techniques include (i) passing different combinations of binaries through the reference point spread function of a single star to find the best fit to the image seen, (ii) using speckle interferometry, which employs fourier transforms to try and capture the original target and (iii) using lucky imaging, which takes a large number of very short snapshots, and adds the best of the exposures together to get an image. Adaptive optics, whilst effective, are often complicated and time consuming.

Visual binaries tend not to be binaries with a small separation or low mass-ratio. This is because there is a brightness-separation bias relating to visual binaries. The closer a companion is to its primary star, the brighter (and hence more massive) it has to be in order to be detected. This also means that binaries need to be relatively close by in order to be identified as such.

Stars that happen to sit either in front or behind a star can appear to be associated with the star along the line of sight, especially for large separations where contamination from field

stars becomes significant. However, these chance projections can be weeded out by considering either their parallax, or their proper motion/radial velocities. If any of these quantities differ largely between the two objects, it can be said that they are simply a chance projection.

If the distance is known, and the system has been observed for a large fraction of its period, then the orbital parameters can be used to find the masses. The average of the separation as seen by the observer, through a combination of projection and ellipticity is shown by van Albada (1968b) to be very close to the semi-major axis, which is required for mass estimates. However, many visual binaries have periods of hundreds or even thousands of years, and so only a small fraction of their orbits have been tracked. If the orbital parameters have not yet been fully determined, it is difficult to obtain the masses and other intrinsic properties.

2.1.2 Spectroscopic Binaries

Most binaries are identified using spectroscopy, and so are called spectroscopic binaries. The spectral lines in an individual star shift from bluer wavelengths (moving towards us) to redder wavelengths (moving away from us) periodically as it moves in its orbit. Single line binaries are defined when spectral lines can only be seen from one star - but it can be identified as being part of a binary because of the periodic motion. Double line binaries are defined when spectral lines are seen from both stars.

Spectroscopic methods are very good at identifying companions within a few AU of the primary, as small separations and high angular velocities produce large doppler shifts. However, it is very difficult to detect binaries with low-mass ratios ($q < 0.4$) with spectroscopic methods because of line blending problems. This leads to a bias for high-mass ratio systems detected (i.e. it is even harder to detect low-mass systems spectroscopically than with visual methods). The period of a spectroscopic binary is easily determined.

Spectroscopic methods can only detect motion towards, or away from the observer, with the magnitude of the shift correlated to the stars radial velocity. As motion tangential to the line of sight cannot be determined using spectroscopic methods, it is impossible to determine the complete orbit of a purely spectroscopic binary. However, if the binary is also a visual or eclipsing binary, we have a full picture of the orbit, and from Kepler's laws, the masses can be determined. Many spectroscopic binaries however are too close together to be observed optically, meaning that we have only a small selection of binaries for which complete orbits can be determined.

Although these binaries more often than not cannot be resolved into their separate components, we can still make a good guess at the mass of the primary using the combined lightcurve of the system. If the components are similar in mass, then the lightcurves will also be similar, and the combined lightcurve can be taken as an approximation to that of the primary. If the secondary is much smaller than the primary, then its luminosity will be much smaller, and will

not contribute much to the total spectrum. So again, taking the spectrum of the system as an approximation to that of the primary is reasonable. See Hartigan & Kenyon (2001) for a discussion of the effects when neither of these approximations apply.

2.1.3 Photometric Binaries

Photometric, or eclipsing binaries occur when the plane of the orbit of the binary system lies close to the line of sight. As one star passes in front of the other the total luminosity decreases, and it is this periodic change in luminosity that can be observed. This is an unlikely configuration, to be viewing the system exactly, or close to edge on, so photometric binaries are rare. The binaries also need to be observed over a period of time over which an eclipse takes place, in order to identify a system as a binary. This requires long term observations.

Eclipsing binaries yield a lot of information about their intrinsic properties, and are the primary source for direct mass estimates, so long as mass transfer between the stars has not yet taken place. The relative size (radii), and period can be determined quite easily. The semi-major axis and masses can also be determined if radial velocity (spectroscopic) measurements are also available. See Southworth (2012) for a review of determining the properties of photometric binaries.

2.1.4 Astrometric Binaries

Astrometry is the precise (visual) measurement of the positions and movements of astrophysical objects. Hence all visual binaries are also astrometric binaries, as their components can be tracked astrometrically. However, if a secondary is too faint to be seen visually, the system can still be identifed as binary if the primary is seen to 'wobble' in the sky. This type of binary will be astrometric, but not visual.

2.2 Observations of Multiple Systems

Each sample of multiple systems and observational technique will come with its own biases and incompletenesses. For example, magnitude-limited surveys will overestimate the equal-mass binaries fraction, as the volume over which a binary with a given primary mass can be detected increases with the mass of the secondary (compare with the Malmquist bias). A magnitude-limited sample will also favour the inclusion of double-lined spectroscopic binaries (Branch 1976). A volume-limited sample has better completeness statistics, but smaller number statistics, and often does not include the extremes in primary mass. Different observational techniques and telescopes will only be sensitive to separations within a particular range, and so any binaries with separations outside this sensitivity range will be missed. These incompleteness

issues mean that the observed binary frequency is not going to be the true or intrinsic binary frequency, but by accounting for these biases and incompletenesses, an estimate can be made for the intrinsic properties of the population.

I use the following notation in this section. Solar-mass binaries are binaries whose primary star has a mass $0.7 < M/M_{\odot} < 1.3$. Low-mass binaries have primaries of mass $0.1 < M/M_{\odot} < 0.5$, very low-mass binaries have primaries with mass $M/M_{\odot} \leq 0.1$, intermediate-mass binaries have primaries with mass $1.5 < M/M_{\odot} < 5$ and high-mass binaries have primaries with mass $M/M_{\odot} \geq 8$.

Solar-mass binaries are the most well studied binaries, given their proximity to the sun and relative brightness. The first modern survey of solar-mass stars was Duquennoy & Mayor (1991) and it was the standard for solar-mass stars for many years. Raghavan et al. (2010) have now produced a more complete sample with better observational techniques, which has replaced Duquennoy & Mayor (1991) as the standard for solar-mass stars.

Low-mass binaries are also abundant near the sun, but it can be more difficult to do multiplicity surveys with low-mass stars than solar-mass stars, due to their lower luminosity. The first standard for low-mass binaries was Fischer & Marcy (1992). Modern surveys of low-mass binaries include Delfosse et al. (2004), Dieterich et al. (2012) and Reid & Gizis (1997).

Very low-mass binaries are faint, and so difficult to detect. There are many surveys of very low-mass binaries, but none constitute a large volume-limited survey. See Burgasser et al. (2007) for a review of multiplicity in the sub-stellar regime.

Intermediate-mass stars are more difficult to work with than solar-mass stars, because the steep mass-luminosity function makes detecting companions difficult. Spectroscopic surveys include Carquillat & Prieur (2007) and Carrier et al. (2002). Visual surveys include Balega et al. (2011) and Ivanov et al. (2006).

High-mass stars are very bright, but very far away, so are difficult to study. Most are still found in the massive clusters or OB associations in which they were born, and studying high-mass field stars is likely to paint a biased picture, as the majority of them are 'runaways' whose systems are likely to have been disrupted (see Chini et al. 2012). Spectroscopic surveys of individual clusters and associations include Kiminki et al. (2012), Sana et al. (2009) and Sana et al. (2013) whilst visual surveys include Duchêne et al. (2001), Peter et al. (2012), Preibisch et al. (1999) and Duchêne et al. (2001).

2.2.1 Multiplicity Frequencies

For field stars, the overall trend is for the multiplicity frequency (Equation 2.1) to increase with primary mass (see Table 1 of Duchêne & Kraus 2013). Due to the lack of a large volume-limited survey, a piecewise approach has to be taken to estimate the multiplicity frequency for very low-mass stars. Spectroscopic surveys (Basri & Reiners 2006; Blake et al. 2010; Guenther

& Wuchterl 2003; Reid et al. 2002; Tanner et al. 2012) suggest a multiplicity frequency of about 5.2% for systems with separations less than 1 AU, whilst visual surveys (Bouy et al. 2003; Burgasser et al. 2007) suggest a multiplicity frequency of about 15% for systems with separations greater than 2 AU. Combining these two gives a multiplicity frequency between 20 and 25%, remembering that undetected systems lie in the range 1 to 2 AU. The multiplicity frequency for low-mass stars is about 26% (Delfosse et al. 2004; Dieterich et al. 2012; Reid & Gizis 1997). Raghavan et al. (2010) find a multiplicity frequency of 44±2% for solar mass stars. They subdivide their sample into higher and lower masses, and find a trend for the multiplicity frequency to decrease with primary mass. Duchêne & Kraus (2013) note that intermediate-mass stars probably have a multiplicity frequency ≥ 0.5.

Chen et al. (2013) find that Class 0 protostars, the youngest stars (see Section 1.2.1), have a multiplicity frequency that is approximately twice as high as for their older siblings, Class I protostars, and a multiplicity frequency that is approximately three times larger than for field stars with a similar range of separations. Therefore it would appear that the multiplicity frequency is set in the pre-main sequence stage. (see Duchêne 1999; Duchêne & Kraus 2013).

'O' stars can be grouped into 'cluster and association', 'field' and 'runaway' stars. If we consider only confirmed companions of high-mass stars in clusters and associations as found in Chini et al. (2012), Mason et al. (2009), and Sana & Evans (2011) we find a multiplicity frequency that is greater than ≥ 0.8, and that estimate may increase with more observations. The multiplicity among field and runaway stars is much lower (Chini et al. 2012; Mason et al. 2009).

2.2.2 Mass Ratios

Mass ratios are difficult to measure, and as a result, the mass ratios of binary systems are very poorly constrained. However, there is a general consensus that the distribution of mass ratios is close to flat (excluding $q < 0.1$, as these mass ratios are almost impossible to detect) for all mass ranges greater than $M \geq 0.3\ M_{\odot}$. Below this mass range, the mass ratios favour $q = 1$ systems. The mass ratios are best defined for binaries with solar-mass primaries.

Raghavan et al. (2010) show that solar-mass binaries have an overall mass ratio distribution that is consistent with being flat. They split their sample into long- and short-period binaries, and find that short-period binaries have a mass ratio distribution that peaks at $q = 1$, whilst long-period binaries have a mass ratio distribution that peaks at $q = 0.3$.

For low-mass binaries, the mass ratio appears to be flat, with a possible favouring of high q systems (Janson et al. 2012; Delfosse et al. 2004). Reid & Gizis (1997) find that short-period systems peak more strongly at high mass ratios than long-period systems. Very low-mass binaries are heavily skewed towards equal-mass systems with very few low mass ratio systems (Burgasser et al. 2007).

The mass ratios for intermediate-mass binaries are poorly constrained, but appear to be flat, with a possibility of a small preference of small mass ratios (Shatsky & Tokovinin 2002; Kouwenhoven et al. 2007).

Companions to high-mass stars are still in the pre-main sequence stage, and so making mass estimates is difficult due to the uncertainty in the mass-luminosity models for pre-main sequence stars. Observed mass ratio distributions range from a preference for low mass ratios (Preibisch et al. 1999; Duchêne et al. 2001) to flat (with a possible peak at $q = 0.8$) (Kiminki & Kobulnicky 2012; Sana et al. 2012).

Pre-main sequence binaries with small mass ratios are relatively easy to identify compared to main sequence binaries, as the mass-luminosity function is very shallow. However, mass estimates are not well constrained due to uncertainties in the mass luminosity models for pre-main sequence stars (Hillenbrand & White 2004). Most surveys show that the mass ratio distribution is roughly flat (e.g. Kraus et al. 2008, 2011; Lafrenière et al. 2008).

Chen et al. (2013) show that Class 0 protostars have a strong preference for small mass ratios, with the majority of binaries having a mass ratio less than 0.5.

2.2.3 Periods and Separations

From Kepler's laws, we know the semi-major axis is closely linked to the period ($P^2 \propto a^3$), with a small dependence only on the total mass of the system. Therefore, any qualitative statement relating to trends in the period can also be applied to trends in the separation, and vice versa.

The period distribution is very wide, spanning several orders of magnitude. Overall, the median separation and width of the distribution decrease sharply with decreasing stellar mass. However, high-mass stars show an additional strong peak at the shortest periods (Duchêne & Kraus 2013).

Raghavan et al. (2010) show that solar-mass binaries have a log normal period distribution with mean $P \approx 250$ yr (a ≈ 45 AU) and dispersion $\sigma_{\log[P/\mathrm{yr}]} \approx 2.3$.They also report that younger systems are more likely to have wider separations, further evidence that these systems are disrupted over time.

For low-mass stars, a log normal function is suitable for separations of less than 500 AU with a mean of 5.3 AU and a period dispersion of $\sigma_{\log[P/\mathrm{yr}]} \approx 1.3$ (Duchêne & Kraus 2013). For larger separations of 0.2 to 0.3 pc, an Öpik-like, ($f\,(\mathrm{a}) \propto \mathrm{a}^{-1}$, Öpik 1924) distribution seems to hold.

Very low-mass binaries are rare, but those that have been found tend to to have a separation between 1 and 10 AU (Burgasser et al. 2007). Maxted & Jeffries (2005) and Allen (2007) both fit a log normal to the separation distribution, finding a peak of 4 and 7 AU respectively, and a dispersion of $0.6 \leq \sigma_{\log[\mathrm{a/AU}]} \leq 1.0$ and 0.3 ± 0.1 respectively. But presently the distribution is not well defined.

Spectroscopic surveys are sensitive to small separations, whereas visual surveys find binaries with large separations. Therefore the period, or the separation distribution (especially for intermediate- and high-mass stars, which are further away) can appear to be bi-modal (Mason et al. 1998; Duchêne & Kraus 2013). For example, compare the periods as found by the spectroscopic survey conducted by Sana et al. (2012) and the visual survey conducted by Peter et al. (2012). The bi-modal distribution is in all likelihood due to selection effects rather than an intrinsically bi-modal distribution.

Connelley et al. (2008) investigate the separations of embedded binary systems (i.e. young protostars), and find that the separation distribution is better described by a log uniform function than a log normal.

2.2.4 Eccentricities

Eccentricities are very difficult to observe, as they require well-determined orbits, which can only be found via several astrometric observations over a large fraction of the orbit. However, there is a general trend for short period systems to have an eccentricity close to 0 over all mass ranges. No population has a thermal distribution of eccentricities.

Raghavan et al. (2010) find that solar-mass binaries with periods greater than about 12 days have a flat eccentricity distribution out to $e = 0.6$. Above $e = 0.6$, the eccentricity distribution drops. Systems with periods less than 12 days are usually circularised, but there are a few exceptions, possibly due to young systems that have not had time to be circularised.

Dupuy & Liu (2011) discuss the eccentricities of very low-mass binaries, and find that the eccentricity distribution is flat. Unlike solar-mass binaries, there is no correlation between period and eccentricity, and there are more circular orbits than for solar-mass binaries.

De Rosa et al. (2012) find that intermediate-mass stars have a preference for low-eccentricity binaries, while Kiminki & Kobulnicky (2012) and Sana & Evans (2011) both find that high-mass binaries also have a preference for low-eccentricity binaries.

2.2.5 Higher-order Multiples

Tokovinin (2008) conducts a survey of double quadruples and triple systems, and finds that double quadruples tend to comprise four similar mass stars, i.e. both the inner and outer mass ratios tend towards 1. The two inner pairs also tend to have comparable periods, whose distribution differs from that of pure binaries. The outer period usually has a value 5 to 10 times greater than the inner periods.

Tokovinin also finds that triples have an excess of equal-mass triples, with an inner mass ratio that tends towards 1, and a peak of the outer mass ratios at ≈ 0.39. The inner pairs of triple systems tend to have shorter periods on average than pure binaries. As with the double

quadruples, the outer period is usually about 5 to 10 times larger than the inner period.

Duchêne & Kraus (2013) state that approximately 25% of all solar-mass binaries are part of higher-order multiples, and $\approx 21\%$ of all low-mass multiple systems have three or more components. Estimates cannot be made for any other mass range due to observational difficulties in detecting higher-order multiple systems.

Chapter 3

Mapping from the CMF to the StIMF Setup

This chapter has in part been published in Holman et al. (2013).

In the next two chapters, I test if the observed binary fraction for solar and subsolar-mass stars and mass ratios for G and M-dwarfs are compatible with a self-similar mapping of cores into stars. In this chapter, I discuss the similarity between the CMF and the StIMF, and the possible explanations. I also present the results of previous studies investigating self-similar mapping. I set up my self-similar mapping model, with the parameters and observational data. I will then present and discuss the results in Chapter 4.

3.1 Self-Similar Mapping

A normal distribution is described by the equation

$$p\left(y\right) = \frac{1}{\left(2\pi\right)^{1/2}\sigma} \exp\left\{\frac{-\left(y-\mu\right)^{2}}{2\,\sigma^{2}}\right\} \mathrm{d}y, \tag{3.1}$$

where $p\left(y\right)$ is the probability distribution of y, μ is the mean of the distribution, and σ is the standard deviation.

If we let $y = \log_{10} x$[1], then $\mathrm{d}y \propto \mathrm{d}x/x$. Substituting these expressions into Equation (3.1) gives us,

$$p\left(x\right) = \frac{1}{\left(2\pi\right)^{1/2}\sigma x} \exp\left\{\frac{-\left(\log_{10} x-\mu\right)^{2}}{2\,\sigma^{2}}\right\} \mathrm{d}x, \tag{3.2}$$

[1]Note that throughout the thesis, log is always to be taken to the base 10 unless stated otherwise

which is called a log normal distribution.

When a large number of arbitrary functions with finite mean and variance are added, the resultant distribution will tend towards a normal distribution, according to the central limit theorem. Due to the same theorem when a large number of arbitrary functions are multiplied, the resultant distribution will tend to a log normal distribution, as multiplication is the same as addition in log space.

The CMF appears to have a similar shape to the StIMF, but shifted to higher masses by a factor of ~ 4 (see Könyves et al. 2010; Motte et al. 1998; Testi & Sargent 1998; Johnstone et al. 2001, 2000; Stanke et al. 2006; Nutter & Ward-Thompson 2007; Alves et al. 2007; Rathborne et al. 2009). So why are the CMF and StIMF similar in shape, but shifted in mass? There are several possible explanations for the similarity between the CMF and the StIMF.

- Firstly, it could be coincidence. There are a lot of different physical processes that go into creating a star or a core (e.g. radiation, gravity, magnetic fields, turbulence), and the combination of all these processes could produce two log normal distributions independent of one another, as a result of the central limit theorem (see Chapter 3.1).

- Secondly, the shape of the core mass function may influence, but not completely determine the shape of the StIMF.

- Thirdly, from this, it could be inferred that there is a self-similar mapping between the CMF and the StIMF, i.e. a core of mass $M_{\rm c}$ will statistically produce stars with masses $f\left(M_{\rm c}\right)$.

- Finally, another solution might be that the CMF and StIMF are not similar at all, but that the supposed likeness is due to observational systematics and errors (see Sections 1.2 and 1.3).

Several different groups have investigated the validity of the third consideration (see Section 3.2), and each of them show that it is very easy to reproduce the StIMF from the CMF using statistical methods. Consequently the shape of the StIMF may not place strong constraints on the process of star formation. But none of these groups address whether a self-similar mapping model can reproduce the properties of multiple systems. (Note that although some models do consider multiplicity, observations are used as an input to the model. My model is unique in that multiplicity statistics are predicted by the model). The aim of this project is to incorporate a prescription for creating multiple systems within a self-similar mapping model, and determine whether or not the resultant multiplicity statistics are compatible with observations, and as a result, whether or not self-similar mapping can be ruled out.

3.1.1 Objections to Self-Similar Mapping

There are some strong objections raised to self-similar mapping. In this section, I discuss some of these objections.

Firstly, if each pre-stellar core collapses to create one star, with an efficiency of about 30% as has been suggested by Alves et al. (2007), no multiple systems would be produced. Yet multiple systems are common, especially in young clusters, and observers are continuing to find more and more.

Secondly, low efficiencies of about 30% are inconsistent with the work of Matzner & McKee (2000) who show that winds from a protostar are concentrated along two jets emanating from the poles. Not much gas is dissipated, and the core would have a high efficiency of 25 to 70% (Matzner & McKee 2000). Earlier lower estimates have assumed that the protostar emits winds isotropically (e.g. Nakano et al. 1995).

Thirdly, self-similar mapping assumes that each core lives to about the same age before collapsing to a star. But if some cores live longer than others, then the CMF as observed will not correspond to the probability density of cores collapsing, per unit time, to form stars. For example, if large cores evolve more quickly than smaller cores as suggested by Hatchell & Fuller (2008), (It has been observed in Perseus that low-mass cores are more likely to be starless than the high-mass cores), then we would observe fewer high mass cores in the CMF compared to the distribution of core masses collapsing per unit time. On the other hand, the argument has also been put forth that smaller cores evolve more rapidly than higher mass cores (It is stated in Clark et al. 2007, that if each core contains the same number of Jeans masses, then the density in low-mass cores must be high, and so the free-fall time must be shorter). Hence the CMF would have fewer low mass cores than the distribution of cores collapsing per unit time.

Fourthly, the similarity between the CMF and the StIMF is the only observational evidence for self-similar mapping.

The assumption that high-mass cores form first, and are already in the process of collapsing when the low-mass cores are still being formed. However, this contradicts the turbulent formation idea though, since in turbulence the small scales dissipate first.

Finally, Smith et al. (2009) find that cores in SPH[2] simulations bear no resemblance to the stars they later form, and that the mass of a star depends only on the accretion history of the core and not its initial mass.

3.2 Previous Studies

In this section, I will discuss previous work and studies relating to self-similar mapping and small-N cluster dynamics. This will allow me to form a basis for my own project.

[2]Smoothed Particle Hydrodynamics

3.2.1 Mapping from the CMF to the StIMF

A number of authors have addressed the question of self-similar mapping from cores to stars. A selection of these studies, along with a short summary of their results are given below.

Clarke (1996) considers N = 2 clusters only, and finds that these clusters produce a binary frequency and mass ratio distribution that is only weakly dependent on primary mass. She investigates different distribution functions, and places less emphasis on observational constraints than other studies.

Swift & Williams (2008) develop a statistical model that includes the power law tail of the StIMF. They find significant degeneracy in the nature of core evolution in reproducing the StIMF, and cannot draw any conclusions on N_0 or η_0. They conclude that only mass-dependent core evolution will affect the skew of the StIMF (γ_{St}) whilst all other prescriptions only affect the mean, μ_{St}, and standard deviation, σ_{St}.

Goodwin et al. (2008) discuss the consequences of mapping from the CMF to the StIMF (their mapping is not strictly self-similar) on the multiplicity statistics for very low mass stars. They assume a low efficiency of 27%, and show that a simple one-to-one mapping cannot reproduce the abundance of brown dwarfs, but do not investigate how the binary frequency might vary with primary mass.

Goodwin & Kouwenhoven (2009) make the observation that if each core forms a single long-lived multiple system, then it is the System Initial Mass Function (SysIMF) that should follow from the CMF, rather than the StIMF. They find that the mass ratio distribution and binary frequency distribution assumed do not have much effect on the shape of the resulting StIMF. Goodwin & Kouwenhoven also investigate the effect of mass dependent efficiencies and find that a mass dependent efficiency can significantly change the width (variance) and shape (skew) of the StIMF formed.

Chabrier & Hennebelle (2010) presented a statistical analysis of numerical simulations, and suggest that the StIMF is correlated to the CMF within statistical fluctuations. These statistical fluctuations broaden the StIMF and could possibly explain the excess of brown dwarfs.

Each of the above studies show that the StIMF can easily be derived from the CMF, and that the shape of the StIMF is not strongly dependent on evolutionary parameters. However, even when these papers do take into account multiplicity parameters, the binary statistics (binary frequency and mass ratios) are often assumed in order to define the nature of core evolution. Hence these papers cannot use predictions of multiplicity parameters to distinguish between different evolutionary methods. As a consequence, they cannot draw any firm conclusions on the input parameters, in particular the number of stars each core produces, N_0, or the average efficiency of a core, η_0.

3.2.2 Dynamical Studies

A core-cluster with 3 or more members is often highly unstable, and the core-cluster ejects members as singles to relax and stabilise the remaining members of the core-cluster. For a range of stellar masses, the smaller stars are preferentially ejected, due to their lower gravitational pull. The final stable state will usually result in the two most massive stars from each core forming a binary system, and the rest forming single systems (van Albada 1968a; Anosova 1986).

McDonald & Clarke (1995) built on these results by including a prescription for dissipative interactions between circumstellar disks. As in the purely gravitational case, the system decays to form a binary and N − 2 singles. The primary tends to be the most massive star in the small-N cluster, but the secondary is chosen randomly from the remaining stars. This is due to energy loss between the disks as the stars pass close to one another, and so a star is likely to be captured if it is one of the first to pass close to a massive star, regardless of its mass.

Sterzik & Durisen have published a number of papers investigating the N-body dynamics of small-N clusters including. Sterzik & Durisen (1998) perform N-body simulations for N = 3, 4 and 5. They show that the product of a binary plus N-2 singles is an important mode of decay, but not the only one. For un-equal mass systems, the binaries formed have a semi-major axes about 5 times smaller than the original system size. The lowest mass stars always end up being ejected as singles. zero velocities and a spherical geometries. Sterzik et al. (2001) investigate initial clusters of 4 stars, and show that clusters of 4 stars show promise of reproducing the multiplicity frequencies and mass ratios well. By 300 crossing times, all the clusters have decayed into long-term stable sub-systems. Sterzik & Durisen (2003) show that dynamical decay produces a multiplicity frequency that increases with primary mass. The mass ratio distribution of brown dwarfs is expected to be flat. Finally, Sterzik et al. (2003) show that a 'random pairing' does not reproduce a multiplicity frequency that increases with primary mass, unlike dynamical biasing.

3.3 Set-up

3.3.1 Core Mass Function

We saw in Chapter 1 that both the CMF and StIMF can be described by a log normal merging into a power law at high masses. For simplicity, during the course of this project only the log normal sections of the CMF and the StIMF are considered. This does not change the basic conclusions of the model, but makes the implementation and maths easier to understand and more precise. The results are most relevant in the range $0.03\ M_{\odot} < M < 3\ M_{\odot}$.

Taking this log normal approximation, and considering only variations in the peak and

standard deviation, the CMF becomes:

$$\frac{\mathrm{d}\mathcal{N}}{\mathrm{d}\log_{10}[M_{\mathrm{c}}/M_{\odot}]} = \frac{1}{(2\pi)^{1/2}\sigma_{\mathrm{C}}} \exp\left\{\frac{-\left(\log_{10}[M_{\mathrm{c}}/M_{\odot}]-\mu_{c}\right)^{2}}{2\,\sigma_{\mathrm{C}}^{2}}\right\},$$

where σ_{C} is the logarithmic standard deviation, and μ_c is the peak of the CMF in logarithmic units. Despite this approximation, the analysis still applies to a large proportion of stars. If we consider that the log normal must merge smoothly into a power law, then for values of $\sigma_{_{St}}$ = 0.55 and $\gamma_{_{St}}$ = 1.35, i.e. the Salpeter slope, the log normal includes $\approx 60\%$ of all stars. This fraction increases as either or both $\sigma_{_{St}}$ and $\gamma_{_{St}}$ increases.

3.3.2 Initial Stellar and System Mass Functions

According to Chabrier (2005), the log normal section of the StIMF has a peak at 0.2 $M_{\odot}$ (or $\mu_{_{St}} = -0.7$), and a logarithmic standard deviation of $\sigma_{_{St}} = 0.55$. In contrast, the SysIMF is parametrised by a peak at 0.25 $M_{\odot}$ (or $\mu_{_{Sys}} = -0.6$) and a standard deviation of $\sigma_{sys} = 0.6$. I use Chabrier's StIMF in defining the quality factor (see Section 3.3.7). The SysIMF can also be computed in the program, but is not used in determining the best fit model. This is simply to reduce the number of free parameters of the model, however note that the position of the best fit is not significantly changed by omitting the SysIMF (See Figure 4.13).

Although there are claims of weak dependence of the StIMF on environment (e.g. Elmegreen et al. 2008), the dependence is weak and not established. I assume that the StIMF is universal.

3.3.3 Binary Frequencies

Stars are often found in multiple systems. Therefore any theory of stellar formation must also predict the formation of these multiple systems. To create binary systems in the model, I take two stars from each core (for those cores that fragment into 2 or more stars) and pair them to form a binary system. The remaining N_0-2 stars are assumed to be single stars. I do not investigate higher order systems during the course of the project, in part to simplify the model as much as possible, but also because the observational data on higher-order multiples are currently not statistically robust.

Informed by the results of Section 3.2.2, I assume that at birth, each core forms a bound core-cluster of N_0 stars. Over time, this core-cluster is disrupted, so that the systems that enter the field consist of one binary, and N_0-2 singles. To investigate how much influence dissipation may have during the dynamical evolution of a cluster, I will assume that the probability of a star of mass M becoming a member of the binary system is proportional to M^{β}. Large β represents pure gravitational interaction, with no dissipative forces, whilst small β represents

the influence of dissipation.

I choose to describe the binary population using the multiplicity frequency (see Chapter 2), and as I am not considering higher-order multiples, I refer to it as the binary frequency. Note that the long-lived binaries in the field are not the only ones to form, but simply the only ones which survive long enough to be found in mature field star populations.

3.3.4 Mass Ratios

For each binary system, I define the mass ratio as

$$q = \frac{M_2}{M_1}, \tag{3.3}$$

where M_1 is the mass of the larger star, and M_2 is the mass of its companion.

3.3.5 Assumptions

During the course of the project, I make the following assumptions:

- The central portions of both the CMF and StIMF are log normal.
- Mapping from the CMF to the StIMF is statistically self-similar.
- Initially, each core forms a bound core-cluster of N_0 stars. However, by the time the stars reach the field, the core-cluster has been disrupted, leaving a long-lived binary and N_0-2 single stars.
- The probability of a star being a part of this long-lived binary system is proportional to M^{β}.
- The evolution of cores to stars does not depend on either metallicity or environment.

3.3.6 Parameters

I parametrise the evolutionary model with nine quantities. Five are considered 'primary' and it is with respect to these that a best fit model is found. The influence of the remaining four 'secondary' parameters on the best fit model is then investigated.

Primary Parameters

- N_0: the average number of stars that each core will fragment into. A non-integer value of N_0 is allowed; when this is the case I divide the cores between the integer values so that the average is correct. For example, when $N_0 = 2.2$, 80% of the cores will produce 2 stars, and 20% of the cores will produce 3 stars. I investigate N_0 between 1.0 and 7.0.

- η_0: the average efficiency of a core, i.e. the fraction of the mass of the core at the time of observation that is converted into stars. I allow $\eta_0 > 1$ to account for any accretion that may take place after observation. I investigate η_0 between 0.00 and 2.00.

- σ_0: the average logarithmic standard deviation in the stellar masses produced by a single core. If σ_0 is small, then all the stars produced by a single core will have similar masses. As σ_0 increases, the masses of stars produced by a single core vary more widely. σ_0 is allowed to vary between 0.00 and 0.50. I chose this range to reflect that σ_0 must be smaller than σ_{St}.

- μ_c: the peak of the CMF in logarithmic units, where the peak of the CMF in solar masses is equal to 10^{μ_c}. Unlike the previous paramters, μ_c is constrained by observations, and over time we can expect improvements. I allow μ_c to vary between -0.2 and 0.2.

- $\sigma_{\rm C}$: the standard deviation of the CMF in $\log_{10}(M/M_\odot)$. This is the standard deviation of the combined CMFs inferred for all the star formation regions observed. I allow $\sigma_{\rm C}$ to range between 0.30 and 0.70. Note that in order for the mapping to be self similar, $\sigma_{\rm C}$ must be less than σ_{St}.

- β: the components of the binary system are chosen according to the probability distribution M^β. $\beta \gg 1$ implies purely gravitational interaction (the two most massive stars form the binary), whilst a smaller β suggests some form of dissipation. β ranges between -2 and 5.

Secondary Parameters

- χ_t: χ_t allows for a variation in the lifetimes of the cores, where the lifetime of a core it proportional to $M_{\rm c}^{\chi_t}$ allowing either larger cores to evolve faster ($\chi_t < 0$), or smaller cores ($\chi_t > 0$), as discussed in Section 3.1.1. So although the log normal CMF (Equation 3.3) is still the CMF observed, the number of cores evolving into stars per unit time becomes

$$P\left(\log_{10}\left[M_{\rm c}\right]\right) \propto \int_{\log_{10}[M'_{\rm c}]=-\infty}^{\log_{10}[M'_{\rm c}]=\log_{10}[M_{\rm c}]} \frac{{M'_{\rm c}}^{-\chi_t}}{(2\pi)^{1/2}\,\sigma_{\rm C}} \exp\left\{\frac{-(\log_{10}[M'_{\rm c}]-\mu_c)^2}{2\,\sigma_{\rm C}^2}\right\} {\rm d}\log_{10}\left[M'_{\rm c}\right] . \tag{3.4}$$

- χ_{σ_0}: σ_0 is replaced with $\sigma_0\left(\frac{M_{\rm c}}{M_\odot}\right)^{\chi_{\sigma_0}}$. This allows σ_0 to vary with the core mass. For $\chi_{\sigma_0} > 0$, larger cores have a greater standard deviation, and for $\chi_{\sigma_0} < 0$, smaller cores have a greater standard deviation.
- χ_{N_0}: N_0 is replaced with $N_0\left(\frac{M_{\rm c}}{M_\odot}\right)^{\chi_{N_0}}$. This allows the number of stars produced to vary from core to core. For $\chi_{N_0} > 0$, the larger cores fragment into more stars than the smaller cores, for $\chi_{N_0} > 0$; the smaller cores fragment into more stars.
- χ_{η_0}: η_0 is replaced with $\eta_0\left(\frac{M_{\rm c}}{M_\odot}\right)^{\chi_{\eta_0}}$. This allows feedback from massive stars to be included in the model. Since massive stars are thought to form in the larger cores, feedback can either suppress star formation in the high mass cores, ($\chi_{\eta_0} < 0$), or promote it ($\chi_{\eta_0} > 0$).

It is decided given the size of the parameter space, that the Markov Chain Monte Carlo method would be the most efficient way to find the optimum set of parameters. I assume that within these limits, all values are equally probably, outside these limits all values have a probability of 0.

Output parameters

The program is written to calculate the following parameters,

- $\mu_{_{St}}$: The peak of the StIMF in logarithmic units. The position of this peak in solar masses is therefore equal to $10^{\mu_{St}}$.
- $\sigma_{_{St}}$: The standard deviation of the StIMF in $\log_{10} M/M_\odot$.
- ${\rm BF}_i$: The binary frequency as a function of primary mass.
- ${\rm MR}_{ij}$: The mass ratio distribution as a function of primary mass.
- $\mu_{_{Sys}}$: The peak of the SysIMF in logarithmic units.
- σ_{sys}: The standard deviation of the SysIMF in $\log_{10} M/M_\odot$.

Observational constraints are strongest for μ_c, $\sigma_{\rm C}$, $\mu_{_{St}}$, $\sigma_{_{St}}$ and ${\rm BF}_i$. I hope to use the observational constraints on these parameters to provide an estimate of the parameters, N_0, η_0, σ_0 and β.

3.3.7 Quality Factor

I can determine how well a set of model outputs correspond to observations by defining a quality of fit. This is given by a sum of terms

$$Q_x = -\sum_{y=1}^{y=N_p} \frac{W_y(X_y - V_y)^2}{U_y^2}, \tag{3.5}$$

where Q_x is the quality factor that is associated with the combination of input variables $\boldsymbol{x} = (N_0, \eta_0, \sigma_0, \beta, \mu_c)$. W_y is the weight, V_y the observed value, U_y the uncertainty associated with the output parameter y, and N_p is the number of parameters we wish to use in calculating the quality factor. Thus the full expression becomes

$$\begin{aligned} Q\left(\mu_c, \sigma_{\rm C}, \eta_0, N_0, \sigma_0, \beta\right) \;=\; & -\frac{W_{\mu_{St}}(\mu_{St} - V_{\mu_{St}})^2}{2U^2_{\mu_{St}}} - \frac{W_{\sigma_{St}}(\sigma_{St} - V_{\sigma_{St}})^2}{2U^2_{\sigma_{St}}} \\ & -\sum_{i=1}^{i=6}\left\{\frac{W_{\rm BF_i}({\rm BF}_i - V_{BFi})^2}{2U^2_{\rm BF_i}}\right\} \\ & -\sum_{i=3}^{i=4}\left\{\sum_{j=1}^{j=6}\left\{\frac{W_{{\rm MR}_{ij}}({\rm MR}_{ij} - V_{{\rm MR}_{ij}})^2}{2U^2_{{\rm MR}_{ij}}}\right\}\right\}. \end{aligned} \tag{3.6}$$

Tables 3.1 to 3.3 give the weights, observed values and uncertainties associated with each of the parameters used in computing the quality factor. The observed values and uncertainties of the StIMF are given by Chabrier (2005), and I give both the mean and the standard deviation a weighting of 0.25, a total weight of 0.5 for the StIMF. This is summarised is Table 3.1.

Table 3.1: The first row of the table shows the observational, or expectation values for the StIMF parameters, μ_{St} and σ_{St} as given by Chabrier (2005). The second row gives the parameters weighting, and the bottom row gives the uncertainty on the expectation value.

Parameter	Logarithmic mean μ_{St}	Logarithmic standard deviation σ_{St}
Expectation values	-0.70	0.55
Weights	0.25	0.25
Uncertainties	0.1	0.05

Table 3.2 shows the data for the parameters associated with the binary frequency. I use four mass ranges over which to calculate the binary frequency. For very low-mass binaries, with primaries of masses between 0.05 $M_\odot$ and 0.1 $M_\odot$, I use the observed values and uncertainties

given in Close et al. (2003), and label it i=1. For binaries with primaries with masses between 0.05 and 0.17 $M_{\odot}$, I use the binary frequency and uncertainty given by Basri & Reiners (2006), and label it i=2. For M-dwarf binaries with primary masses between 0.15 and 0.59 $M_{\odot}$, I use the binary frequency and uncertainty given in Janson et al. (2012), and label it i=3. Finally, for solar-mass binaries, I use the binary frequency and uncertainty given by Raghavan et al. (2010), and label it i=4. The binary frequency is given a total weight of 0.25 (0.0625 for each observational bin).

I do not use the multiplicity of high-mass ($M/M_{\odot} \geq 8$) stars in computing the quality factor as our analysis is most pertinent to the mass range where the log normal form of the StIMF appears to be an acceptable approximation, i.e. 0.03 to 3 $M_{\odot}$.

Table 3.2: I use four mass ranges over which to calculate the binary frequency, to correspond with the following studies, Close et al. (2003) (i=1), Basri & Reiners (2006) (i=2), Janson et al. (2012) (i=3), and Raghavan et al. (2010) (i=4). The mass ranges are given in the top half of the table, with the observed multiplicity frequencies and their errors given in the bottom half. Each expectation value has a weight of 0.0625, giving a total weight of 0.25 for the binary frequencies.

Indicies, i	1	2	3	4
Min Masses, $M_{min}/M_{\odot}$	0.05	0.05	0.15	0.8
Max Masses, $M_{max}/M_{\odot}$	0.1	0.17	0.59	1.2
Expectation values, BF_i	0.20	0.26	0.27	0.44
Uncertainties	0.15	0.10	0.03	0.02

I use two mass ranges over which to calculate the mass ratio distribution, corresponding to the two studies with the most robust results. I use the mass ratio distribution and errors as determined by Raghavan et al. (2010) (i=4) and Janson et al. (2012) (i=3). The mass ratio distribution is binned into five bins of equal width 0.2, giving five observed values for each study. Each observed value has a weighting of 0.025, with a combined weighting for the mass ratios of 0.25. The sum of the weights for all the parameters is then equal to 1. I choose to weight the observations in this way because the StIMF has only 3 parameters, whilst the binary frequency has 4 parameters, and the mass ratios have 10 parameters. As the StIMF is the best constrained observationally, I want these parameters to contribute more to the fitting than the binary frequencies and mass ratios, hence those parameters have a heavier weighting. Between the parameters for the mass ratios/binary frequencies, the errors will ensure that the best data points will have a bigger affect on the quality factor.

A perfect fit, i.e. one where all the computed values are equal to their expectation values, will have $Q = 0$. The best fit is the fit with the largest Q value. The magnitude of Q can be interpreted as the number of standard deviations by which the predictions of a particular

Table 3.3: I use two mass ranges over which to calculate the mass ratio distribution, corresponding to the two studies with the most robust results. The top half of the table gives the expectation values and errors relating to (i=4), or Raghavan et al. (2010), whilst the bottom half of the table gives the expectation values and errors for (i=3), or Janson et al. (2012). The mass ranges are given in the final column. Each value has a weighting of 0.025, with a combined weighting of 0.25. The mass ratio distribution is binned into 5 bins.

Ratio	1 0.0-0.2	2 0.2-0.4	3 0.4-0.6	4 0.6-0.8	5 0.8-1.0	Mass range ($M_\odot$)
Expectation values, MR_{ij}, (i = 4)	0.10	0.25	0.21	0.19	0.25	0.80-1.20
Uncertainties	0.03	0.05	0.05	0.04	0.05	
Expectation values, $\overline{\mathrm{MR}_{ij}}$, (i = 3)	0.20	0.20	0.20	0.20	0.20	0.15-0.59
Uncertainties	0.05	0.05	0.05	0.05	0.05	

integration depart from the observations.

3.3.8 Normalisation

I investigate two methods for normalising the masses of stars produced by a single core.

- Scaling 1: The random gaussian variables $\mathcal{G}_i$ are divided by the sum of the random variables $\sum_i \mathcal{G}_i$. This ensures that the sum of the masses of the stars is exactly $\eta_0 M_\mathrm{c}$. However, the larger random variables have a disproportionate effect on the normalisation, producing (usually) one large star and several much smaller ones. The StIMF from this normalisation is skewed towards low masses, and the skewness increases dramatically with both σ_0 and σ_C. The effect is most noticeable when $\sigma_0 \gg \sigma_\mathrm{C}$.

- Scaling 2: The random variables $\mathcal{G}_i$ are divided by $N_0 m(\sigma_0)$, where $m(\sigma_0)$ is the arithmetic mean of a log normal centred at $x = 1$ ($\log(x) = 0$) with logarithmic standard deviation σ_0. The resulting StIMF does not have a skew, but the sum of the masses is no longer exactly equal to $\eta_0 M_\mathrm{c}$. Occasionally the sum of the mass of the stars even exceeds the original mass of the core, especially at very large efficiencies. However, I note that it does not matter if the sum of the masses of the stars exceeds the mass of the core on occasion, as cores may continue to accrete material between the time of observation and when star formation is complete.

Figures 3.1a and 3.1b, along with Table 3.4 show the comparison between these two normalisations. Figure 3.1a shows how the StIMF produced using Scaling 1 changes with N_0. A core of mass 1.25 $M_\odot$, efficiency $\eta_0 = 0.8$ and a variance in the stellar masses $\sigma_0 = 0.2$ is used. The continuous, long dash, dotted and dot-dash lines show $N_0 = 2$, 3, 4 and 5 respectively. The

parameters of the resulting StIMF are shown on the left hand side of Table 3.4. Figure 3.1b shows how the distribution of the total mass of stars ($\sum_i^{N_0} M_i$) changes with σ_0. A 1.25 solar mass core with efficiency $\eta_0 = 0.8$ is used. The continuous, long dash, dotted and dot-dash lines show $\sigma_0 = 0.1$, 0.2, 0.3 and 0.4 respectively. The variance of ($\sum_i^{N_0} M_i$) is given in the σ_{TOT} column in Table 3.4. The vertical line in Figure 3.1 is plotted at $M = 1.25\ M_\odot$, and indicates the proportion of cases in which $\sum M_i > M_c$, the values for these proportions are given in the final column of Table 3.4.

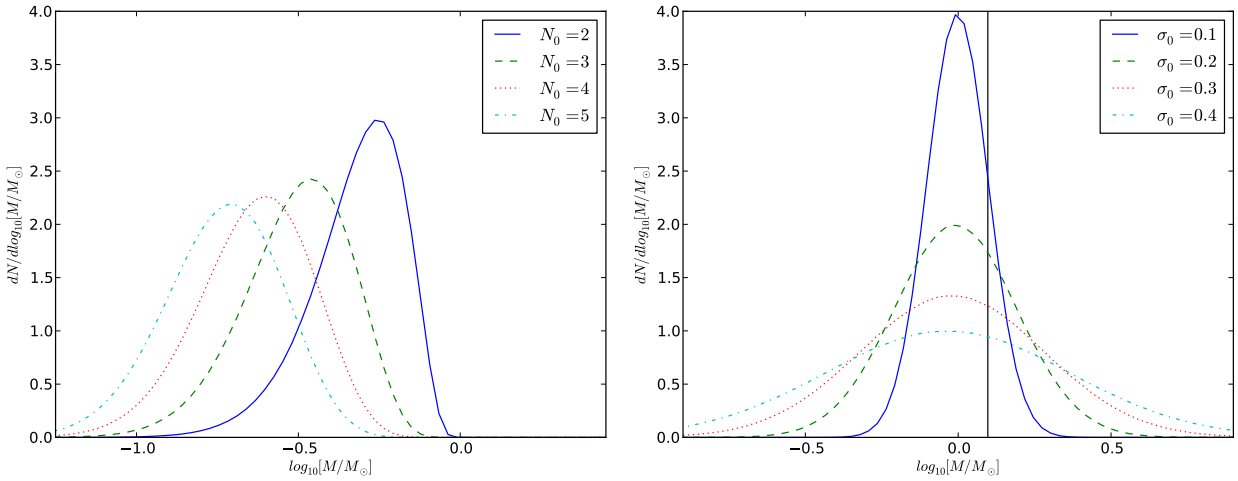

Figure 3.1: Normalisation of Stellar masses within a core. Figure 3.1a shows the StIMF produced using Scaling 1, with a core of mass 1.25 $M_\odot$, efficiency 0.8 and a variance in the stellar masses of 0.2. The continuous, long dash, dotted and dot-dash lines show $N_0 = 2$, 3, 4, and 5 respectively. Figure 3.1b shows the distribution of the total mass of stars ($\sum_i^{N_0} M_i$) created from a 1.25 solar mass core with efficiency 0.8 using scaling 2. The continuous, long dash, dotted and dot-dash lines show $\sigma_0 = 0.1$, 0.2, 0.3 and 0.4 respectively. The vertical line in Figure 3.1 is plotted at $M = 1.25\ M_\odot$, and indicates the proportion of cases in which $\sum M_i > M_c$.

When Monte Carlo searches using Scaling 1 and Scaling 2 are compared, it is found that the results are almost identical and hence it does not matter which scaling I use. Note that these two normalisations converge as $N_0 \to \infty$, but the difference becomes negligible even for $N_0 \sim 4$. We could expect an error of 10% in the peak of the StIMF with Scaling 1, and an error in σ_{St} that decreases with σ_0. errors would be more significant for small N_0. I proceed using Scaling 2 only.

Table 3.4: The parameters of the resulting StIMF as shown in Figure 3.1a are shown on the left hand side of the table. The variance of the sum of the masses of stars produced in a core, as shown in Figure 3.1b are given in the σ_{TOT} column. The final column of Table 3.4 gives the fraction of cases where the mass of the sum of the stars exceeds the mass of the core when the efficiency is 80% for Scaling 2, Figure 3.1b. The values given in bold are the expected values for a perfect self-similar mapping, by comparing these values with the actual values, we can get a feel for how much the scalings will change the results.

Scaling 1							Scaling 2			
μ_{St}		σ_{St}		γ_{St}	N_0		σ_0	σ_{TOT}		$f_{80\%}$
-0.33	(-0.30)	0.16	(0.2)	-0.92	2		0.4	0.17	(0.40)	0.39
-0.51	(-0.47)	0.18	(0.2)	-0.56	3		0.3	0.13	(0.30)	0.32
-0.64	(-0.60)	0.19	(0.2)	-0.40	4		0.2	0.11	(0.20)	0.26
-0.74	(-0.70)	0.20	(0.2)	-0.32	5		0.1	0.10	(0.10)	0.21

Chapter 4

Mapping from the CMF to the StIMF Results

I run a numerical program that evolves a given CMF according to a simple set of rules into a sample of binary and single stars. The properties of the resultant stars are compared with observations of the StIMF, binary frequency and mass ratios as a function of primary mass. I find that self-similar mapping is capable of reproducing the current observations if cores fragment into about 4 or 5 of stars with an average notional efficiency of $\eta_0 \approx 1.0 \pm 0.3$.

In this chapter I present and discuss the results of the mapping study described in Chapter 3. This chapter has in part been published in Holman et al. (2013).

4.1 Results

The density of points in the Markov chain with $Q > -1$ is plotted in Figure 4.1. The mean and standard deviation of the peaks give us the best fit, and are given in Table 4.1. The best fit has a quality factor of $Q = -0.33$. Note that the errors as quoted in Table 3.4 for Scaling 1 are of the same magnitude as the errors for the best fit values, but that Scaling 2 has an error for the peak for the StIMF much smaller than that quoted in Table 4.1, but the error for μ_c is greater than the error for the best fit. However, as will be explained later on, we are more interested in constraining N_0, which governs μ_c, than σ_0, which governs $\sigma_{\rm C}$, as observations are closer to observing N_0 than σ_0.

Figures 4.2 to 4.9 are slices through the parameter space centred on the best fit. The y-axis parameter is the same for all the plots on a single row, as is the x-axis parameter on all plots on a single column. The contours are 1σ, 2σ, 3σ, 4σ and 5σ, and the colour encodes the values of Q (Figures 4.2 and 4.3), the contribution to the quality factor due to the StIMF, $Q_{\rm IMF}$ (Figures 4.4 and 4.5), the contribution to the quality factor due to the binary frequency, $Q_{\rm BF}$ (Figures 4.6 and 4.7) and the contribution to the quality factor due to the mass ratios, $Q_{\rm MR}$ (Figures

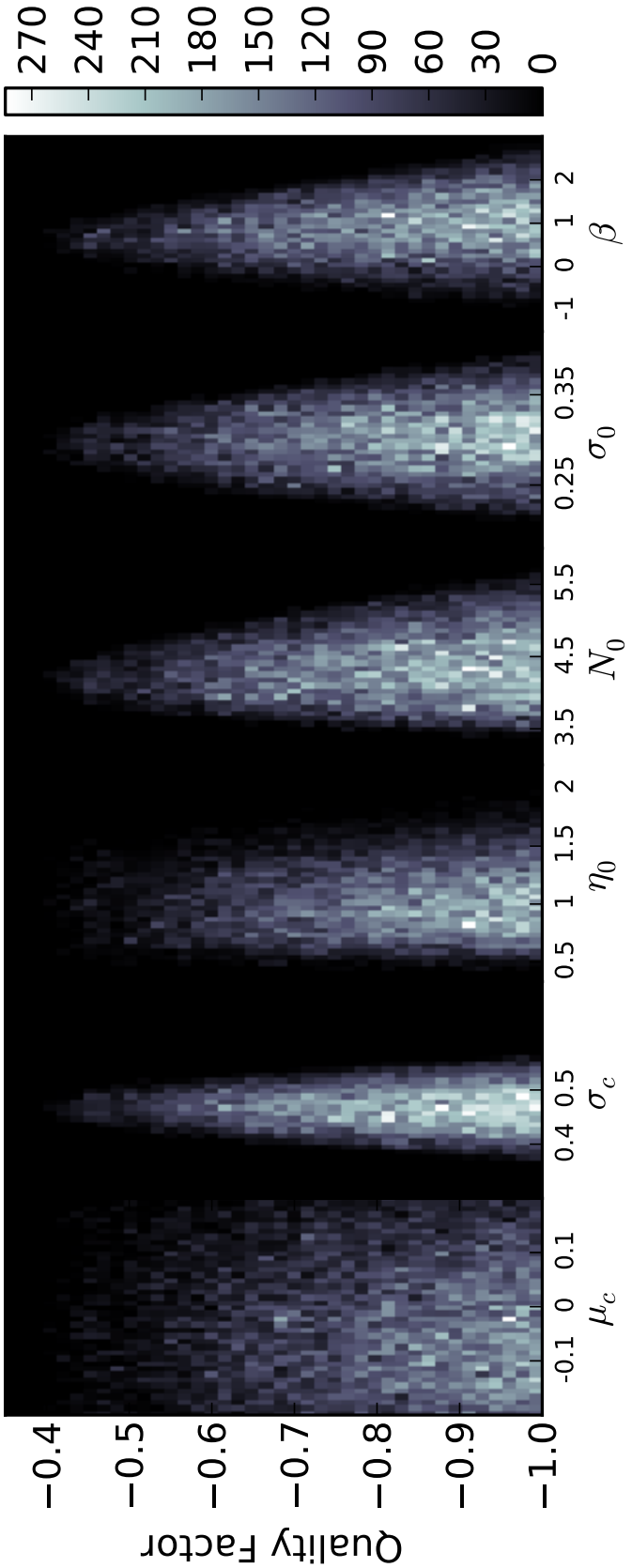

Figure 4.1: Density of Markov Chain Monte Carlo points accepted. For each graph, I have plotted a histogram of Q against primary parameter, with a cutoff at $Q = -1$. We can see clearly the peaks of the distributions. The mean and standard deviation of these peaks give us the best fit.

Table 4.1: This table gives the mean and standard deviation of the peaks as shown in Figure 4.1, and are the values that give the best fit to observations.

Parameter	Best Fit
μ_c	-0.03 ± 0.10
σ_{C}	0.47 ± 0.04
η_0	1.01 ± 0.27
N_0	4.34 ± 0.43
σ_0	0.30 ± 0.03
β	0.87 ± 0.64
Q	-0.33

4.8 and 4.9).

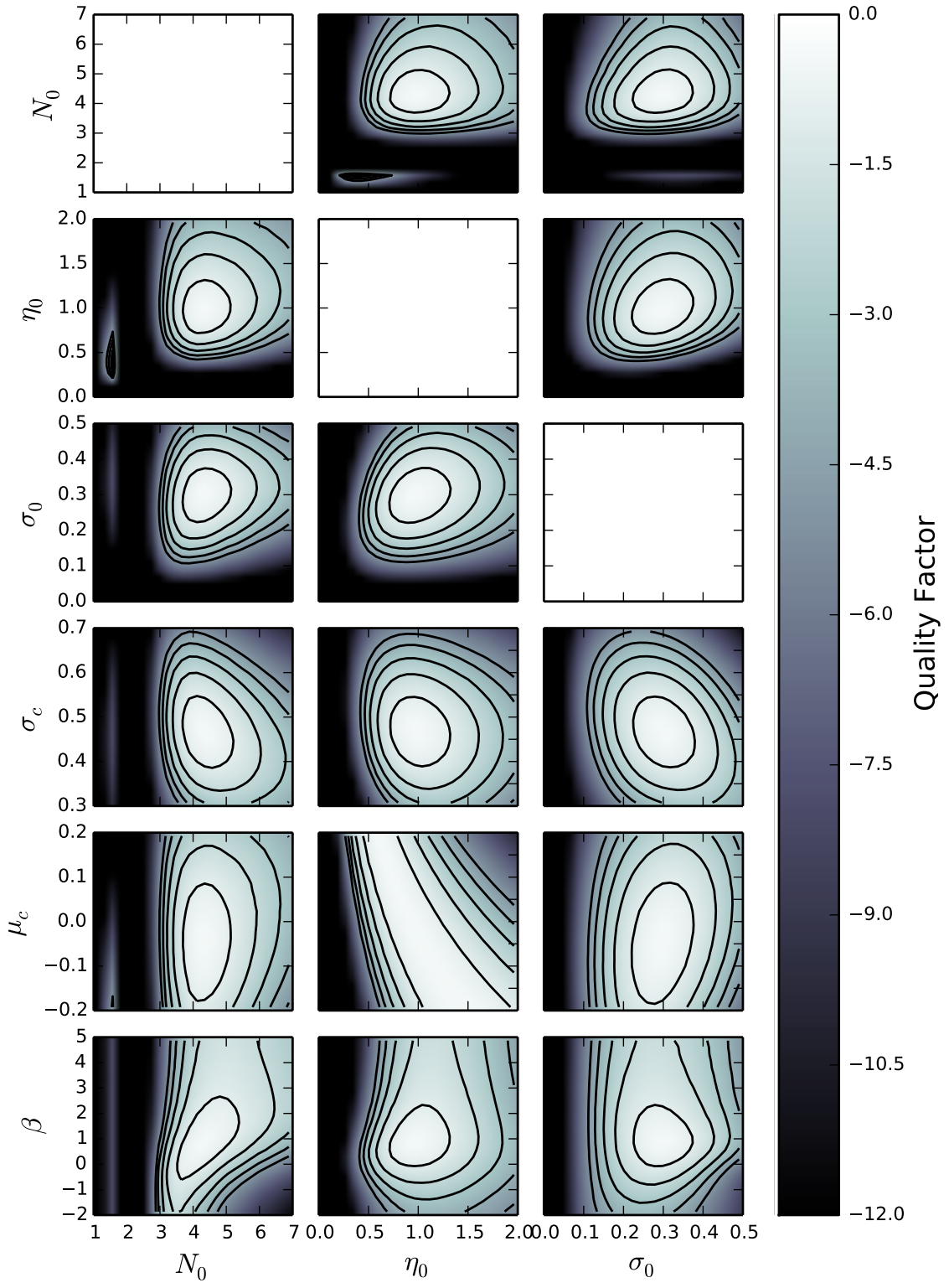

Figure 4.2: Slices through the parameter space centred on the best fit. The contours show 1, 2, 3, 4 and 5σ, and the colour encodes the values of Q, getting darker as the value of Q decreases. The montage is shown over two pages for ease of reading. For a given column, the x-axis parameter is the same, and for a given row, the y-axis parameter is the same. One can see which parameters are correlated and which are tightly constrained by scanning along either a row or a column.

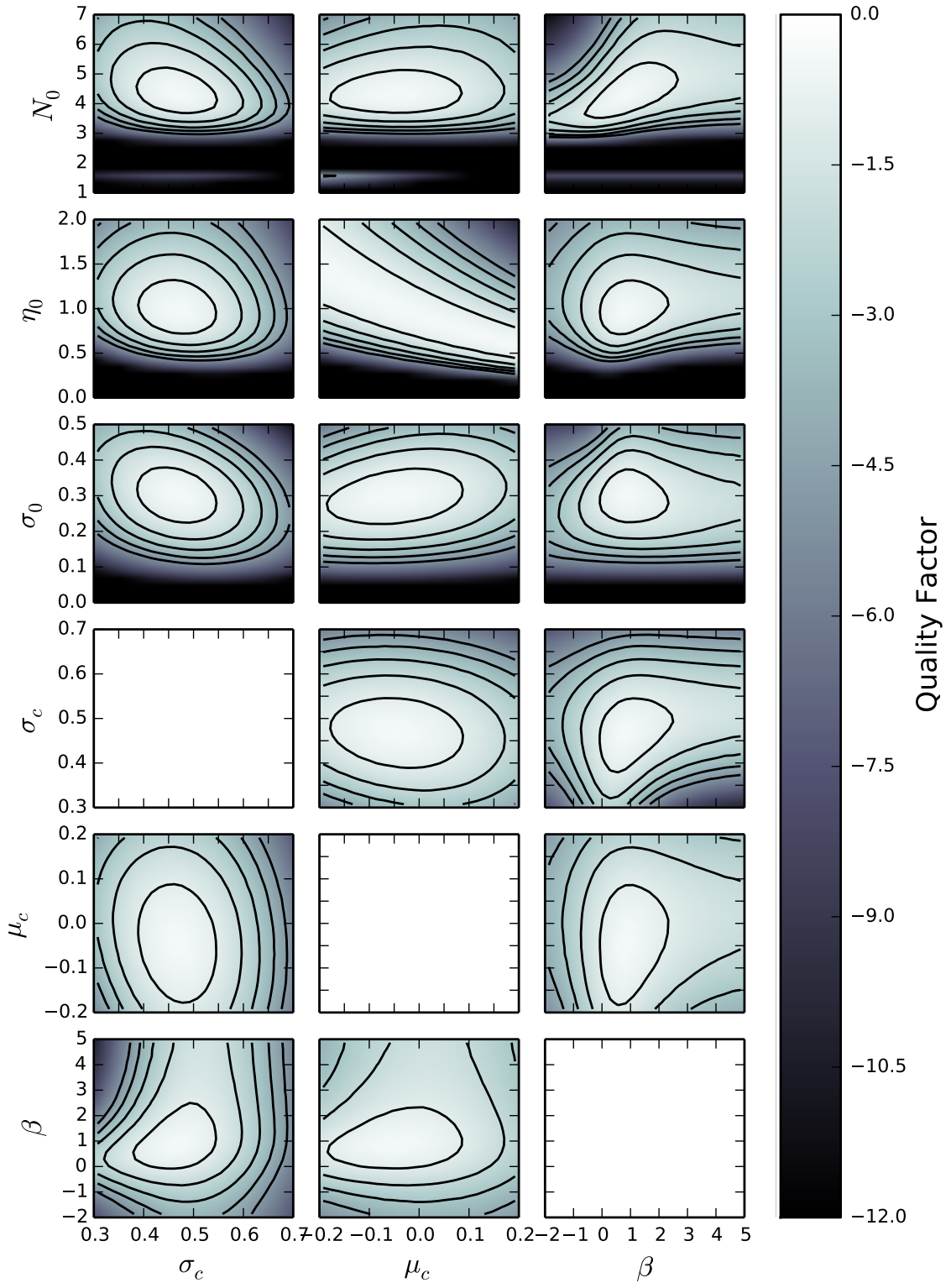

Figure 4.3: Slices through the parameter space centred on the best fit. The contours show 1, 2, 3, 4 and 5σ, and the colour encodes the values of Q, getting darker as the value of Q decreases. The montage is shown over two pages for ease of reading. For a given column, the x-axis parameter is the same, and for a given row, the y-axis parameter is the same. One can see which parameters are correlated and which are tightly constrained by scanning along either a row or a column.

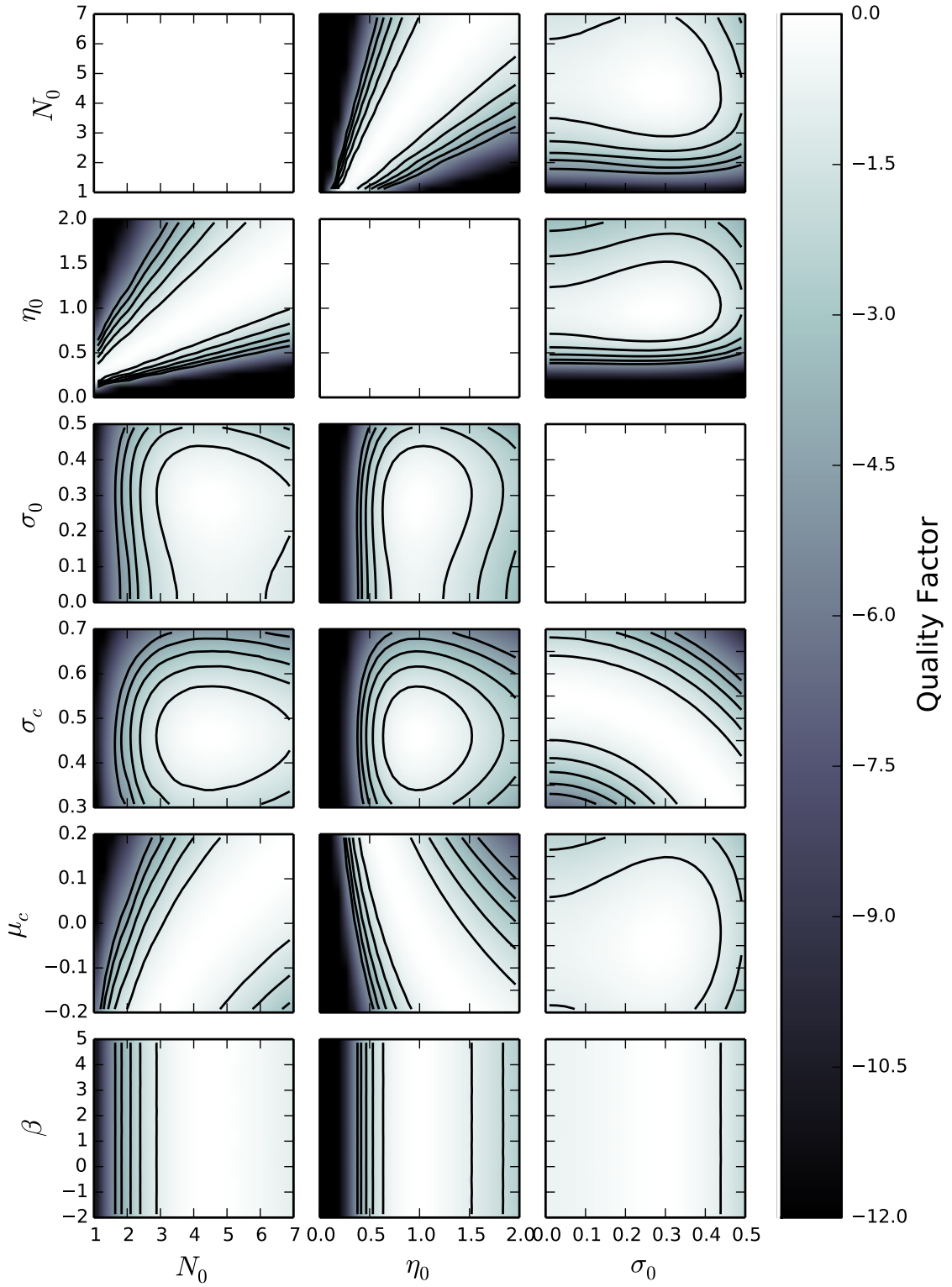

Figure 4.4: See caption for Figure 4.2. The colour now encodes the contribution to the quality factor due to the StIMF.

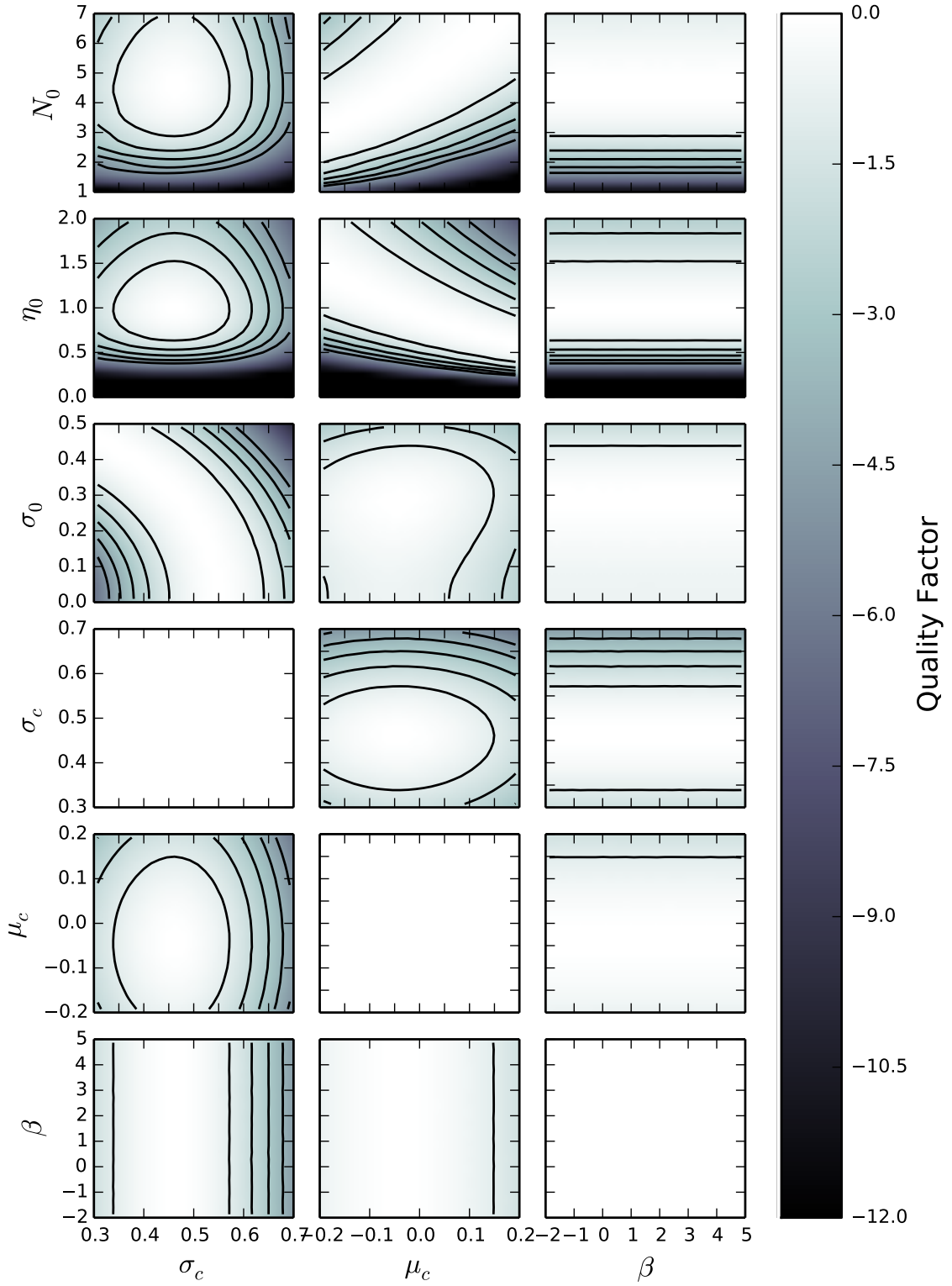

Figure 4.5: See caption for Figure 4.2. The colour now encodes the contribution to the quality factor due to the StIMF.

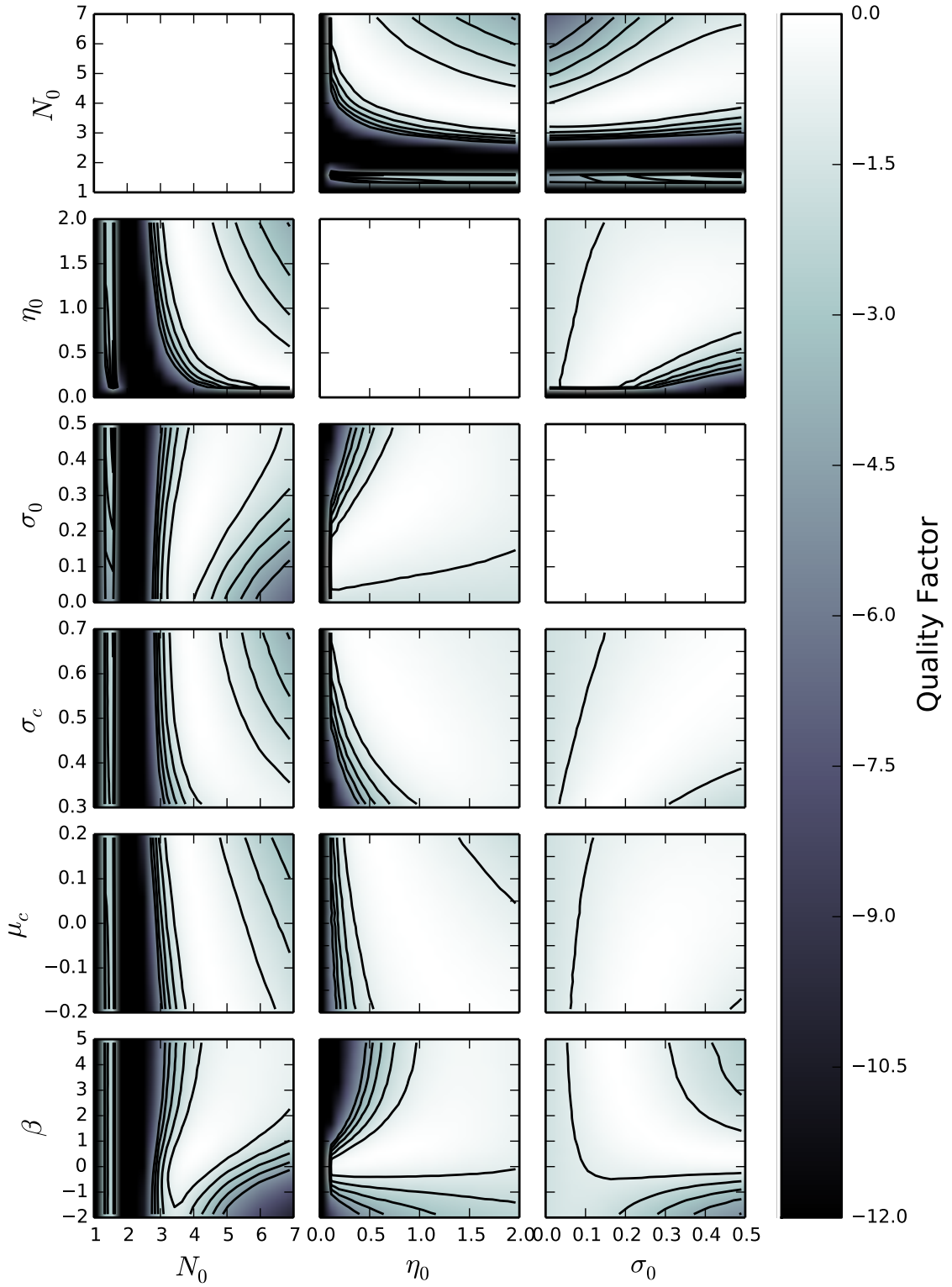

Figure 4.6: See caption for Figure 4.2. The colour now encodes the contribution to the quality factor due to the binary frequency.

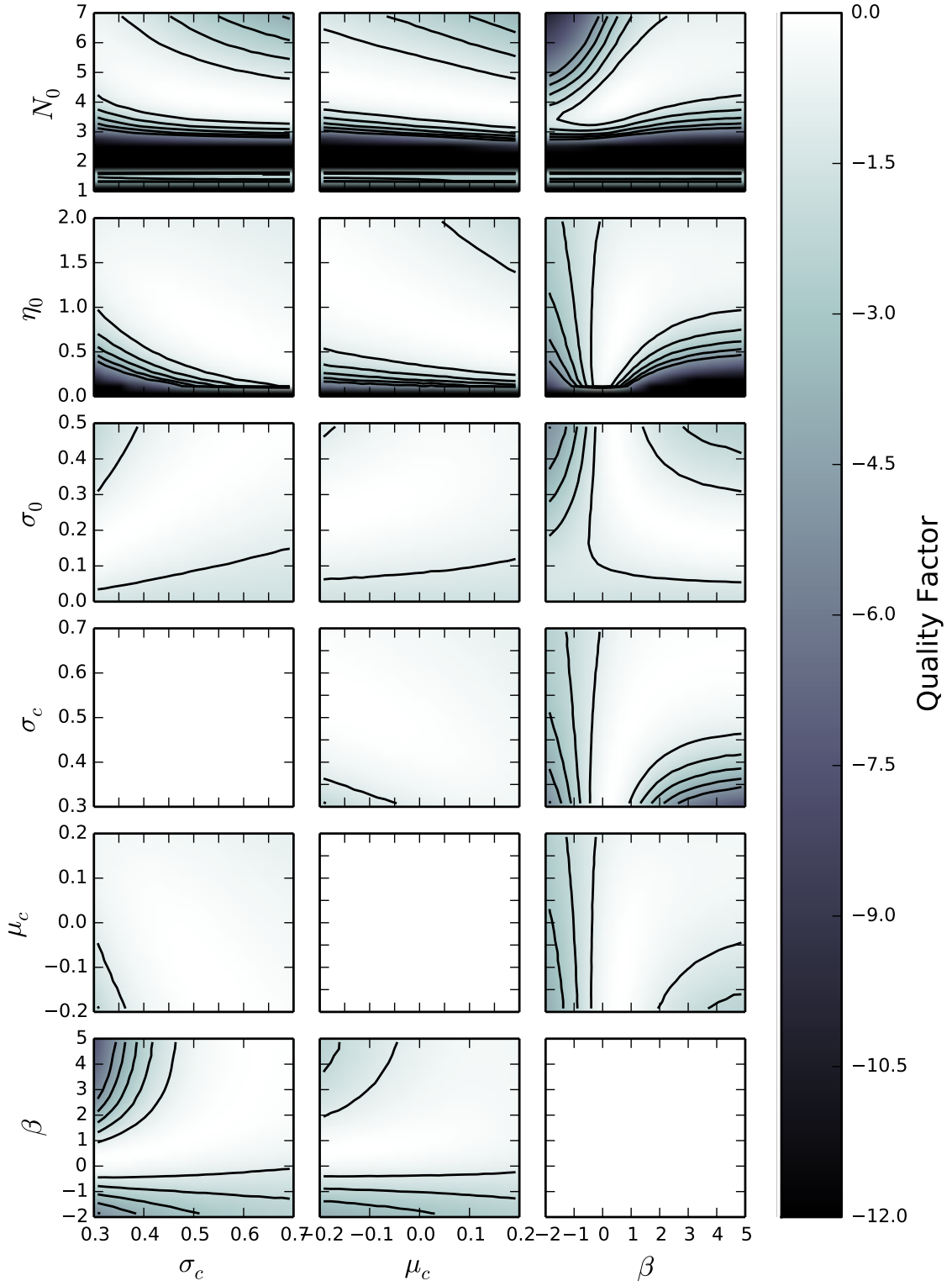

Figure 4.7: See caption for Figure 4.2. The colour now encodes the contribution to the quality factor due to the binary frequency.

Figure 4.10 shows the best fit binary frequency, and observations of the same mass ranges. The best fit model reproduces the observational results very well for Close et al. (2003), Basri & Reiners (2006), Janson et al. (2012) and Raghavan et al. (2010), the four lowest mass bins. The two highest mass bins represent surveys of O and B stars by Preibisch et al. (1999) and Mason et al. (1998). I plot these to show that despite not being included in defining the best fit, they agree very well with the model.

Figures 4.11 and 4.12 demonstrate that the mass ratios are reproduced fairly well by the best fit model.

4.2 Discussion

4.2.1 Stellar Initial Mass Function

It is found when fitting the calculated StIMF to Chabrier's model, that the primary variables divide naturally into 2 groups, (N_0, η_0, μ_c), and ($\sigma_{\rm C}$, σ_0).

N_0, η_0, and μ_c: This set of variables has a high influence on μ_{St}, with very little effect on the standard deviation σ_{St}. By hypothesising that the peak of the CMF is shifted to lower values by a factor equal to the effective efficiency relating to one star, i.e. η_0/N_0, and by taking logs of both side we get

$$\mu_{St} = \mu_c + \log_{10}(\eta_0) - \log_{10}(N_0), \tag{4.1}$$

or equivalently,

$$F = 10^{(\mu_c - \mu_{St})} = \frac{N_0}{\eta_0} \approxeq 4 \pm 1. \tag{4.2}$$

$\sigma_{\rm C}$ and σ_0: These two standard deviations have a large influence on the standard deviation of the final StIMF distribution, but changes in these parameters do not affect μ_{St}. The standard deviations add in quadrature to produce the StIMF standard deviation.

$$\sigma_{St} = \sqrt{\sigma_0^2 + \sigma_{\rm C}^2} \tag{4.3}$$

From this, we can infer that, as σ_{St} and $\sigma_{\rm C}$ are similar in size, σ_0 cannot be too large.

As can be seen from Figures 4.2 to 4.9, μ_c has no effect on the quality factor at all - any change is compensated for by a simple shift in the efficiency. Looking at Equation (4.1) in more

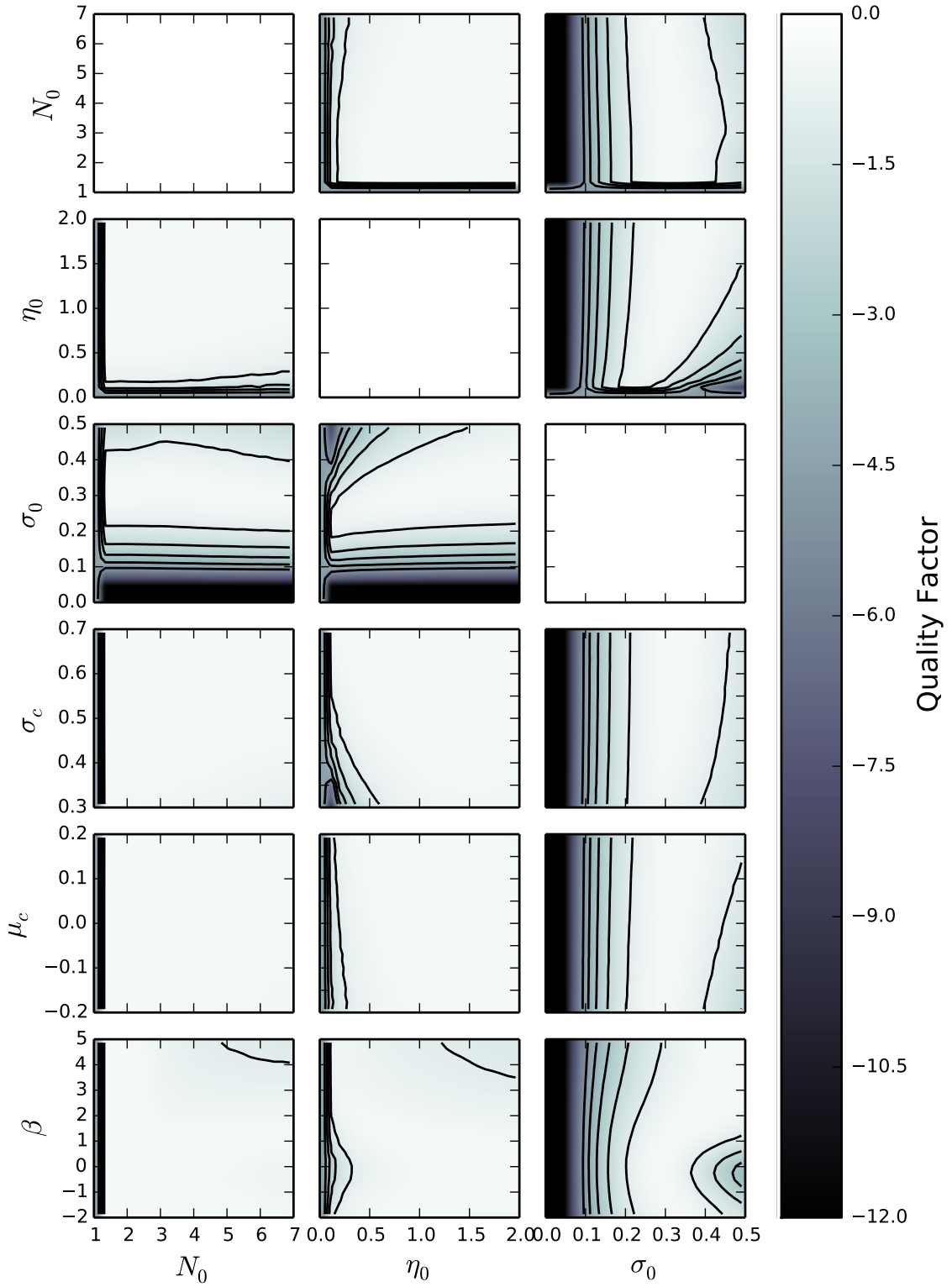

Figure 4.8: See caption for Figure 4.2. The colour now encodes the contribution to the quality factor due to the mass ratios.

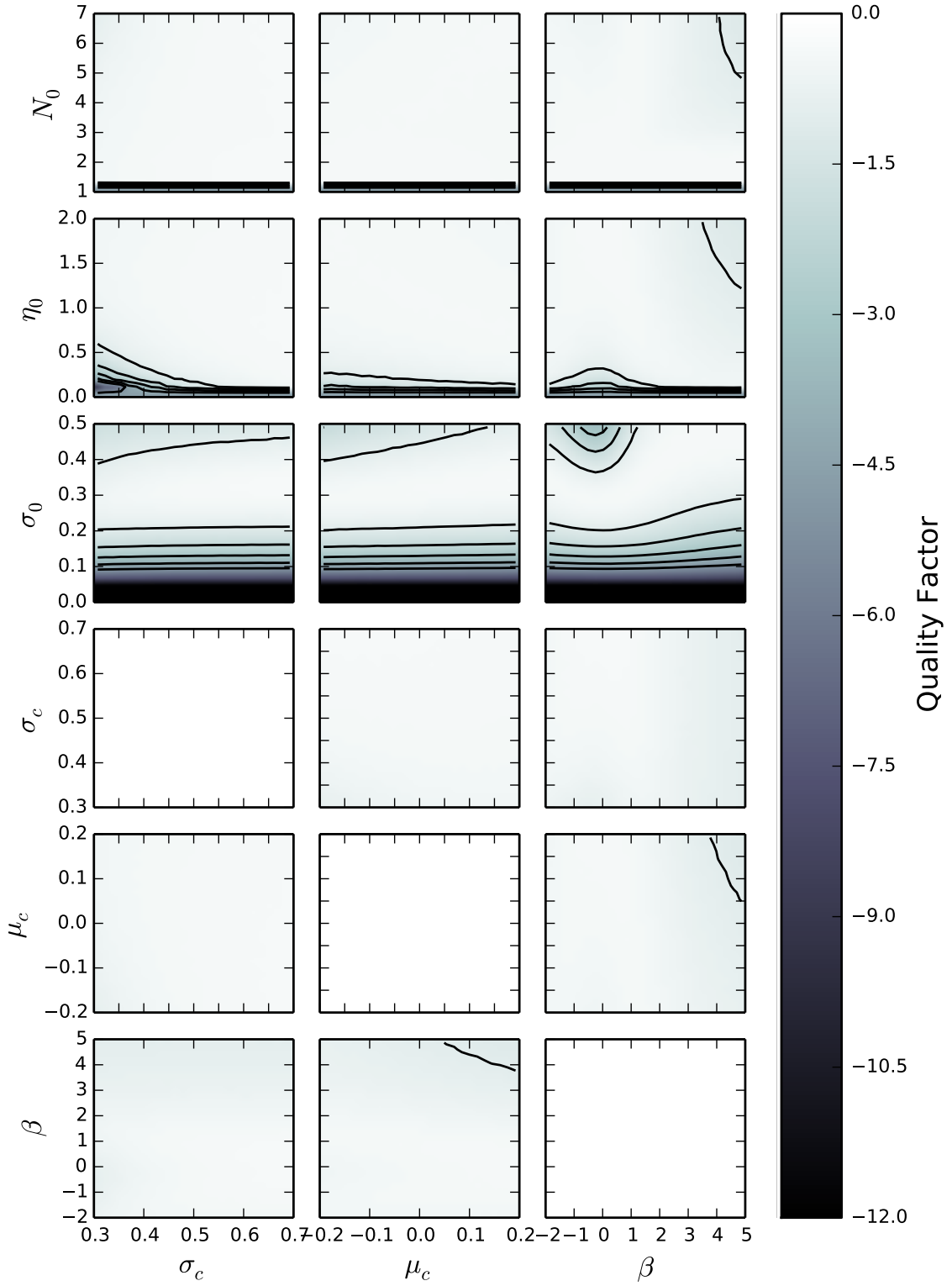

Figure 4.9: See caption for Figure 4.2. The colour now encodes the contribution to the quality factor due to the mass ratios.

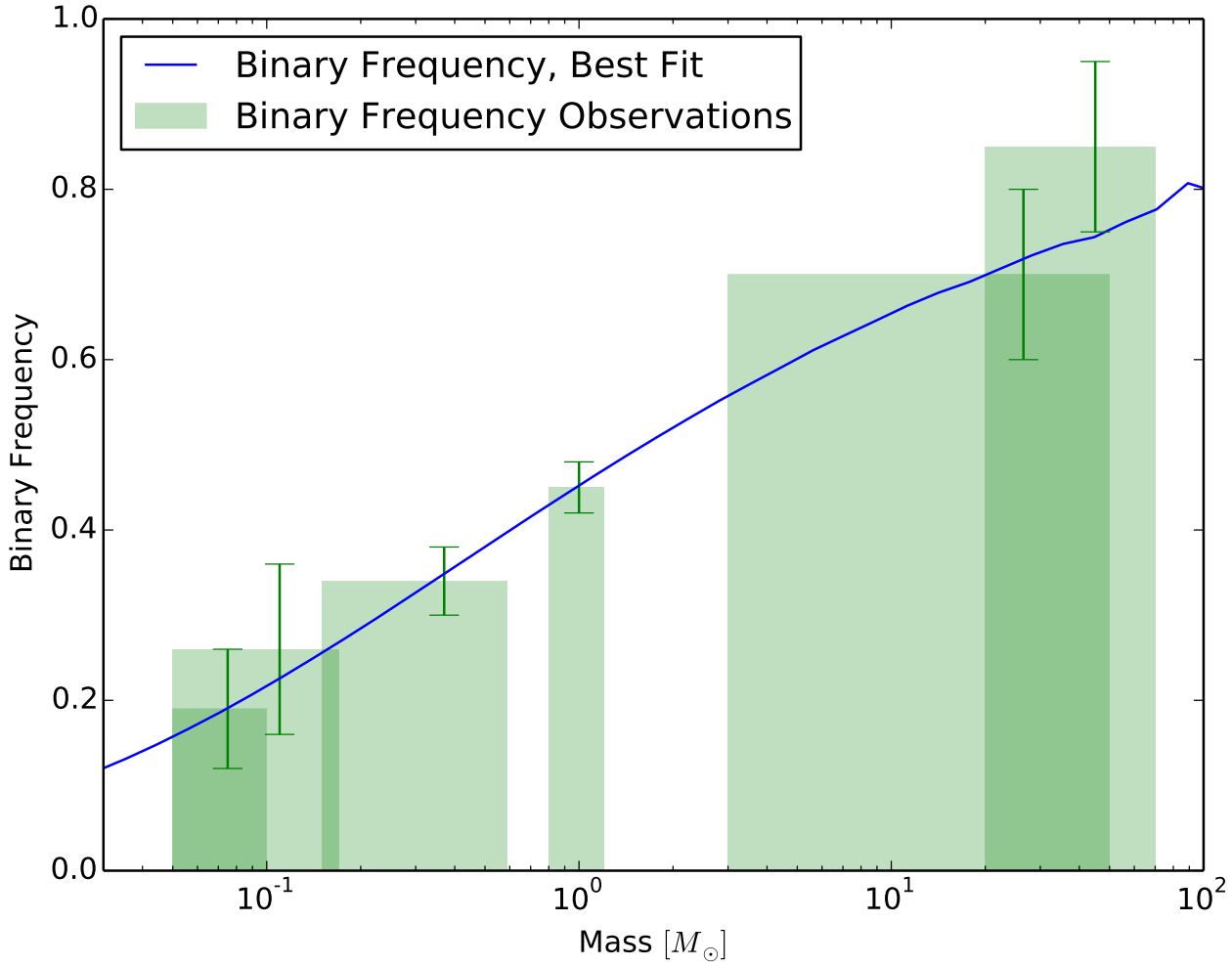

Figure 4.10: The Binary Frequency (solid line) as predicted by the best fit model. The boxes are the observational data, and the error bars are their uncertainties. Note that the two most massive bins are not used in the fitting procedure, but nevertheless fit the model very well indeed.

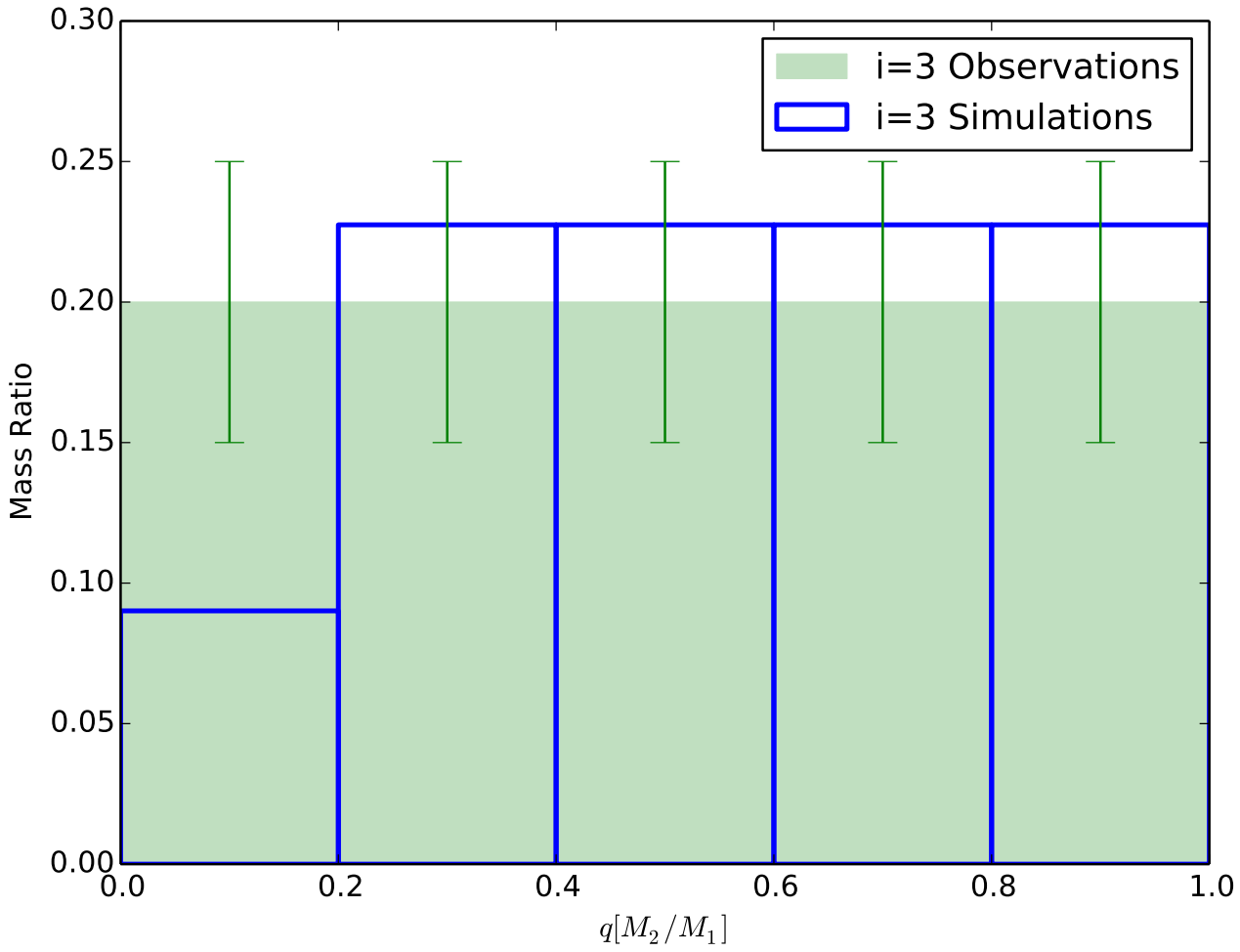

Figure 4.11: The mass ratios (filled boxes) as predicted by the best fit model in the mass range of Bin 3. The non-filled boxes and their errors bars are the observational data according to Janson et al. (2012).

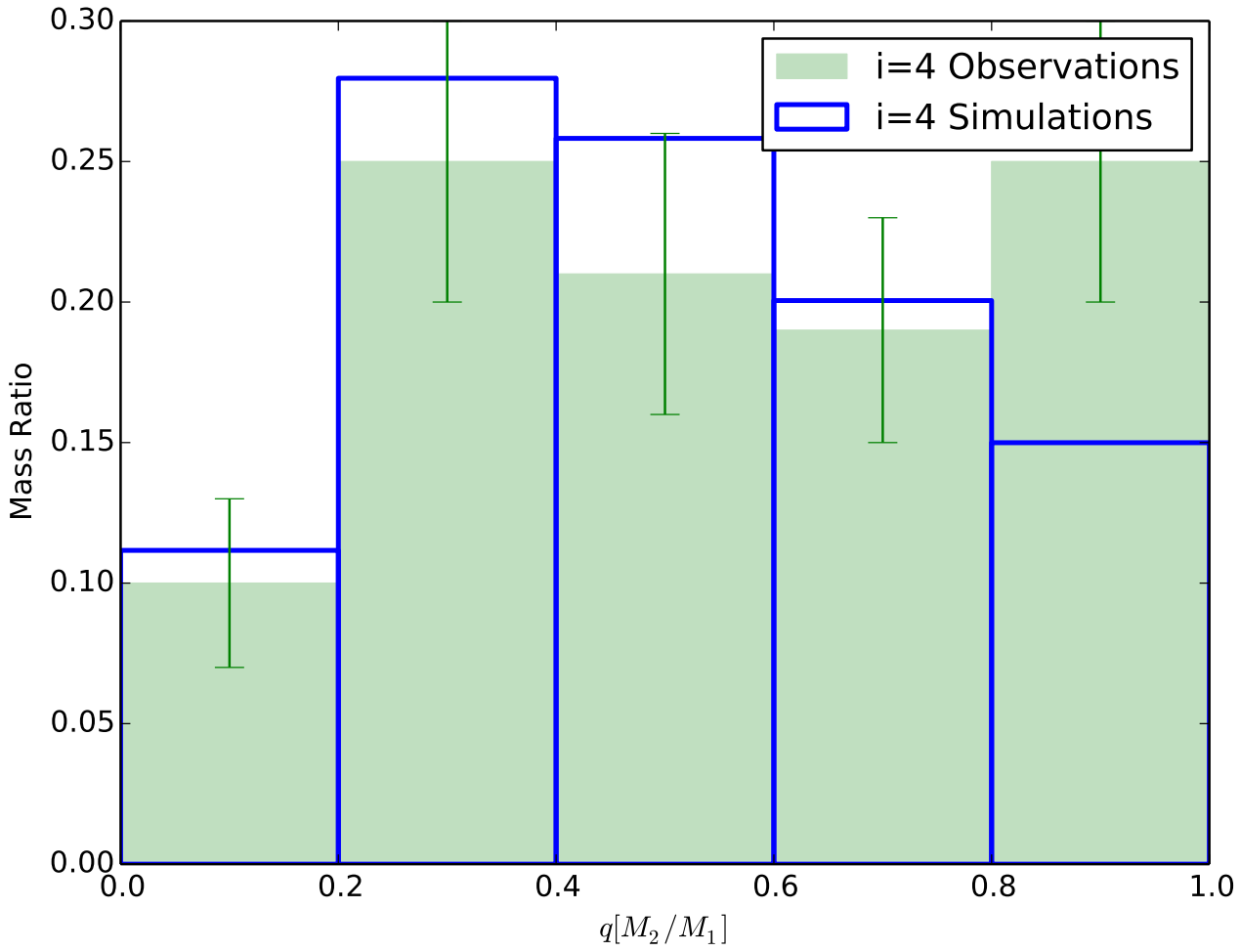

Figure 4.12: The mass ratios (filled boxes) as predicted by the best fit model in the mass range of Bin 4. The non-filled boxes and their errors bars are the observational data according to Raghavan et al. (2010).

detail, it can be seen that for a given value of N_0, any change in μ_c is compensated for by a change in η_0, i.e.

$$10^{\mu_c}\eta_0 = 10^{\mu_{St}}N_0. \tag{4.4}$$

We can see that it is very easy to reproduce the StIMF from the CMF, but there is a degeneracy between N_0 and η_0. I now show that binary statistics can break this degeneracy.

4.2.2 Binary Frequencies

The binary frequency is influenced strongly by N_0 (see Figures 4.6 and 4.7)with troughs in the quality factor at both $N_0 = 1$ and 2, with a small peak at $N_0 = 1.5$, and a larger peak for $N_0 > 2$. The troughs occur because when $N_0 = 1$ or 2, all the systems produced are singles or binaries respectively. Since astronomers observe a mixture of both single and binary systems, these scenarios clearly cannot satisfy the expectation values, and so there is a poor quality factor at these values.

To understand why the best fir occurs for $N_0 > 2$, assume that on average, 60% of systems are single, and 40% are binaries. For $N_0 = 1.4$, the ratio of binaries to singles is correct. However, consider that for $1 < N_0 < 2$ each core will either fragment into two stars, or collapse to a single star with equal efficiency. The single stars will therefore always be larger on average than the primaries in the binary systems. As a consequence, the binary frequency decreases with primary mass. $N_0 = 3.5$ also produces the correct ratio of binaries to singles. However, in this case, the single stars are the ones left over after two stars from each core have been selected for the binary system, and so they will tend to be the smaller stars. The binary frequency now increases with primary mass, which is why the best fit occurs for $N_0 > 2$.

As N_0 increases, the binary frequency decreases across the mass range, preferentially in the low mass regions, due to more low mass singles being produced, resulting in a steeper binary frequency. A larger σ_0 value will also produce a steeper slope due to the greater difference in masses between the primary produced by a core, and its singles. Finally, a larger value of β also produces a steeper slope of binary frequency against primary mass. This is because as β increases, the high-mass stars in a core will almost always form the binary system, whereas the smaller stars are almost always singles.

4.2.3 Mass Ratios

The best fit reproduces the mass ratios satisfactorily.

For $N_0 < 2$, the mass ratio distribution is independent of N_0. This is because only the number of cores fragmenting into a binary changes. The manner in which a core forms a binary

is the same.

$\beta \gg 1$ favours binaries with mass ratios approximately 1, as the two largest stars are commonly chosen to form a binary. Since the stars will often be similar in size, the mass ratio tends to 1.

As σ_0 is increased, the larger the difference in masses, and the more likely it is that unequal mass binaries are going to be produced. For $\sigma_0 = 0$, every mass ratios is equal to 1, whilst intermediate values of σ_0 reproduce a flat mass ratio distribution.

Hubber & Whitworth (2005) find that the distribution of mass-ratios is strongly dependent on σ_0, and only lightly dependent on N_0. That result is reproduced in this experiment.

4.2.4 System Initial Mass Function

The SysIMF is given as an output from the program, but its dependence on the input parameters was not investigated. However, I do find that the SysIMF peaks at higher masses, has a larger standard deviation than the StIMF and skews slightly to lower masses. This is a result of pairing stars with a probability biased towards the more massive stars, i.e. larger stars are either removed (secondaries), or are given a greater mass (primaries), hence pushing the peak to higher values. But low-mass stars are less likely to be in a binary system, and are not affected so much as higher-mass stars, hence the distribution at low masses approaches that of the StIMF, and the SysIMF has a skew towards lower masses.

4.2.5 Exponents

Now that a 'best fit' has been obtained, the values of χ_t, χ_{σ_0}, χ_{N_0} and χ_{η_0} are allowed to vary, and the effects on the StIMF are investigated.

Table 4.2: Fixed Parameters. The following parameters were kept fixed as the exponents were allowed to vary.

N_0	η_0	σ_0	$\sigma_{\rm C}$	μ_c
3.6	0.73	0.22	0.51	0.00

Figure 4.14 shows the effect of χ_{η_0} on the StIMF. η_0 accounts for feedback from massive stars. This feedback can either suppress star formation in the high mass cores, ($\chi_{\eta_0} < 0$), or promote it ($\chi_{\eta_0} > 0$). There is no observable effect on either the mean or the skew of the StIMF. The standard deviation of the StIMF however, increases as χ_{η_0} increases. This is because as χ_{η_0} increases, the high-mass cores produce even bigger stars, and the low-mass core produce even smaller stars, and so the spread in stellar masses is greater. As χ_{η_0} decreases, the low-mass cores produce more massive stars, and the high-mass cores produce smaller mass stars. The

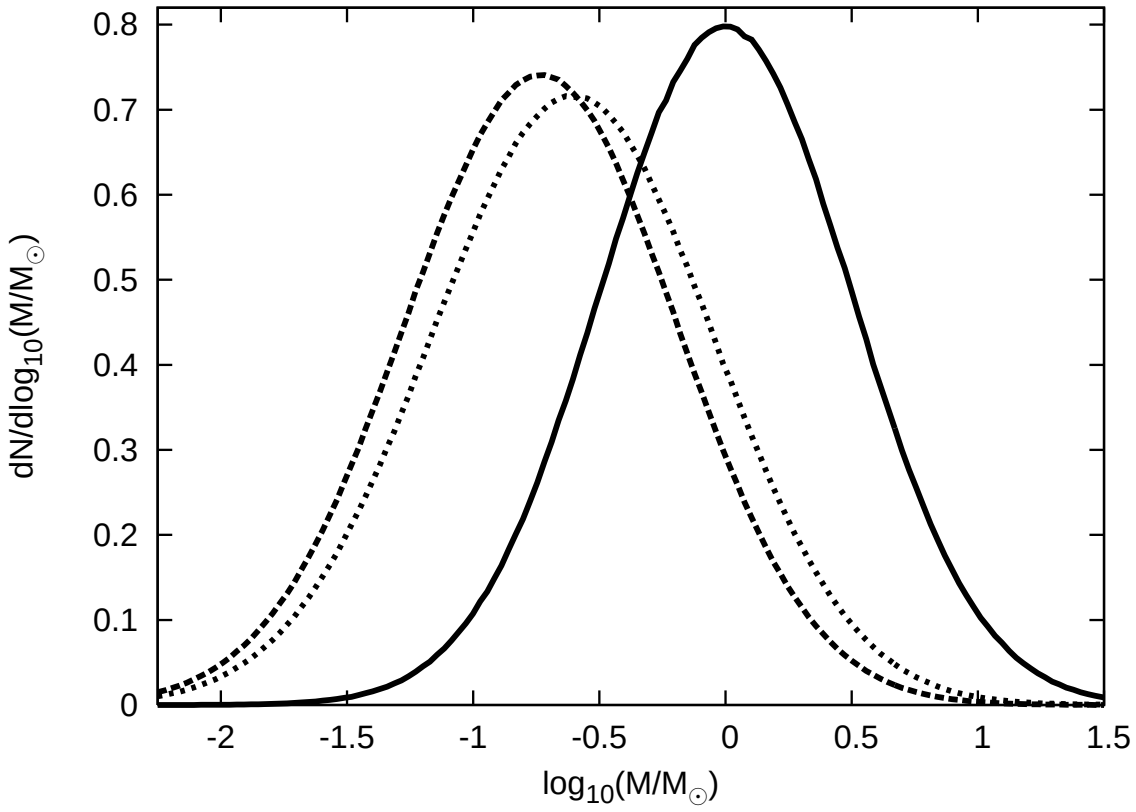

Figure 4.13: This graph shows the best fit CMF (solid black line) and StIMF (dashed line), along with the SysIMF (dotted line). Note that if we were to plot Chabrier's StIMF, it would lie directly on top of the best-fit StIMF.

average mass of a star is less dependent on the mass of the parent core, with all masses of cores producing similar size stars. Hence, the standard deviation of the StIMF decreases.

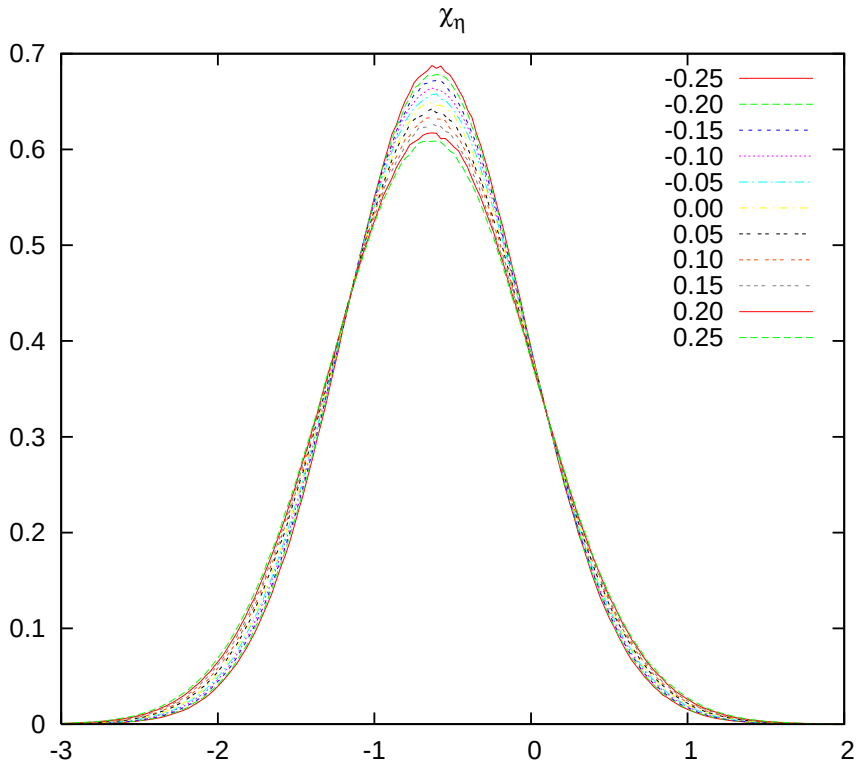

Figure 4.14: Variation of the StIMF with χ_{η_0}. The mean and skew of the StIMF remain roughly constant with χ_{η_0}. The standard deviation of the StIMF increases as χ_{η_0} goes to higher positive values, and decreases as χ_{η_0} goes to more negative values.

Figure 4.15 shows the variation of the StIMF with χ_{N_0}. For $\chi_{N_0} > 0$, the larger cores fragment into more stars than the smaller cores, for $\chi_{N_0} > 0$; the smaller cores fragment into more stars.

The peak of the StIMF moves towards larger masses as χ_{N_0} increases, and moves towards smaller masses as χ_{N_0} decreases. This is because as χ_{N_0} increases, the smaller cores produce fewer, more massive stars, meaning that fewer low-mass stars are produced. With increasing χ_{N_0}, the skew of the StIMF towards lower masses increases, as smaller cores produce fewer, more massive stars. The larger cores produce more stars, but these stars are limited in mass by the core mass, and so the high-mass tail of the StIMF does not increase by as much as the low-mass tail. This effect also means that the standard deviation of the StIMF decreases as χ_{N_0} increases.

Figure 4.16 shows the variation of the StIMF with χ_t. χ_t allows either larger cores to evolve faster ($\chi_t < 0$), or smaller cores ($\chi_t > 0$). The standard deviation and skew of the StIMF both

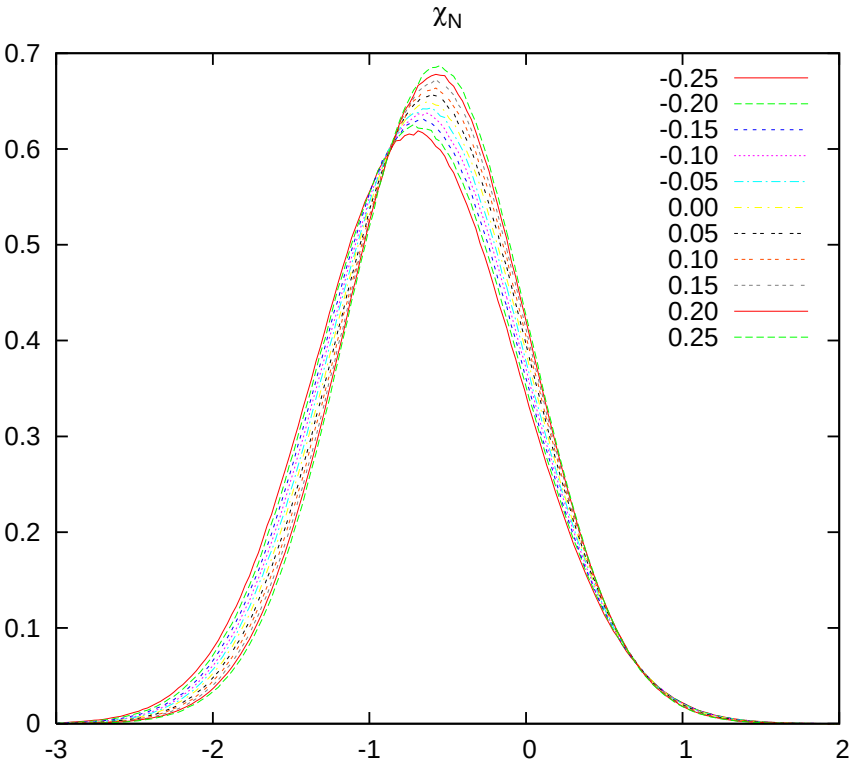

Figure 4.15: Variation of the StIMF with χ_{N_0}. The peak of the StIMF moves towards larger values as χ_{N_0} increases, and moves towards more negative values as χ_{N_0} decreases. With increasing χ_{N_0}, both the skew of the StIMF and the standard deviation decrease.

remain constant with any variation in χ_t, whilst the mean of the StIMF moves towards lower masses as χ_t increases. As χ_t increases, fewer large cores collapse to form stars per unit time, and so fewer high-mass stars are formed, and vice versa.

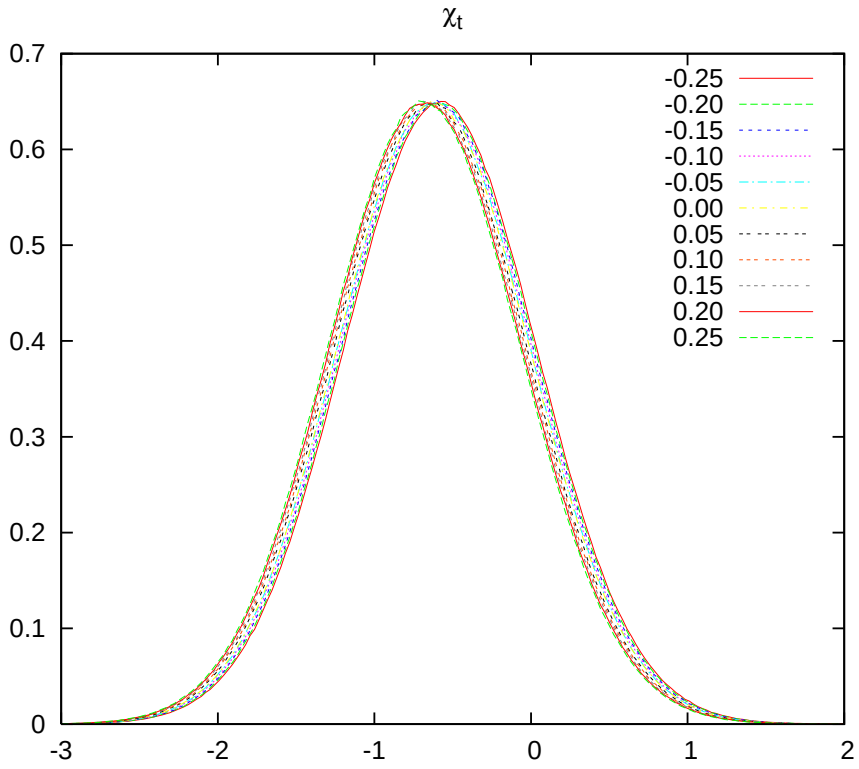

Figure 4.16: Variation of the StIMF with χ_t. The standard deviation and skew of the StIMF are constant. The peak of the StIMF moves to the left as χ_t increases.

Figure 4.17 shows the variation of the StIMF with χ_{σ_0}. For $\chi_{\sigma_0} > 0$, larger cores have a greater standard deviation, and for $\chi_{\sigma_0} < 0$, smaller cores have a greater standard deviation. The skew of the StIMF towards low-mass stars increases as χ_{σ_0} decreases. As χ_{σ_0} decreases, the smaller cores have a larger σ_0, and so smaller stars than usual can be formed. This has the effect of both shifting the peak towards lower masses, and producing a low-mass tail on the log normal. The mass of the biggest star is limited by the mass of the core, and each core can only produce one very massive star, and so, although the peak moves to higher masses still when χ_{σ_0}, so we do not get a high-mass power law tail. The mean and standard deviation of the StIMF remain constant.

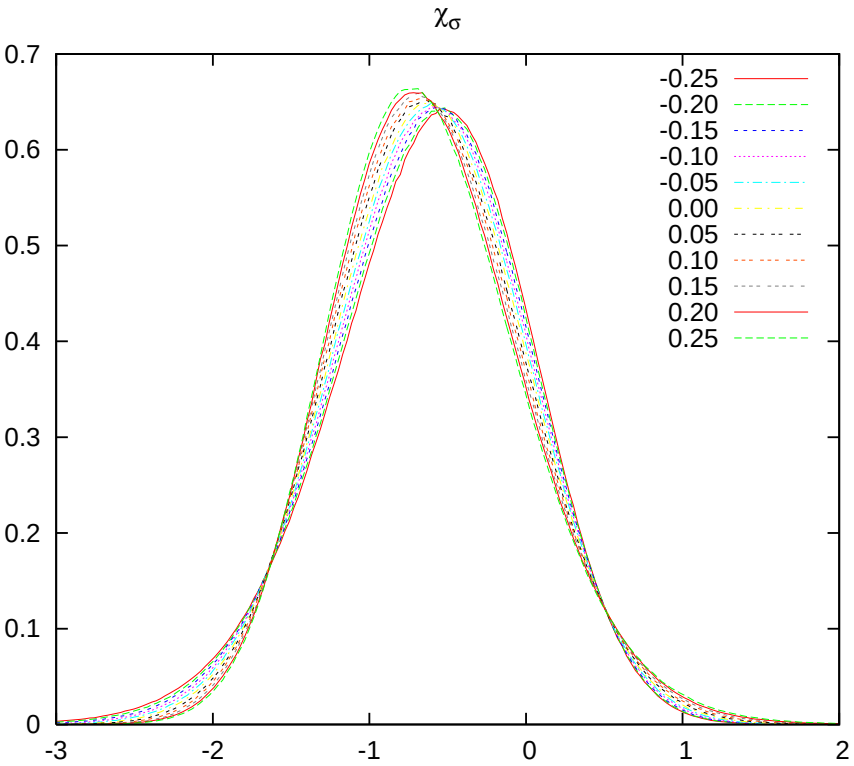

Figure 4.17: Variation of the StIMF with χ_{σ_0}. The skew of the StIMF increases with χ_{σ_0}, giving a low-mass tail to the log normal. The mean and standard deviation of the StIMF remain constant.

4.3 Conclusions

I find during the course of this project that a self-similar mapping can explain the similarity between the CMF to the StIMF , so long as Equations (4.1) and (4.3) are satisfied. This leads to a degeneracy between N_0 and η_0. I can constrain the parameters by invoking the binary frequency and mass ratios, leading to the best fit model given in Table 4.1. It is a combination of fitting both the StIMF and the binary frequency that constrains the parameter space most critically. This model is unique in that it fits the StIMF, binary frequency and mass ratios.

Self-similar mapping fits the observational constraints for the StIMF, binary frequency and mass ratios for sun-like and M-dwarf primaries, so long as the efficiency is rather high, approximately 100%. This is higher than previously proposed (e.g. $\eta_0 \sim 0.3$ Alves et al. 2007). We would therefore expect that most of the mass of the core would end up on the mass of the stars. Additional accretion would counteract any mass lost via outflows. Each core needs to fragment into about 4 or 5 stars, and so most stars would not form in isolation. Higher values of N_0 may be possible, but the efficiency would have to be increased even further and each core would have to produce more than one binary. β is smallish for the best fit, suggesting that there is some form of dissipation between the stars, allowing the lower mass stars an opportunity to be part of a long-lived binary.

Currently, observations cannot be used to break the N_0, η_0 degeneracy. However, as angular resolutions improve, multiple protostars can now be directly observed in a core (Chen et al. 2013). As more observations are made, with increasingly better angular resolutions, it is likely that observational contraints on N_0 can be made, breaking the N_0, η_0 degeneracy.

Note that I do not claim, nor have I claimed at any point, that self-similar mapping is the one and only answer. I do however say that at this point in time it cannot be ruled out, and at the very least, can be used as a quick, back of the envelope guess of star formation conditions.

Chapter 5

Core Cluster Simulations

The second half of my thesis is concerned with the dynamical evolution of small-N core clusters. A variety of different initial conditions are evolved using the N-body integrator in SEREN_VIEW (Hubber et al. 2013). The effect on the properties of multiple systems ($N_{comp} > 1$) due to the initial configuration of the system is analysed, with a view to explaining the observed properties of binary and multiple systems. The results of the N-body dynamics will also be analysed to see if they support, or contradict the results of the self-similar mapping of the first part of my thesis.

The first work on small N-body clusters with a view to explaining the multiplicity properties is due to van Albada (1968a). He starts with clusters of sizes 10 and 24, and finds that the system disintegrates after on the order of ten to one hundred times the characteristic time scale of the original group. What is left is a more or less stable multiple system with an average membership of 5 for the 10-body cluster, and 8 members for the 24-body cluster.

5.1 Fiducial Model

The fiducial model is one that is closest to the self similar mapping model identified in Holman et al. (2013), and is shown in Table 5.1.

5.1.1 Initial Positions

For a sphere with a power law density profile, the probability of a star being placed in $(r, r + \mathrm{d}r)$ is

$$p_r \, \mathrm{d}r = \frac{n(r) 4\pi r^2 \, \mathrm{d}r}{\int\limits_{r=0}^{r=R_B} n(r) 4\pi r^2 \, \mathrm{d}r} = \frac{n(r) r^2 \, \mathrm{d}r}{\int\limits_{r=0}^{r=R_B} n(r) r^2 \, \mathrm{d}r} \tag{5.1}$$

Table 5.1: The parameters for the fiducial model are given in this table, with the parameter in the left hand column, and its value in the right hand column. The fiducial model is chosen to be the one closest to the self similar mapping model identified in Holman et al. (2013).

Parameter	Value
N_0	4
$\mathcal{V}$	0.5
σ_0	0.3
d_m	0.0
Core Cluster Type	Spherical
α	0
Plummer Potential	OFF

From Equation (5.19), we can substitute $n(r)$ into Equation (5.1).

$$p_r \, \mathrm{d}r = \frac{n_B \left(\frac{r}{R_B} \right)^{-\alpha} r^2 \, \mathrm{d}r}{\int_{r=0}^{r=R_B} n_B \left(\frac{r}{R_B} \right)^{-\alpha} r^2 \, \mathrm{d}r} \tag{5.2}$$

We can then sample from this distribution by integrating Equation (5.2) to give us $P(r)$. We set this equal to a linear random deviate, $\mathcal{R}$, and rearrange to find the radius r

$$\begin{aligned} P(r) &= \frac{2-\alpha}{R_B^{3-\alpha}} \frac{r^{3-\alpha}}{2-\alpha} = \left(\frac{r}{R_B} \right)^{3-\alpha} = \mathcal{R} \\ r &= \mathcal{R}^{\frac{1}{3-\alpha}} R_B \end{aligned} \tag{5.3}$$

Note that for a uniform sphere, $\alpha = 0$ and that all cores have a radius of 1 unless stated otherwise (see Section 7.2.1.) We follow a similar prescription for θ and ϕ. For θ we have

$$p_\theta \, \mathrm{d}\theta = \begin{cases} 0, & \theta < -\pi/2 \\ \sin(\theta) \, \mathrm{d}\theta/2, & -\pi/2 \leq \theta \leq \pi/2 \\ 0, & \theta < \pi/2. \end{cases} \tag{5.4}$$

Integrating and rearranging Equation (5.4) gives us

$$\theta = \cos^{-1}(1 - 2\mathcal{R}_\theta) \, . \tag{5.5}$$

For ϕ we have

$$p_\phi \, \mathrm{d}\phi = \begin{cases} 0, & \phi < 0 \\ \mathrm{d}\phi/2\pi, & 0 \leq \phi \leq 2\pi \\ 0, & \phi > 2\pi. \end{cases} \tag{5.6}$$

Integrating and rearranging Equation (5.6) gives

$$\phi = 2\pi \mathcal{R}_\phi. \tag{5.7}$$

Care has to be taken when using random number generators, as inbuilt functions will often draw from the distribution [0,1), meaning that 1 will never be drawn as a random number. In this case, one effect would be that a star would never be placed exactly on the z-axis. For a large number of particles, this effect becomes a problem, but as I am using $N_0 < 6$, this will not affect my results.

5.1.2 Initial Velocities

We need to choose the velocities of the protostars in the cluster carefully, so that they satisfy the required value for the virial parameter $\mathcal{V} = \dfrac{E_{kin}}{|E_{grav}|}$ (see Section 5.3).

The self-gravitational potential energy is computed as

$$E_{grav} = -\sum_{s=1}^{s=N_0-1} \sum_{s'=s+1}^{s'=N_0} \frac{M_s M_{s'}}{|\boldsymbol{r}_s - \boldsymbol{r}_{s'}|}, \tag{5.8}$$

and the kinetic energy is computed as

$$E_{kin} = -\sum_{s=1}^{s=N_0} \frac{1}{2} M_s |\boldsymbol{v}_s|^2. \tag{5.9}$$

Random, unscaled velocities are drawn from a Maxwellian distribution,

$$P_{v'_k} \, \mathrm{d}v'_k = \frac{1}{(2\pi)^{1/2}} \exp\left(\frac{-v'^2_k}{2}\right) \mathrm{d}v'_k. \tag{5.10}$$

We want to scale these velocities to a user-specified virial parameter. The new velocities are

$$\boldsymbol{v}_s = \gamma \boldsymbol{v}'_s, \tag{5.11}$$

where

$$\gamma = \sqrt{\frac{|E_{grav}|\mathcal{V}}{E_{kin}}}. \tag{5.12}$$

Therefore,

$$\boldsymbol{v}_s = \sqrt{\frac{|E_{grav}|\mathcal{V}}{E_{kin}}} d\boldsymbol{v}'_s. \tag{5.13}$$

5.1.3 Drawing and Normalising Stellar Masses

In Chapter 3, two different methods of scaling the stellar masses of a core are discussed. Scaling 1 produces a group of stars with the correct total mass, but the distribution is skewed towards lower masses. Scaling 2 produces a log normal distribution of stellar masses, but the total mass of the stars does not equal exactly the efficiency times the mass of the core. For this chapter a new method is introduced, Scaling 3, which scales the masses of the protostars in such a way that the variance in the masses of stars formed in each core is always exactly equal to $\sigma_{_0}$, and the total mass is always exactly equal to 1 dimensionless unit. This new method is as follows.

We draw N_0 random gaussian deviates,

$$\ell_i = \sigma_{_0} \mathcal{G}_i, \qquad i = 1 \text{ to } N_0. \tag{5.14}$$

The standard deviation of these deviates is

$$\sigma_\ell = \sqrt{\overline{\ell^2} - \overline{\ell}^2}. \tag{5.15}$$

When each deviate is scaled by $\sigma_{_0}/\sigma_\ell$,

$$\ell'_i = \frac{\sigma_{_0} \ell_i}{\sigma_\ell}, \tag{5.16}$$

the deviates have the correct standard deviation. However, the sum of the masses is not yet correct, so the deviates are rescaled simply by dividing throughout by the total desired mass

$$M_i = \frac{10^{\ell'_i}}{\sum_{i=1}^{i=N_0} 10^{\ell'_i}} = \frac{M'_i}{\sum_{i=1}^{i=N_0} M'_i} \tag{5.17}$$

We now have a distribution of masses whose sum equals the desired total mass, and whose standard deviation equals σ_0. All the cores will have a total mass equal to 1 (see Section 7.2.1)

5.1.4 Duration of Simulations

The simulations run for at least 500 computer times units. After this, if all systems in the simulation have a fidelity factor of 0.99999 or greater, the simulation is allowed to terminate, as the parameters are unlikely to change with further computation. There is a maximum time limit of 10,000 computer time units, at which time the simulation is terminated whatever the values of the fidelity parameters.

5.2 The Number of Stars Produced by a Core

Holman et al. (2013) carry out a study in mapping from the core mass function to the initial mass function, and find that for the binary frequency to have the correct form, each core cluster needs to collapse to form on average 4 or 5 stars. Goodwin & Kroupa (2005) argue that each core needs to produce between 2 and 3 stars in order to reproduce the high multiplicity frequency for young stellar populations.

Observations of Class 0 protostars have found that several cores show evidences of two or more bright sources (Chen et al. 2013). It can be expected that N_0 will be more tightly constrained as observational techniques improve.

In order to investigate the parameter space, I will consider values of N_0 (the number of stars produced per core) in the range 2 to 6.

5.3 Virialisation

The virial parameter $\mathcal{V}$, is defined as the ratio of the total kinetic energy of a core cluster to its total potential energy. For an isolated core cluster, this can be written as:

$$\mathcal{V} = \frac{\sum_i \frac{1}{2} M_i |\boldsymbol{v}_i|^2}{-\sum_{i=1}^{i=N_0-1} \sum_{j=i+1}^{j=N_0} \frac{M_i M_j}{|\boldsymbol{r}_i - \boldsymbol{r}_j|}} = \frac{\text{total kinetic energy}}{\text{total potential energy}} \tag{5.18}$$

The overall expected behaviour of the core cluster can be determined by considering the magnitude of the virial parameter, $\mathcal{V}$. If $\mathcal{V} < 0.5$, then the core cluster is sub-virial, and will collapse. If $\mathcal{V} = 0.5$, then the core cluster is stable, and will remain at roughly the same size. If $\mathcal{V} > 0.5$ then the core cluster is super-virial, the stars will move apart, and the core cluster will expand.

To cover each of these three cases, I will consider three values for the virial parameter, 0.2 (sub-virial), 0.5 (virial) and 0.8 (super-virial).

5.4 Variance in Stellar Masses Produced by a Single Core

In their mapping study, Holman et al. (2013) find that the optimum value for σ_0, the standard deviation in the stellar masses produced by a single core to be of the order 0.3. Hubber & Whitworth (2005) find that a higher value of $\sigma_0 = 0.5$ is optimal when the stars are initially placed within a ring core cluster. Current observational limits prevent the determination of σ_0 from observations. However, multiple protostars are now beginning to be resolved within individual cores (Chen et al. 2013), and it is expected that as techniques improve, better mass estimates of the protostars will be gained, and estimates of σ_0 can be made.

I will consider values of σ_0 in the range 0.0 to 0.5.

5.5 Density Gradient

The stars formed by a single core are placed randomly within a spherically symmetric density profile. This density is chosen to have the form

$$n(r) = \begin{cases} n_{_B} \left(\dfrac{r}{R_{_B}} \right)^{-\alpha}, & r < R_{_B} \\ 0, & r > R_{_B}. \end{cases} \tag{5.19}$$

Here, $n_{_B}$ is the density of stars at the surface of a sphere with radius $R_{_B}$.

Three values for α are considered. Firstly $\alpha = 0$, which corresponds to a uniform density sphere, and then $\alpha = -1$ and $\alpha = -2$, which correspond to the density falling off with radius. Note however, that the change in distribution is unlikely to have an affect on the final statistics, due to the small number of stars being considered.

5.6 Ring Cluster

When rotation is included in models of core collapse (e.g. Bonnell & Bate 1994; Cha & Whitworth 2003; Hennebelle et al. 2004) the core sometimes overshoots centrifugal balance and bounces back at the end of the second collapse phase to form a dense ring which fragments into a small ($N_0 < 6$) number of protostars. The systems formed by this process will have separations of a few $R_\odot$, and will tend to have components of similar mass. Hubber & Whitworth (2005) perform N-body simulations of various realisations of a ring cluster, and compare the multiplicity statistics to those in the field. However, they fail to find a satisfactory model that reproduces both the StIMF and the multiplicity fraction satisfactorily. In order to investigate this scenario, I consider the situation where stars form on the circumference of a circle. For the ring cluster, each star is assigned a circular velocity equal to $|v_i| \propto \sum m_i/r$. To generate initial conditions for the ring cluster, stars are placed on the circumference of a circle with a radius of 1 (dimensionless units), with each star occupying an arc of the circle with length proportional to its mass.

5.7 Line Cluster

When a turbulent core collapses, shock-waves create filamentary structures. If conditions are right, contraction along the filament will stall, and the filament will fragment (Krumholz et al. 2007). (See also Bate et al. 2002a,b, 2003). For certain equations of state, filaments can also form via gravitational collapse. This happens when $\Gamma < 1$ for a polytropic equation of state, in this case, pressure support is too weak to form cores, so gravitational contraction proceeds much quicker than $\Gamma > 1$, and shocks creating a network of sheets and filaments (Peters et al. 2012). Bonnell et al. (2008) also show that fragments can form through gravitational compression as the filament infalls into a gravitational well. The tidal shears act to limit the mass increase due to accretion. In order to investigate the filament scenario, I will consider the situation where stars form along a line. The stars in the line cluster are assigned random initial transverse velocities as informed by Krumholz et al. (2007). For the line cluster, stars are placed along a filament of length 2 dimensionless units, taking up a length proportional to their mass.

5.8 Protostellar Disks

Protostellar disks are inferred through interferometry and SED modelling. They form almost as soon as the molecular core has collapsed, and have masses that scale with the associated stellar masses (Chen et al. 2013). They have lifetimes ranging from 1 Myr to 10 Myr, with a median between 2 Myr and 3 Myr (Williams & Cieza 2011). Sicilia-Aguilar et al. (2013) conclude that disks are likely to play a role in early time protostar interactions.

The parameter d_m is defined to be the ratio of the mass of the circumstellar disk, M_{disk}, to the mass of its host star, M_{star},

$$d_m = \frac{M_{disk}}{M_{star}}. \tag{5.20}$$

Stars with disks essentially have a larger interaction cross-sectional area than stars without disks. When a star passes through the disk of another star, the energy used in disrupting and unbinding some of the disk material comes from the kinetic energy of the star, slowing it down, and making it easier to be captured. The extent to which a disk affects the momentum of a passing star depends on both the orientation of the disk and the direction of the passing star with respect to the rotation of the disk. McDonald & Clarke (1995) investigate N-body interactions including effects of massive disks ($d_m = 0.75$), and find that the dissipative effects of the disks increases the low fraction of low-q systems.

The disks are assumed to be massless as far as the N-body dynamics are concerned, they only play a role when interactions take place. Three cases will be considered, $d_m = 0$ (i.e. the stars have no disks), $d_m = 0.5$ and $d_m = 1.0$.

Star A is considered to be within the disk of star B if it lies within a spherical region around star B with the same radius as the disk of star B. To find the velocity shift for star A, I find all the neighbours which have disks that A lies within. We call these stars B. For each disk B, I find all the stars that lie within its disk, and call them C (but not including star A).

For each disk that star A lies within, I move to the center of mass frame for stars A, B and C. I compute the estimated time and distance at periastron (t_{peri}, r_{peri}) between A and B, and $X1$, the energy lost in the interaction, which we have assumed to be the energy required to unbind the disk material down to a radius r_{peri}.

$$X1 = \frac{M_A M_{dB}}{R_{dB}} \left(\sqrt{\frac{R_{dB}}{r_{peri}}} - 1 \right) - \sum_{C}^{r_A < r_C < R_{dB}} \frac{M_C M_{dB}}{R_{dB}} \left(\sqrt{\frac{R_{dB}}{r_C}} - 1 \right). \tag{5.21}$$

Here, M_{dB}, R_{dB} is the mass and radius of the disks surrounding star B and r_C is the distance between star B and star C. The second term of Equation (5.21) reduces $X1$ by the amount of

energy that each other star contributes to unbinding the same section of disk. This will be all stars that lie further out than A, but still within the disk of B.

Dummy variables $X2$ and $X3$ are also computed,

$$X2 = \begin{cases} 0, & \text{star } B \text{ is not within the disk of star } A \\ \dfrac{M_B M_{dA}}{R_{dA}} \left(\sqrt{\dfrac{R_{dA}}{r_{peri}}} - 1 \right), & \text{star } B \text{ is within the disk of star } A \end{cases}, \tag{5.22}$$

$$X3 = M_A \left| \boldsymbol{v}_A \right| + M_B \left| \boldsymbol{v}_B \right| + \sum_C M_C \left| \boldsymbol{v}_C \right|. \tag{5.23}$$

If $(X1 + X2)/X3 < 1$, then the stars have the energy required to unbind the disk material outside periastron. If they don't, then no interaction takes place.

We cannot follow exactly the same prescription as McDonald & Clarke (1995), who introduce instantaneous velocity changes at the point of periastron. This is because the Hermite integration scheme that SEREN_VIEW uses requires a smoothly changing acceleration and jerk. Therefore we smooth out the interaction as given by McDonald & Clarke (1995) to avoid the instantaneous velocity changes. I choose to use an inverse tan function to smooth out the interaction,

$$\boldsymbol{v}'_A = \boldsymbol{v}_A \left\{ 1 - \lambda \left[\frac{1}{2} + \frac{2}{\pi} \tan^{-1} \left(\frac{t - t_{peri}}{t_\square} \right) \right] \right\}. \tag{5.24}$$

where lambda is a factor governing by how much the velocities are reduced during the interaction. Here, t_{peri} is the time at periastron, $\boldsymbol{v}_A$ is the velocity of star A before interaction with the disk, and $\boldsymbol{v}'_A$ is the corrected velocity. Using the above quantities, we can now determine the quantities needed for the Hermite integration.

$$\lambda = \sqrt{1 - \frac{X1 + X2}{X3}} \tag{5.25}$$

$$\boldsymbol{a} = \frac{-2\lambda \boldsymbol{v}_A}{\pi \left(1 + \left(\dfrac{t - t_{peri}}{t_\square} \right)^2 \right)} \tag{5.26}$$

$$\dot{\boldsymbol{a}} = \frac{-4\lambda \boldsymbol{v}_A}{\pi \left(1 + \left(\dfrac{t - t_{peri}}{t_\square} \right)^2 \right)^2} \tag{5.27}$$

If stars A and B are moving apart, and A is the outermost star in the disk, then the disk mass and radius of star B are updated,

$$M_{dB} = \frac{M_{dB} r_B}{R_{dB}} \tag{5.28}$$

$$R_{dB} = r_B, \tag{5.29}$$

where r_B is the current separation between A and B.

5.9 Background Potential

When stars form, they find themselves embedded within an envelope of gas - i.e. the core from which they have formed. This envelope of dust and gas provides a gravitational potential well, which keeps the stars from moving too far away, at least while it has significant mass (Classes 0 and I). When a core forms multiple stars, it is thought that this gravitational potential well may help in forming a stable multiple system.

Instead of doing a full-blown hydrodynamical simulation involving the residual gas, which would be very time-consuming, the potential of the residual gas of a core can be treated analytically, approximating it with a Plummer potential. Reipurth & Mikkola (2012) perform N-body simulations of triple systems embedded in a time varying Plummer potential.

$$Pot_p = \frac{-M_p}{\sqrt{r^2 + R_p\left(t\right)^2}}, \tag{5.30}$$

where M_p is the mass of the residual gas and R_p is the radius over which it extends. They find that over time, an initially compact system evolves to form a close binary orbited distantly by the third star. They find that stable triple systems have wide outer orbits compared to their inner orbits, and hence the outer star is well separated from the inner pair, even at periastron.

I use the same Plummer sphere as used by Reipurth & Mikkola (2012), with $M_p = 1$. R_p is set initially to a value of 1, but is allowed to expand linearly with time as follows,

$$R_p = \bar{s}\left(1 + \frac{t}{t_{expansion}}\right). \tag{5.31}$$

Here, $\bar{s}$ is the average initial separation between the stars, t is the time and $t_{expansion}$ is the time scale over which the Plummer sphere expands.

$$t_p = \frac{t_{expansion}}{t_{crossing}}, \tag{5.32}$$

where $t_{crossing}$ is the crossing time of the core cluster. Note that as $t_{crossing} = 1$, then $t_p = t_{expansion}$.

I will set $t_p = 10$, 30, 100 and 300.

I use a Plummer sphere with a mass that is constant, but radius that increases linearly as

$$R_p\left(t\right) = \bar{s}\left(1 + \frac{t}{t_p}\right), \tag{5.33}$$

where $R_p\left(t\right)$ is the radius of the Plummer sphere after a time t, and $\bar{s}$ is the average initial separation between the stars, and the initial radius of the Plummer sphere, at time 0. The potential at radius r due to the Plummer sphere with a time-varying radius is then

$$\text{Pot} \;=\; \frac{-M_p}{\sqrt{r^2 + R(t)^2}}, \tag{5.34}$$

and the acceleration of a particle at radius r due to the Plummer sphere is

$$a\left(r\right) \;=\; \frac{-M_p r}{\left(r^2 + R(t)^2\right)^{3/2}}, \tag{5.35}$$

and the jerk on the same particle due to the Plummer sphere is

$$\dot{a}\left(r\right) \;=\; \frac{3M_p r R(t)^2}{t_p\left(r^2 + R(t)^2\right)^{5/2}} \tag{5.36}$$

The expression for the virial parameter has to be updated to include the effects of the Plummer potential:

$$\mathcal{V}_0 = \frac{\sum\limits_i \frac{1}{2} M_i |\boldsymbol{v}_i|^2}{\sum\limits_{i=1}^{i=I-1} \sum\limits_{j=i+1}^{j=I} \left\{ \frac{M_i M_j}{|\boldsymbol{r}_i - \boldsymbol{r}_j|} + \frac{-M_p}{\sqrt{|\boldsymbol{r}_i|^2 + R_0^2}} + \frac{M_P}{R_0} \right\}} \tag{5.37}$$

where the last term in the denominator is to shift the zero of the background potential to

the centre. Hence the velocities will not be changed much by the addition of the background potential.

5.10 Summary

The previous sections represent a large parameter space which is difficult to explore fully. Therefore a fiducial, or reference, model is defined and each of the parameters are varied one at a time. By comparing the output to that of the fiducial model, we can get a feel for how that particular parameter affects the multiplicity statistics.

Table 5.2 summarises all the initial conditions that are investigated, as discussed in the previous sections, with the fiducial model parameters shown in bold.

Table 5.2: This table summarises all the initial conditions that are investigated, with the fiducial model parameters shown in bold.

Parameter	Description	Values
N_0	Number of stars per core	2, 3, **4**, 5, 6
$\mathcal{V}$	Virial parameter	0.2, **0.5**, 0.8
σ_0	Variance of stellar masses	0.1, 0.2, **0.3**, 0.4, 0.5
d_m	Disk to stellar mass ratio	**0.0**, 0.5, 1.0
Core Cluster type	Initial distribution of stars	**Spherical**, Ring, Filament
α	Density gradient	**0**, -1, -2
Background Potential	Dissipation time scale	**0**, 10, 30, 100, 300

Chapter 6

Fidelity

I define a multiple system as a group of two or more stars that are both mutual nearest neighbours, and are gravitationally bound. But for a system with three or more members, the association will never be permanent, one or more of its members will be ejected in time, leaving behind a more tightly bound system with fewer members. However, some of these systems are stable enough to survive for a many thousands of orbits, and could be called quasi-stable.

As the three body problem is non-integrable, there is no firm criterion for defining the longevity of a triple system. A few definitions of 'stability' have been suggested. Eggleton & Kiseleva (1995) introduce the idea of 'n-stability'. For a system to be 'n-stable', it must be in an hierarchical configuration, and it must persist in the same hierarchical configuration for a period of $10^n P_o$, where P_o is the period of the outermost orbit. This usually occurs when the inner system and outer stars are well separated at closest approach (see their Equation 2). Anosova (1986) suggested that generally, a triple system is unstable with a half-life of

$$t_{decay} = 14 \left(\frac{R}{\mathrm{AU}} \right)^{3/2} \left(\frac{M_{stars}}{M_\odot} \right)^{-1/2} \mathrm{yr}, \tag{6.1}$$

where R is the size of the system and M_{stars} is the total mass of the components.

In this Chapter, I first present the equations used to determine the orbital parameters of a pairwise orbit in a system. I define a fidelity parameter, that tracks the changes in the orbital parameters for each of the pairwise orbits in a multiple system. If these do not change significantly over the period of an orbit, I consider the system to be long-lived. If the system's orbital properties are changing significantly, the system is considered unstable and short-lived.

6.1 Equations of Motion for Binary Systems

The equation for the acceleration of particle i due to gravitational influence of i_{tot} - 1 other particles in physical units is

$$\frac{d^2\boldsymbol{r}_i}{dt^2} = \sum_{j=1(j\neq i)}^{j=i_{tot}} \frac{\mathrm{G}M_j(\boldsymbol{r}_j - \boldsymbol{r}_i)}{|\boldsymbol{r}_j - \boldsymbol{r}_i|^3}, \tag{6.2}$$

where $\boldsymbol{r}_i$ is the position of the particle i, G is the gravitational constant, and M_j is the mass of particle j.

6.2 Multiple System Parameters

At any instant during the course of the simulation, I know the masses, positions, velocities and accelerations of the particles. What I would like to know, is if any combination of those stars constitute a multiple system; and, if it does, what are its parameters, e.g. eccentricity, period, energy, semi-major axis, mass ratio and fidelity.

When a binary or multiple system has been identified, and its parameters computed, it is, for the purposes of searching for multiple systems, replaced with a single point at the centre of mass. It is with respect to this centre of mass that other stars are compared when computing the binding energy, reducing the problem to a two-body problem each time.

6.2.1 Binding Energy

The binding energy of a multiple system is the sum of the kinetic and gravitational potential energies in the centre of mass frame,

$$E_{binding} = \sum_{i}^{N} \frac{1}{2} M_i |\boldsymbol{v}_i|'^2 - \sum_{i}^{N-1} \sum_{j=i+1}^{N} \frac{\mathrm{G}M_iM_j}{|\boldsymbol{r}'_i - \boldsymbol{r}'_j|}, \tag{6.3}$$

where $\boldsymbol{v}'_i$ is the velocity and $\boldsymbol{r}'_i$ is the position of star i in the centre of mass frame, computed using

$$\boldsymbol{v}' = \boldsymbol{v} - \boldsymbol{v}_c, \qquad \boldsymbol{v}_c = \frac{\sum_i M_i \boldsymbol{v}_i}{\sum_i M_i}, \tag{6.4}$$

$$\boldsymbol{r}' = \boldsymbol{r} - \boldsymbol{r}_c, \qquad \boldsymbol{r}_c = \frac{\sum_i M_i \boldsymbol{r}_i}{\sum_i M_i}. \tag{6.5}$$

Here $\boldsymbol{v}$ is the velocity in the original frame of reference, $\boldsymbol{v}_c$ is the velocity of the centre of mass, and M_i is the mass of particle i.

For two particles, Equation (6.3) expands out to

$$E_{binding} = \frac{M_1|\boldsymbol{v}_1|^2}{2} + \frac{M_2|\boldsymbol{v}_2|^2}{2} - (M_1\boldsymbol{v}_1 + M_2\boldsymbol{v}_2)\,\boldsymbol{v}_c + \frac{(M_1+M_2)\,|\boldsymbol{v}_c|^2}{2} - \frac{\mathrm{G}M_1M_2}{|\boldsymbol{r}_1 - \boldsymbol{r}_2|}, \quad (6.6)$$

where

$$\boldsymbol{v}_c = \frac{M_1\boldsymbol{v}_1 + M_2\boldsymbol{v}_2}{M_1 + M_2}. \quad (6.7)$$

Simplifying further gives us

$$E_{binding} = M_1M_2\left\{\frac{|\boldsymbol{v}_1 - \boldsymbol{v}_2|^2}{2\,(M_1+M_2)} - \frac{\mathrm{G}}{|\boldsymbol{r}_1 - \boldsymbol{r}_2|}\right\}. \quad (6.8)$$

If the binding energy is negative, then the pairwise orbit is gravitationally bound, and is it a potential multiple system.

6.2.2 Semi-Major axis

The semi-major axis a, gives the characteristic size of the pairwise orbit, and is equal to

$$\mathrm{a} = \frac{\mathrm{G}M_1M_2}{(-2E_{binding})}, \quad (6.9)$$

where $E_{binding}$ is the binding energy of the system, and is given by Equation (6.8).

6.2.3 Mass Ratio

The mass ratio of each pairwise orbit is taken to be

$$q = \frac{M_s}{M_p}. \quad (6.10)$$

For a pairwise orbit involving only two stars, M_s is the mass of the smaller star, and M_p is the mass of the larger star. For a pairwise orbit involving more than two stars, M_p is the total mass of the inner system and M_s is the mass of the outermost star (which is usually smaller

than M_p). In the case of double quadruples, M_p is the total mass of the more massive pair, whilst M_s is the total mass of the less massive pair.

6.2.4 Eccentricity

The eccentricity e relates to the shape of the orbit. An eccentricity of 0 denotes a circular orbit, a value of eccentricity $0 < \mathrm{e} < 1$ is an elliptical orbit, getting longer and thinner as e increases.

$$\mathrm{e}^2 = 1 + \frac{2\left(M_1 + M_2\right) L_{total}^2 E_{binding}}{\mathrm{G}^2 M_1^3 M_2^3} \tag{6.11}$$

where L_{total} is the total angular momentum of the pairwise orbit.

6.2.5 Period

The period of an orbit P is the length of time it takes for a system to return to its original position in the centre of mass frame of reference.

$$P = \frac{2\pi \mathrm{G}}{\left(M_1 + M_2\right)^{1/2}} \left\{ \frac{M_1 M_2}{\left(-2E_{binding}\right)} \right\}^{3/2}. \tag{6.12}$$

6.2.6 Fidelity Parameter

I test the fidelity of a system by tracking how much the orbital parameters change with time. Consider an orbital parameter, which I will call X. The inertial average of X is defined as

$$\bar{X}\left(t\right) = \int_{t'=-\infty}^{t'=t} X\left(t'\right) \exp\left(\frac{t'-t}{P\left(t\right)}\right) \frac{\mathrm{d}t'}{P\left(t\right)} \tag{6.13}$$

where $P\left(t\right)$ is the period of the pairwise orbit being tested, and t is the current time . As a result,

$$\frac{\mathrm{d}\bar{X}}{\mathrm{d}t} = \frac{X\left(t\right) - \bar{X}\left(t\right)}{P\left(t\right)}, \tag{6.14}$$

and we can update $\bar{X}$ with

$$\bar{X}\left(t + \Delta t\right) = \bar{X}\left(t\right) \left\{ 1 - \frac{\Delta t}{P\left(t\right)} \right\} + X\left(t\right) \left\{ \frac{\Delta t}{P\left(t\right)} \right\}. \tag{6.15}$$

The fidelity parameter is computed using at least two of the orbital parameter inertial averages, which I call a and b.

$$F(t) = \left\{ \left(\frac{a(t)}{|a(t) - \bar{a}(t) + \ell|} \right)^2 + \left(\frac{b(t)}{|b(t) - \bar{b}(t) + \ell|} \right)^2 \right\}^{1/2} \frac{\ell}{(a^2(t) + b^2(t))^{1/2}}. \quad (6.16)$$

ℓ is an arbitrary number, to prevent singularities. I choose to use the energy and semi-major axis to calculate the fidelity parameter. If the orbital parameters remain constant, the fidelity parameter will approach a value of 1.00 after the pairwise orbit has completed approximately ten orbits.

Equations (6.17) to (6.21) are expressions for the number of possible combinations for binaries, triples, hierarchical quadruples and double binary quadruples respectively for a cluster of N_0 stars.

$$\begin{aligned}
\#\text{ possible binaries} &= \frac{N_0^2 - N_0}{2} && (6.17)\\
\#\text{ possible triples} &= \left(\frac{N_0^2 - N_0}{2} \right)(N_0 - 2) && (6.18)\\
\#\text{ possible double binaries} &= \frac{1}{2}\left[\left(\frac{N_0^2 - N_0}{2} \right) \left(\frac{(N_0 - 2)^2 - (N_0 - 2)}{2} \right) \right] && (6.19)\\
\#\text{ possible hierarchical quadruples} &= \left(\frac{N_0^2 - N_0}{2} \right)(N_0 - 2)(N_0 - 3). && (6.20)\\
& && (6.21)
\end{aligned}$$

Table 6.1 shows the number of possible combination of binaries etc for core-clusters of size $N_0 = 2$ to $N_0 = 6$, along with the total number of possible combination of multiple systems, up to 4 components. For small-N core clusters, it is well within the capabilities of modern computers to test every possible combination, to see if they form a bound multiple system.

A matrix is created to store the fidelity parameters of each of the possible multiple system combinations. Each of the possible combinations are checked, to see if they form a bound system. If they are not bound (See Section 6.2.1), then the fidelity of the system and all higher order hierarchical systems involving that sub-system are set to 0. Consequently any systems that become dissociated, and then recombine, will have no memory of previous associations. If they are bound, the fidelity is computed, and the binding energy of higher order multiples involving that binary are also computed. A binary is only retained for testing if the components are mutual nearest neighbours. Hierarchical triple systems are only retained for testing if the separation between the binary centre of mass and the third star is greater than the binary

Table 6.1: The table lists the number of possible combinations for binaries (column 2), triples (column 3), double binaries (column 4) and hierarchical quadruples (column 5) for various values of N_0 (column 1). The total number of combinations I have to keep track of are given in the final column. Although this number rises quite rapidly, of the order $O(N_0^3)$, it is still well within the capabilities of todays computers even for quite large values of N_0

N_0	B	T	Q_B	Q_H	Number of Combinations
2	1	0	0	0	1
3	3	3	0	0	4
4	6	12	3	12	25
5	10	30	15	60	95
6	15	60	45	45	180

separation, and the binary centre of mass and the outer star are mutual nearest neighbours. A similar prescription is followed for hierarchical quadruples. A double quadruple is retained for testing if both pairs of stars consist of mutual nearest neighbours, the two pairs of stars are mutual nearest neighbours and the semi-major axis of the outer orbit is greater than both the semi-major axes of the inner pairs.

The simulation is ended when all the bound systems have a fidelity greater than 0.9999 (and the simulation has run for a minimum of 500 crossing times), or the simulation has run for 10,000 crossing times, which ever comes first.

Chapter 7

SEREN_VIEW

SEREN_VIEW is a hybrid SPH[1] and N-body code based on the code SEREN (Hubber et al. 2011). In this chapter I describe the Hermite integration scheme used for the N-body calculations of SEREN_VIEW, and finish with a simple test for identifying and evaluating the parameters of eccentric binaries and triple systems.

7.1 The Hermite Integrator

SEREN_VIEW uses a fourth order Hermite integration scheme based on Makino & Aarseth (1992) to integrate the motion of the star particles. The fourth order Hermite integration scheme has been chosen over the leapfrog integrator that is used for the SPH calculations, as it conserves energy better than the leapfrog. The fourth order Hermite integration scheme can also be considered the higher order equivalent of the leapfrog scheme, meaning that the force, prediction and corrections steps are all computed at the same point in the timestep for both schemes (Hubber et al. 2013).

The acceleration $\boldsymbol{a}_s$ of a star particle s is given by

$$\boldsymbol{a}_s = -\mathrm{G} \sum_{i=1}^{N_s} M_i \phi'_{si} \hat{\boldsymbol{r}}_{si}, \tag{7.1}$$

where G is the gravitational constant, M_i is the mass of star i, N_s is the total number of stars and $\hat{\boldsymbol{r}}_{si}$ is the unit vector pointing from star i to star s. The gravitation force kernel ϕ'_s includes a smoothing length, over which gravity is softened, which prevents violent two-body collisions with other stars. ϕ'_{si} is computed by integrating W, the SPH smoothing kernel,

[1] Smoothed Particle Hydrodynamics

$$\phi'_{si}\left(r_{si},h\right)=\frac{4\pi}{r_{si}^2}\int_0^{r_{si}}W\left(r',h\right)r'^2dr' \tag{7.2}$$

where r_{si} is the scalar distance between stars s and i. The jerk, or time derivative of the acceleration is given by the time derivative of Equation (7.1),

$$\dot{\boldsymbol{a}}_s^n=\frac{\partial}{\partial t}\left(-\mathrm{G}\sum_{i=1}^{N_s}M_i\phi'_{si}\frac{\boldsymbol{r}_{si}}{|\boldsymbol{r}_{si}|}\right). \tag{7.3}$$

Expanding out and computing all the partial derivatives gives

$$\begin{aligned}\dot{\boldsymbol{a}}_s^n=&-\mathrm{G}\sum_{i=1}^{N_s}M_i\phi'_{si}\frac{1}{|\boldsymbol{r}_{si}|}\frac{\partial\boldsymbol{r}_{si}}{\partial t} \quad -\mathrm{G}\sum_{i=1}^{N_s}M_i\phi'_{si}\boldsymbol{r}_{si}\frac{\partial}{\partial t}\frac{1}{|\boldsymbol{r}_{si}|}-\mathrm{G}\sum_{i=1}^{N_s}M_i\frac{\partial\phi'_{si}}{\partial t}\hat{\boldsymbol{r}}_{si}\\ =&-\mathrm{G}\sum_{i=1}^{N}\frac{M_i\phi'}{|\boldsymbol{r}_{si}|}\boldsymbol{v}_{si} \qquad +3\mathrm{G}\sum_{i=1}^{N}\frac{M_i\left(\boldsymbol{r}_{si}\cdot\boldsymbol{v}\right)\phi'}{|\boldsymbol{r}_{si}|^3}\boldsymbol{r}_{si}-4\pi\mathrm{G}\sum_{i=1}^{N}\frac{M_i\left(\boldsymbol{r}_{si}\cdot\boldsymbol{v}\right)W}{|\boldsymbol{r}_{si}|^2}\boldsymbol{r}_{si}.\end{aligned} \tag{7.4}$$

Once the jerk and acceleration have been computed, the predicted positions and velocities of the stars at the end of the timestep can be calculated.

$$\boldsymbol{r}_s^{n+1}=\boldsymbol{r}_s^n+\boldsymbol{v}_s^n\Delta t+\frac{1}{2}\boldsymbol{a}_s^n\Delta t^2+\frac{1}{6}\dot{\boldsymbol{a}}_s^n\Delta t^3 \tag{7.5}$$

$$\boldsymbol{v}_s^{n+1}=\boldsymbol{v}_s^n+\boldsymbol{a}_s^n\Delta t+\frac{1}{2}\dot{\boldsymbol{a}}_s^n\Delta t^2. \tag{7.6}$$

The acceleration and jerk $(\boldsymbol{a}^{n+1},\dot{\boldsymbol{a}}^{n+1})$ are then recomputed using the updated positions and velocities. From this we can work out

$$\ddot{\boldsymbol{a}}_s^n=\frac{2\left[-3\left(\boldsymbol{a}_s^n-\boldsymbol{a}_s^{n+1}\right)-\left(2\dot{\boldsymbol{a}}_s^n+\dot{\boldsymbol{a}}_s^{n+1}\right)\Delta t\right]}{\Delta t^2} \tag{7.7}$$

$$\dddot{\boldsymbol{a}}_s^n=\frac{6\left[2\left(\boldsymbol{a}_s^n-\boldsymbol{a}_s^{n+1}\right)+\left(\dot{\boldsymbol{a}}_s^n+\dot{\boldsymbol{a}}_s^{n+1}\right)\Delta t\right]}{\Delta t^3}. \tag{7.8}$$

The last step is the correction step where the higher order terms are added to the position and the velocity vectors.

$$\boldsymbol{r}_s^{n+1} = \boldsymbol{r}_s^{n+1} + \frac{1}{24}\ddot{\boldsymbol{a}}_s^n \Delta t^4 + \frac{1}{120}\dddot{\boldsymbol{a}}_s^n \Delta t^5 \tag{7.9}$$

$$\boldsymbol{v}_s^{n+1} = \boldsymbol{v}_s^{n+1} + \frac{1}{6}\ddot{\boldsymbol{a}}_s^n \Delta t^3 + \frac{1}{24}\dddot{\boldsymbol{a}}_s^n \Delta t^4. \tag{7.10}$$

SEREN_VIEW uses standard block timestepping, $\Delta t = \Delta t_{Max}/2^n$ where $n = 0, 1, 2, 3....$, i.e. any positive integer. A particle can move to any lower timestep at the end of its step, but can only move up one level, and then only if the steps are syncronised. This prevents the timesteps oscillating, but allows the timesteps to be reduced quickly when needed.

7.2 Dimensionless Units

The computations themselves are done using dimensionless units. This is so that the numbers don't get so large/small that information is lost due to computer precision. The results are then scaled to physical units after the simulations have finished.

To convert physical units (x) to dimensionless units ($\hat{x}$), the physical units are divided by a characteristic scale, (x_{char}), i.e.

$$\hat{x} = \frac{x}{x_{char}}, \tag{7.11}$$

where x is any physical quantity, for example mass, length, time etc. These characteristic scales have the same units as their corresponding physical units. They can be related to one another via the following equations,

$$t_{char} = \sqrt{\frac{L_{char}^3}{\mathrm{G}M_{char}}}, \tag{7.12}$$

$$v_{char} = \sqrt{\frac{\mathrm{G}M_{char}}{L_{char}}}, \tag{7.13}$$

where L is length, t is time, M is mass and v is velocity.

For ease of computation, both the dimensionless mass of the core and its dimensionless radius are set to 1. As a result, the crossing time is approximately one dimensionless unit as well.

7.2.1 Convolving

For ease of integration, dimensionless units are used during the simulations. Each core has a mass and radius equal to 1, meaning that the line cluster has a length of 2, and the ring cluster has a radius of 1 also. After the simulations have finished, the dimensionless mass and radius are convolved with observed distributions of core masses and radii to produce the final binary frequency and period distributions.

Before a core collapses, its radius is approximately

$$R_{core}\left(M_{\rm c}\right) = \begin{cases} 0.1\,{\rm pc}\ \left(M_{\rm c}/M_{\odot}\right), & M_{\rm c} < M_{\odot} \\ 0.1\,{\rm pc}\ \left(M_{\rm c}/M_{\odot}\right)^{1/2}, & M_{\rm c} > M_{\odot} \end{cases} \tag{7.14}$$

(c.f. Larson 1981; Myers 1983). If we substitute Equation (7.14) into Equation (7.12) we can determine what the characteristic time is for a core of a given mass.

$$t_{\square} = \begin{cases} 0.5\,{\rm Myr}\ \left(M_{\rm c}/M_{\odot}\right) & M_{\rm c} < M_{\odot} \\ 0.5\,{\rm Myr}\ \left(M_{\rm c}/M_{\odot}\right)^{1/4} & M_{\rm c} > M_{\odot}. \end{cases} \tag{7.15}$$

7.3 Testing for Eccentric Binaries and Triples

Seren_view calculates the properties of any binary and higher-order multiple systems that form during the simulation. Whilst the code has been tested with circular binaries, to see that the binary properties are accurately recovered, no testing had been done with eccentric binaries. So in order to test the accuracy of the parameters as measured by Seren_view, binaries are set up with known period, mass ratio and eccentricity. The values found by Seren_view are compared to the input values, giving an idea of the accuracy. The same test is then repeated for triple systems, but with the eccentricity set to zero.

7.3.1 Initial Conditions of Multiple Systems

For this test I set up binary and triple systems with known parameters. I then allow them to evolve with Seren_view for 1000 dimensionless time units, and compare the output values with the initial values.

Binaries

In this section I derive the initial conditions for eccentric binaries. The orientation of the orbit is arbitrary, so for ease, I choose that at periastron, the system is aligned with the x axis, the

plane of the orbit lies in the (x, y) plane, and the primary, M_1, lies at positive x. The separation of the stars at periastron (i.e. the minimum separation) is

$$s_{min} = \mathrm{a}_{total}\,(1 - \mathrm{e})\,. \tag{7.16}$$

Here e is the eccentricity, and a_{total} is the sum of the semi-major axes of the system, and is equal to

$$\mathrm{a}_{total} = \frac{\mathrm{G}M_1M_2}{(-2E_{binding})}, \tag{7.17}$$

where M_i is the mass of star i. Subscript 1 denotes a property of the primary star, and subscript 2 denotes a property of the secondary. Rearranging Equation (6.12) gives

$$-2E_{binding} = \left(\frac{2\pi\mathrm{G}}{P\sqrt{M_1 + M_2}}\right)^{2/3} M_1M_2, \tag{7.18}$$

where P is the period of the binary. Substituting this into Equation (7.17) and rearranging gives

$$s_{min} = \mathrm{G}\,(1 - \mathrm{e})\left(\frac{P\sqrt{M_1 + M_2}}{2\pi\mathrm{G}}\right)^{2/3}. \tag{7.19}$$

To put the center of mass at $x = 0$, the following equations need to be satisfied,

$$M_1x_1 + M_2x_2 = 0 \tag{7.20}$$

$$x_1 - x_2 = s_{min}, \tag{7.21}$$

where x_i is the distance from the centre of mass of star i. I choose that the initial positions lie on the x-axis. Therefore,

$$x_2 = -\frac{M_1s_{min}}{M_2 + M_1} \tag{7.22}$$

$$x_1 = s_{min} + x_2. \tag{7.23}$$

By substituting Equation (7.19) into Equation (7.22), we get the following expression for the

initial position of star 2,

$$x_2 = -\mathrm{G}M_1\left(1-\mathrm{e}\right)\left(\frac{P}{2\pi\mathrm{G}\left(M_2+M_1\right)}\right)^{2/3}. \tag{7.24}$$

We can now substitute this into Equation (7.23) to get the initial position for star 1,

$$x_1 = \mathrm{G}M_2\left(1-\mathrm{e}\right)\left(\frac{P}{2\pi\mathrm{G}\left(M_1+M_2\right)}\right)^{2/3}. \tag{7.25}$$

We can also derive the initial velocities of each star. If we substitute

$$\dot{y}_2 = \frac{M_1\dot{y}_1}{M_2}, \tag{7.26}$$

$$|x_1 - x_2| = s_{min}, \tag{7.27}$$

and Equation (7.18) into Equation (6.6) (noting that the binary is set up in the centre of mass frame, i.e. $\boldsymbol{v}_c = 0$) we get

$$-\frac{1}{2}\left(\frac{2\pi\mathrm{G}}{P\sqrt{M_1+M_2}}\right)^{2/3}M_1M_2 = \frac{1}{2}M_1|\dot{y}_1|^2 + \frac{1}{2}M_2\left(\frac{M_1|\dot{y}_1|}{M_2}\right)^2 - \frac{\mathrm{G}M_1M_2}{s_{min}} \tag{7.28}$$

Rearranging, and substituting in Equation (7.19) gives

$$|\dot{y}_1| = \frac{M_2}{M_1+M_2}\sqrt{\frac{1+\mathrm{e}}{1-\mathrm{e}}}\left(\frac{2\pi\mathrm{G}\left(M_1+M_2\right)}{P}\right)^{1/3}. \tag{7.29}$$

Using $M_2|\dot{y}_2| = M_1|\dot{y}_1|$, we know that

$$|\dot{y}_2| = \frac{M_1}{M_2}|\dot{y}_1|, \tag{7.30}$$

and so

$$|\dot{y}_2| = \frac{M_1}{M_1+M_2}\sqrt{\frac{1+\mathrm{e}}{1-\mathrm{e}}}\left(\frac{2\pi\mathrm{G}\left(M_1+M_2\right)}{P}\right)^{1/3}. \tag{7.31}$$

At periastron, the velocity will be perpendicular to the position vector. I choose the binary to

be in the (x, y) plane. As the stars are placed on the x axis, the velocities need to be in the y direction. The velocities then become

$$\dot{y}_1 = \frac{M_2}{M_1 + M_2}\sqrt{\frac{1+\mathrm{e}}{1-\mathrm{e}}}\left(\frac{2\pi \mathrm{G}\,(M_1+M_2)}{P}\right)^{1/3}\hat{y} \tag{7.32}$$

$$\dot{y}_2 = \frac{-M_1}{M_1 + M_2}\sqrt{\frac{1+\mathrm{e}}{1-\mathrm{e}}}\left(\frac{2\pi \mathrm{G}\,(M_1+M_2)}{P}\right)^{1/3}\hat{y}. \tag{7.33}$$

7.3.2 Results

The binaries are allowed to run for 500 time units, and their parameters computed at the end of the simulation.

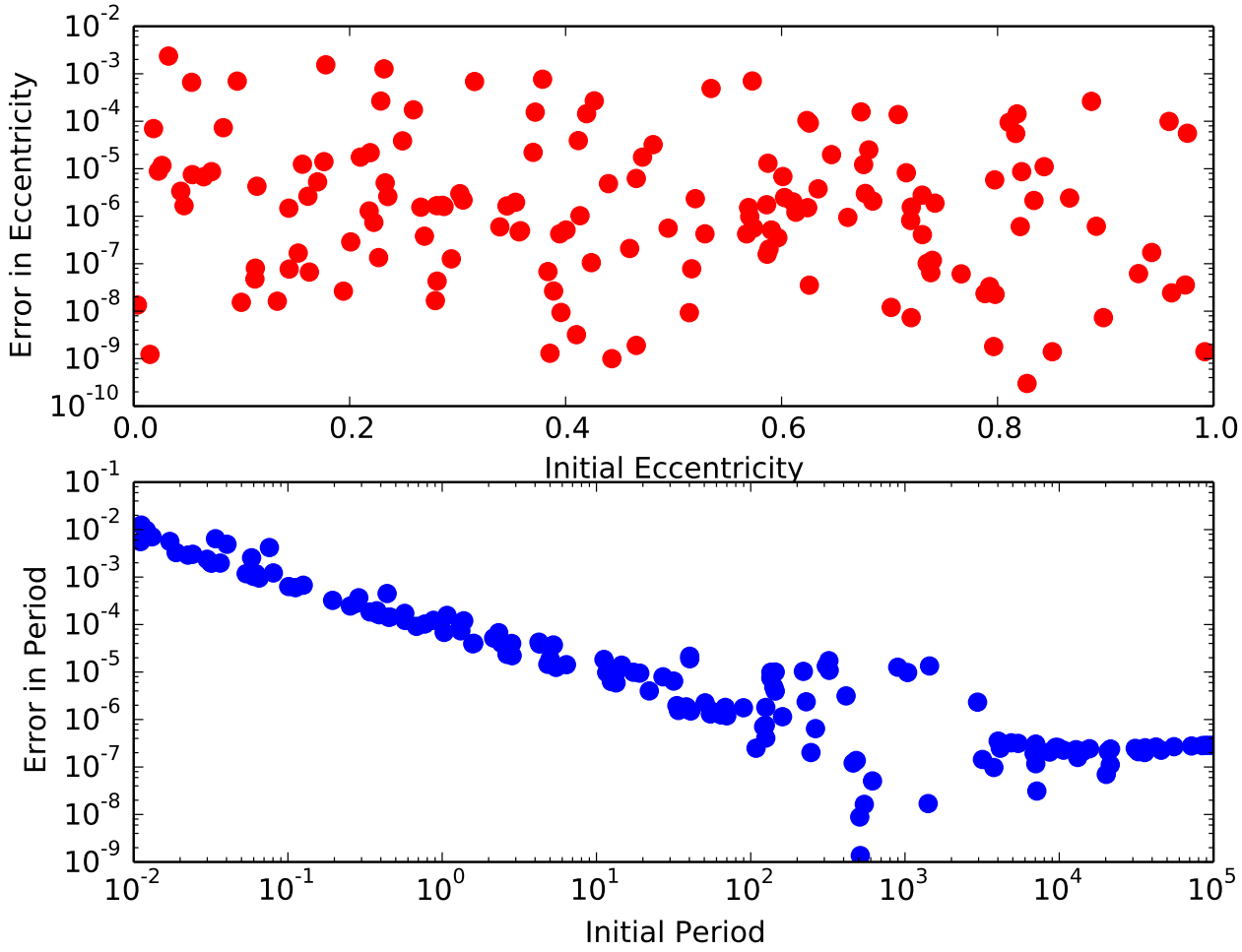

Figure 7.1: 100 eccentric binary systems are set up and allowed to evolve for 500 computer time units. At the end of the simulation, the eccentricity and period of the binary systems are determined. The top graph plots the error between the initial and final values for eccentricity against the initial eccentricity. The bottom plot shows the same for the period.

The errors in the period and eccentricity for the eccentric binaries can be seen in Figure 7.1, with eccentricity plotted on the top graph, and period plotted below. The error in the eccentricity has no dependence on the initial eccentricity of the system. The error in the period decreases with the initial period.

Chapter 8

Core Cluster Results: Part I

In this chapter I present and discuss the properties of long-lived multiple systems that form in the core-cluster simulations described in Chapter 5. The first section deals with the fiducial model, and the sections thereafter investigate N_0, the number of stars produced per core, $\mathcal{V}$, the initial virial balance of the core cluster and $\sigma_{_0}$, the variance in the stellar masses in a single core cluster.

I define the mass ratio of the outer orbit of a triple to be

$$q = \frac{M_{outer}}{M_{binary}}. \tag{8.1}$$

Similarly for the orbits of quadruples,

$$q = \frac{M_{mid}}{M_{binary}} \qquad \text{Mid orbits of hierarchical quadruples} \tag{8.2}$$

$$\frac{M_{outer}}{M_{triple}} \qquad \text{Outer orbits of hierarchical quadruples} \tag{8.3}$$

$$\frac{M_{binary_2}}{M_{binary_1}} \qquad \text{Outer orbits of double binary quadruples.} \tag{8.4}$$

Note that in the final case $M_{binary_1} > M_{binary_2}$. No systems are double counted, for example, if a binary system is found to form part of a triple system, then its properties are only included in the inner orbits of triples, they will not contribute to the binary graphs and statistics.

The dimensionless masses of the cores are convolved with the CMF (Equation 3.3) to produce a multiplicity frequency as a function of primary mass. The dimensionless radii are convolved with Equation (7.14) to find the radii of the core in physical units. Together with the masses of the cores, the radii are used to compute the periods in years (Section 7.2.1).

8.1 Fiducial Model

In this section I present and discuss the results of the fiducial model (see Table 5.1). I run 8920 models, which produces 6065 binaries, 2725 triples, 33 hierarchical quadruples and 165 double quadruples.

Figure 8.1 shows the properties of the binaries. The eccentricities are thermally distributed, as shown in Sub-figure 8.1a. The mass ratio distribution shown in Sub-figure 8.1b is the distribution over the entire primary mass range. Note that the small number of systems with $q < 0.2$ is due to the relatively small σ_0, i.e. for the majority of cores, there are no stars disparate enough in mass to produce such low mass ratios. The period distribution shown in Sub-figure 8.1c is very narrow (possibly due to the narrow range of core sizes and virial ratios assumed), with a standard deviation of $\sigma_P \sim = 0.6$ and a mean of $\mu_P \approx 10^{2.2} \sim 160$ yr. The corresponding distribution of semi-major axes has the mean $\mu_{sma} = 10^{1.4} = 25$ AU and standard deviation $\sigma_{sma} \sim 0.4$ (see also Table 8.1).

Table 8.1: Mean and standard deviations of $\log_{10}(a/\mathrm{AU})$ and $\log_{10}(P/\mathrm{yr})$.

Fiducial			
	Binaries	Triples	
		Inner	Outer
period	2.246±0.480	2.297±0.436	4.484±1.041
sma	12.57±0.401	12.61±0.376	14.09±0.732

Table 8.2: Mean and standard deviations of $\log_{10}(a/\mathrm{AU})$ and $\log_{10}(P/\mathrm{yr})$.

Fiducial					
	Quad, Hierarchical			Quad, Double	
	Inner	Mid	Outer	Inner	Outer
period	2.443±0.407	4.666±1.031	7.268±0.835	3.236±1.206	4.720±1.033
sma	12.70±0.370	14.21±0.739	15.97±0.608	13.16±0.778	14.27±0.716

The multiplicity frequency as a function of primary mass (Sub-figure 8.1d) has a steeper slope than was predicted by the purely statistical arguments presented in Chapters 3 and 4, due to the lack of dissipation (i.e. $\beta \gg 0$ in these simulations). In Sub-figure 8.1e) the graph of M_1 against M_2 is plotted. The boundary is simply due to the allowed mass ratios given that the total variance of the masses of the stars must equal σ_0. The plots as shown in Reipurth & Mikkola (2012) spread across the entire plot. This is because in the Reipurth & Mikkola (2012)

paper there was no set limit to the total mass of the system, nor to the standard deviation of the masses in the core-cluster.

When looking at the properties of the triple systems (Figure 8.2), it can be seen in Sub-figure 8.2a that there are fewer outer orbits with a high eccentricity than would be expected with a thermal distribution. This is because the very eccentric outer orbits tend to be disrupted at periastron, due to the close approach of the components, and the system is broken up. The inner orbits (blue line), however, still have a thermal distribution. The mass ratio plot in Sub-figure 8.2b shows an outer mass ratio distribution that tends toward $q = 0$. This is where a binary tends to be orbited by a star that is smaller than the components of the binary. The period distribution given in Sub-figure 8.2c for the outer orbits has a larger spread and is shifted to longer periods than both the pure binaries, and the inner pairs of hierarchical triples (see also Table 8.1). The graph of M_1 against M_2 is plotted in Sub-figure 8.2d, showing a distribution that is similar to the distribution for pure binaries, save for a lack of low-mass components. The graph of M_3 against $M_2 + M_1$ is plotted in Sub-figure 8.2e. It can be seen that the majority of systems have a dominant binary, for the majority of cases the third star is much smaller than the inner binary.

Only a handful of hierarchical quadruples are produced (33 in total, see also Table 8.3) and so the results shown in Figure 8.3 are less well constrained. The orbits of the inner pairs and mid stars appear to have similar properties to the triple systems. The outermost orbits have a high eccentricity (Subfigure 8.3a) as there have not been any stars have been ejected from the core cluster, so no energy has been lost from the system, and the quadruple is only just bound ($\mathcal{V} = 0.5$). As we can see from Equation 6.11, a small binding energy means a high eccentricity. The outermost star tends to be smaller than any of the inner components, as evidenced by the strong mass ratio peak at $q < 0.2$ in Sub-figure 8.3b. The period of the outer orbits are shifted again to longer times, with a mean of ∼20,000,000 yrs. The graph of M_1 against M_2 is plotted in Sub-figure 8.3d, the graph of M_3 against $M_2 + M_1$ in Sub-figure 8.3e and the graph of M_4 against $M_3 + M_2 + M_1$ in Sub-figure 8.3f. Due to low-number statistics, conclusions cannot be drawn. Note however, that the straight line in Sub-figure 8.3d is simply a result of the condition that the sum of the components by definition must add up to 1.

The statistics for double quadruples are shown in Figure 8.4, with the properties of the inner pairs shown by blue lines, and the properties of the outer orbits by red lines. Sub-figure 8.4a shows that there is a high fraction of outer orbits with high eccentricity for the same reason as given above. The distribution of both inner and outer mass ratios (Subfigure 8.4b) shows that the two inner pairs tend to have an intermediate mass ratio, with the majority of systems having a mass ratio between $q = 0.2$ and 0.4. The period distribution for the outer orbits peaks at a higher value than the inner pairs ($\sim 10^{4.7}$ yrs, see Table 8.2), and is comparable in scale to the outer orbit of triples, rather than the outer orbit of hierarchical quadruples. The graph

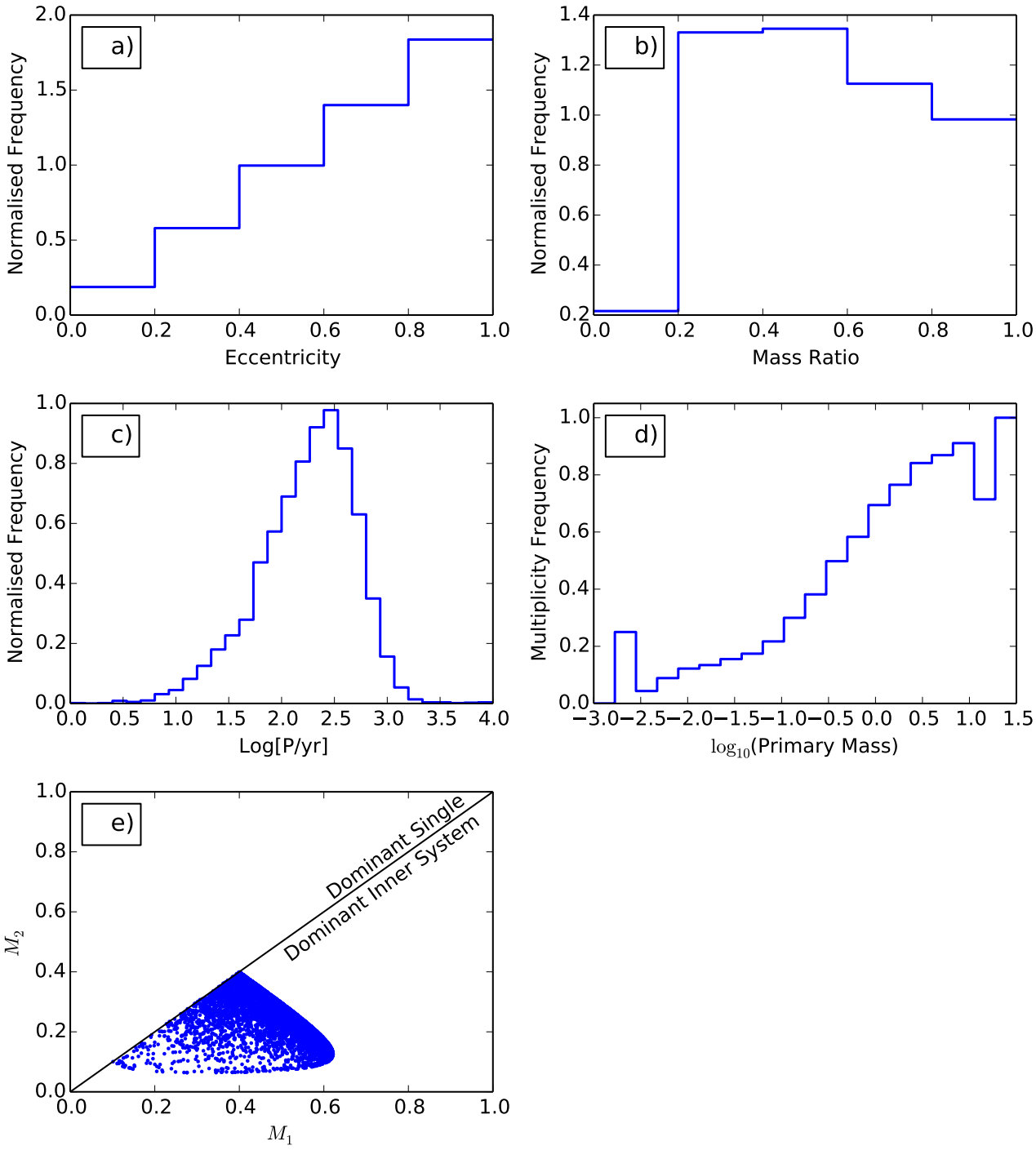

Figure 8.1: The properties for the 6065 binaries produced by the fiducial model. Frame a) shows the normalised distribution of eccentricities, Frame b) shows the normalised distribution of mass ratios, Frame c) shows the normalised distribution of periods [yr], Frame d) shows the multiplicity frequency as a function of primary mass, and Frame e) plots M_2 against M_1.

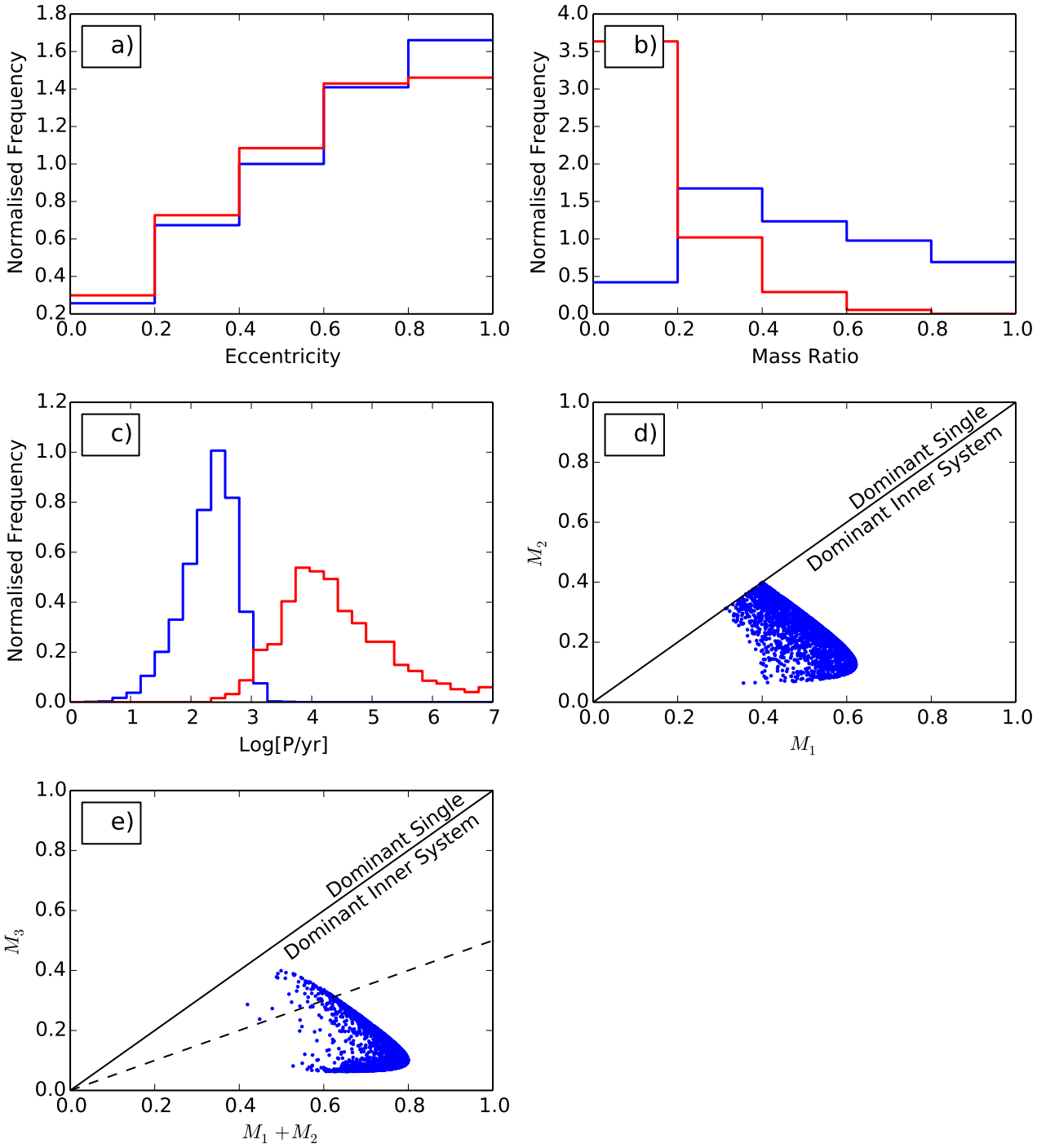

Figure 8.2: The properties of the 2725 triples formed in the fiducial model. Frame a) shows the normalised distribution of eccentricities, Frame b) shows the normalised distribution of mass ratios and Frame c) shows the normalised distribution of periods [yr]. The blue lines show the inner periods, whilst the red lines show the outer periods. Frame d) plots M_2 against M_1, whilst Frame e) plots M_3 against $M_2 + M_1$.

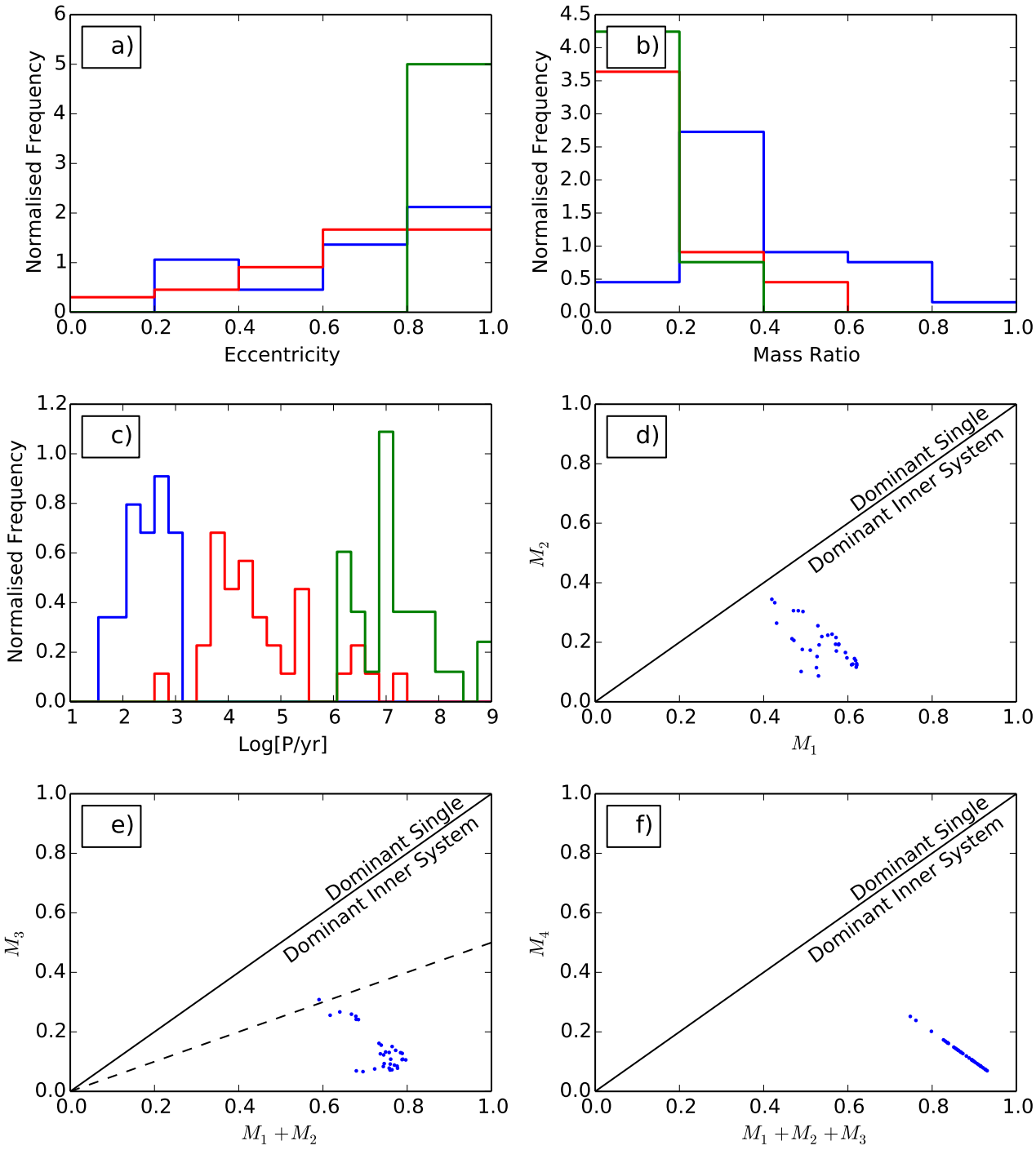

Figure 8.3: The properties of the 33 hierarchical quadruples produced by the fiducial model. Frame a) shows the normalised distribution of eccentricities, Frame b) shows the normalised distribution of mass ratios and Frame c) shows the normalised distribution of periods [yr]. The blue lines show the inner periods, the red lines show the mid periods and the green lines show the outer periods. Frame d) plots M_2 against M_1, whilst Frame e) plots M_3 against $M_2 + M_1$, and Frame f) plots M_4 against $M_3 + M_2 + M_1$.

of M_2 against M_1 and M_4 against M_3 is plotted in 8.4c. The higher-mass binary lies in the same distribution as the pure binaries, but the second binary tends to comprise smaller stars, and so populate the bottom left corner of the graph. The graph of $M_4 + M_3$ against $M_2 + M_1$ is plotted in 8.4d. Note again, that the straight line in Sub-figure d is simply a a result of the condition that the sum of the components must add up to 1.

Further analysis shows that the two larger stars tend to pair up, and the two smaller stars tend to pair up. The more massive of the two pairs tend to have a smaller period, with a similar distribution to the pure binaries. The period of the less massive pair has a much larger standard deviation, ranging from a period of less than 1 to more than 100 dimensionless crossing times (the pure binaries peak at 1 dimensionless crossing time). As pure binaries of the same high period are not found, it can be assumed that being a part of a double quadruple helps to stabilise the system. Or that every time a wide binary forms, a double quadruple is formed around it. The can be seen in the high period tail for the inner pairs in Sub-figure 8.4c.

Figures 8.5a, 8.5b, 8.5c and 8.5d show plots of period against eccentricity for binaries, triples, hierarchical quadruples and double quadruples respectively. We can see in Figure 8.5a that there appears to be no correlation between the period and the eccentricity of the binaries, other than the long-period binaries tend to have higher eccentricity. Almost all the binary systems are very stable, with the fidelity approaching 1. The data for the triple systems displayed in Figure 8.5b shows that there is a trend for the outer orbits of triples with very high eccentricity to have longer periods and lower fidelity parameters. This is because orbits with the same eccentricity but smaller periods will have a smaller separation at periastron with the inner pair, and hence the system is more likely to be disrupted. Whilst Figure 8.5c shows that the outermost orbits of hierarchical quadruples have a very low fidelity, this could just be due to the fact that these orbits have not yet completed a full orbit before the simulation was terminated. The data for the double quadruples displayed in Figure 8.5d shows that the outer orbits have a lower fidelity than the inner orbits. It also shows that the fidelity decreases as the eccentricity and/or period increases, i.e. the more compact, circular systems are the most stable.

Table 8.3 shows the average number of multiple systems produced per core. Note that the sum of binaries, triples and quadruples needs to add up to 1 or greater. This is because a core will produce a minimum of one multiple system, or potentially an additional binary system, giving a total of two for said core. The majority of cores produce a single binary, with most others producing a triple system. It is noteworthy that approximately 5 times as many double quadruples are produced as hierarchical quadruples.

The simulations show that the majority of cores (69%) produce systems involving the two most massive stars in the core, and 85% of cores produce systems involving the most massive star. As gravity is the only method of interaction between the stars, stellar mass plays a big role in determining the components of multiple systems, explaining the large fraction of cores

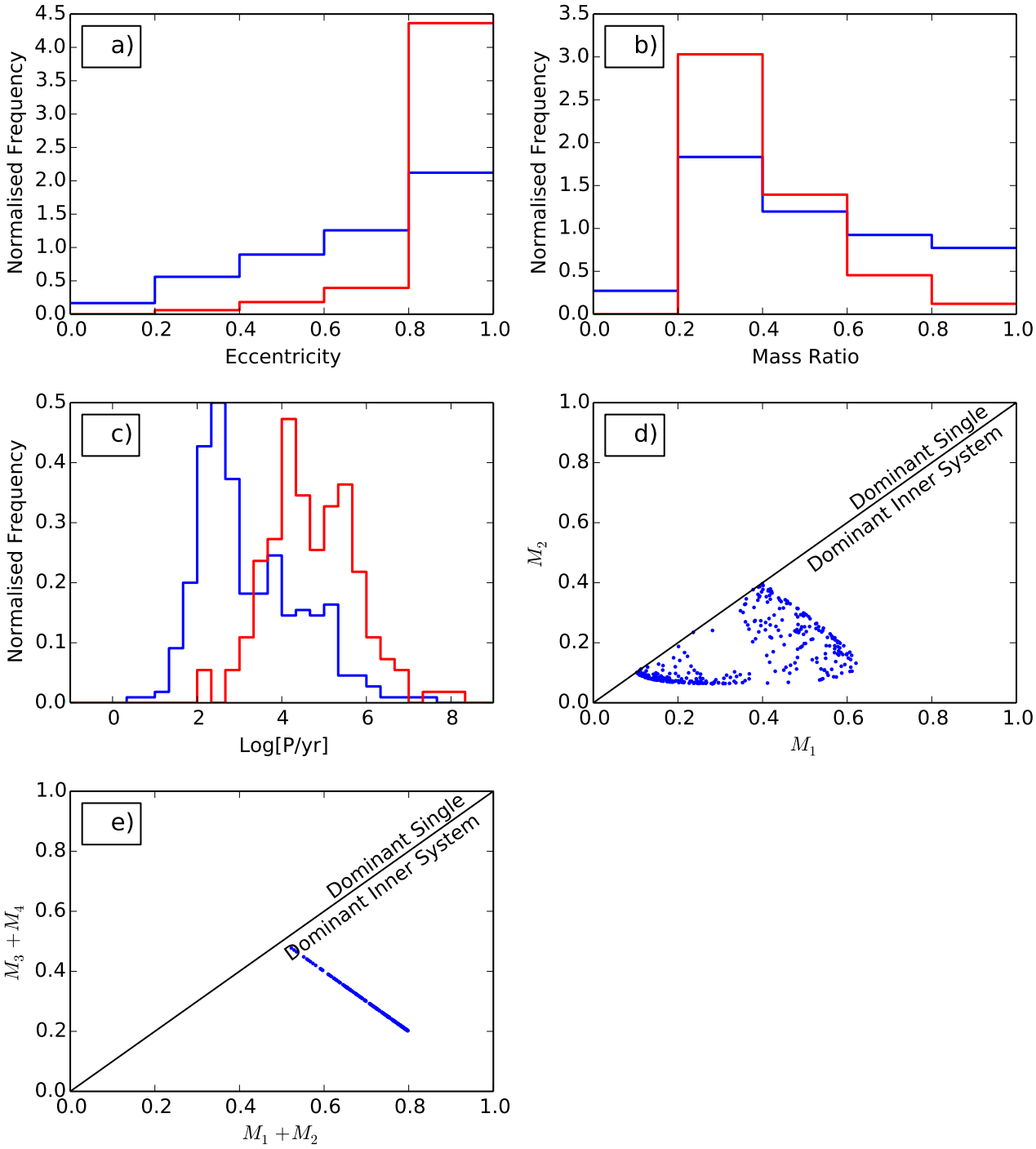

Figure 8.4: The properties of the 165 double quadruples produced by the fiducial model. Frame a) shows the normalised distribution of eccentricities, Frame b) shows the normalised distribution of mass ratios and Frame c) shows the normalised distribution of periods [yr]. The blue lines show the inner periods, whilst the red lines show the outer periods. Frame d) plots M_2 against M_1 and M_4 against M_3, and Frame e) plots $M_4 + M_3$ against $M_2 + M_1$.

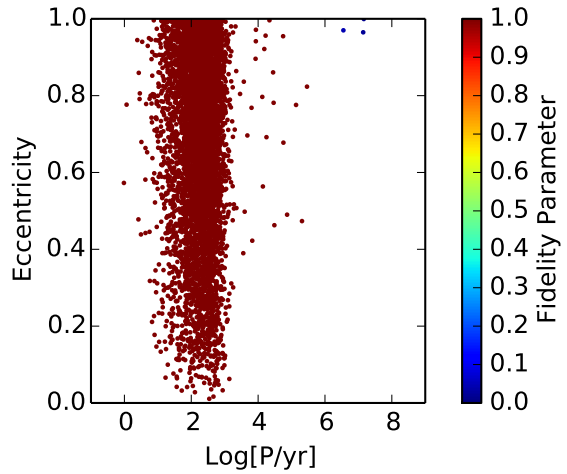

(a) The distribution of the 6065 binary systems in the $(\log_{10}(P/\mathrm{yr}), \mathrm{e})$-plane for the fiducial model. The colour of the points encodes the fidelity parameter.

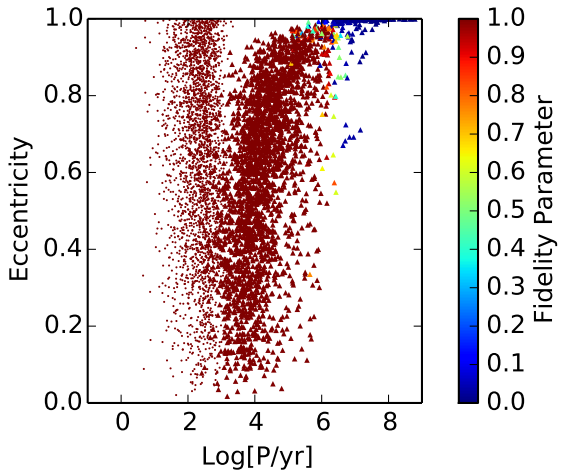

(b) The distribution of the 2725 triple systems in the $(\log_{10}(P/\mathrm{yr}), \mathrm{e})$-plane for the fiducial model. Small circles represent inner orbits and triangles represent outer orbits. The colour of the points encodes the fidelity parameter.

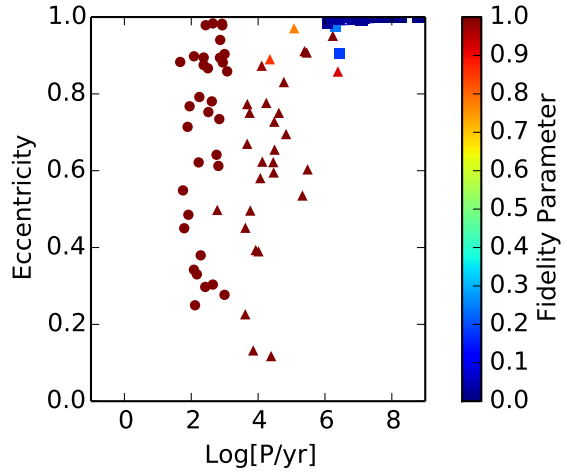

(c) The distribution of the 33 hierarchical quadruple systems in the $(\log_{10}(P/\mathrm{yr}), \mathrm{e})$-plane for the fiducial model. circles represent inner orbits, red triangles represent mid orbits and squares represent outer orbits. The colour of the points encodes the fidelity parameter.

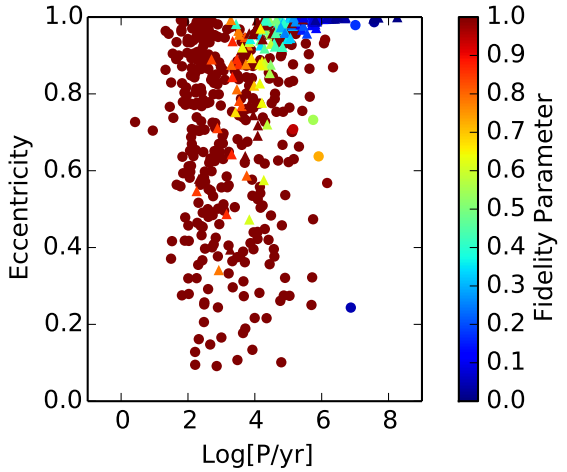

(d) The distribution of the 165 double quadruple systems in the $(\log_{10}(P/\mathrm{yr}), \mathrm{e})$-plane for the fiducial model. Circles represent inner orbits and triangles represent outer orbits. The colour of the points encodes the fidelity parameter.

Table 8.3: Average number of multiple systems produced per core.

Fiducial	Binaries	Triples	Hierarchical Quadruples	Double Quadruples
Fiducial	0.6799	0.3055	0.0037	0.0185

producing systems involving the most massive stars.

8.2 The Number of Stars in a Core

In this section I present the results of varying the number of stars a core produces. I run 10000, 9873, 8920, 7595, 2728 simulations each for $N_0 = 2$, 3, 4, 5, and 6 respectively, the reduced number of simulations reflecting the increased computational time required. These sets of simulations produce 9993, 9873, 6065, 4356, 1658 binaries for $N_0 = 2$, 3, 4, 5 and 6 respectively. There are 0, 0, 2725, 3159, 1087 triples produced, 0, 0, 33, 146, 110 hierarchical quadruples and 0, 0, 165, 223, 93 double quadruples are produced.

The properties of the binary systems produced are shown in Figure 8.5. There is a marked effect on the resulting eccentricity distribution for binaries between $N_0 = 2$ and $N_0 > 2$ (see Sub-figure 8.5a). For $N_0 = 2$, there is no opportunity to redistribute energy by ejecting other stars from the cluster. Therefore, the eccentricity distribution is no longer thermal, but is instead $f(e) = 1.5e^2 + 2e^3$, where there are fewer low-eccentricity binaries, and more binaries with eccentricities tending towards 1. For $N_0 > 2$, the eccentricity distribution is thermal, $f(e) \sim 2e$, as energy can now be redistributed when stars are ejected. The final eccentricity distribution does not alter as N_0 is further increased.

In Sub-figure 8.5b we can see that there is also a marked difference between the mass ratio distributions for $N_0 = 2$ and $N_0 > 2$. The standard deviation is always equal to σ_0, this being a direct consequence of the normalisation technique (Section 5.1.3). For two stars, this is equal to giving them a separation in logspace of $2\sigma_0$ as shown by the following proof,

$$\begin{aligned} \text{Separation} = 2\sigma_0 &= \log_{10}(M_1) - \log_{10}(M_2) \\ 2\sigma_0 &= -\log_{10}\left(\frac{M_2}{M_1}\right) = -\log_{10}(q) \\ q &= 10^{-2\sigma_0} \end{aligned} \tag{8.5}$$

For $N_0 = 2$, and $\sigma_0 = 0.3$, q is always equal to 0.25, and a vertical bold black line has been drawn on Sub-figure 8.5b to show where this lies. As N_0 increases, the mass ratio distribution flattens out, and the peak at $10^{-2\sigma_0}$ becomes less prominent. For $N_0 = 4$, the peak is no longer visible. $q < 0.2$ always has a small population, due to the fiducial value for σ_0. In Sub-figure 8.5c, the period distributions have been plotted. We can see in both this figure and Table 8.4 that as N_0 increases, the peak of the period shifts to smaller values and the width of the distribution also increases. This is because as N_0 increases, there are more stars to kick out. Each time a star is kicked out, energy is lost from the system, and the period of the remaining system decreases. The total amount of energy lost varies each time a star is ejected. With a larger N_0, there is a greater spread in the total energy lost, and hence a greater spread in the distribution of periods.

Table 8.4: Mean and standard deviation of $\log_{10}(P/\mathrm{yr})$

Nstar			
	Binaries	Triples	
		Inner	Outer
$N_0 = 2$	2.957±0.438	—±nan	—±nan
$N_0 = 3$	2.559±0.460	—±nan	—±nan
$N_0 = 4$	2.242±0.482	2.291±0.438	4.478±1.034
$N_0 = 5$	2.116±0.663	2.062±0.436	4.386±0.926
$N_0 = 6$	2.082±0.908	1.897±0.431	4.382±0.898

Table 8.5: Mean and standard deviation of $\log_{10}(P/\mathrm{yr})$

Nstar					
	Quad, Hierarchical			Quad, Double	
	Inner	Mid	Outer	Inner	Outer
$N_0 = 2$	—±nan	—±nan	—±nan	—±nan	—±nan
$N_0 = 3$	—±nan	—±nan	—±nan	—±nan	—±nan
$N_0 = 4$	2.455±0.393	4.677±0.942	7.280±0.837	3.221±1.221	4.706±1.052
$N_0 = 5$	2.103±0.439	4.206±0.858	6.335±1.133	3.233±1.434	4.918±1.131
$N_0 = 6$	1.907±0.415	4.017±0.908	6.020±1.046	3.242±1.567	5.133±1.070

For $N_0 = 2$, every star is part of a binary system, and so the multiplicity frequency is 100% for every primary mass range (see Subfigure 8.5 d, dotted line). The slope of the graph of multiplicity frequency against primary mass becomes steeper as N_0 increases, especially in the high primary mass regime. Table 8.6 shows that as N_0 increases, the percentage of cores producing systems that involve the most massive stars decreases. Therefore, the more massive stars are more likely to be singles, and the multiplicity frequency decreases in the high primary mass regime. The graph of M_1 against M_2 is plotted in Sub-figure 8.5e. As N_0 increases, the average size of the components becomes smaller, as a result of dividing the total mass between more stars. However, the shape of the distribution is constant with any changes in N_0.

Table 8.6: Percentage of cores producing systems involving the most massive stars

Nstar	Most massive star	Two most massive stars
$N_0 = 2$	1.00	1.00
$N_0 = 3$	0.99	0.84
$N_0 = 4$	0.96	0.77
$N_0 = 5$	0.95	0.72
$N_0 = 6$	0.93	0.66

Figure 8.6 shows the properties of the triple systems that are produced with the different values of $N_0 = 4$, 5 and 6 (neither $N_0 = 2$ nor 3 produces any triples). The eccentricity distributions for all orbits (see Figure 8.6a) follow the same distribution as the fiducial model. In Sub-figure 8.6b we can see that both the outer and the inner period of the triples have a lower fraction of low-q orbits as N_0 increases, the effect being greater for the outer orbit. The inner orbit has a flatter distribution for $q > 0.2$ as N_0 increases, i.e. the outermost star becomes larger compared to the inner pair, whilst the mass ratio distribution for the inner pairs are much flatter than for pure binaries. The period distributions are shown in Sub-figure 8.6c. The mean of the inner period decreases with increasing N_0, for both the inner and the outer orbits. This can be explain using the same argument as was invoked for the binaries, as N_0 increases, there are more stars to eject, and so more energy can be lost, hardening and decreasing the period of the orbits. As the mean of the outer periods are not affected, the peaks of the inner and outer period distributions move apart with increasing N_0. In Sub-figure 8.6d M_2 is plotted against M_1, and in Sub-figure 8.6d M_3 is plotted against $M_2 + M_1$. The same trends are seen for both the outer orbits and inner orbits as were seen for the binaries.

The properties of the hierarchical quadruples are shown in Figure 8.7. The eccentricity distributions given in Sub-figure 8.7a show an outer orbit that has a strong peak at high eccentricities, similar to the effect on the eccentricity of the binaries for $N_0 = 2$. This peak at $e = 1$ for the outer orbits decreases as N_0 increases. Both the middle and inner orbits

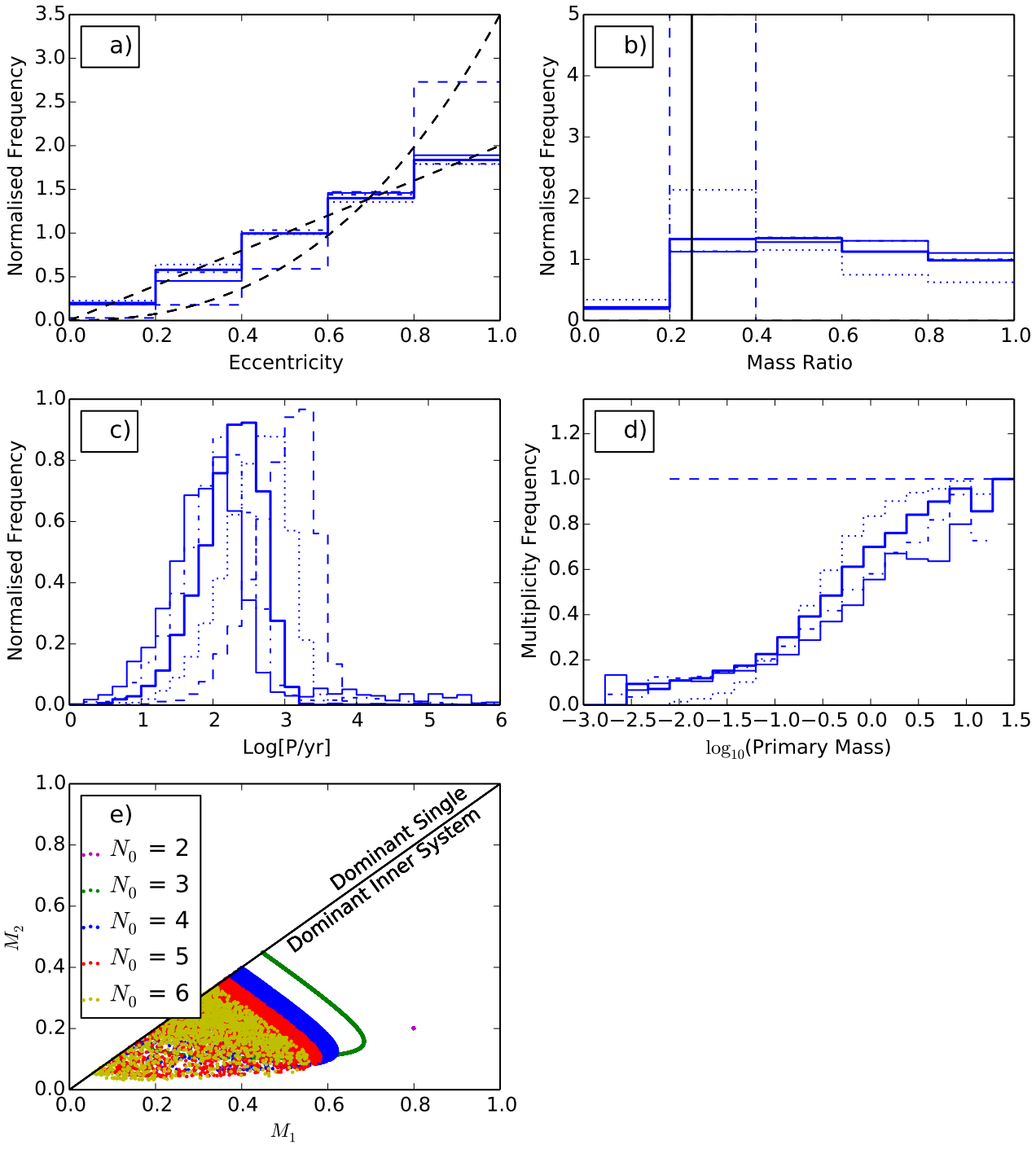

Figure 8.5: The variation of binary properties with N_0. The dashed/dotted/thick solid/dot-dashed/thin solid lines in each of the Frames describes the distributions attained when N_0 = 2, 3, 4, 5 and 6 respectively. Frame a) shows the normalised distribution of eccentricities. The black dashed lines show a thermal distribution (the straight line), and $f\,(\mathrm{e}) = 1.5e^2 + 2e^3$, which is a good fit to the $N_0 = 2$ case. Frame b) shows the normalised distribution of mass ratios, Frame c) shows the normalised distribution of periods [yr] and Frame d) shows the multiplicity frequency as a function of primary mass, and Frame e) plots M_2 against M_1. 9993, 9873, 6065, 4356, 1658 binaries are plotted for N_0 = 2, 3, 4, 5 and 6 respectively.

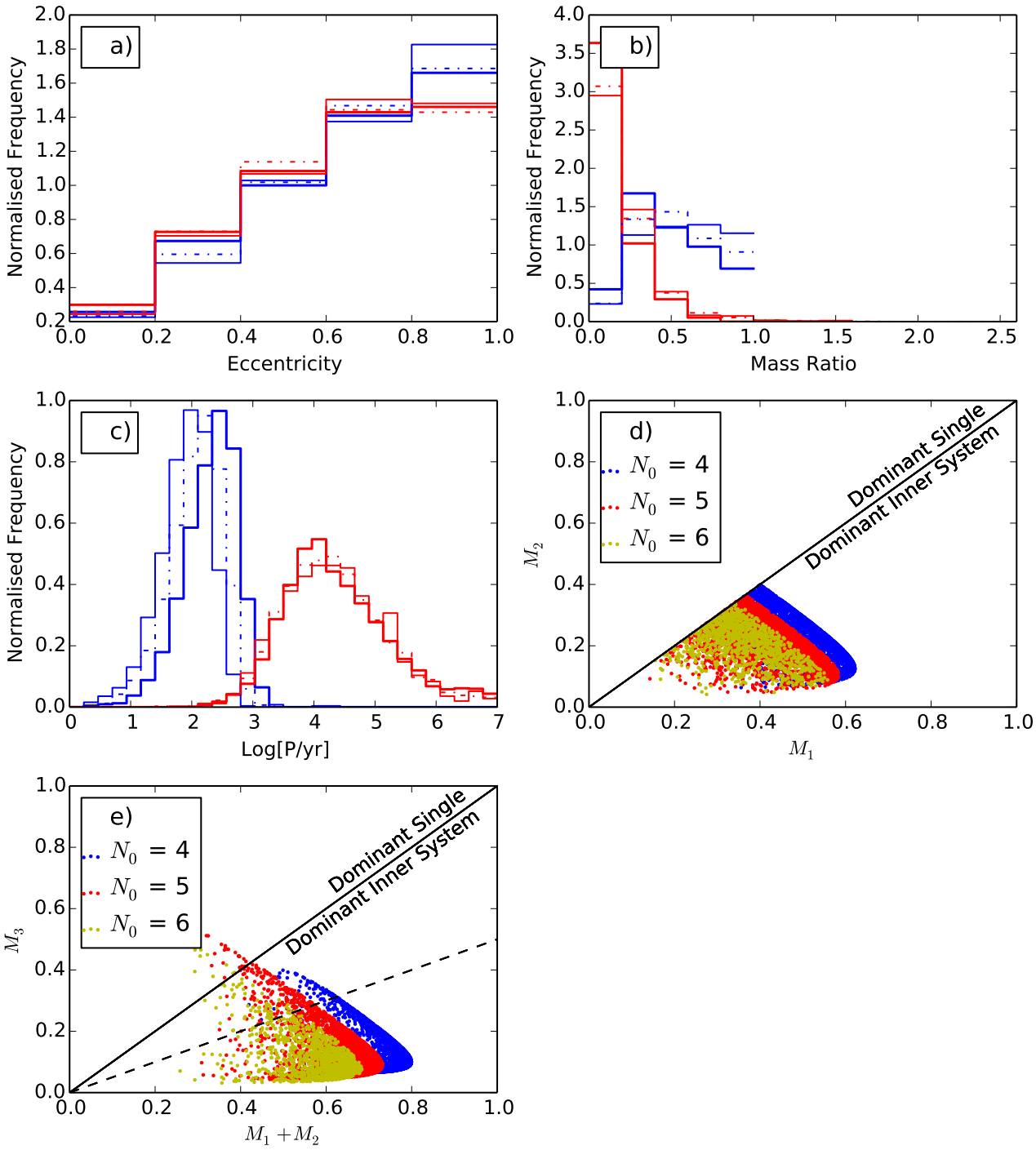

Figure 8.6: The variation of properties of triples formed with N_0. The thick solid/dot-dashed/thin solid lines in each of the Frames describes the distributions attained when N_0 = 4, 5 and 6 respectively. The blue lines show the inner periods, whilst the red lines show the outer periods. Frame a) shows the normalised distribution of eccentricities, Frame b) shows the normalised distribution of mass ratios and Frame c) shows the normalised distribution of periods [yr]. Frame d) plots M_2 against M_1, whilst Frame e) plots M_3 against $M_2 + M_1$. 0, 0, 2725, 3159, 1087 triples are plotted for N_0 = 2, 3, 4, 5, and 6 respectively.

possibly become more circular as N_0 increases, but better number statistics would be needed to confirm the trend. The mass ratios in Sub-figure 8.7b show that as N_0 increases, the innermost pair tends towards equal masses, inhibited perhaps only by the availability of equal mass companions. Both the middle and outer mass ratio distributions have a peak between $q = 0$ and 0.2, but the size of this peak for the middle orbit decreases as N_0 increases. We have a situation where the components of the quadruple become more and more equal in mass as N_0 increases. The period distributions for hierarchical quadruples can be seen in Sub-figure 8.7c, and Table 8.5. The mean and standard deviations of the inner and middle orbits are comparable to the inner and outer orbits of the triple systems. The mean period of each of the orbits decreases as N_0 increases. In Sub-figure 8.7d M_2 is plotted against M_1, in Sub-figure 8.7e M_3 is plotted against $M_2 + M_1$ and in Sub-figure 8.7f M_4 is plotted against $M_3 + M_2 + M_1$. Although the number statistics are small, it can be seen that the quadruples follow the same trends as seen in both the triples and binaries.

The properties of double quadruples are shown in Figure 8.8. The peak of the eccentricity distribution (See Sub-figure 8.8 a) of the outer period at 1 becomes less prominent as N_0 increases. The eccentricity of the inner orbits remains unaffected by any change in N_0. Sub-figure 8.8b shows the mass ratios distributions. Both the outer mass ratio and the inner mass ratio distributions become flatter as N_0 increases, again suggesting that equal mass components are preferred for quadruples than disparate mass components. The mean period of both the inner orbits and outer orbits of double quadruples as seen in Sub-figure 8.8c and Table 8.5 increase with increasing N_0. The effect is greater for the outer orbits, so that there is a greater separation between the two pairs compared to their internal orbits. This is due to a combination of effects. Firstly, given that there are more masses to choose from, the mass ratios become flatter, so that equal masses are more likely. For a given orbit, a high mass ratio system is more stable than a small mass ratio system. Secondly, ejecting excess stars can circularise the orbit, which again is more stable than an eccentric orbit with the same period. Together, this means that outer orbits with a given orbit that may have disintegrated in a core with lower N_0 are more likely to be stabilised in a core with higher N_0. The effect is greater for higher periods. Because the higher periods are not destroyed so effectively, the standard deviations of the periods also increase with increasing N_0. In Sub-figure 8.8d, M_2 is plotted against M_1 and M_4 is plotted against M_3. In Sub-figure 8.8e $M_4 + M_3$ is plotted against $M_2 + M_1$. The trend of the inner binaries follows the same as all previous cases. The masses of the pairs also decreases on average, as before, but with the added trend that the standard deviation of the masses increases with N_0. this is because as N_0 increases, there is a greater range of masses that 4 stars can add up to, or in other words, a greater range in masses that can be ejected with escaping singles.

The period against eccentricity plots for the binaries are shown in Figure 8.9. Sub-figure

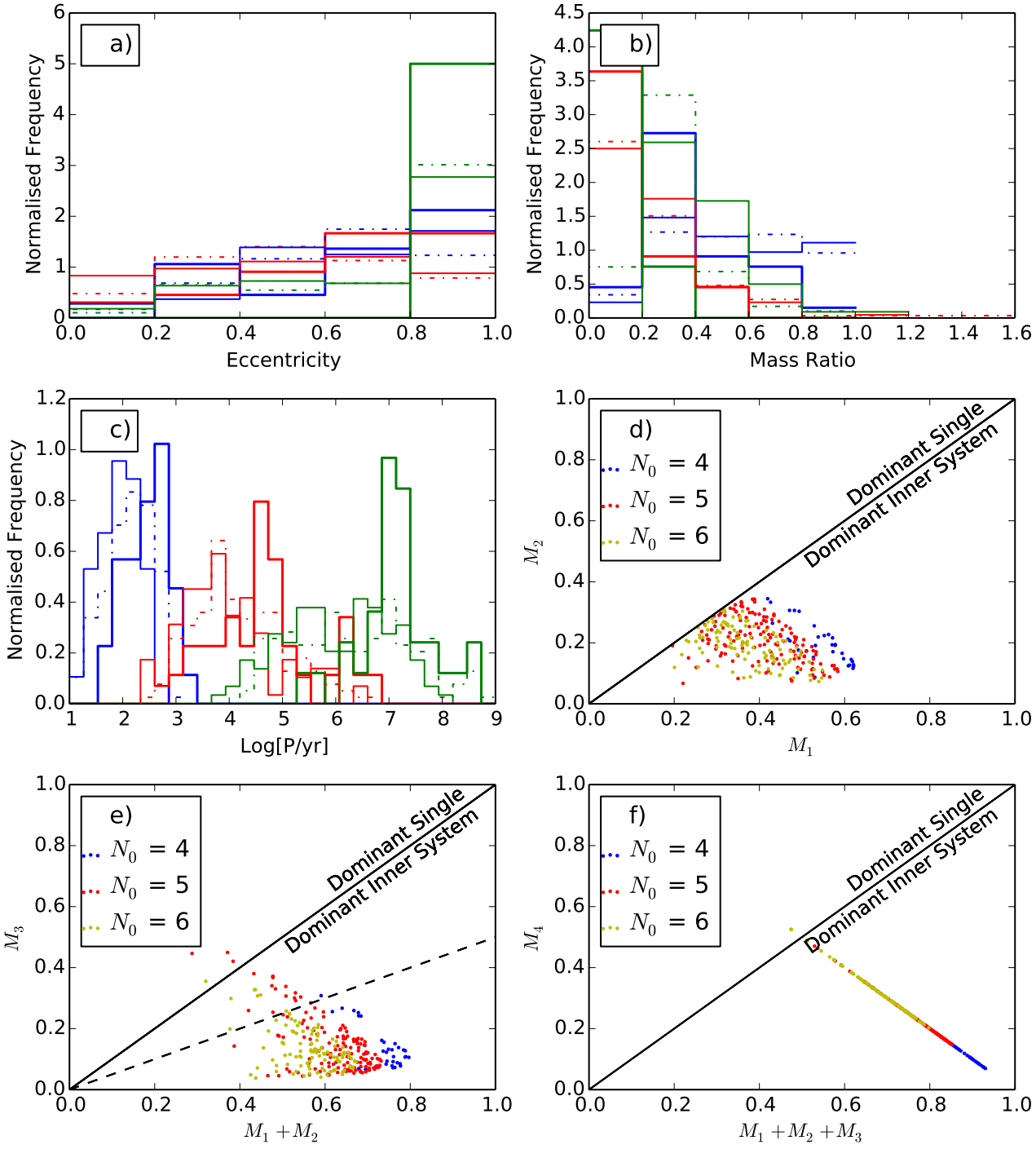

Figure 8.7: The variation of properties of hierarchical quadruples formed with N_0. The thick solid/dot-dashed/thin solid lines in each of the Frames describes the distributions attained when $N_0 = 4$, 5 and 6 respectively. The blue lines show the inner periods, the red lines show the middle periods and the green lines show the outer periods. Frame a) shows the normalised distribution of eccentricities, Frame b) shows the normalised distribution of mass ratios and Frame c) shows the normalised distribution of periods [yr]. Hierarchical quadruples cannot be produced in cores that only produce 2 or 3 stars. Frame d) plots M_2 against M_1, whilst Frame e) plots M_3 against $M_2 + M_1$, and Frame f) plots M_4 against $M_3 + M_2 + M_1$. 0, 0, 33, 146, 110 hierarchical quadruples are plotted for $N_0 = 2$, 3, 4, 5, and 6 respectively.

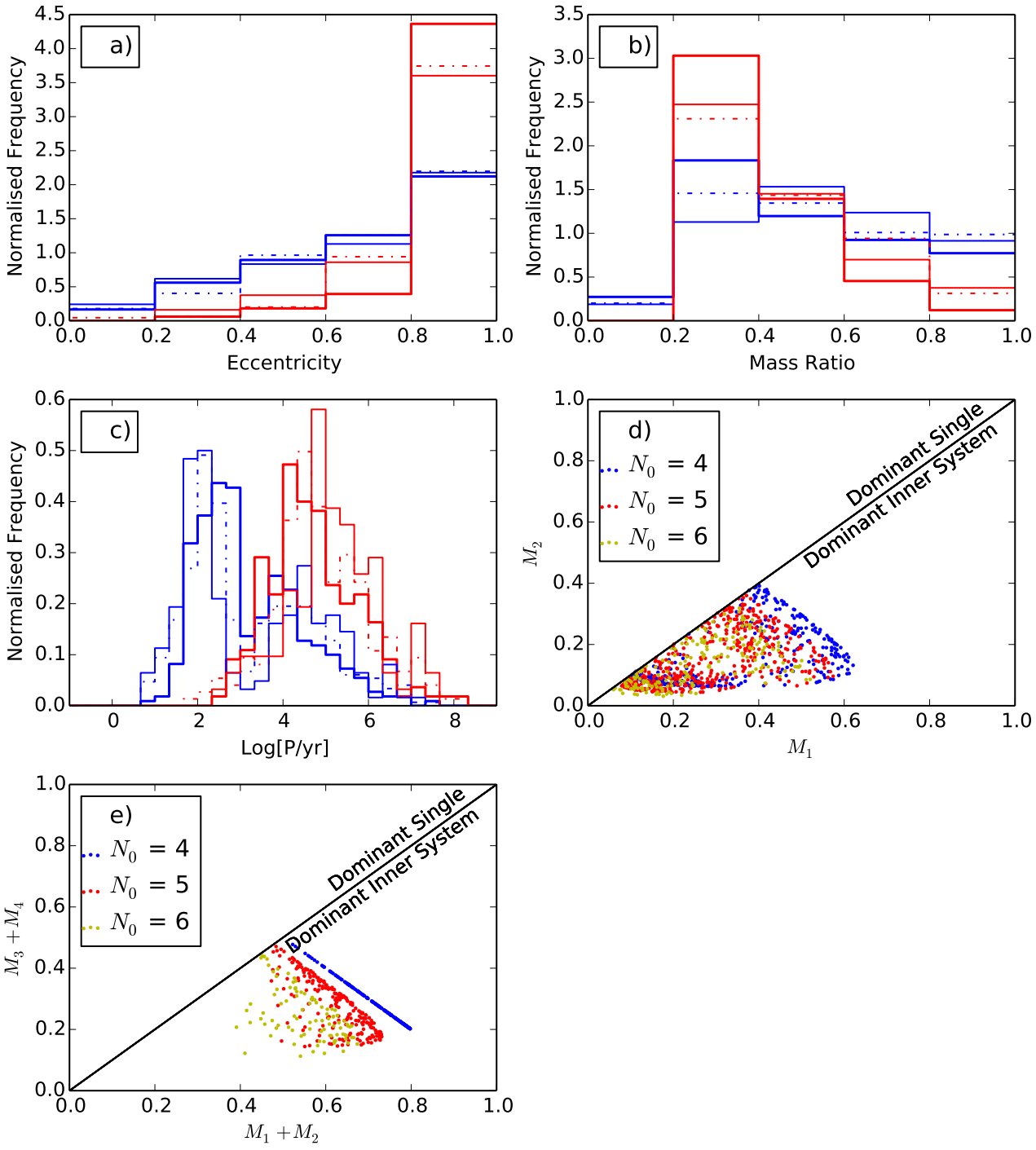

Figure 8.8: The variation of properties of double quadruples formed with N_0. The thick solid/dot-dashed/thin solid lines in each of the Frames describes the distributions attained when $N_0 = 4$, 5 and 6 respectively. The blue lines show the inner periods, whilst the red lines show the outer periods. Frame a) shows the normalised distribution of eccentricities, Frame b) shows the normalised distribution of mass ratios and Frame c) shows the normalised distribution of periods [yr]. Frame d) plots M_2 against M_1 and M_4 against M_3, and Frame e) plots $M_4 + M_3$ against $M_2 + M_1$. 0, 0, 165, 223, 93 double quadruples are plotted for $N_0 = 2$, 3, 4, 5, and 6 respectively.

8.9a shows the distribution for $N_0 = 2$, Sub-figure 8.9b shows $N_0 = 3$, 8.9c shows $N_0 = 4$, 8.9d shows $N_0 = 5$ and 8.9e shows $N_0 = 6$. The colour of the points encodes the fidelity parameter. As N_0 increases, small eccentricities are more likely to be occupied, especially for small periods. $N_0 = 5$ and 6 help to produce long period tails and a flat distribution of mass ratios. The upper limit to P in Subfigure 8.9a is set by the maximum size of a core (see Section 7.2.1).

The period against eccentricity plots for the triple systems are shown in Figure 8.10. Sub-figure 8.10a shows the distribution for $N_0 = 2$, Sub-figure 8.10b shows $N_0 = 3$, 8.10c shows $N_0 = 4$, 8.10d shows $N_0 = 5$ and 8.10e shows $N_0 = 6$. The small circle represent the inner orbits, whilst the triangles represent the outer orbits. The colour of the points represents the fidelity parameter. The very high eccentricity systems have a very low fidelity parameter, and thus are unlikely to survive long enough to reach the field. There is not much difference between the different cases for N_0.

The period against eccentricity plots for the hierarchical quadruples are shown in Figure 8.11. Sub-figure 8.11a shows the distribution for $N_0 = 2$, Sub-figure 8.11b shows $N_0 = 3$, 8.11c shows $N_0 = 4$, 8.11d shows $N_0 = 5$ and 8.11e shows $N_0 = 6$. The colour of the points represents the fidelity parameter. The outermost orbits are more likely to have a higher fidelity parameter, and hence survive into the field if N_0 has a higher value. Lower eccentricities for the outermost orbits are also more likely as N_0 increases. All the very high eccentric outer orbits have a small fidelity parameter, independent of N_0.

The period against eccentricity plots for the double quadruples are shown in Figure 8.12. Sub-figure 8.12a shows the distribution for $N_0 = 2$, Sub-figure 8.12b shows $N_0 = 3$, 8.12c shows $N_0 = 4$, 8.12d shows $N_0 = 5$ and 8.12e shows $N_0 = 6$. The colour of the points represents the fidelity parameter. As N_0 increases, smaller eccentricity outer orbits are more likely.

It can be seen in Table 8.7 that as N_0 increases, the fraction of binaries are diminished in favour of triples and quadruples. This is because there are more excess stars that can be ejected, carrying away energy, leaving behind a hardened system. The percentage of hierarchical quadruples increases more dramatically than double quadruples.

Table 8.7: Average number of multiple systems produced per core.

Nstar	Binaries	Triples	Hierarchical Quadruples	Double Quadruples
$N_0 = 2$	0.9993	0.0000	0.0000	0.0000
$N_0 = 3$	1.0000	0.0000	0.0000	0.0000
$N_0 = 4$	0.6799	0.3055	0.0037	0.0185
$N_0 = 5$	0.5735	0.4159	0.0192	0.0294
$N_0 = 6$	0.6078	0.3985	0.0403	0.0341

With the requirement that the KS test must be rejected at the 1% level for all values of N_0

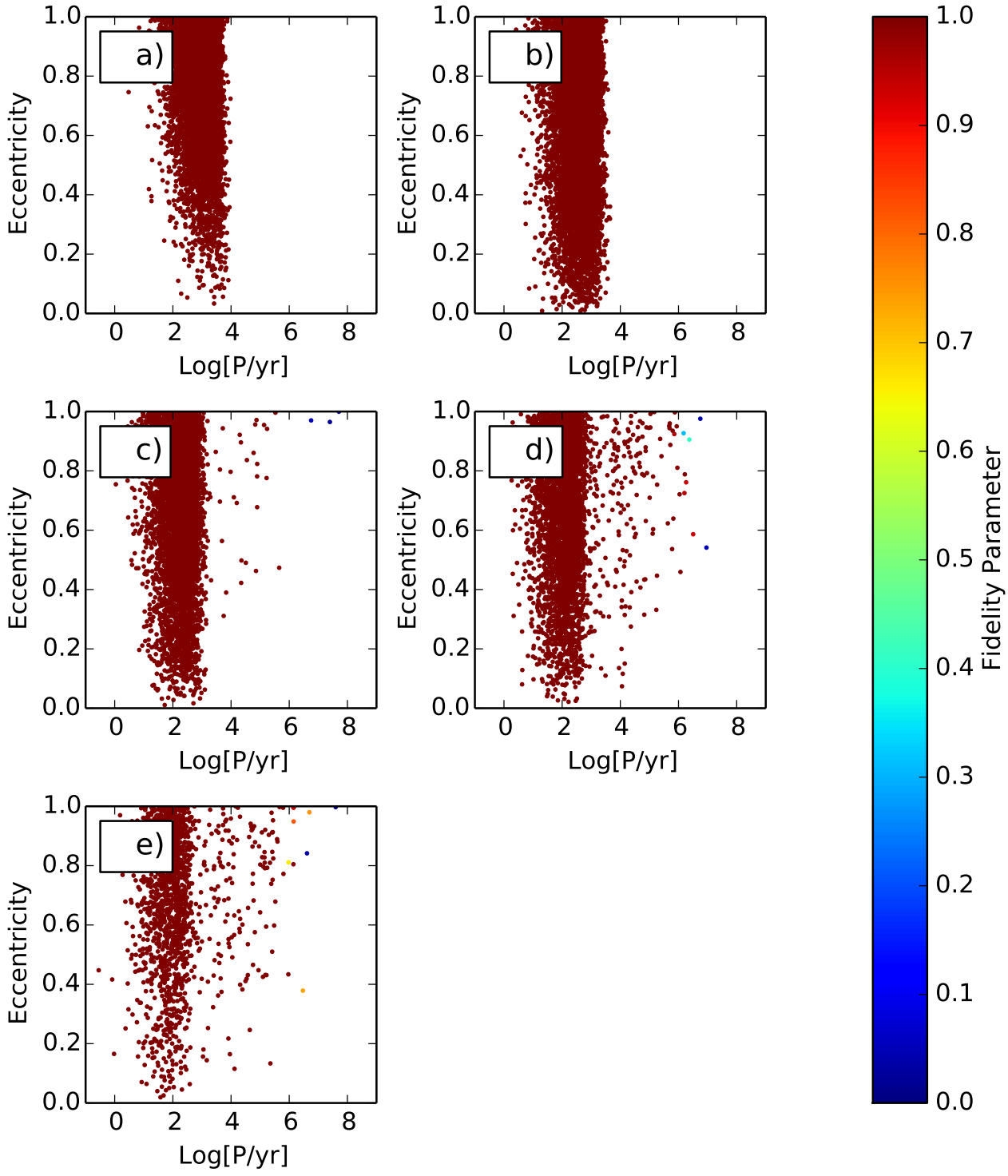

Figure 8.9: The distribution of binary systems in the $(\log_{10}(P/\mathrm{yr}), \mathrm{e})$-plane. The colour of the points encodes the fidelity parameter. Frame a) corresponds to N_0=2, b) 3, c) 4, d) 5, and e) 6. 9993, 9873, 6065, 4356, 1658 binaries are plotted for N_0 = 2, 3, 4, 5 and 6 respectively.

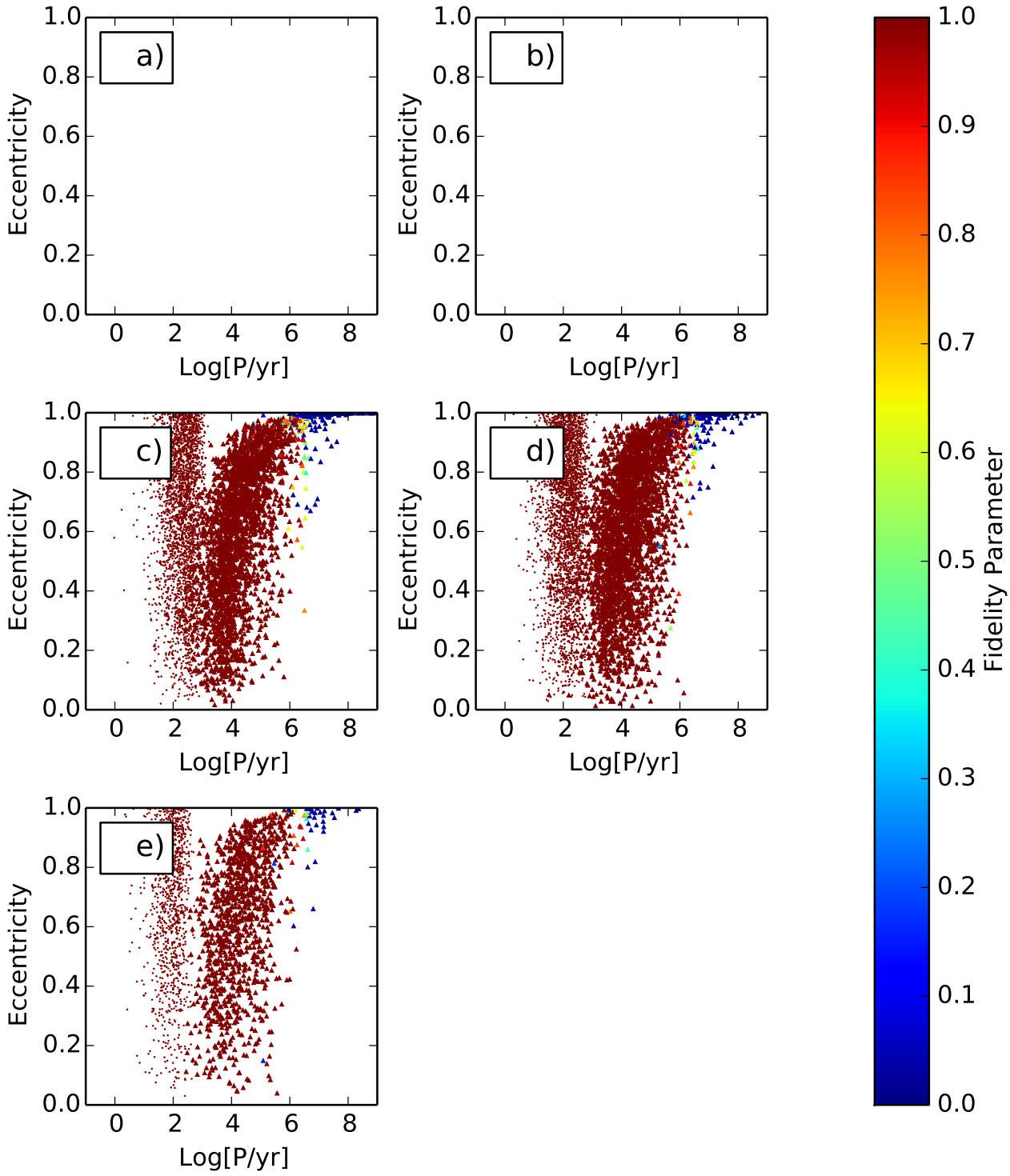

Figure 8.10: The distribution of triple systems in the $(\log_{10}(P/\mathrm{yr}), \mathrm{e})$-plane. Small circles represent inner orbits and triangles represent outer orbits. The colour of the points encodes the fidelity parameter. Frame a) corresponds to N_0=2, b) 3, c) 4, d) 5, and e) 6. 0, 0, 2725, 3159, 1087 triple systems are plotted for N_0 = 2, 3, 4, 5, and 6 respectively.

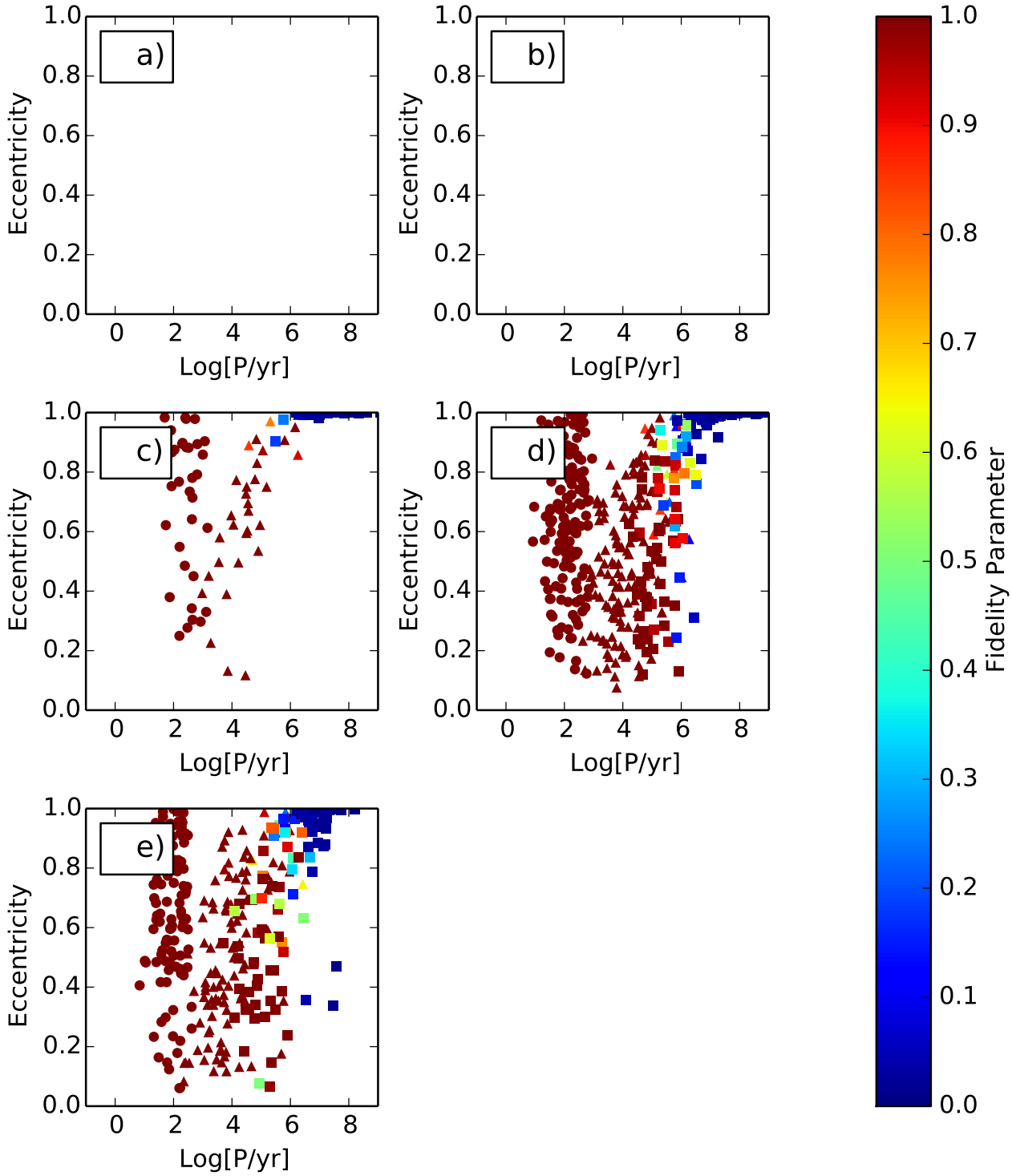

Figure 8.11: The distribution of hierarchical quadruple systems in the $(\log_{10}(P/\mathrm{yr}), \mathrm{e})$-plane. Circles represent inner orbits, triangles represent middle orbits and squares represent outer orbits. The colour of the points encodes the fidelity parameter. Frame a) corresponds to N_0=2, b) 2, c) 4, d) 5, and e) 6. 0, 0, 33, 146, 110 hierarchical quadruple systems are plotted for N_0 = 2, 3, 4, 5, and 6 respectively.

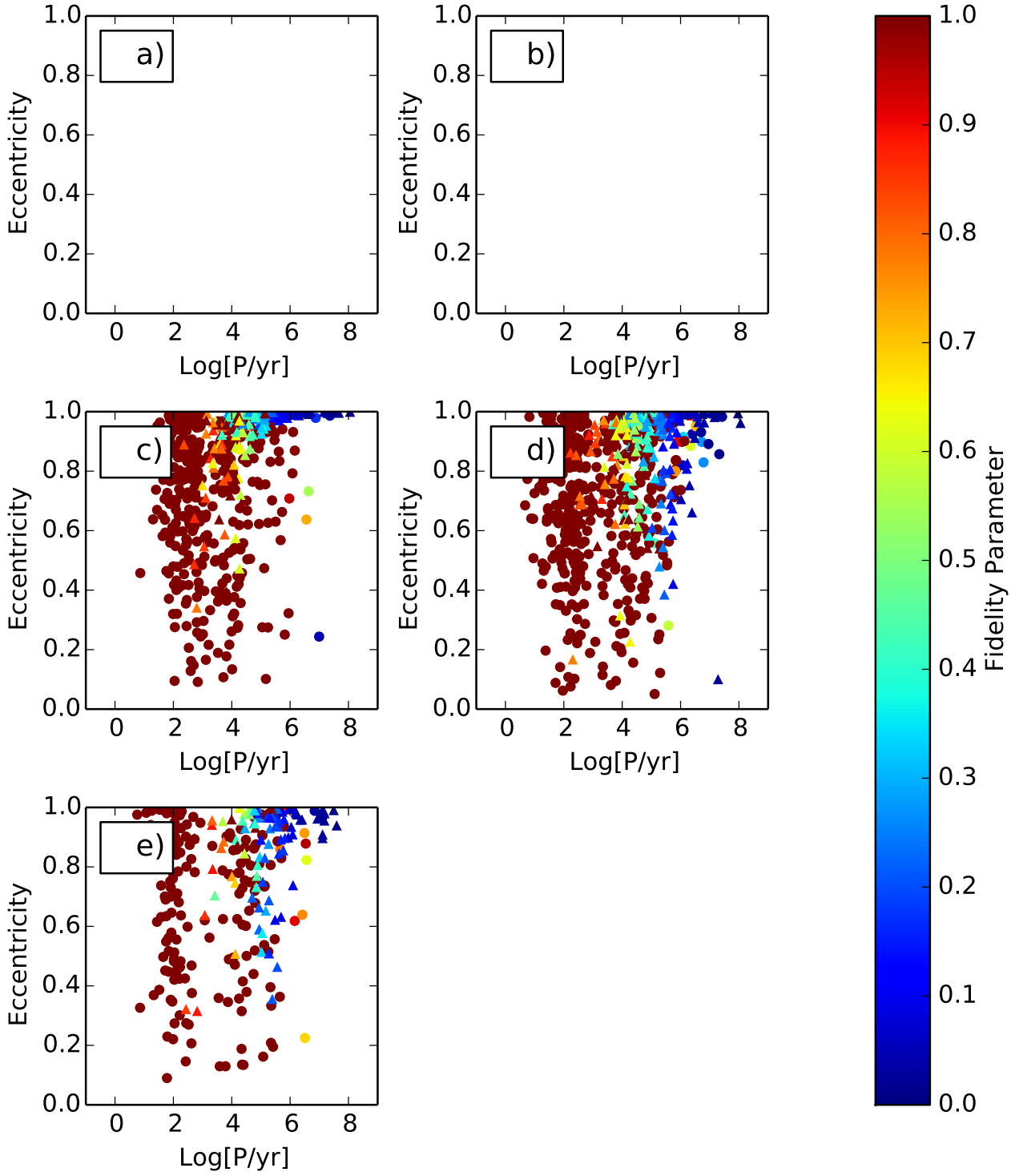

Figure 8.12: The distribution of triple systems in the $(\log_{10}(P/\mathrm{yr}), \mathrm{e})$-plane. Circles represent inner orbits and triangles represent outer orbits. The colour of the points encodes the fidelity parameter. Frame a) corresponds to N_0=2, b) 3, c) 4, d) 5, and e) 6. 0, 0, 165, 223, 93 double quadruple systems are plotted for N_0 = 2, 3, 4, 5, and 6 respectively.

Table 8.8: This table shows the eccentricity, mass ratio and period distributions that for which the null hypothesis can be rejected at the 1% level, as determined by the K-S test for the different values of N_0.

N_0	System Type	Eccentricity	Mass Ratio	Period
2	Binaries	✓	✓	✓
3	Binaries	✓	✓	✓
5	Binaries		✓	✓
6	Binaries		✓	✓
5	Triples inner		✓	✓
6	Triples inner		✓	✓
5	Triples outer		✓	
6	Triples outer		✓	
5	Hierarchical Quadruples inner		✓	✓
6	Hierarchical Quadruples inner		✓	✓
5	Hierarchical Quadruples mid	✓		
6	Hierarchical Quadruples mid			✓
5	Hierarchical Quadruples outer	✓	✓	✓
6	Hierarchical Quadruples outer	✓	✓	✓
5	Double Quadruples inner			✓
6	Double Quadruples inner		✓	✓
5	Double Quadruples outer	✓	✓	
6	Double Quadruples outer	✓		✓

for a given property, we can say that the mass ratios of the binaries, triples, and hierarchical quadruples (inner and outer) and the periods for the binaries, hierarchical quadruples (inner and outer) and inner quadruples change with N_0 with reasonable confidence (see Table 8.8). But although many the distributions are statistically different, they are not different enough that observers could distinguish between them. The possible exception is the mass ratio distribution for $N_0 = 2$ as compared to other values of N_0. Note that the K-S tests have been performed on the un-convolved distributions, and compared to the fiducial model.

8.3 The Virial Parameter

In this section I present the results of varying the virial parameter, $\mathcal{V}$. I run 9276, 8920, 8769 simulations for each case, $\mathcal{V} = 0.2$, 0.5, and 0.8 respectively . These sets of simulations produce 6879, 6065, 6038 binaries, and 2258, 2725, 2221 triples, 8, 33, 25 hierarchical quadruples and 169, 165, 194 double quadruples for $\mathcal{V} = 0.2$, 0.5, and 0.8 respectively.

In Sub-figure 8.13a we can see that as $\mathcal{V}$ increases, the peak of the eccentricity distribution of the binaries at $e = 1$ becomes less prominent. Sub-figure 8.13b shows the mass ratio distributions, which change little with $\mathcal{V}$. However, in Sub-figure 8.13c and Table 8.9 we can see that the peak of the period distribution increases as $\mathcal{V}$ increases. In Sub-figure 8.13c and Table 8.9 we can see that the standard deviation also increases as $\mathcal{V}$ increases.

Table 8.9: Mean and standard deviation of $\log_{10}(P/\mathrm{yr})$

Virial			
	Binaries	Triples	
		Inner	Outer
$\mathcal{V} = 0.2$	2.045±0.458	2.081±0.434	4.395±1.086
$\mathcal{V} = 0.5$	2.243±0.479	2.288±0.442	4.475±1.047
$\mathcal{V} = 0.8$	2.475±0.506	2.492±0.447	4.676±1.033

Table 8.10: Mean and standard deviation of $\log_{10}(P/\mathrm{yr})$

Virial					
	Quad, Hierarchical			Quad, Double	
	Inner	Mid	Outer	Inner	Outer
$\mathcal{V} = 0.2$	2.379±0.298	4.526±0.681	7.530±1.214	3.015±1.323	4.462±1.315
$\mathcal{V} = 0.5$	2.474±0.311	4.697±0.996	7.299±0.823	3.252±1.202	4.736±1.021
$\mathcal{V} = 0.8$	2.575±0.381	4.877±1.055	6.837±0.489	3.481±1.221	4.910±1.093

Sub-figure 8.13d shows the multiplicity frequency as a function of primary mass. As $\mathcal{V}$ increases, the multiplicity frequency of high-mass stars decreases. If we compare this with Table 8.11, we can see that this is because as $\mathcal{V}$ increases, the fraction of cores producing systems involving the most massive stars decreases. Hence it is more likely that the most massive stars are single, and the multiplicity frequency decreases. The graph of M_1 against M_2 is plotted in Sub-figure 8.13 d. There are no observable differences between the different values of $\mathcal{V}$.

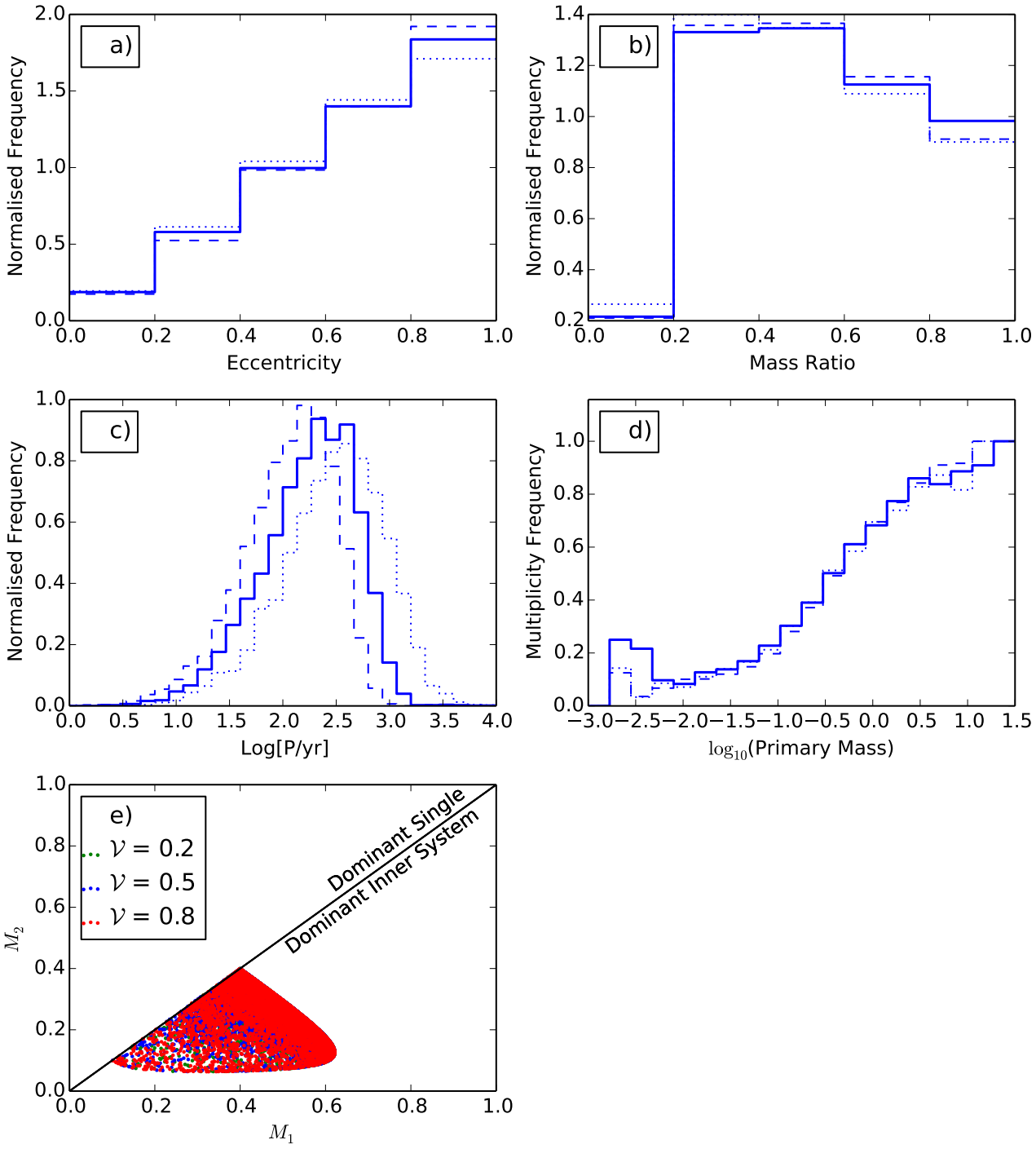

Figure 8.13: The variation of binary properties with $\mathcal{V}$. The dashed/solid/dotted lines in each of the frames describes the distributions attained when $\mathcal{V} = 0.2$, 0.5 and 0.8 respectively. Frame a) shows the normalised distribution of eccentricities, frame b) shows the normalised distribution of mass ratios, frame c) shows the normalised distribution of periods [yr] and frame d) shows the multiplicity frequency as a function of primary mass, and Frame e) plots M_2 against M_1. 6879, 6065, 6038 binary systems are plotted for $\mathcal{V} = 0.2$, 0.5, and 0.8 respectively.

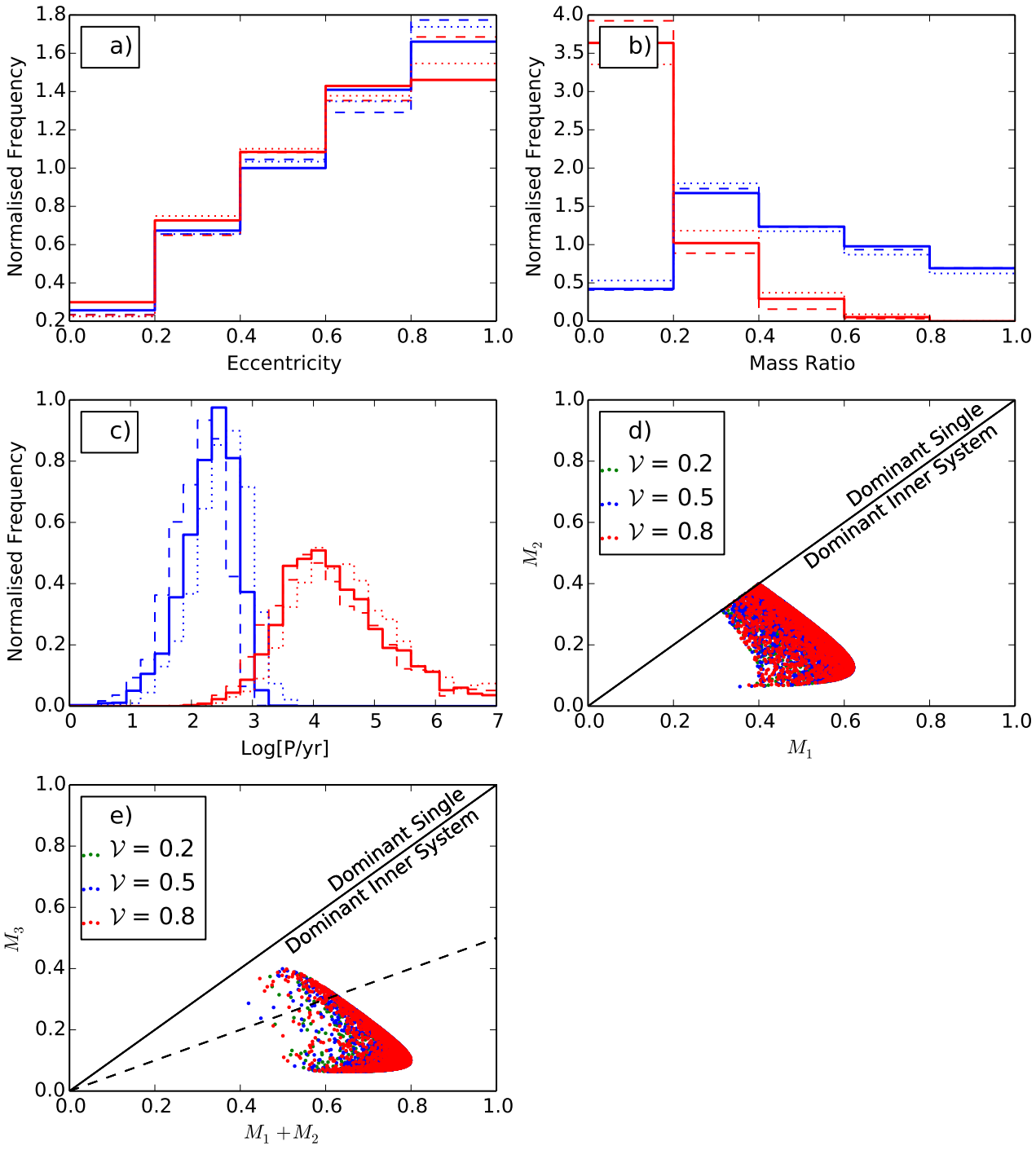

Figure 8.14: The variation of properties of triples formed with $\mathcal{V}$. The dashed/solid/dotted lines in each of the Frames describes the distributions attained when $\mathcal{V} = 0.2$, 0.5 and 0.8 respectively. The blue lines show the inner periods, whilst the red lines show the outer periods. Frame a) shows the normalised distribution of eccentricities, Frame b) shows the normalised distribution of mass ratios and Frame c) shows the normalised distribution of periods [yr]. Frame d) plots M_2 against M_1, whilst Frame e) plots M_3 against $M_2 + M_1$. 2258, 2725, 2221 triple systems are plotted for $\mathcal{V} = 0.2$, 0.5, and 0.8 respectively.

Table 8.11: Percentage of cores producing systems involving the most massive stars

Virial	Most massive star	Two most massive stars
$\mathcal{V} = 0.2$	0.97	0.77
$\mathcal{V} = 0.5$	0.96	0.77
$\mathcal{V} = 0.8$	0.90	0.70

Due to the low number statistics for hierarchical quadruples, (8, 33, 25 hierarchical quadruples for $\mathcal{V} = 0.2$, 0.5, 0.8 respectively), we cannot draw any firm conclusions about how the properties of hierarchical quadruples change with $\mathcal{V}$.

The properties of double quadruples produced are shown in Figure 8.15. Although more double quadruples are produced than hierarchical quadruples (169, 165, 194 double quadruples for $\mathcal{V} = 0.2$, 0.5, 0.8 respectively), the number statistics are still too few, making it difficult to draw any firm conclusions about the variation of double quadruples properties with $\mathcal{V}$.

Figures 8.16, 8.17, 8.18 and 8.19 show the period against eccentricity graphs for binaries, triples, hierarchical quadruples and double quadruples respectively. None of these graphs show any significant difference between the different values of $\mathcal{V}$.

Table 8.12 shows the average number of systems produced per core cluster. The total number of systems produced on average decreases as $\mathcal{V}$ increases, as would be expected.

Table 8.12: Average number of multiple systems produced per core.

Virial	Binaries	Triples	Hierarchical Quadruples	Double Quadruples
$\mathcal{V} = 0.2$	0.7416	0.2434	0.0009	0.0182
$\mathcal{V} = 0.5$	0.6799	0.3055	0.0037	0.0185
$\mathcal{V} = 0.8$	0.6886	0.2533	0.0029	0.0221

In summary, the only properties of multiple systems that are affected by the initial virial balance of the core are the mean and standard deviation of the period distributions.

With the requirement that the KS test must be rejected at the 1% level for all values of $\mathcal{V}$ for a given property, we can say that the periods of the binaries triples, inner periods of double quadruples, and outer mass ratios of the triples change with $\mathcal{V}$ with reasonable confidence (see Table 8.13). However, none of these distributions are different enough to be distinguishable from the fiducial model observationally. Note that the K-S tests have been performed on the un-convolved distributions, and compared to the fiducial model.

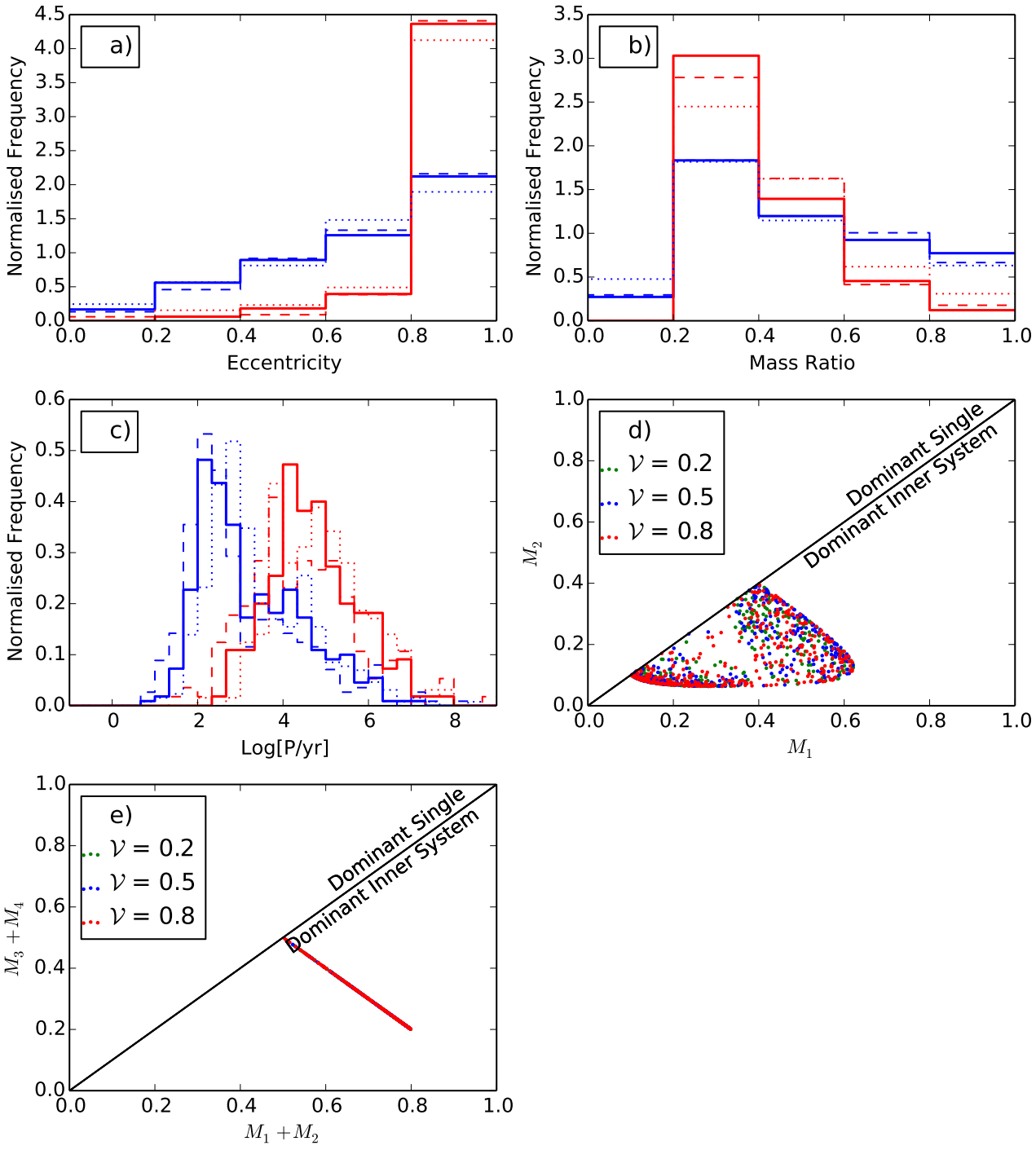

Figure 8.15: The variation of properties of double quadruples formed with $\mathcal{V}$. The dashed/solid/dotted lines in each of the Frames describes the distributions attained when $\mathcal{V}$ = 0.2,0.5 and 0.8 respectively. The blue lines show the inner periods, whilst the red lines show the outer periods. Frame a) shows the normalised distribution of eccentricities, Frame b) shows the normalised distribution of mass ratios and Frame c) shows the normalised distribution of periods [yr]. Frame d) plots M_2 against M_1 and M_4 against M_3, and Frame e) plots $M_4 + M_3$ against $M_2 + M_1$. 169, 165, 194 double quadruple systems are plotted for $\mathcal{V} = 0.2$, 0.5, and 0.8 respectively.

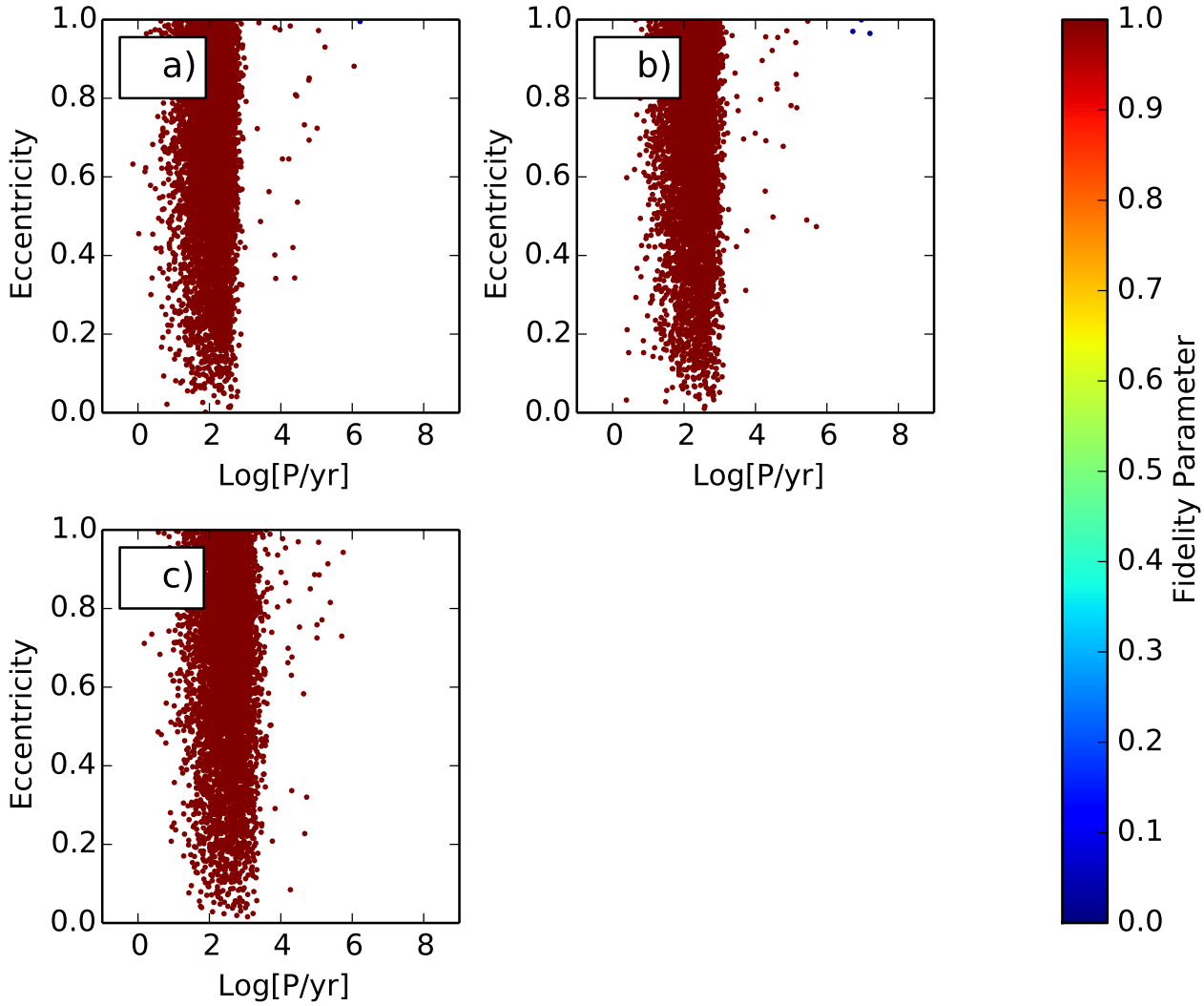

Figure 8.16: The distribution of binary systems in the $(\log_{10}(P/\mathrm{yr}), \mathrm{e})$-plane. The colour of the points encodes the fidelity parameter. Frame a) corresponds to $\mathcal{V} = 0.2$, b) 0.5, and c) 0.5. 6879, 6065, 6038 binary systems are plotted for $\mathcal{V} = 0.2$, 0.5, and 0.8 respectively.

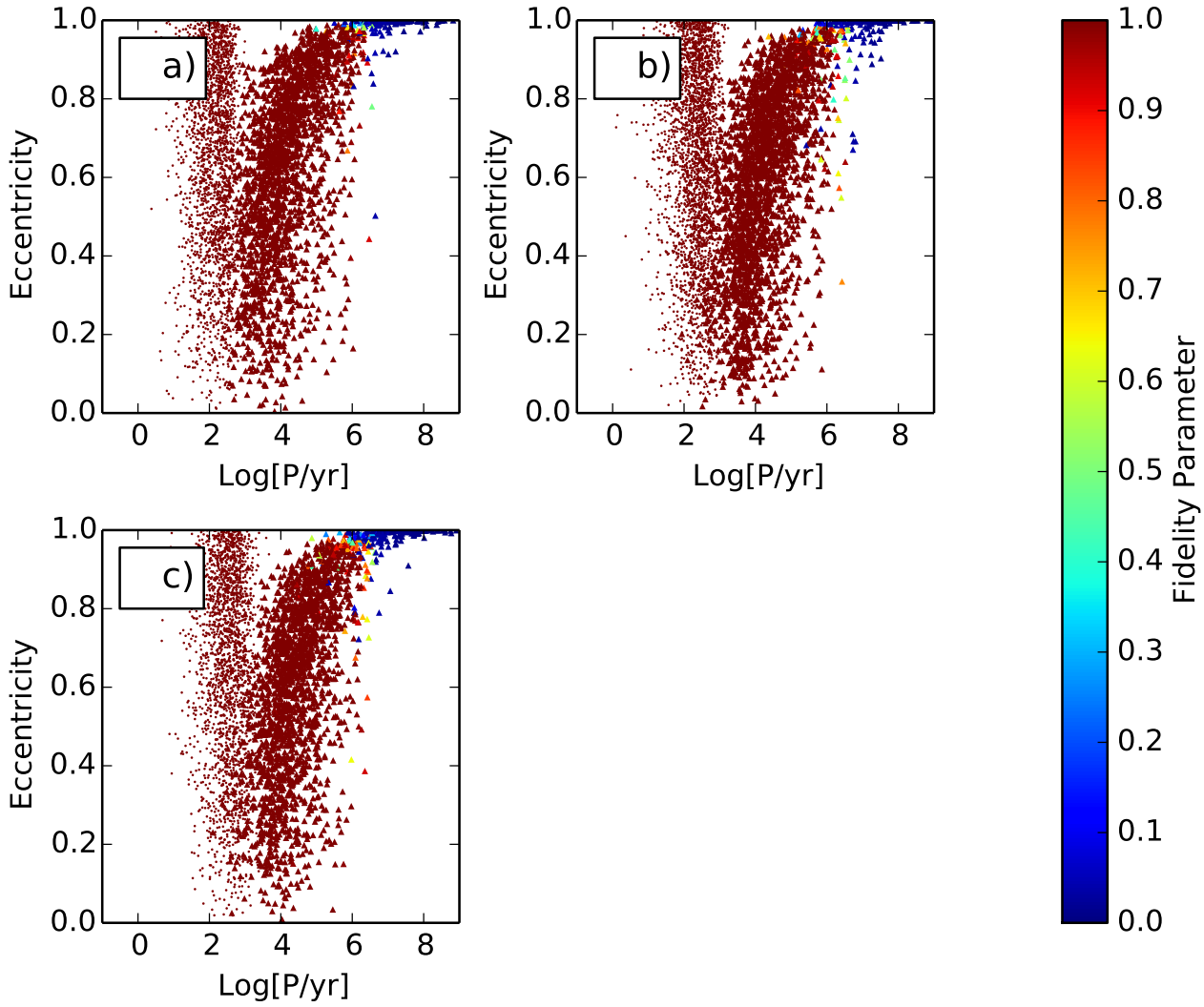

Figure 8.17: The distribution of triple systems in the $(\log_{10}(P/\mathrm{yr}), \mathrm{e})$-plane. Small circles represent inner orbits and triangles represent outer orbits. The colour of the points encodes the fidelity parameter. Frame a) corresponds to $\mathcal{V} = 0.2$, b) 0.5, and c) 0.8. 2258, 2725, 2221 triple systems are plotted for $\mathcal{V} = 0.2$, 0.5, and 0.8 respectively.

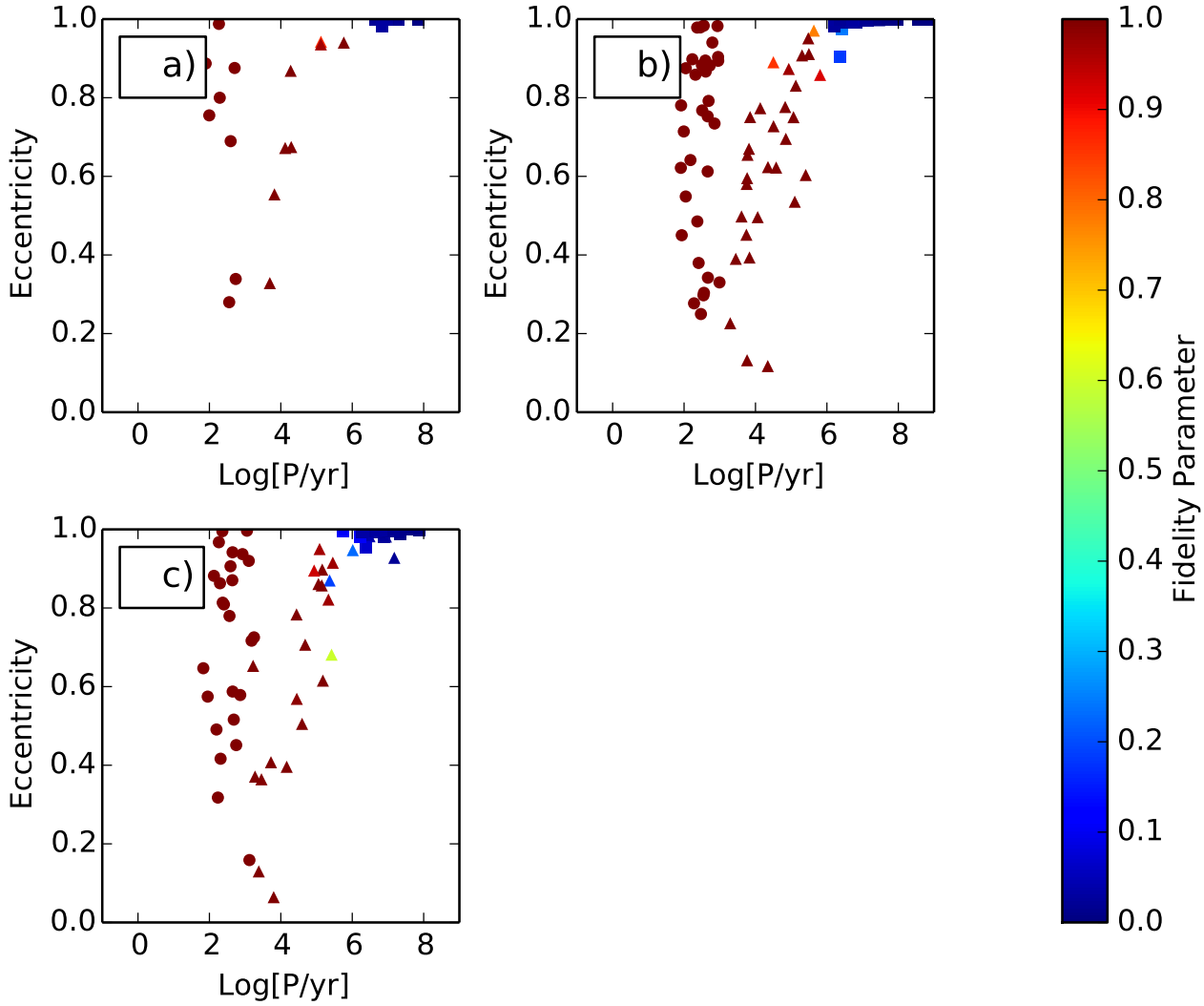

Figure 8.18: The distribution of hierarchical quadruple systems in the $(\log_{10}(P/\mathrm{yr}), \mathrm{e})$-plane. Circles represent inner orbits, triangles represent middle orbits and squares represent outer orbits. The colour of the points encodes the fidelity parameter. Frame a) corresponds to $\mathcal{V} = 0.2$, b) 0.5, and c) 0.8. 8, 33, 25 hierarchical quadruple systems are produced for $\mathcal{V} = 0.2$, 0.5, and 0.8 respectively.

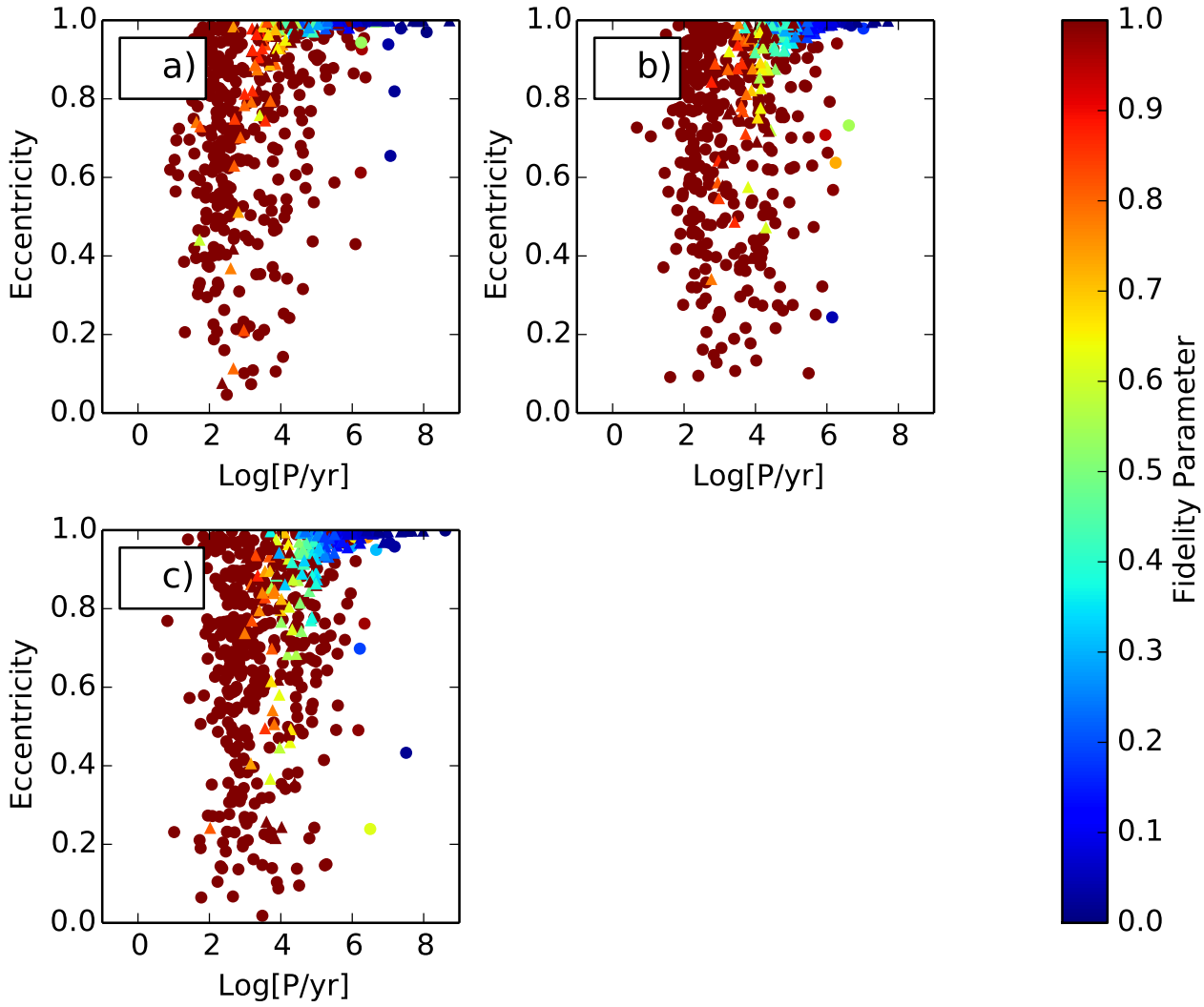

Figure 8.19: The distribution of double quadruples in the $(\log_{10}(P/\mathrm{yr}), \mathrm{e})$-plane. Circles represent inner orbits and triangles represent outer orbits. The colour of the points encodes the fidelity parameter. Frame a) corresponds to $\mathcal{V} = 0.2$, b) 0.5, and c) 0.8. 169, 165, 194 double quadruples are produced for $\mathcal{V} = 0.2$, 0.5, and 0.8 respectively.

Table 8.13: This table shows the eccentricity, mass ratio and period distributions that for which the null hypothesis can be rejected at the 1% level, as determined by the K-S test for the different values of $\mathcal{V}$.

$\mathcal{V}$	System Type	Eccentricity	Mass Ratio	Period
0.2	Binaries			✓
0.8	Binaries		✓	✓
0.2	Triples inner			✓
0.8	Triples inner		✓	✓
0.2	Triples outer	✓	✓	✓
0.8	Triples outer		✓	✓
0.2	Hierarchical Quadruples inner			
0.8	Hierarchical Quadruples inner			
0.2	Hierarchical Quadruples mid			
0.8	Hierarchical Quadruples mid			
0.2	Hierarchical Quadruples outer			
0.8	Hierarchical Quadruples outer	✓		
0.2	Double Quadruples inner			✓
0.8	Double Quadruples inner			✓
0.2	Double Quadruples outer			✓
0.8	Double Quadruples outer			

8.4 Standard Deviation of Stellar Masses Produced by a Core

In this section, I present the results of changing the variance in the stellar masses produced by a single core. I run 9427, 9218, 8920, 8709, 8350 simulations for each of the cases $\sigma_0 = 0.1$, 0.2, 0.3, 0.4, and 0.5 respectively. These sets of simulations produce 6855, 6134, 6065, 6222, 6226 binaries, 2443, 2923, 2725, 2397, 2042 triples, 32, 48, 33, 22, 26 hierarchical quadruples and 380, 242, 165, 106, 84 double quadruples for $\sigma_0 = 0.1$, 0.2, 0.3, 0.4 and 0.5 respectively.

Figure 8.20 shows the binary properties. The eccentricity distributions become flatter as σ_0 increases (see Sub-figure 8.20a). The mass ratios as seen in Sub-figure 8.20b are strongly affected by σ_0. As σ_0 increases, low q values become more and more populated. The peak shifts from the $q = 0.6$ to 0.8 bin, with no instances of $q < 0.4$ ($\sigma_0 = 0.1$) to $q = 0.2$ to 0.4 ($\sigma_0 = 0.5$), with a smooth transition for the intermediate values of σ_0. This is due simply to the availability of companions. For a small σ_0, the stars are all of similar masses, and so small mass ratios are not possible. For large σ_0, because there are only 4 stars, the probability of a similar mass star being formed in the same core is unlikely.

$$\begin{aligned}
&\text{For} \quad \sigma_0 = 0.1, \qquad q_{min} = 0.5, \qquad q_{peak} = 0.6 \text{ to } 0.8 \\
&\text{For} \quad \sigma_0 = 0.2, \qquad q_{min} = 0.2, \qquad q_{peak} = 0.4 \text{ to } 0.6 \\
&\text{For} \quad \sigma_0 = 0.3, \qquad q_{min} = 0.1, \qquad q_{peak} = 0.2 \text{ to } 0.4 \\
&\text{For} \quad \sigma_0 = 0.4, \qquad q_{min} = 0.0, \qquad q_{peak} = 0.2 \text{ to } 0.4 \\
&\text{For} \quad \sigma_0 = 0.5, \qquad q_{min} = 0.0, \qquad q_{peak} = 0.2 \text{ to } 0.4
\end{aligned} \tag{8.6}$$

In Sub-figure 8.20c and Table 8.14, we can see that the peak of the period distribution increases with increasing σ_0. This is because for small σ_0, all the stars are of similar masses. So when two stars are ejected, a lot of energy is carried away, and the binary is strongly hardened. When σ_0 is large, there is a greater range in masses. Preferentially, the two smallest stars are ejected, but these don't carry as much energy away, so the binary isn't strongly hardened. The standard deviation decreases as σ_0 increases.

The multiplicity frequency as shown in Sub-figure 8.20d is also strongly affected by σ_0, as a consequence of the mass ratio distributions. A smaller σ_0 will produce a much flatter multiplicity frequency distribution than the fiducial, whilst a higher value of σ_0 than the fiducial will produce a steeper multiplicity frequency. This is because for small σ_0, stars formed in a single core are of a similar size, the smaller cores producing smaller stars and the larger cores producing larger stars. Due to the fact that the large and small stars are more segregated from each other, the smaller stars have a greater opportunity to become primaries. For a larger σ_0

Table 8.14: Mean and standard deviation of $\log_{10}(P/\mathrm{yr})$

Sigma			
	Binaries	Triples	
		Inner	Outer
0.1	2.020±0.573	2.082±0.409	4.477±0.958
0.2	2.133±0.522	2.230±0.409	4.459±0.924
0.3	2.243±0.482	2.305±0.430	4.493±1.031
0.4	2.350±0.474	2.327±0.455	4.416±1.009
0.5	2.448±0.476	2.329±0.473	4.416±1.112

Table 8.15: Mean and standard deviation of $\log_{10}(P/\mathrm{yr})$

Sigma					
	Quad, Hierarchical			Quad, Double	
	Inner	Mid	Outer	Inner	Outer
0.1	2.239±0.383	4.637±0.858	7.120±0.571	3.094±1.267	4.426±1.079
0.2	2.403±0.424	4.691±0.812	7.195±0.599	3.253±1.332	4.735±1.125
0.3	2.443±0.382	4.665±1.000	7.267±0.836	3.239±1.219	4.724±1.067
0.4	2.447±0.515	4.926±0.902	7.115±0.799	3.362±1.319	5.006±1.205
0.5	2.486±0.581	4.396±0.819	6.905±0.540	3.361±1.336	4.997±1.310

there is a much greater range of masses in a single core, and the smaller stars almost always give way to their larger siblings. The graph of M_1 against M_2 is plotted in Sub-figure 8.5 e. As σ_0 increases, the area of the graph that the distribution covers increases, due to the greater disparity in stellar masses.

Figure 8.21 shows the change in properties of triples as σ_0 is varied. Sub-figure 8.21a shows the eccentricity distribution, which does not change much from the fiducial result, apart from perhaps a tendency towards high eccentricities for $\sigma_0 = 0.1$ for the inner orbit. The mass ratio distribution of inner orbits as seen in Sub-figure 8.21b shows much the same result as the binaries in Sub-figure 8.20b. The outer mass ratios peak more and more strongly at $q = 0.0$ to 0.2 for large values of σ_0, i.e. the binary is increasingly more likely to be orbited by a star much less massive than itself. When σ_0 is greater than the fiducial value of 0.3, a peak is seen in the bin q = 0.2 to 0.4, while $\sigma_0 = 0.1$ does not populate the q = 0.0 to 0.2 bin at all, simply due to the non-availability of low-mass companions.

Sub-figure 8.21a, along with Tables 8.14 and 8.14 show the change in the period distribution with σ_0. The inner periods change as discussed in the binaries section. The mean of the outer periods on average decrease with σ_0, but the effect is much smaller. In Sub-figure 8.6d M_2 is plotted against M_1, and in Sub-figure 8.6d M_3 is plotted against M_2+M_1. As for the binaries, as σ_0 increases, the distribution covers a larger proportion of the graph. The distribution plotted in Sub-figure 8.6d also approaches the asymptote of $M_3 + M_2 + M_1 = 1$, i.e. as M_4 approaches 0

Due to small number statistics, it is difficult to discern any trends in any of the properties of hierarchical quadruples.

The properties for the double quadruples produced are shown in Figure 8.22. The eccentricity distributions as shown in Sub-figure 8.22a do not show much change, apart from a slight preference for high eccentricity outer orbits for large σ_0. As σ_0 decreases, the mass ratios (Sub-figure 8.22b) all tend towards 1, as all the stars are of a similar mass. Sub-figure 8.22c and Table 8.15 do not show any clear trend, possibly due to the low number statistics. In Sub-figure 8.8d, M_2 is plotted against M_1 and M_4 is plotted against M_3. In Sub-figure 8.8e $M_4 + M_3$ is plotted against $M_2 + M_1$. The trend seen here is the same as seen previously, that is as σ_0 increases, the distribution covers are larger portion of the graph. The distribution notably populates the lower left corner of the graph, unlike the distribution of pure binaries.

Figures 8.23, 8.24, 8.25 and 8.26 show the period against eccentricity diagrams for the binaries, triples, hierarchical quadruples and double quadruples respectively. Apart from more low eccentricity binaries as σ_0 increases, there is no variation between the different values of σ_0.

From Table 8.16 we can see that the average number of double quadruples decreases as σ_0 increases, showing that double quadruples are easiest to produce when stars are of similar masses. The average number of binaries produced increases for $\sigma_0 > 0.3$ because double

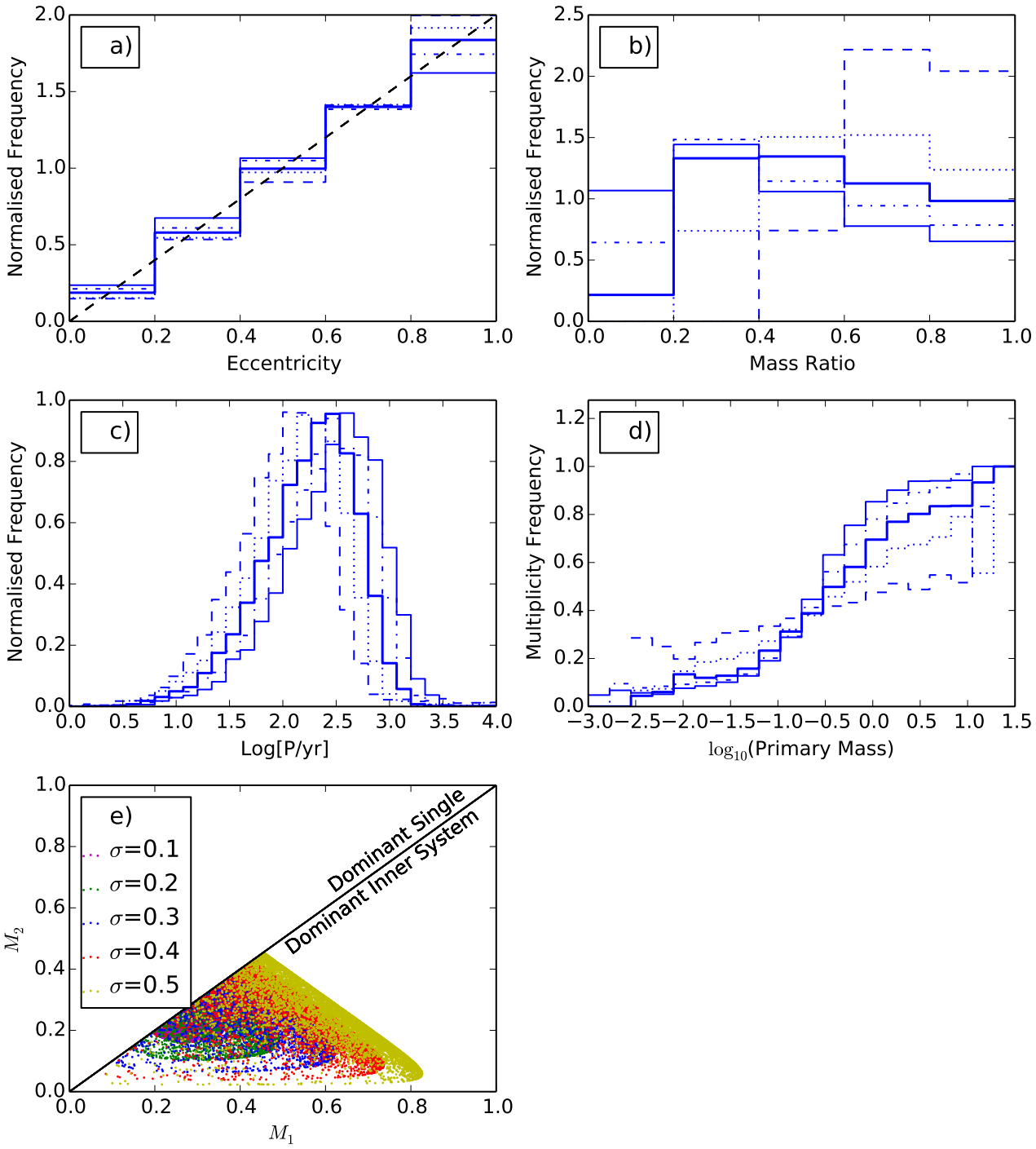

Figure 8.20: The variation of binary properties with σ_0. The dashed/dotted/thick solid/dot-dashed/thin solid lines in each of the Frames describes the distributions attained when $\sigma_0 = 0.1$, 0.2, 0.3, 0.4 and 0.5 respectively. Frame a) shows the normalised distribution of eccentricities, Frame b) shows the normalised distribution of mass ratios, Frame c) shows the normalised distribution of periods [yr] and Frame d) shows the multiplicity frequency as a function of primary mass, and Frame e) plots M_2 against M_1. 6855, 6134, 6065, 6222, 6226 binary systems are plotted for $\sigma_0 = 0.1$, 0.2, 0.3, 0.4 and 0.5 respectively.

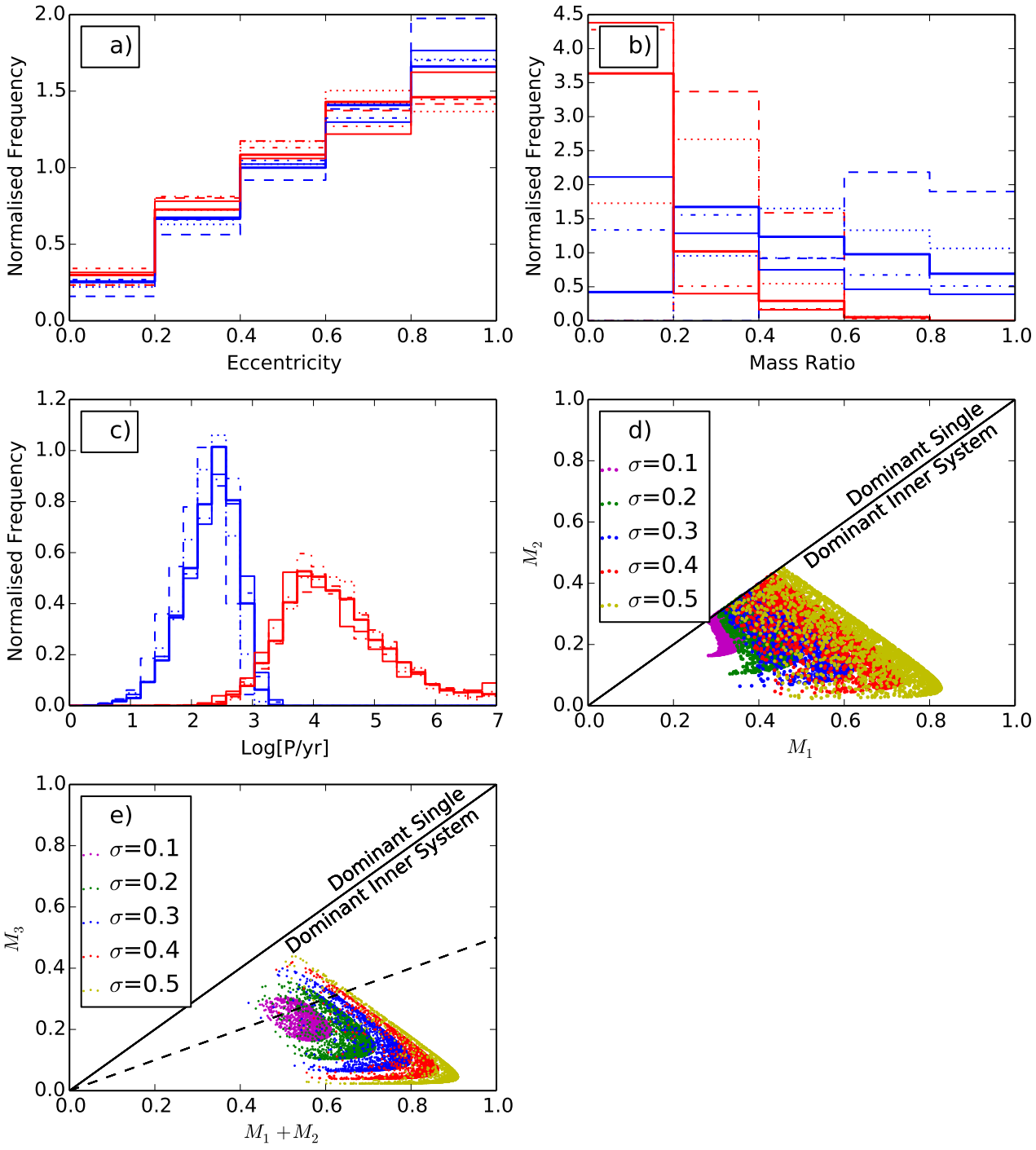

Figure 8.21: The variation of properties of triples formed with σ_0. The dashed/dotted/thick solid/dot-dashed/thin solid lines in each of the Frames describes the distributions attained when σ_0 = 0.1, 0.2, 0.3, 0.4 and 0.5 respectively. The blue lines show the inner periods, whilst the red lines show the outer periods. Frame a) shows the normalised distribution of eccentricities, Frame b) shows the normalised distribution of mass ratios and Frame c) shows the normalised distribution of periods [yr]. Frame d) plots M_2 against M_1, whilst Frame e) plots M_3 against $M_2 + M_1$. 2443, 2923, 2725, 2397, 2042 triple systems are plotted for σ_0 = 0.1, 0.2, 0.3, 0.4 and 0.5 respectively.

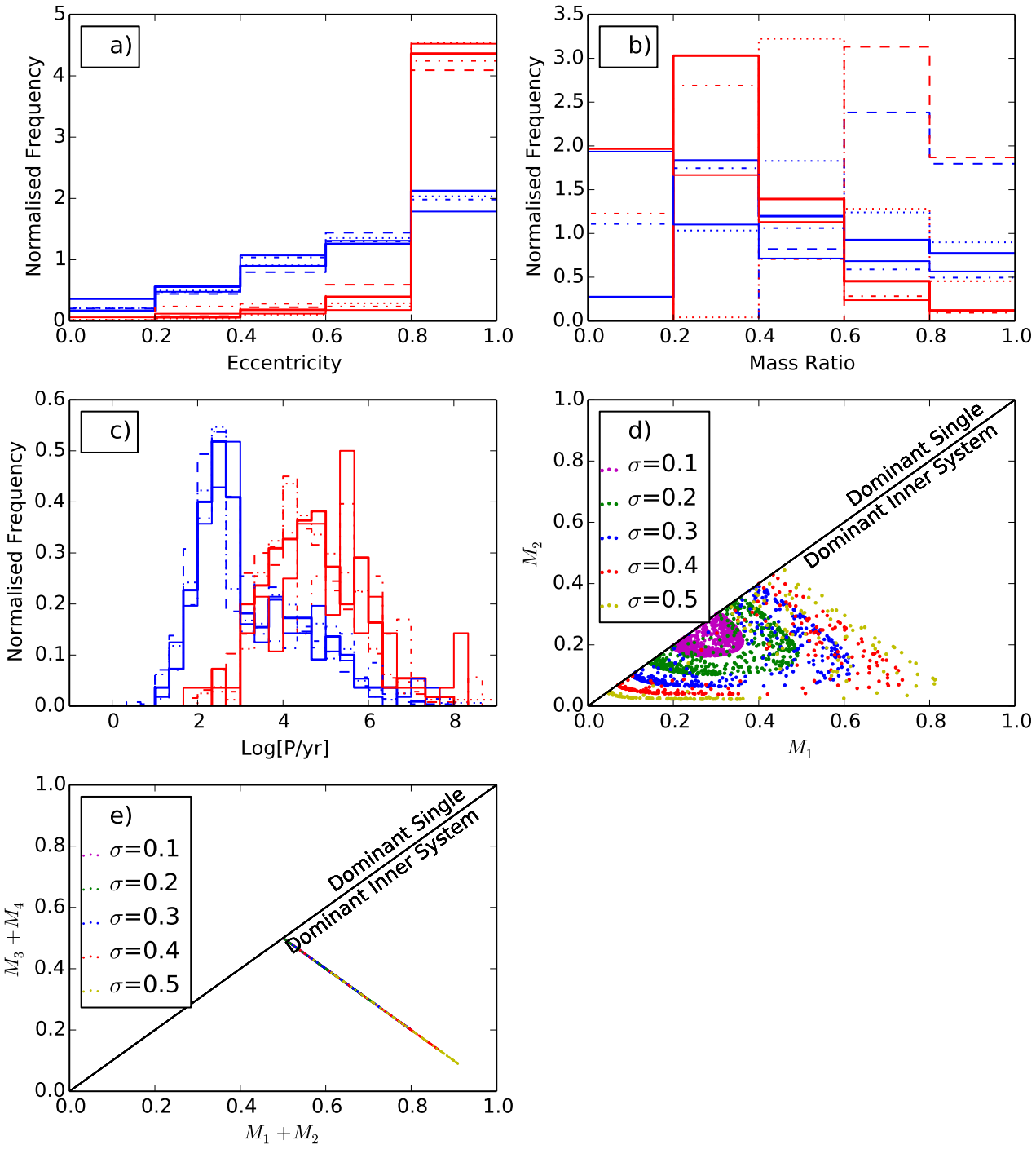

Figure 8.22: The variation of properties of double quadruples formed with σ_0. The dashed/dotted/thick solid/dot-dashed/thin solid lines in each of the Frames describes the distributions attained when σ_0 = 0.1, 0.2, 0.3, 0.4, and 0.5 respectively. The blue lines show the inner periods, whilst the red lines show the outer periods. Frame a) shows the normalised distribution of eccentricities, Frame b) shows the normalised distribution of mass ratios and Frame c) shows the normalised distribution of periods [yr]. Frame d) plots M_2 against M_1 and M_4 against M_3, and Frame e) plots $M_4 + M_3$ against $M_2 + M_1$. 380, 242, 165, 106, 84 double quadruple systems are plotted for σ_0 = 0.1, 0.2, 0.3, 0.4 and 0.5 respectively.

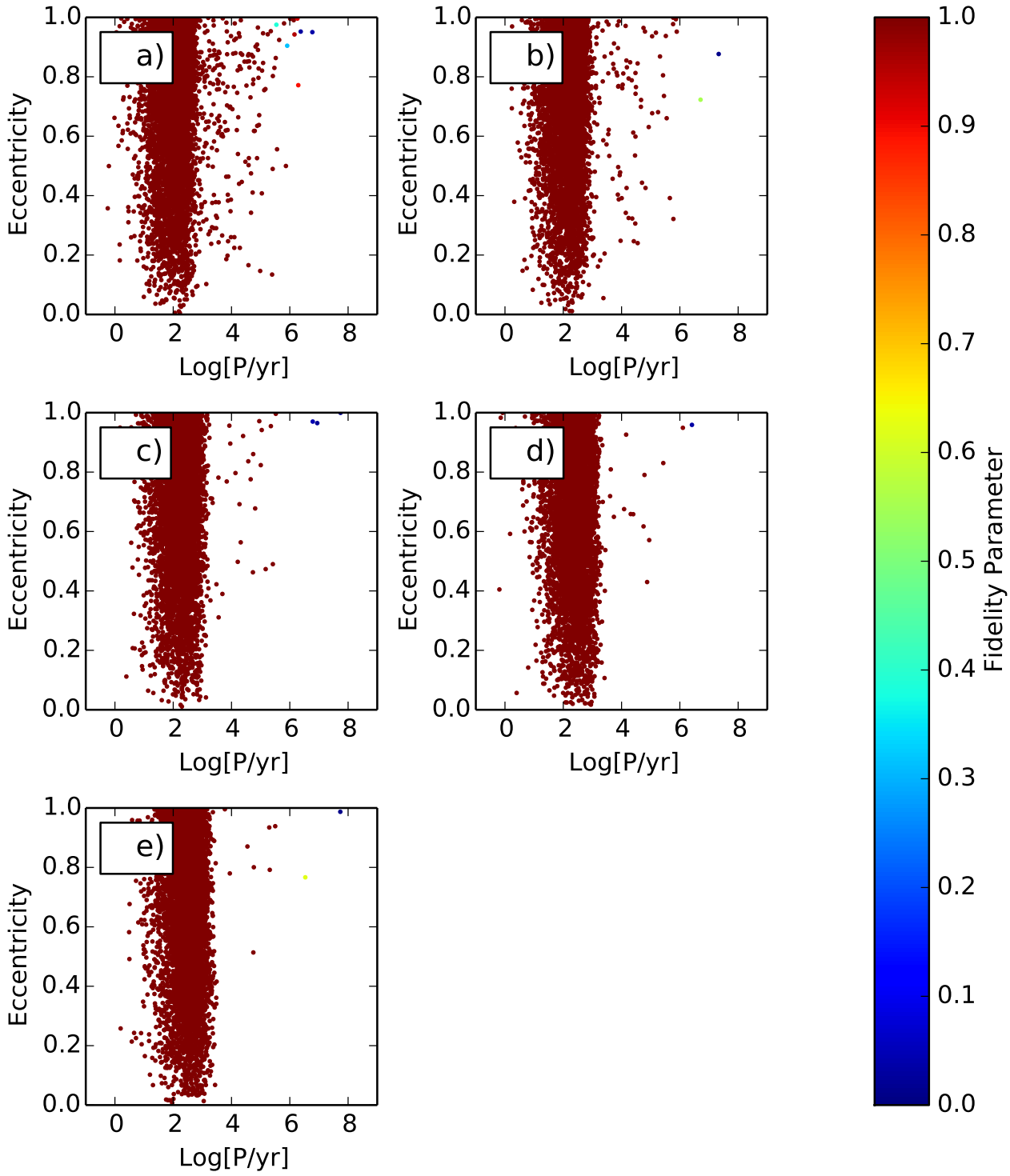

Figure 8.23: The distribution of binary systems in the $(\log_{10}(P/\mathrm{yr}), \mathrm{e})$-plane. The colour of the points encodes the fidelity parameter. Frame a) corresponds to $\sigma_0 = 0.1$, b) 0.2, c) 0.3, d) 0.4 and e) 0.5. 6855, 6134, 6065, 6222, 6226 binaries are plotted for $\sigma_0 = 0.1$, 0.2, 0.3, 0.4 and 0.5 respectively.

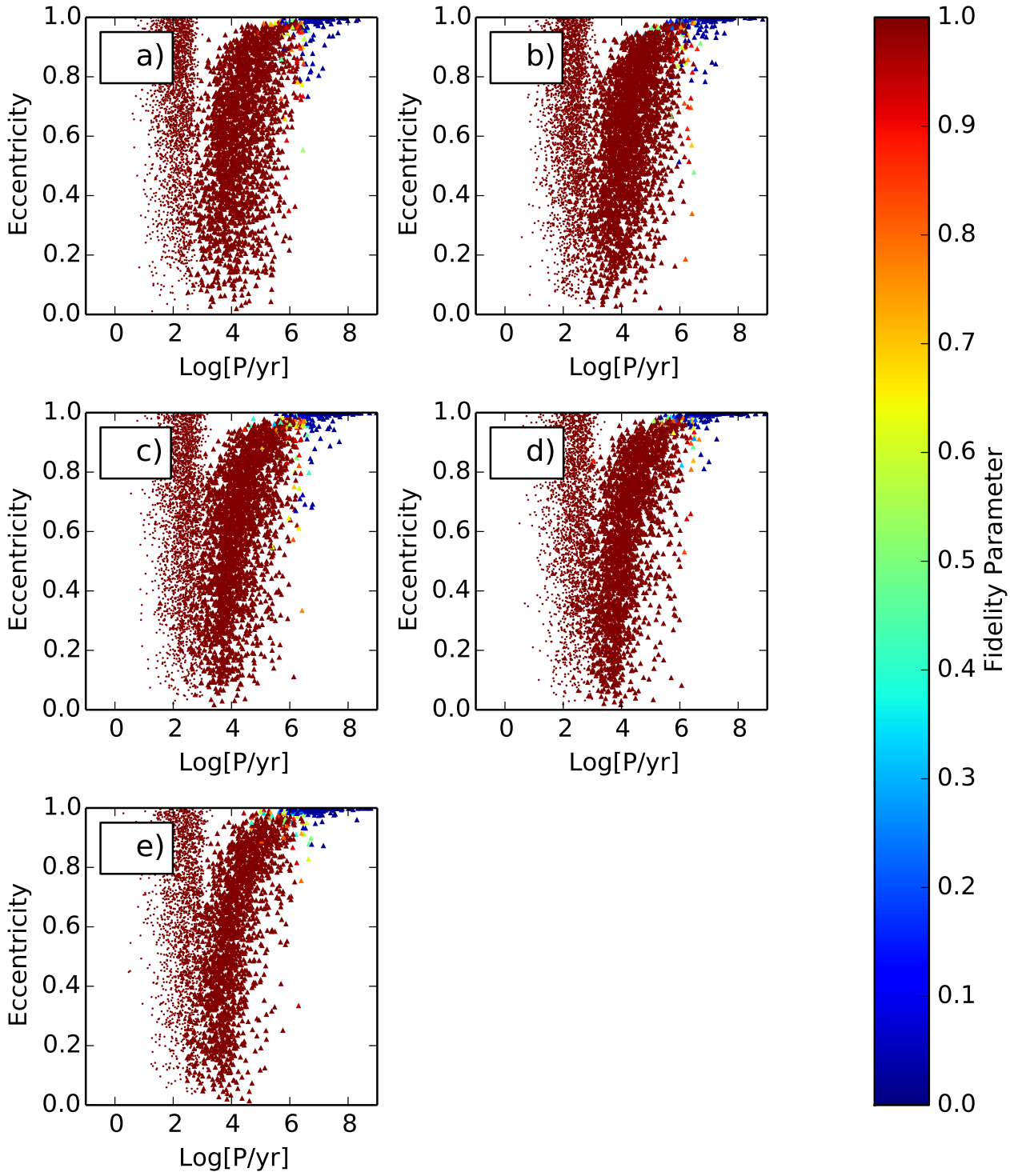

Figure 8.24: The distribution of triple systems in the $(\log_{10}(P/\mathrm{yr}), \mathrm{e})$-plane. Small circles represent inner orbits and triangles represent outer orbits. The colour of the points encodes the fidelity parameter. Frame a) corresponds to $\sigma_0 = 0.1$, b) 0.2, c) 0.3, d) 0.1 and e) 0.5. 2443, 2923, 2725, 2397, 2042 triple systems are plotted for $\sigma_0 = 0.1$, 0.2, 0.3, 0.4 and 0.5 respectively.

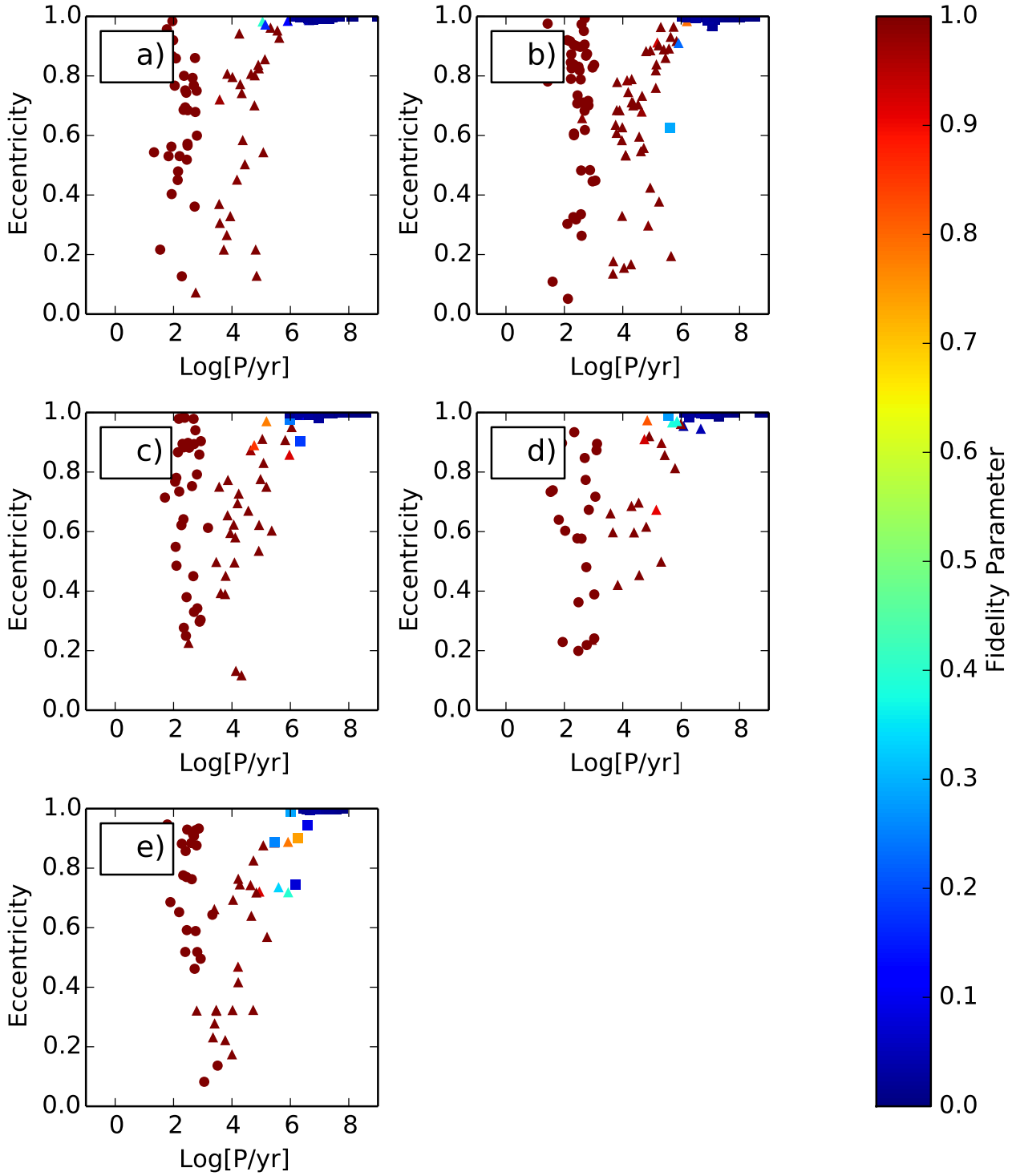

Figure 8.25: The distribution of hierarchical quadruple systems in the $(\log_{10}(P/\mathrm{yr}), \mathrm{e})$-plane. Circles represent inner orbits, triangles represent middle orbits and squares represent outer orbits. The colour of the points encodes the fidelity parameter. Frame a) corresponds to $\sigma_0 = 0.1$, b) 0.1, c) 0.3, d) 0.4, and e) 0.5. 32, 48, 33, 22, 26 hierarchical quadruples are plotted for $\sigma_0 = 0.1$, 0.2, 0.3, 0.4 and 0.5 respectively.

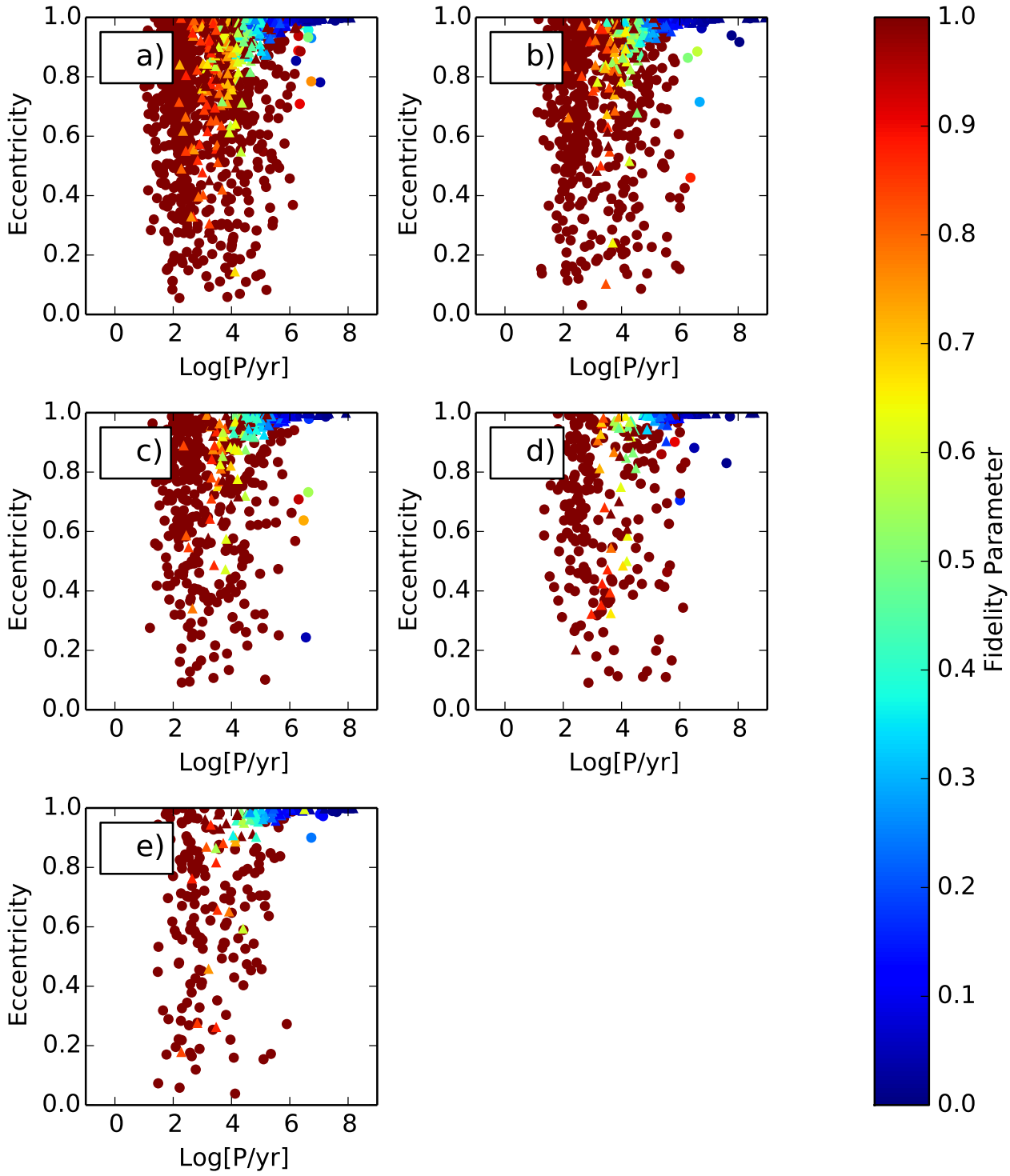

Figure 8.26: The distribution of double quadruple systems in the $(\log_{10}(P/\mathrm{yr}), \mathrm{e})$-plane. Circles represent inner orbits and triangles represent outer orbits. The colour of the points encodes the fidelity parameter. Frame a) corresponds to $\sigma_0 = 0.1$, b) 0.2, c) 0.3, d) 0.4, and e) 0.5. 380, 242, 165, 106, 84 double quadruples for $\sigma_0 = 0.1$, 0.2, 0.3, 0.4 and 0.5 respectively.

quadruples are no longer being produced, and are disintegrating to form binaries instead. The number of binaries also increases for $\sigma_0 < 0.3$, as it is easier to form binaries with equal mass stars. The average number of both triples and hierarchical quadruples increases as σ_0 decreases, apart from at the smallest values of σ_0 where double quadruples are preferentially produced.

Table 8.16: Average number of multiple systems produced per core.

Sigma	Binaries	Triples	Hierarchical Quadruples	Double Quadruples
0.1	0.7272	0.2591	0.0034	0.0403
0.2	0.6654	0.3171	0.0052	0.0263
0.3	0.6799	0.3055	0.0037	0.0185
0.4	0.7144	0.2752	0.0025	0.0122
0.5	0.7456	0.2446	0.0031	0.0101

We can see in Table 8.17 that the most massive stars are more likely to be singles when σ_0 is small. This is because all the stars in a given core cluster have similar masses, and hence have similar chances of being singles.

Table 8.17: Percentage of cores producing systems involving the most massive stars

Sigma	Most massive star	Two most massive stars
0.1	0.81	0.52
0.2	0.92	0.69
0.3	0.96	0.77
0.4	0.97	0.81
0.5	0.98	0.84

With the requirement that the KS test must be rejected at the 1% level for all values of σ_0 for a given property, we can say that the mass ratios of the binaries, triples (inner and outer), hierarchical quadruples (mid) and double quadruples (inner and outer) and period for the binaries and inner triples change with σ_0 with reasonable confidence (See Table 8.18). The mass ratio distributions would be possible to distinguish between observationally.

Table 8.18: This table shows the eccentricity, mass ratio and period distributions that for which the null hypothesis can be rejected at the 1% level, as determined by the K-S test for the different values of σ_0.

σ_0	System Type	Eccentricity	Mass Ratio	Period
0.1	Binaries	✓	✓	✓
0.2	Binaries		✓	✓
0.4	Binaries		✓	✓
0.5	Binaries	✓	✓	✓
0.1	Triples inner	✓	✓	✓
0.2	Triples inner		✓	✓
0.4	Triples inner		✓	✓
0.5	Triples inner		✓	✓
0.1	Triples outer		✓	✓
0.2	Triples outer		✓	
0.4	Triples outer		✓	✓
0.5	Triples outer		✓	✓
0.1	Hierarchical Quadruples inner		✓	
0.2	Hierarchical Quadruples inner		✓	
0.4	Hierarchical Quadruples inner			
0.5	Hierarchical Quadruples inner		✓	
0.1	Hierarchical Quadruples mid		✓	
0.2	Hierarchical Quadruples mid		✓	
0.4	Hierarchical Quadruples mid		✓	
0.5	Hierarchical Quadruples mid		✓	
0.1	Hierarchical Quadruples outer		✓	
0.2	Hierarchical Quadruples outer		✓	
0.4	Hierarchical Quadruples outer			
0.5	Hierarchical Quadruples outer		✓	
0.1	Double Quadruples inner		✓	✓
0.2	Double Quadruples inner		✓	
0.4	Double Quadruples inner		✓	
0.5	Double Quadruples inner		✓	
0.1	Double Quadruples outer		✓	
0.2	Double Quadruples outer		✓	
0.4	Double Quadruples outer		✓	
0.5	Double Quadruples outer		✓	

Chapter 9

Core Cluster Results: Part II

In this chapter, I move away from spherically uniform density of stars, and investigate three other initial configurations. These include a density profile that decreases with a power law, $n(r) = r^{-\alpha}$, a ring cluster and a line cluster. I also investigate the influence of disks, and add these to the fiducial model, line cluster and ring cluster.

9.1 Density Gradient

In this section I present the results of varying α. I run 8920, 8932, 8852 simulations for the values of $\alpha = 0$, -1, and -2 respectively. These sets of simulations produce 6065, 6102, 6029 binaries, 2725, 2710, 2682 triples, 33, 33, 26 hierarchical quadruples and 165, 162, 187 double quadruples for $\alpha = 0$, -1 and -2 respectively.

Few of the multiplicity properties change with a varying α. The means of the periods increase as α is decreased, whilst the standard deviations decrease. The eccentricity distribution of the outer orbit of triples becomes flatter, whilst the eccentricity of the corresponding inner orbits becomes steeper. The outer mass ratio distribution also becomes flatter. The quadruples have too few samples to discern any trends. There is no significant change in any other properties, and even the changes mentioned are within the errors. Therefore, I simply present the results of varying α, and do not discuss them any further.

With the requirement that the KS test must be rejected at the 1% level for all values of α for a given property, we can say that only the period of the binaries and inner period of the triples change with α with reasonable confidence. (See Table 9.5). However, the differences are so small that they wouldn't be able to be distinguished between observationally.

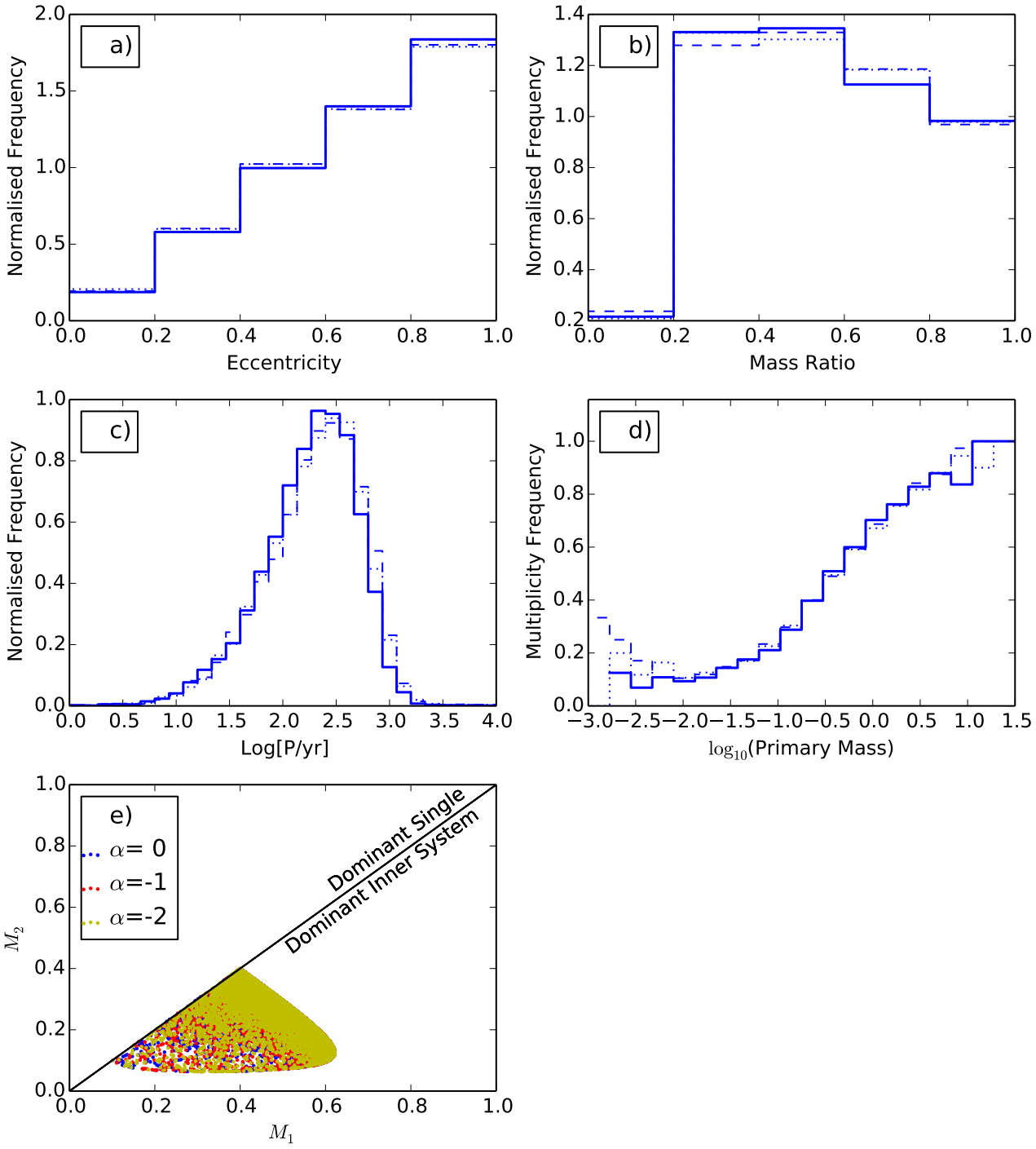

Figure 9.1: The variation of binary properties with α. The solid/dotted/dashed lines in each of the frames describes the distributions attained when $\alpha = 0$, -1 and -2 respectively. Frame a) shows the normalised distribution of eccentricities, Frame b) shows the normalised distribution of mass ratios, Frame c) shows the normalised distribution of periods [yr] and Frame d) shows the multiplicity frequency as a function of primary mass, and Frame e) plots M_2 against M_1. 6065, 6102, 6029 binaries for $\alpha = 0$, -1 and -2 respectively.

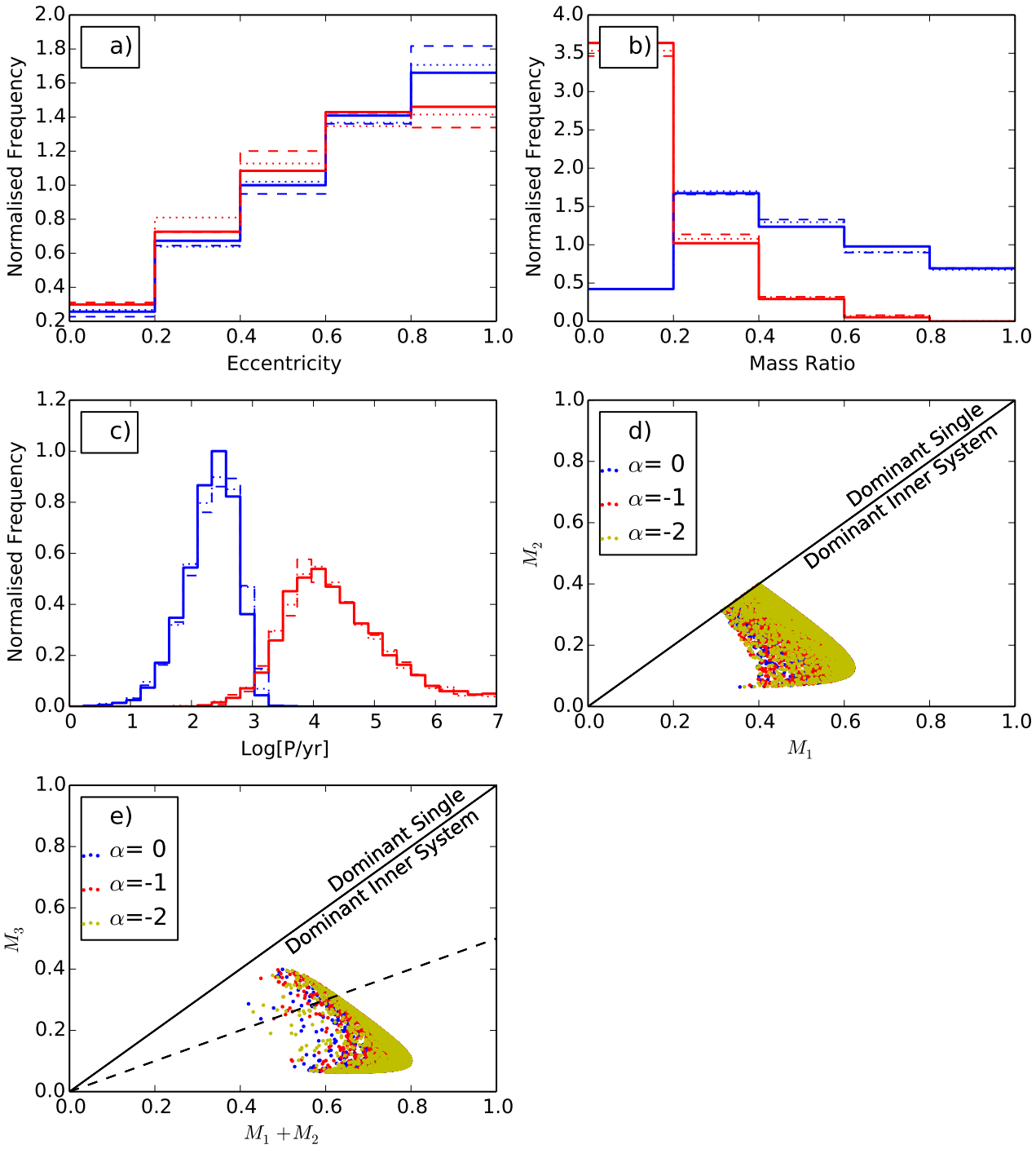

Figure 9.2: The variation of properties of triples formed with α. The solid/dotted/dashed lines in each of the Frames describes the distributions attained when $\alpha = 0$, -1 and -2 respectively. The blue lines show the inner periods, whilst the red lines show the outer periods. Frame a) shows the normalised distribution of eccentricities, Frame b) shows the normalised distribution of mass ratios and Frame c) shows the normalised distribution of periods [yr]. Frame d) plots M_2 against M_1, whilst Frame e) plots M_3 against $M_2 + M_1$. 2725, 2710, 2682 triple systems are produced for $\alpha = 0$, -1 and -2 respectively.

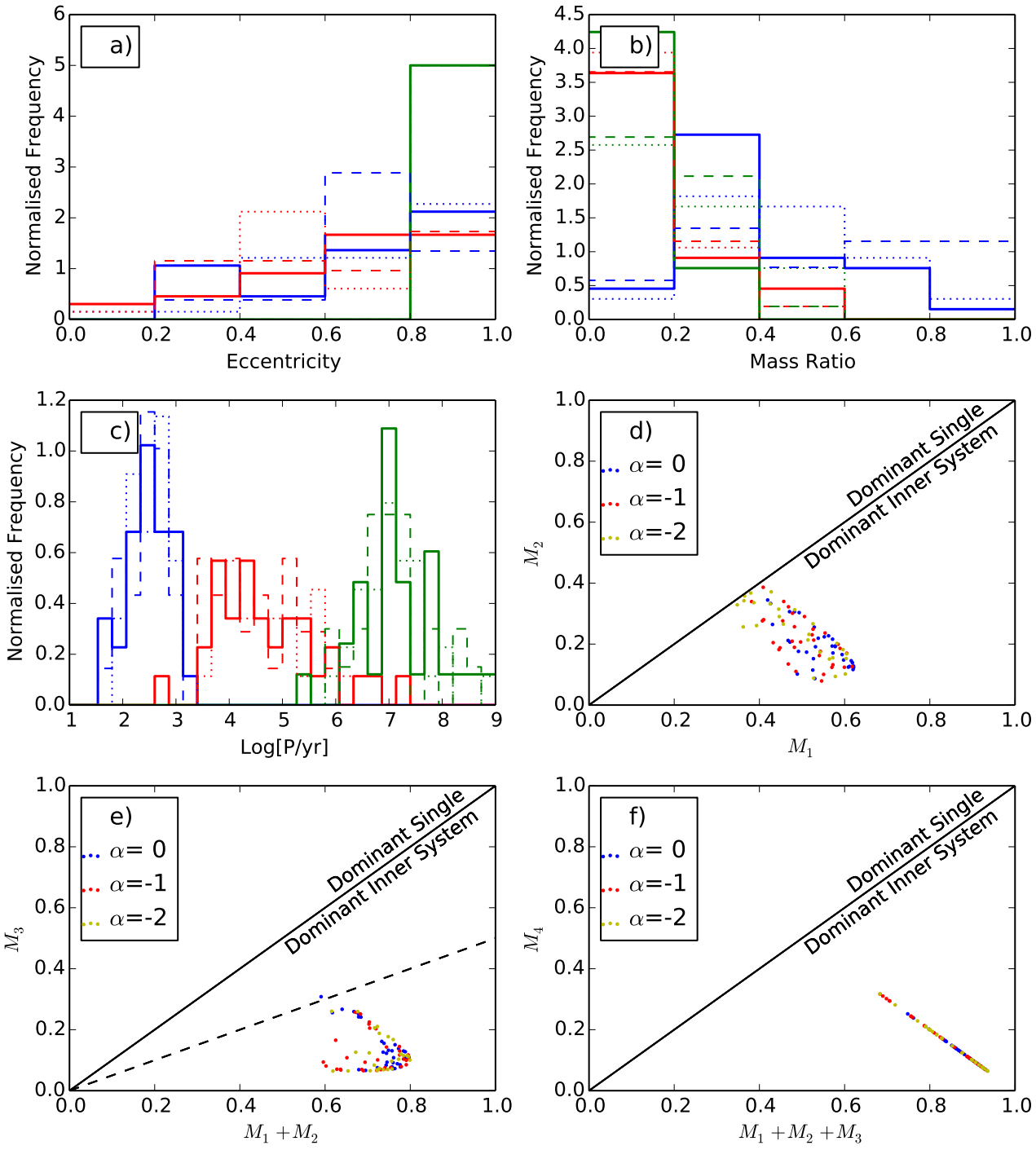

Figure 9.3: The variation of properties of hierarchical quadruples formed with α. The solid/dotted/dashed lines in each of the Frames describes the distributions attained when $\alpha = 0, -1$, and -2 respectively. The blue lines show the inner periods, the red lines show the mid periods and the green lines show the outer periods. Frame a) shows the normalised distribution of eccentricities, Frame b) shows the normalised distribution of mass ratios and Frame c) shows the normalised distribution of periods [yr]. Frame d) plots M_2 against M_1, whilst Frame e) plots M_3 against $M_2 + M_1$, and Frame f) plots M_4 against $M_3 + M_2 + M_1$. 33, 33, 26 hierarchical quadruple systems are plotted for $\alpha = 0$, -1 and -2 respectively.

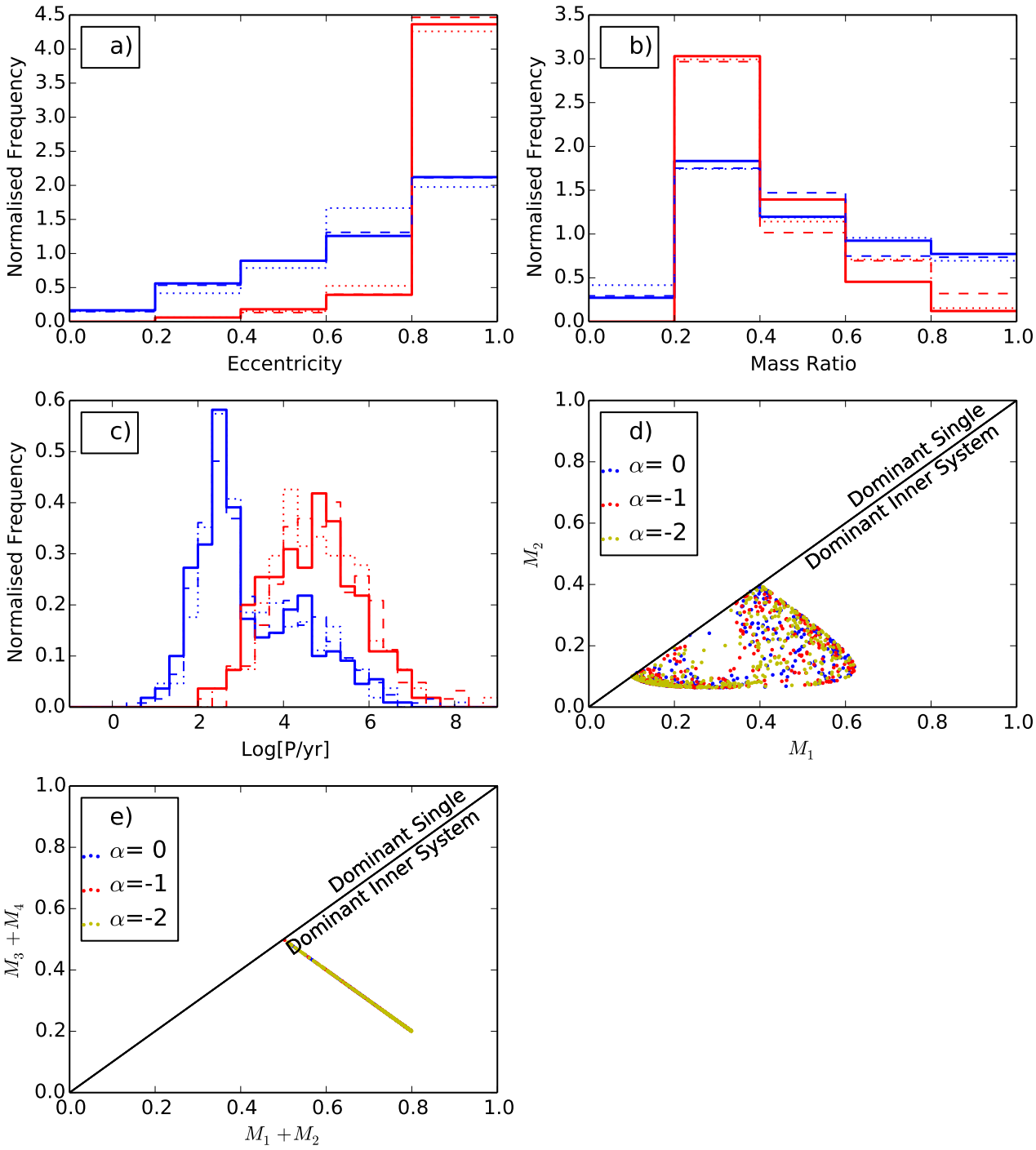

Figure 9.4: The variation of properties of double quadruples formed with α. The solid/dotted/dashed lines in each of the Frames describes the distributions attained when $\alpha = 0,-1$, and -2 respectively. The blue lines show the inner periods, whilst the red lines show the outer periods. Frame a) shows the normalised distribution of eccentricities, Frame b) shows the normalised distribution of mass ratios and Frame c) shows the normalised distribution of periods [yr]. Frame d) plots M_2 against M_1 and M_4 against M_3, and Frame e) plots $M_4 + M_3$ against M_2+M_1. 165, 162, 187 double quadruples are plotted for $\alpha = 0$, -1 and -2 respectively.

Table 9.1: Mean and standard deviation of $\log_{10}(P/\mathrm{yr})$

Alpha			
	Binaries	Triples	
		Inner	Outer
0	2.251±0.479	2.303±0.418	4.490±1.025
-1	2.282±0.473	2.318±0.441	4.451±0.989
-2	2.289±0.470	2.342±0.450	4.474±0.990

Table 9.2: Mean and standard deviation of $\log_{10}(P/\mathrm{yr})$

Alpha					
	Quad, Hierarchical			Quad, Double	
	Inner	Mid	Outer	Inner	Outer
0	2.483±0.406	4.706±1.001	7.308±0.875	3.188±1.223	4.673±1.063
-1	2.541±0.329	4.826±0.883	7.063±0.665	3.309±1.235	4.805±1.049
-2	2.464±0.371	4.540±0.761	7.181±0.811	3.358±1.292	4.911±1.055

Table 9.3: Average number of multiple systems produced per core.

Alpha	Binaries	Triples	Hierarchical Quadruples	Double Quadruples
0	0.6799	0.3055	0.0037	0.0185
-1	0.6832	0.3034	0.0037	0.0181
-2	0.6811	0.3030	0.0029	0.0211

Table 9.4: Percentage of cores producing systems involving the most massive stars

Alpha	Most massive star	Two most massive stars
0	0.96	0.77
-1	0.95	0.77
-2	0.95	0.76

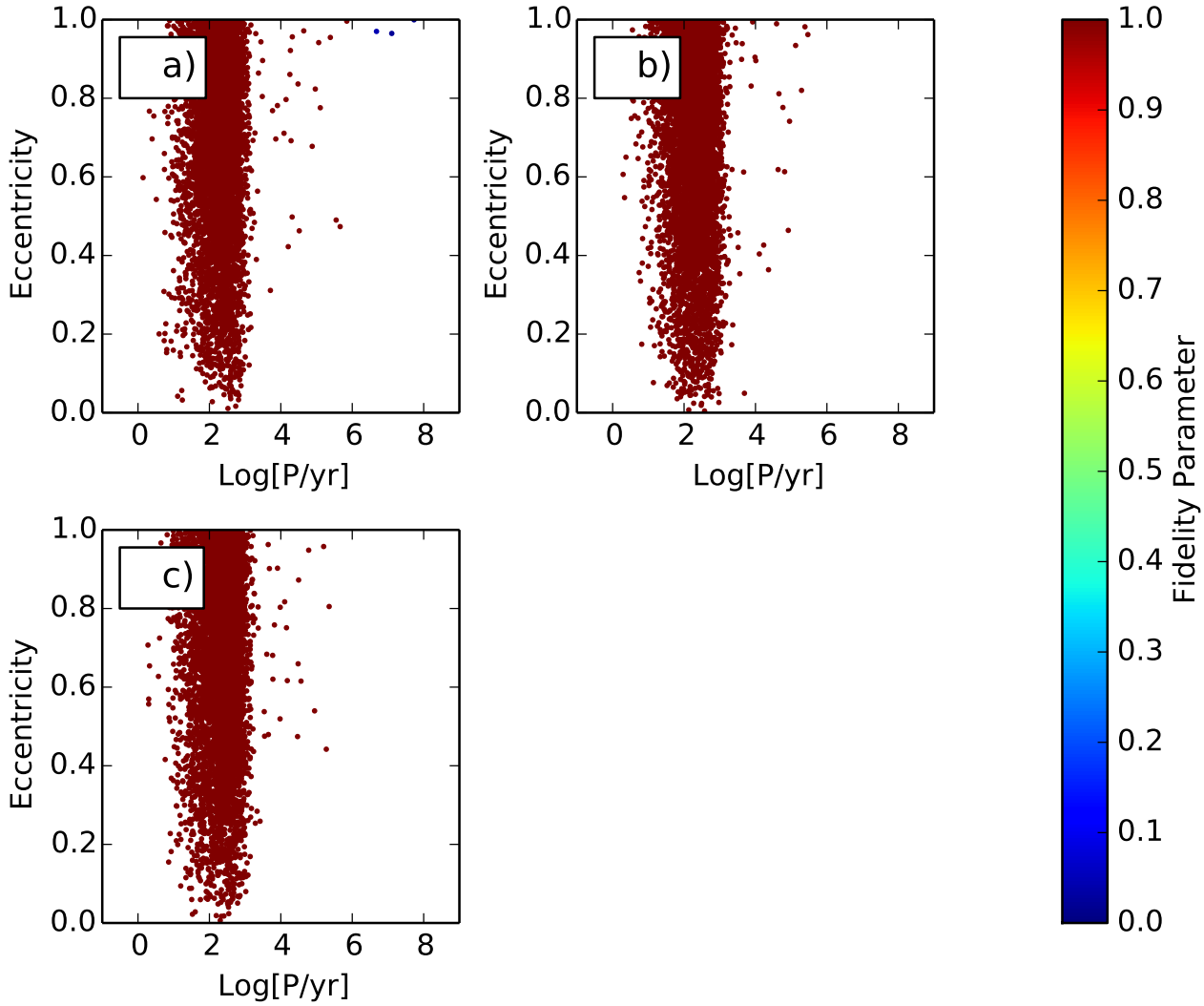

Figure 9.5: The distribution of binary systems in the $(\log_{10}(P/\mathrm{yr}), \mathrm{e})$-plane. The colour of the points encodes the fidelity parameter. Frame a) corresponds to $\alpha = 0$, b) -1, and d) -2. 6065, 6102, 6029 binary systems are plotted for $\alpha = 0$, -1 and -2 respectively.

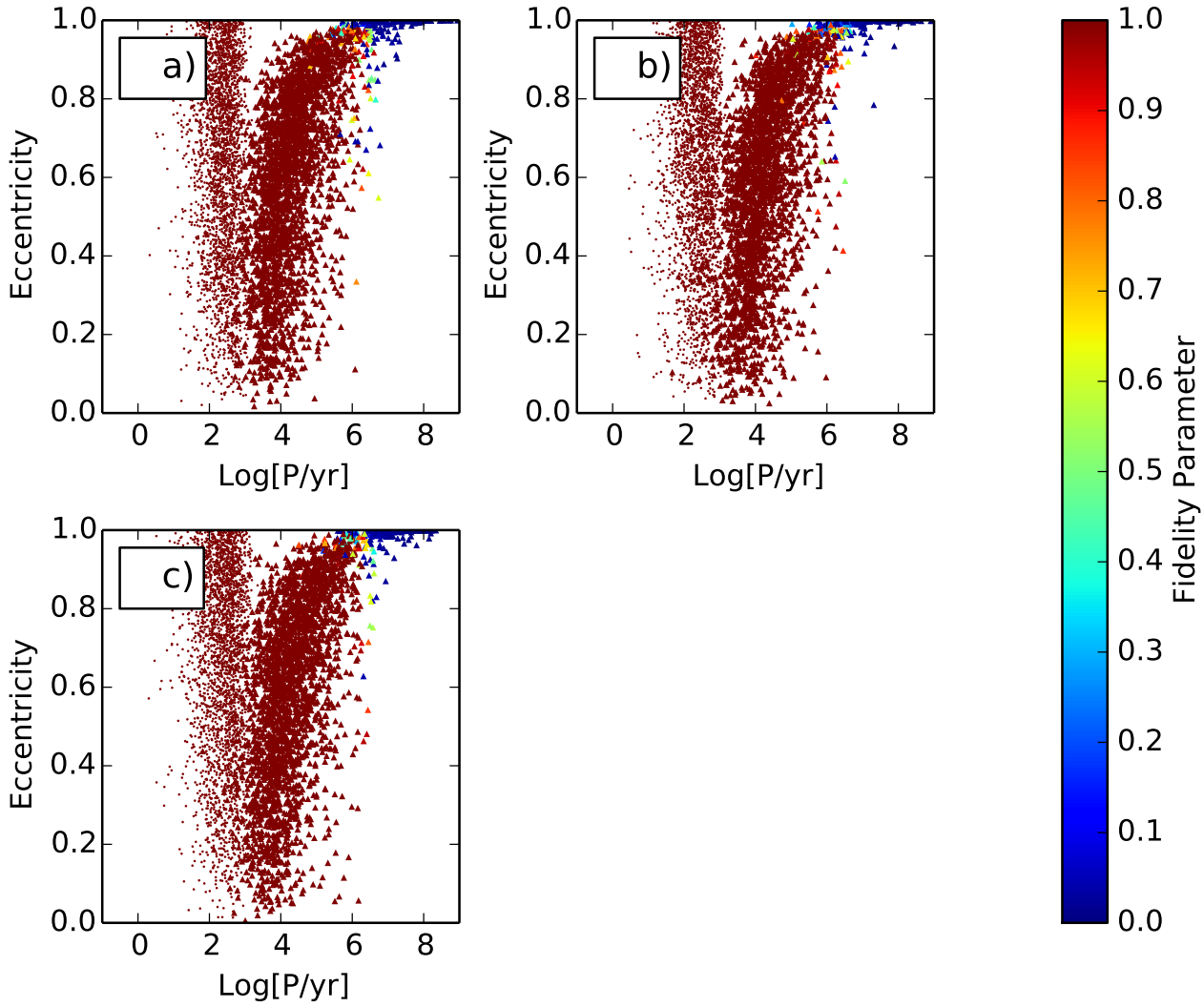

Figure 9.6: The distribution of triple systems in the $(\log_{10}(P/\mathrm{yr}), \mathrm{e})$-plane. Small circles represent inner orbits and triangles represent outer orbits. The colour of the points encodes the fidelity parameter. Frame a) corresponds to $\alpha = 1$, b) -1, and c) -2. 2725, 2710, 2682 triples are plotted for $\alpha = 0$, -1 and -2 respectively.

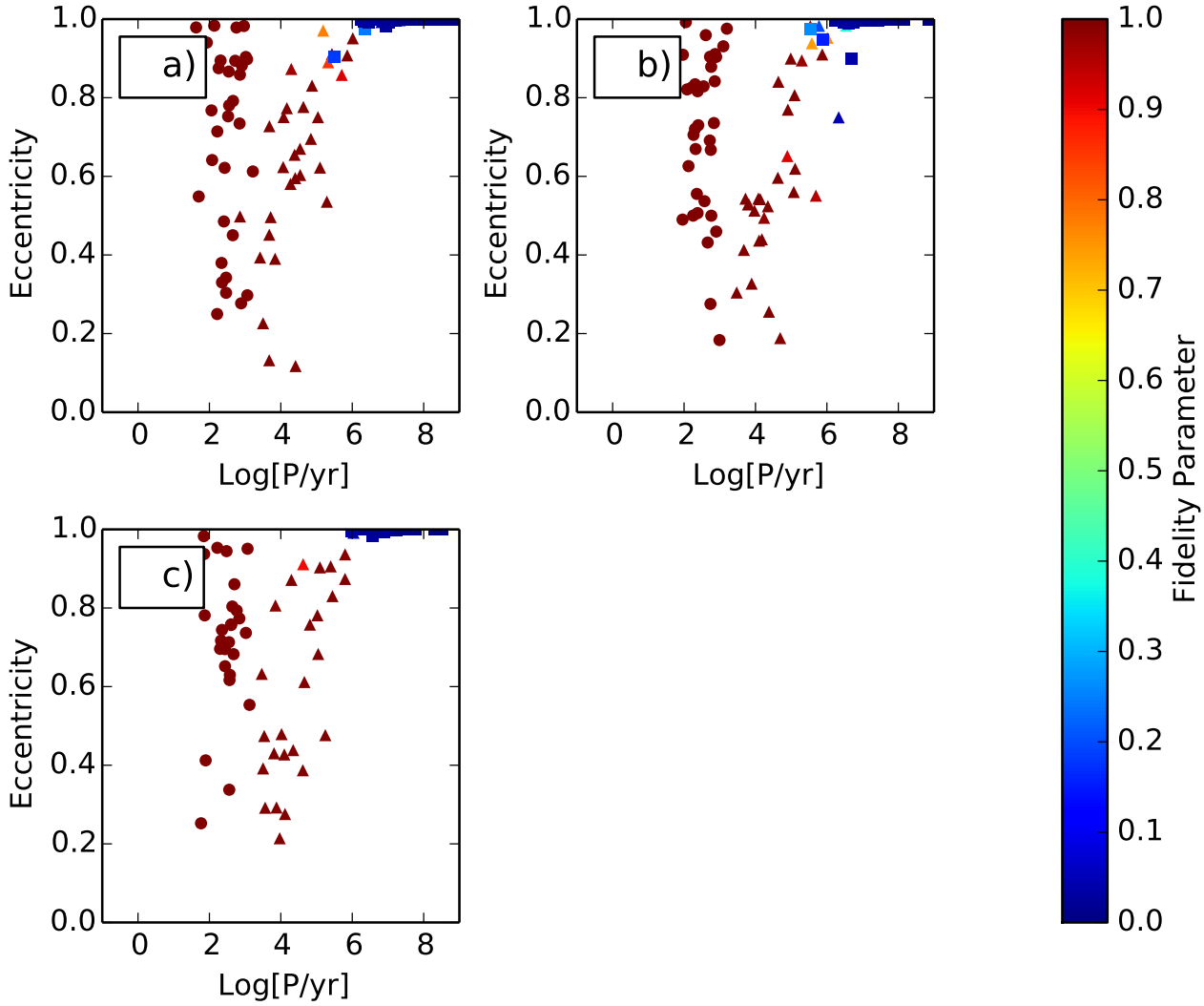

Figure 9.7: The distribution of hierarchical quadruple systems in the $(\log_{10}(P/\mathrm{yr}), \mathrm{e})$-plane. Circle represent inner orbits, triangles represent mid orbits and squares represent outer orbits. The colour of the points encodes the fidelity parameter. Frame a) corresponds to $\alpha = 0$, b) -1, and c) -2. 33, 33, 26 hierarchical quadruple systems are plotted for $\alpha = 0$, -1 and -2 respectively.

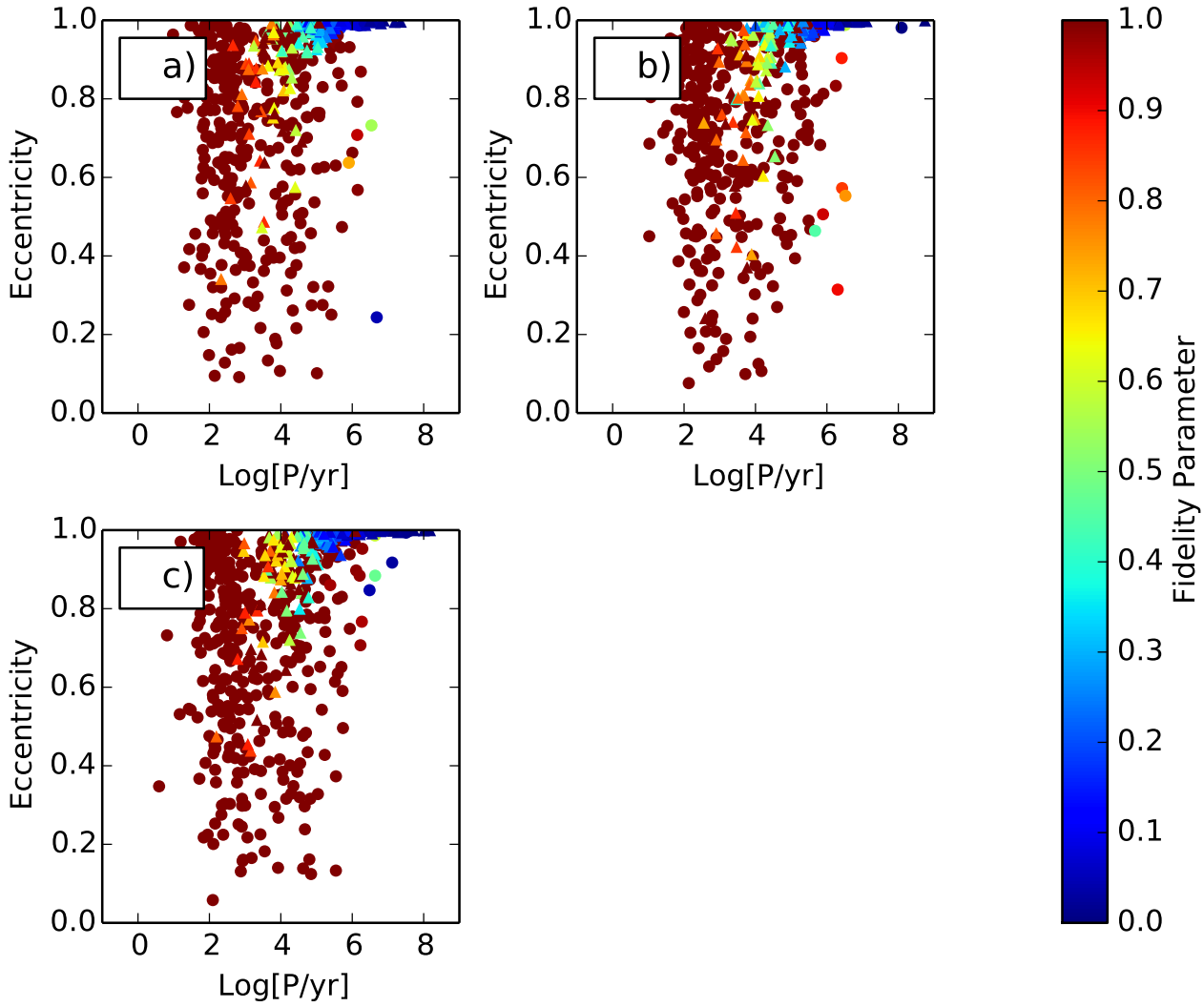

Figure 9.8: The distribution of double quadruple systems in the $(\log_{10}(P/\mathrm{yr}), \mathrm{e})$-plane. Circles represent inner orbits and triangles represent outer orbits. The colour of the points encodes the fidelity parameter. Frame a) corresponds to $\alpha = 0$, b) -1, and c) -2. 165, 162, 187 double quadruple systems are plotted for $\alpha = 0$, -1 and -2 respectively.

Table 9.5: This table shows the eccentricity, mass ratio and period distributions that for which the null hypothesis can be rejected at the 1% level, as determined by the K-S test for the different values of α.

α	System Type	Eccentricity	Mass Ratio	Period
-1	Binaries			✓
-2	Binaries			✓
-1	Triples inner			✓
-2	Triples inner			✓
-1	Triples outer			
-2	Triples outer			
-1	Hierarchical Quadruples inner			
-2	Hierarchical Quadruples inner			
-1	Hierarchical Quadruples mid			
-2	Hierarchical Quadruples mid			
-1	Hierarchical Quadruples outer			
-2	Hierarchical Quadruples outer			
-1	Double Quadruples inner			
-2	Double Quadruples inner			
-1	Double Quadruples outer			
-2	Double Quadruples outer			

9.2 Spherical Cluster with Disks

In this section I present the results of varying the size of the disks attending a star. I run 8920, 7427, 9082 simulations for $d_m = 0.0$, 0.5, and 1.0 respectively. These sets of simulations produce 6065, 4931, 5986 binaries, 2725, 2435, 2998 triples, 33, 18, 22 hierarchical quadruples and 165, 110, 149 double quadruples for $d_m = 0.0$, 0.5 and 1.0 respectively.

Due to the ad-hoc nature of the prescription for interactions including disks, the period and eccentricity distributions cannot be wholly relied upon. They can be used as an indication of what is likely to happen, but are not definitive. The mass ratios on the other hand are more likely to be faithful.

The properties of the binaries produced are shown in Figure 9.9. Sub-figure 9.9a shows that the eccentricities are not affected by the disk mass, whilst Sub-figure 9.9b shows that there is no clear trend in the mass ratios distributions. Sub-figure 9.9c and Table 9.6 show that as the mass of the attending disks is increased, the mean period of the binaries decreases. The multiplicity frequency in Sub-figure 9.9d remains largely unaffected. The graph of M_1 against M_2 is plotted in Sub-figure 8.5e. There are no observable differences that occur by adding disks.

Figure 9.10 shows the properties of triple systems. The eccentricities of orbits as seen in Sub-figure 9.10a do not change. The mass ratios as shown in Sub-figure 9.10b show a distribution for outer periods that decreases slightly in the low mass ratio regime. The mean of the period as shown in Sub-figure 9.10c and Table 9.6 decreases as the disk mass is increased, whilst the standard deviation for the outer periods decreases with disk mass. In Sub-figure 8.6d M_2 is plotted against M_1, and in Sub-figure 8.6d M_3 is plotted against M_2+M_1. Again, no observable differences can be seen.

Due to low number statistics, no clear trends can be seen for any of the properties of either hierarchical quadruples, or double quadruples.

Table 9.6: Mean and standard deviation of $\log_{10}(P/\mathrm{yr})$

Disks			
	Binaries	Triples	
		Inner	Outer
$M_d = 0.0M_*$	2.257±0.476	2.289±0.434	4.476±1.034
$M_d = 0.5M_*$	2.167±0.505	2.176±0.467	4.303±0.998
$M_d = 1.0M_*$	2.161±0.496	2.185±0.474	4.330±0.972

Figures 9.11, 9.12, 9.13 and 9.14 show the distributions of period against eccentricity for binaries, triples, hierarchical quadruples and double quadruples respectively. These distributions do not change much as d_m is increases, apart from increasing the number of low eccentricity systems.

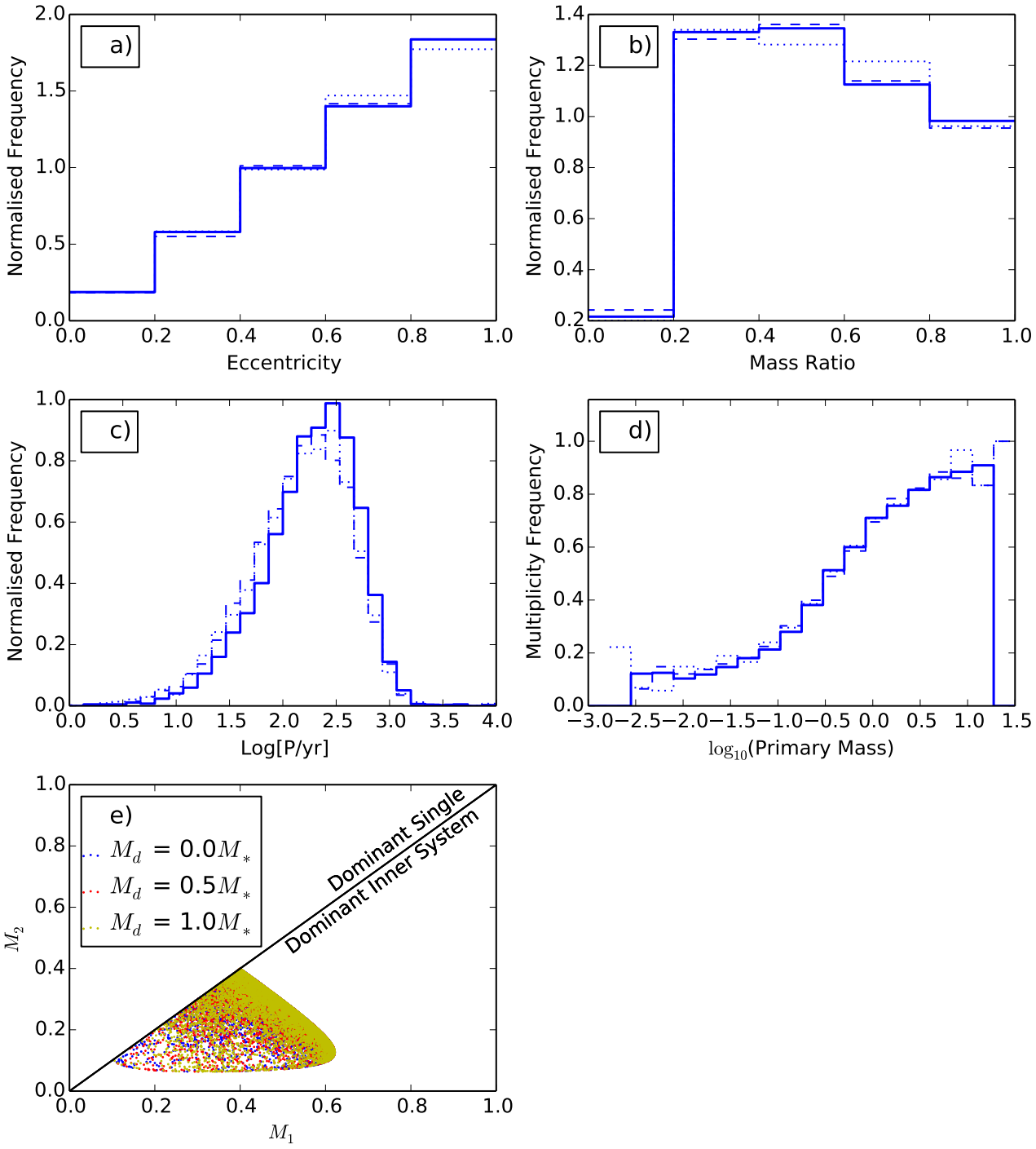

Figure 9.9: The variation of binary properties with disk mass. The solid/dotted/dashed lines in each of the Frames describes the distributions attained when $d_m = 0.0$, 0.5 and 1.0 respectively. Frame a) shows the normalised distribution of eccentricities, Frame b) shows the normalised distribution of mass ratios, Frame c) shows the normalised distribution of periods [yr] and Frame d) shows the multiplicity frequency as a function of primary mass, and Frame e) plots M_2 against M_1. 6065, 4931, 5986 binary systems are plotted for $d_m = 0.0$, 0.5 and 1.0 respectively.

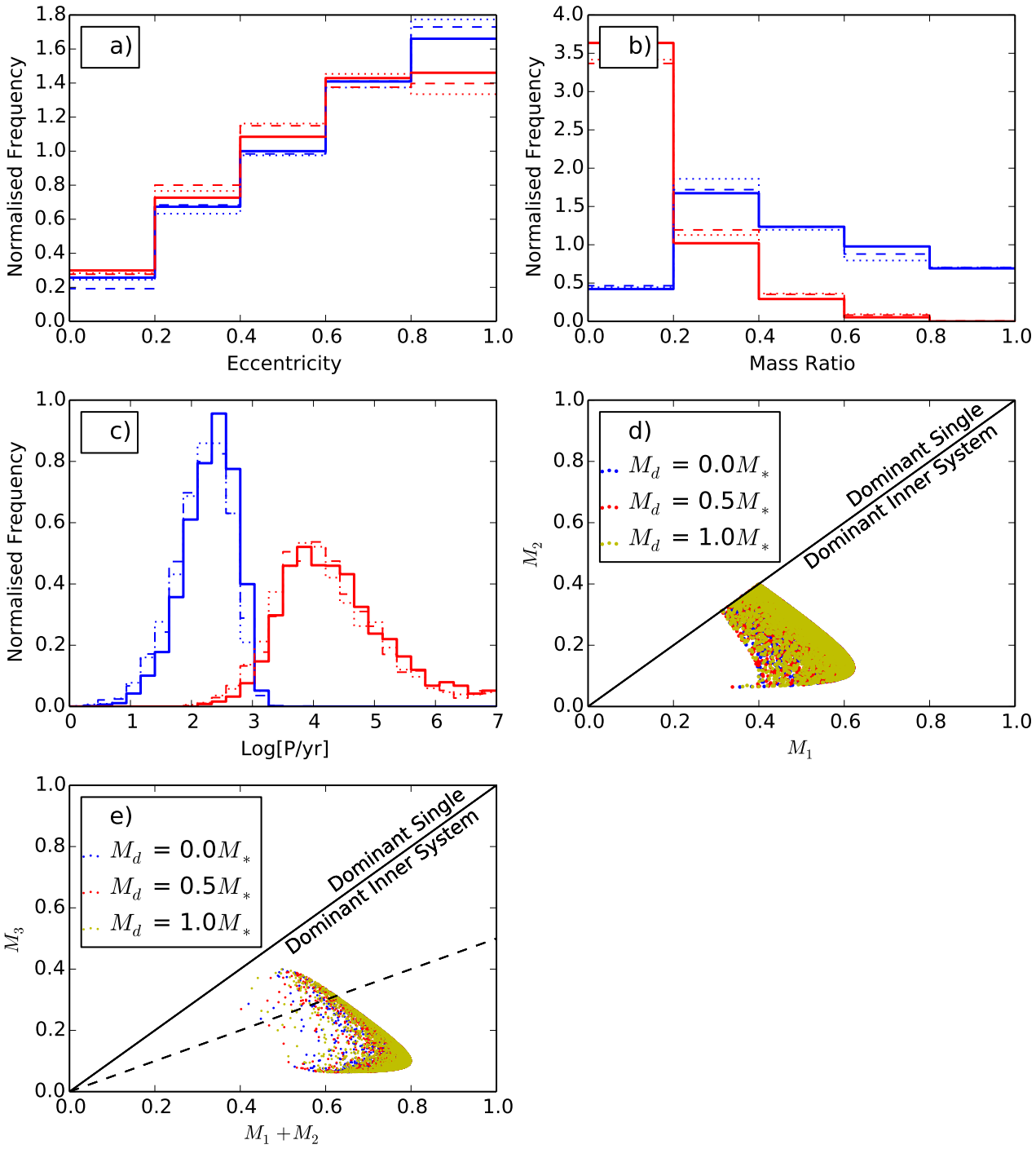

Figure 9.10: The variation of properties of triples formed with disk mass. The solid/dotted/dashed lines in each of the Frames describes the distributions attained when d_m = 0.0, 0.5 and 1.0 respectively. The blue lines show the inner periods, whilst the red lines show the outer periods. Frame a) shows the normalised distribution of eccentricities, Frame b) shows the normalised distribution of mass ratios and Frame c) shows the normalised distribution of periods [yr]. Frame d) plots M_2 against M_1, whilst Frame e) plots M_3 against $M_2 + M_1$. 2725, 2435, 2998 triple systems are plotted for d_m = 0.0, 0.5 and 1.0 respectively.

Table 9.7: Mean and standard deviation of $\log_{10}(P/\mathrm{yr})$

Disks					
	Quad, Hierarchical			Quad, Double	
	Inner	Mid	Outer	Inner	Outer
$M_d = 0.0M_*$	2.448±0.356	4.670±0.940	7.273±0.777	3.239±1.207	4.724±1.023
$M_d = 0.5M_*$	2.216±0.578	4.436±0.941	7.120±0.791	3.304±1.333	4.883±1.128
$M_d = 1.0M_*$	2.383±0.503	4.630±0.870	7.004±0.716	3.237±1.282	4.782±1.066

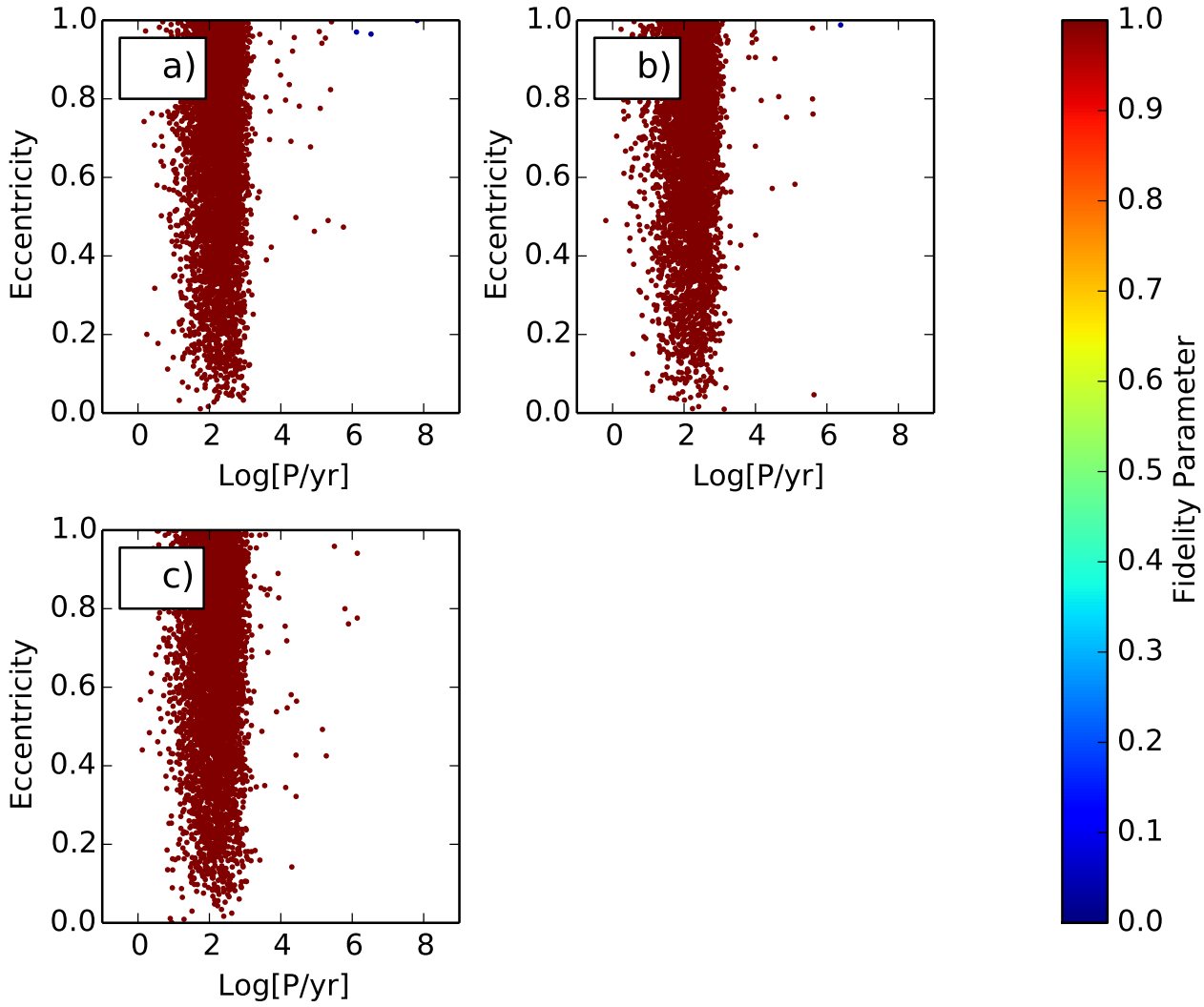

Figure 9.11: The distribution of binary systems in the $(\log_{10}(P/\mathrm{yr}), \mathrm{e})$-plane. The colour of the points encodes the fidelity parameter. Frame a) corresponds to $d_m = 0.0$, b) 0.5, and c) 1.0. 6065, 4931, 5986 binary systems are plotted for $d_m = 0.0$, 0.5 and 1.0 respectively.

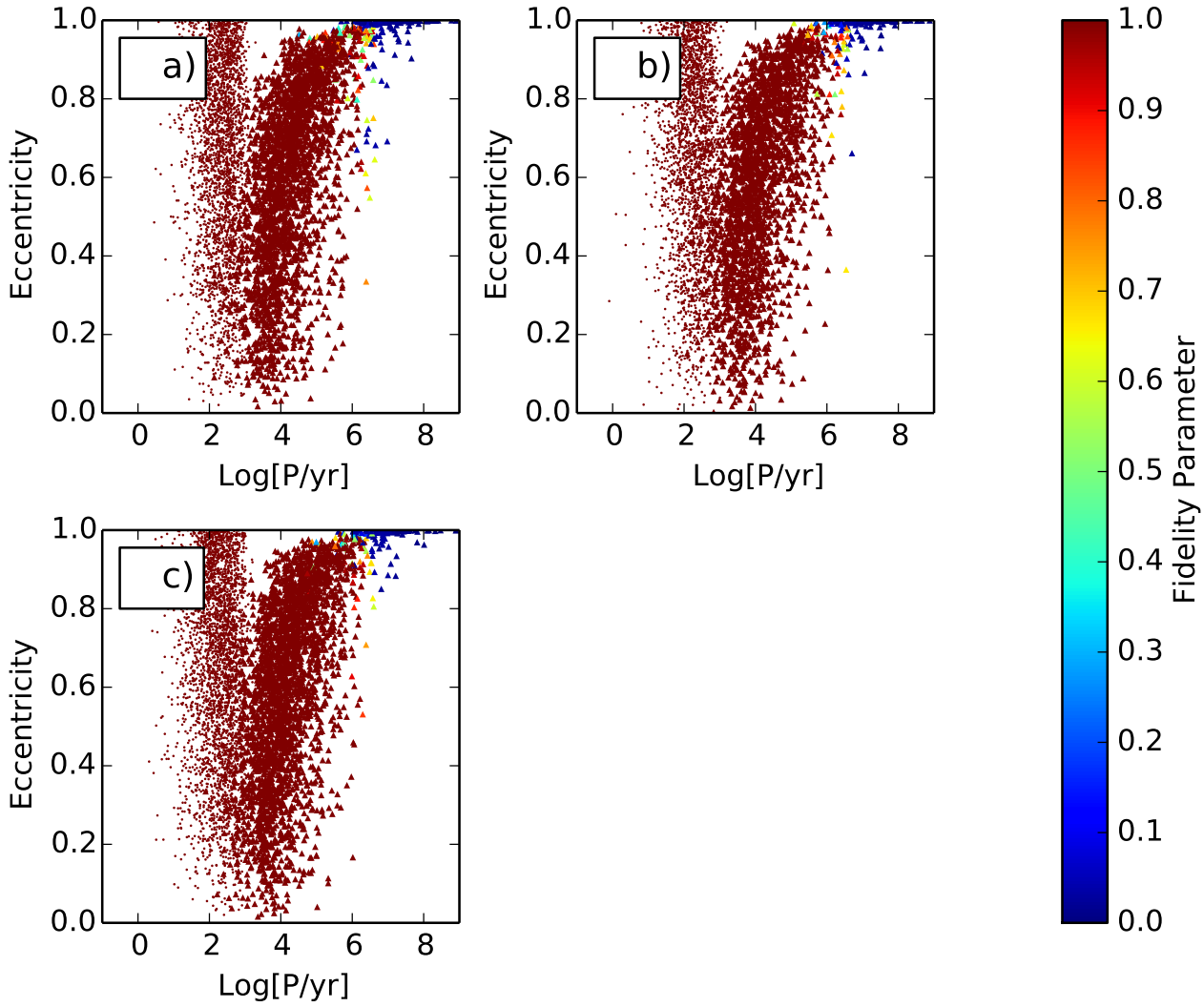

Figure 9.12: The distribution of triple systems in the $(\log_{10}(P/\mathrm{yr}), \mathrm{e})$-plane. Small circles represent inner orbits and triangles represent outer orbits. The colour of the points encodes the fidelity parameter. Frame a) corresponds to $d_m = 0.0$, b) 0.5, and c) 1.0. 2725, 2435, 2998 triple systems are plotted for $d_m = 0.0$, 0.5 and 1.0 respectively.

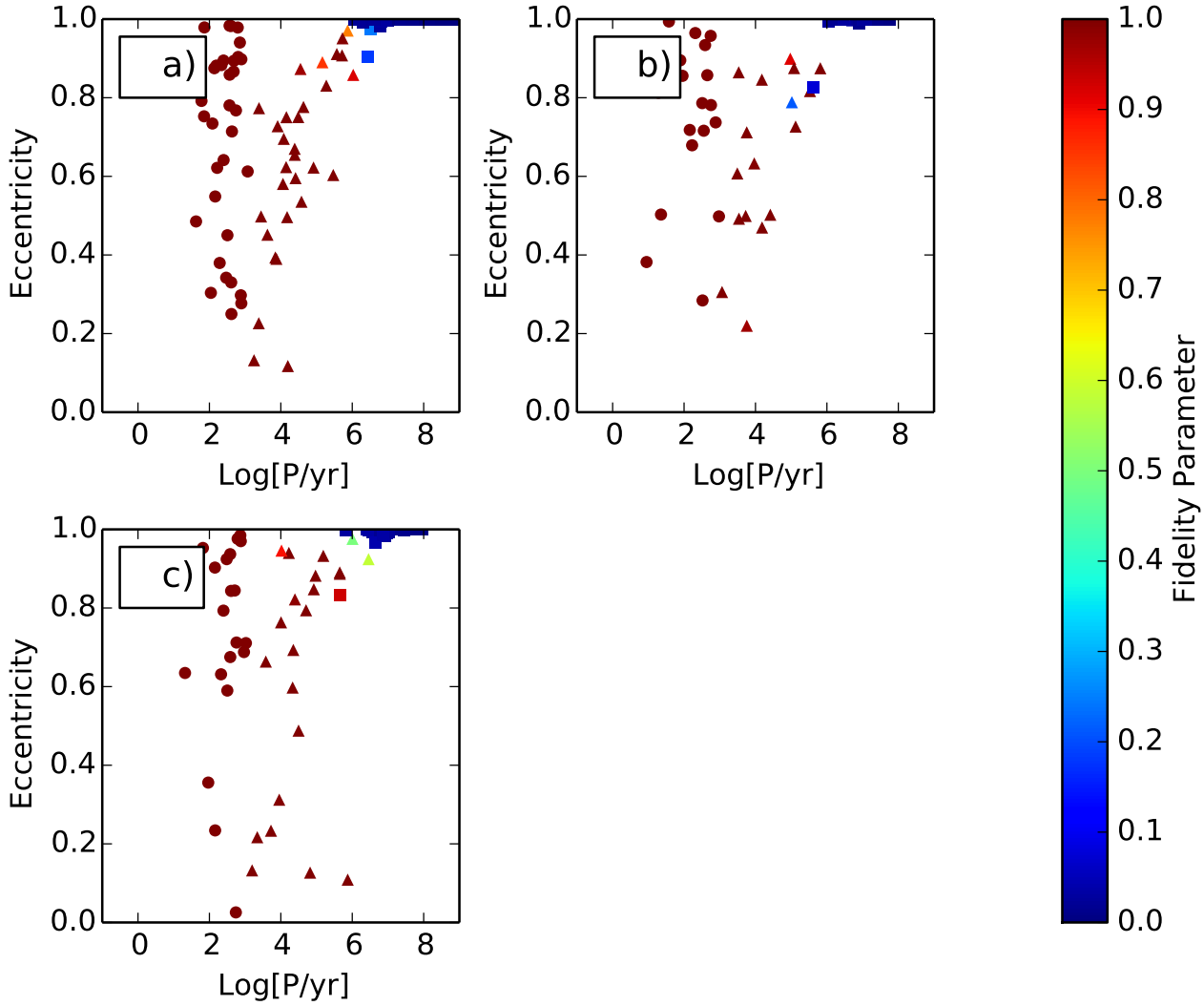

Figure 9.13: The distribution of hierarchical quadruple systems in the $(\log_{10}(P/\mathrm{yr}), \mathrm{e})$-plane. Circles represent inner orbits, red triangles represent mid orbits and squares represent outer orbits. The colour of the points encodes the fidelity parameter. Frame a) corresponds to $d_m = 0.0$, b) 0.5, and c) 1.0. 33, 18, 22 hierarchical quadruple systems are plotted for $d_m = 0.0$, 0.5 and 1.0 respectively.

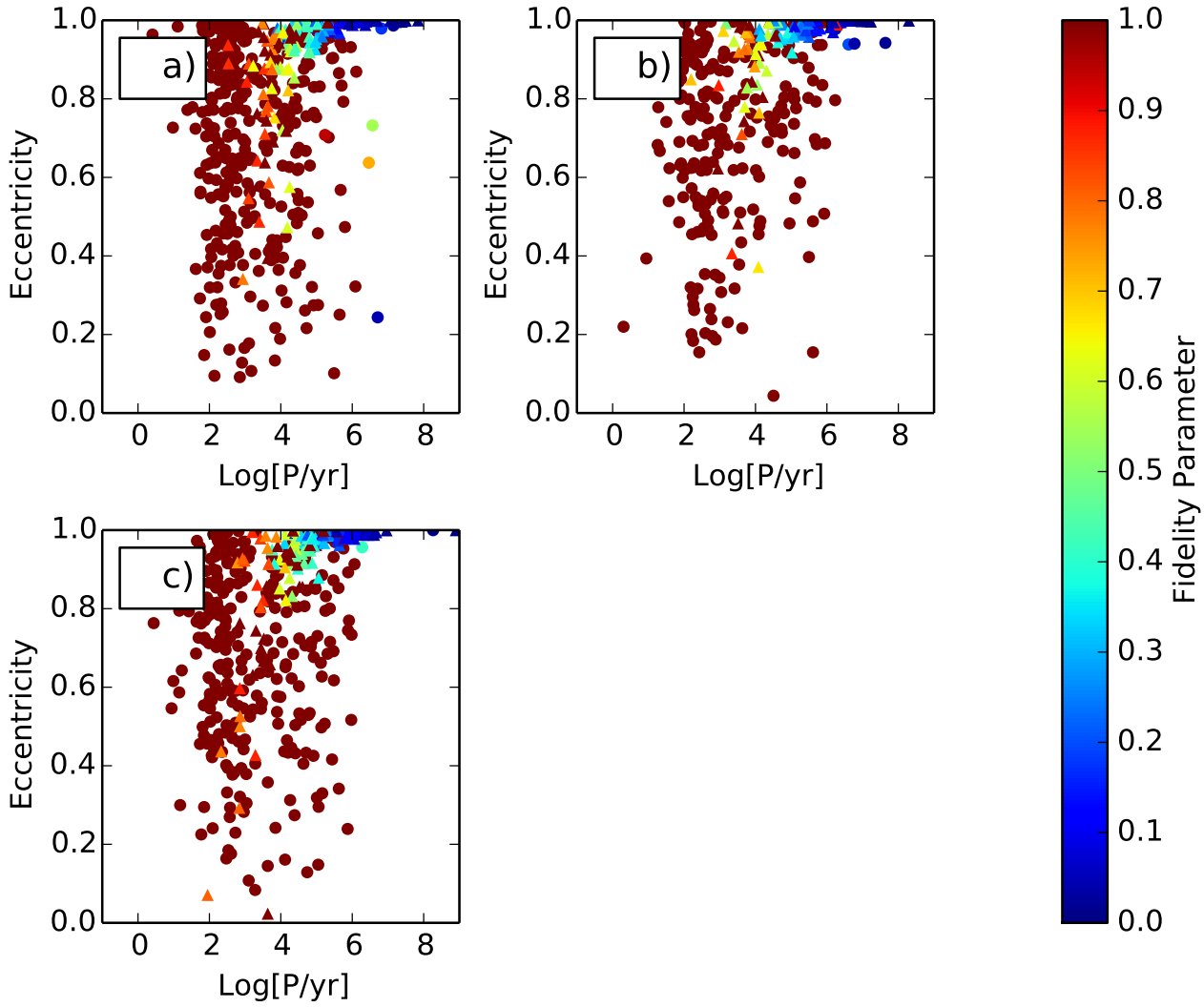

Figure 9.14: The distribution of double quadruple systems in the $(\log_{10}(P/\mathrm{yr}), \mathrm{e})$-plane. Circles represent inner orbits and triangles represent outer orbits. The colour of the points encodes the fidelity parameter. Frame a) corresponds to $d_m = 0.0$, b) 0.5, and c) 1.0. 165, 110, 149 double quadruple systems are plotted for $d_m = 0.0$, 0.5 and 1.0 respectively.

Table 9.8 shows that there isn't any firm trend in the average number of multiple systems produced per core with d_m, whilst Table 9.9 shows that the percentage of cores producing a multiple system involving the most massive star, or the two most massive stars does not change with d_m.

Table 9.8: Average number of multiple systems produced per core.

Disks	Binaries	Triples	Hierarchical Quadruples	Double Quadruples
$M_d = 0.0M_*$	0.6799	0.3055	0.0037	0.0185
$M_d = 0.5M_*$	0.6639	0.3279	0.0024	0.0148
$M_d = 1.0M_*$	0.6591	0.3301	0.0024	0.0164

Table 9.9: Percentage of cores producing systems involving the most massive stars

Disks	Most massive star	Two most massive stars
$M_d = 0.0M_*$	0.96	0.77
$M_d = 0.5M_*$	0.95	0.76
$M_d = 1.0M_*$	0.94	0.76

The presence of these disks has little influence on the properties of the multiple systems formed. This can be explained by the following argument. For the spherical cluster, the average distance between stars is 1 dimensionless unit. The radius of the disk is taken to be 0.5 and 1.0 times the mass of the star for $d_m = 0.5$, 1.0 respectively. So even in the most massive case, it is unlikely that a star will start the simulation within another star's disk. By the time stars get close enough for the disks to interact, gravitational biasing has already taken effect, and so the stars that get close enough to interact with the disks are those stars that would have formed a multiple system anyway. The overall influence of the disks in this instance is simply to harden the systems that would have formed anyway.

With the requirement that the KS test must be rejected at the 1% level for both values of d_m for a given property, we can say that the period for the binaries and triples (inner and outer) and the outer mass ratio of the triples change with the addition of disks with reasonable confidence (See Table 9.10). However, the differences are so small that the distributions could not be distinguished between observationally.

Table 9.10: This table shows the eccentricity, mass ratio and period distributions that for which the null hypothesis can be rejected at the 1% level, as determined by the K-S test for the different values of d_m.

d_m	System Type	Eccentricity	Mass Ratio	Period
0.5	Binaries			✓
1	Binaries			✓
0.5	Triples inner		✓	✓
1	Triples inner			✓
0.5	Triples outer		✓	✓
1	Triples outer		✓	✓
0.5	Hierarchical Quadruples inner			
1	Hierarchical Quadruples inner			
0.5	Hierarchical Quadruples mid			
1	Hierarchical Quadruples mid			
0.5	Hierarchical Quadruples outer			
1	Hierarchical Quadruples outer			
0.5	Double Quadruples inner			
1	Double Quadruples inner			
0.5	Double Quadruples outer			
1	Double Quadruples outer			

9.3 Ring Cluster with Disks

In this section I present the results of setting the initial positions of stars on the circumference of a ring, and then adding disks. I run 8920, 9116, 9056 simulations for the fiducial model, a ring cluster and a ring cluster with disks of mass $d_m = 0.5$ respectively. These sets of simulations produce 6065, 8491, 8412 binaries, 2725, 1012, 1007 triples, 33, 28, 20 hierarchical quadruples and 165, 176, 153 double quadruples for the fiducial model, ring cluster and ring cluster with disks respectively.

The properties of pure binaries are shown in Figure 9.15. The eccentricity distribution (Sub-figure 9.15a) shows a small tendency to produce more high-eccentricity orbits for the ring cluster than the fiducial model. This is because in the ring cluster, binaries tend to consist of stars that were initially nearest neighbours in the ring. As the stars are set up with purely rotational velocities, the angle between the velocity of a star and the position vector with its companion is initially very small. Circular orbits always have a velocity that is perpendicular to the position vector, and so the system is set up in such a way that eccentric binaries are favoured. The mass ratio distribution as shown in Sub-figure 9.15b shows a preference for low mass ratio binaries. This can be explained by considering that the stars are initially placed on the circumference of a circle, taking up an arc proportional to their mass. Smaller mass stars will therefore be placed closer to a given star than stars with a larger mass. Because of their proximity to their neighbours, smaller stars now have a greater chance to form a part of a multiple system, and more low mass ratio binaries are produced. The lack of binaries with mass ratio between 0.0 and 0.2 is due to a lack of low mass companions to choose from. As seen in Sub-figure 9.15c and Table 9.11, the period distribution increases by a factor of 4.5 when the stars are placed in a ring core cluster as compared to the fiducial spherical core cluster, due to conservation of angular momentum. There is more angular momentum in the ring clusters than the other clusters simply because of the way the clusters are set-up, and because there isn't an efficient method to transfer out the angular momentum, the orbits remain quite wide. The multiplicity frequency as seen in Sub-figure 9.15d is slightly flatter for the ring cluster, reflecting the fact that low mass stars have a greater opportunity to form part of a multiple system. The plots of M_1 against M_2 as seen in Subfigure 8.5e show that the distribution does not change with a ring cluster. The effects of disks on the distributions are the same as discussed in Section 9.2. Note that as the stars are placed taking up an arc proportional to their mass, the separation between stars is greater than the size of the disks.

The properties of triple systems are shown in Figure 9.16. As seen in Sub-figure 9.16a, more high-eccentricity orbits are produced by the ring cluster for the inner orbits than the fiducial model, similar to the pure binaries. The ring cluster produced far fewer low mass ratio outer orbits, as can be seen in Sub-figure 9.16b. It can be observed that mass ratios of up to 2.5 are populated, meaning that occasionally the outer star is more massive than the combined masses

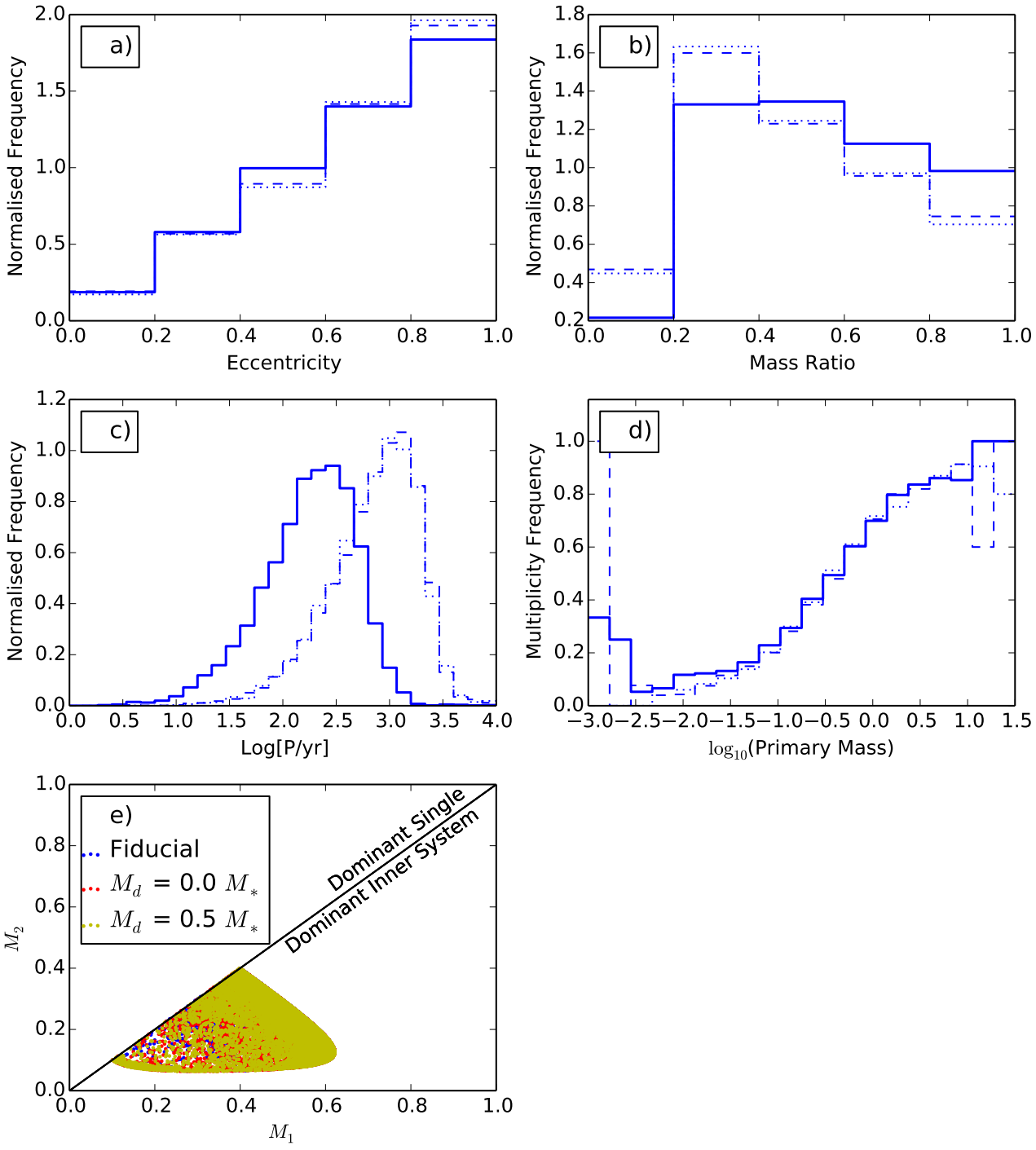

Figure 9.15: The variation of binary properties formed in ring clusters. The solid/dotted/dashed lines in each of the Frames describes the distributions attained for the fiducial model, ring cluster, and ring cluster with disks respectively. Frame a) shows the normalised distribution of eccentricities, Frame b) shows the normalised distribution of mass ratios, Frame c) shows the normalised distribution of periods [yr] and Frame d) shows the multiplicity frequency as a function of primary mass, and Frame e) plots M_2 against M_1. 6065, 8491, 8412 binary systems are plotted for the fiducial model, ring cluster and ring cluster with disks respectively.

Table 9.11: Mean and standard deviation of $\log_{10}(P/\mathrm{yr})$

Ring			
	Binaries	Triples	
		Inner	Outer
Fiducial	2.244±0.475	2.300±0.425	4.487±1.049
$M_d = 0.0\ M_*$	2.896±0.550	2.794±0.435	5.049±1.002
$M_d = 0.5\ M_*$	2.898±0.549	2.784±0.429	5.025±0.976

Table 9.12: Mean and standard deviation of $\log_{10}(P/\mathrm{yr})$

Ring					
	Quad, Hierarchical			Quad, Double	
	Inner	Mid	Outer	Inner	Outer
Fiducial	2.517±0.322	4.739±1.017	7.342±0.829	3.264±1.211	4.748±1.048
$M_d = 0.0\ M_*$	2.754±0.459	5.105±0.815	7.127±0.544	3.912±1.291	5.474±1.002
$M_d = 0.5\ M_*$	2.929±0.345	5.354±0.874	7.117±0.631	3.869±1.332	5.457±1.060

of the pair of inner stars that it orbits. This occurs when two small stars are placed next to each other in the initial ring. Due to their proximity, they form a small binary, which is then bound to a larger star in the cluster. The period distributions as shown in Sub-figure 9.16c and Table 9.11 show that the mean of the period increases for both the outer and inner orbits when the stars are placed in a ring cluster. In Sub-figure 8.6d M_2 is plotted against M_1, and in Sub-figure 8.6d M_3 is plotted against $M_2 + M_1$. Neither distribution changes with the ring cluster.

The properties of hierarchical quadruples are shown in Figure 9.17. Due to low number statistics, there are no discernible trends in the eccentricity distributions (see Sub-figure 9.17a). The fraction of low mass-ratio systems decreases for both the mid and outer orbits, as shown in Sub-figure 9.17b, whilst the mass ratio distribution for the inner pairs becomes flatter. The mean of both the inner- and mid- orbits increase in period with the ring cluster (See Sub-figure 9.17 c and Table 9.12). However the mean of the outer-period remains unaffected. In Sub-figure 8.7d M_2 is plotted against M_1, in Sub-figure 8.7e M_3 is plotted against $M_2 + M_1$ and in Sub-figure 8.7f M_4 is plotted against $M_3 + M_2 + M_1$, no plot chows any change with the ring cluster.

The properties of double quadruples are shown in Figure 9.18. Fewer high-eccentricity outer orbits are produced than for the fiducial model (see Sub-figure 9.18a), and more high-eccentricity inner orbits are produced. The reduction of the fraction of high-eccentricity outer orbits can be explained as follows. Binaries are often formed with stars that were initially placed

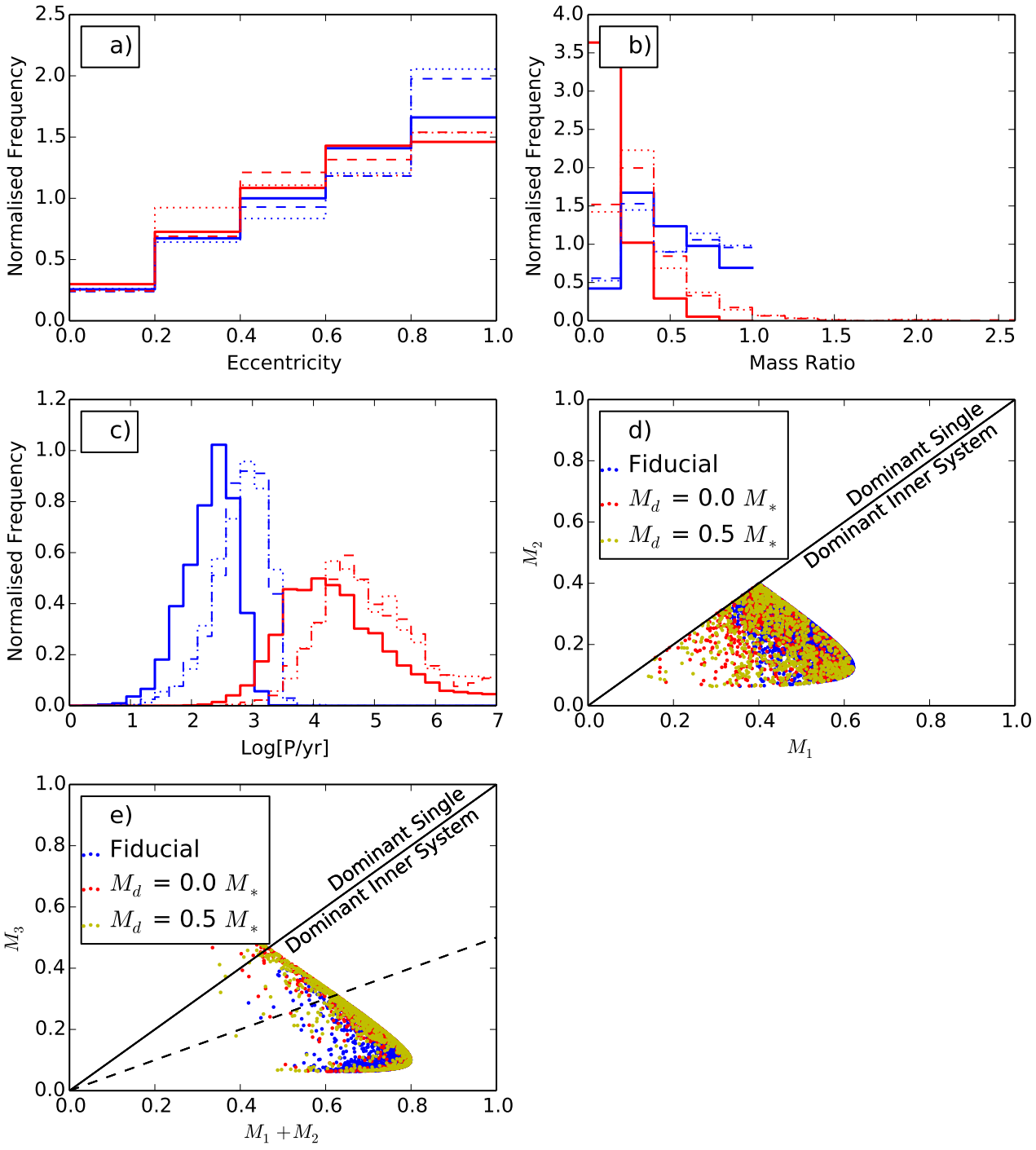

Figure 9.16: The variation of properties of triples formed in ring clusters. The solid/dotted/dashed lines in each of the Frames describes the distributions attained for the fiducial model, ring cluster, and ring cluster with disks respectively. The blue lines show the inner periods, whilst the red lines show the outer periods. Frame a) shows the normalised distribution of eccentricities, Frame b) shows the normalised distribution of mass ratios and Frame c) shows the normalised distribution of periods [yr]. Frame d) plots M_2 against M_1, whilst Frame e) plots M_3 against $M_2 + M_1$. 2725, 1012, 1007 triple systems are plotted for the fiducial model, ring cluster and ring cluster with disks respectively.

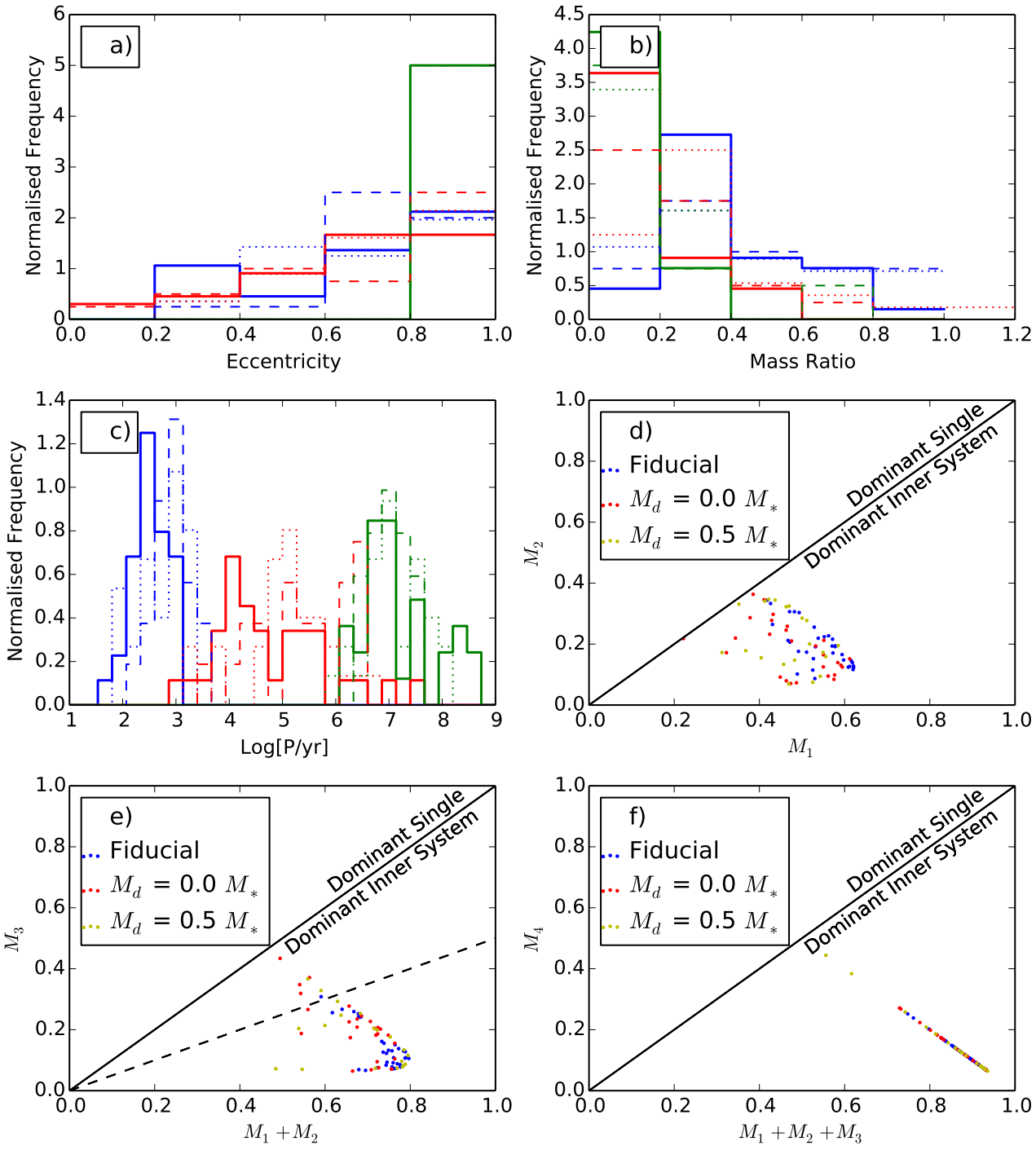

Figure 9.17: The variation of properties of hierarchical quadruples formed in ring clusters. The solid/dotted/dashed lines in each of the Frames describes the distributions attained for the fiducial model, ring cluster, and ring cluster with disks respectively. The blue lines show the inner periods, the red lines show the mid periods and the green lines show the outer periods. Frame a) shows the normalised distribution of eccentricities, Frame b) shows the normalised distribution of mass ratios and Frame c) shows the normalised distribution of periods [yr]. Frame d) plots M_2 against M_1, whilst Frame e) plots M_3 against $M_2 + M_1$, and Frame f) plots M_4 against $M_3 + M_2 + M_1$. 33, 28, 20 hierarchical quadruple systems are plotted for the fiducial model, ring cluster and ring cluster with disks respectively.

side by side in the ring. Double quadruples are two of these pairs orbiting each other. As there are only four stars in a ring, the centres of mass of the two pairs are likely to be on opposite sides of the circle. The initial velocity of these centres of mass will therefore be approximately perpendicular to the position vector between the two centres of mass, a favourable condition for producing low-eccentricity orbits. The inner pairs have a larger fraction of highly eccentric orbits for the same reason as given for the binaries (see beginning of this section). As seen in Sub-figure 9.18b, the inner mass ratio distribution is flatter than the fiducial, whilst the outer mass ratio distribution has a larger high mass ratio fraction. Sub-figure 9.18c and Table 9.12 show that the mean of the period increases with the ring cluster for both the inner and the outer orbits. In Sub-figure 8.8d, M_2 is plotted against M_1 and M_4 is plotted against M_3. In Sub-figure 8.8e $M_4 + M_3$ is plotted against $M_2 + M_1$. No changes are seen with the ring cluster.

The period against eccentricity plots for binaries, triples, hierarchical quadruples and double quadruples are shown in Figures 9.19, 9.20, 9.21 and 9.22 respectively. Figure 9.19 shows that more high-eccentricity, long-period systems are produced in the ring cluster compared to the fiducial model, and the whole distribution is shifted to longer periods. The distribution for triple systems and hierarchical systems are unaffected by the change in cluster type. Double quadruple systems have outer orbits that not only populate the low eccentricities more than the fiducial, but their fidelity is also much higher.

Table 9.13 shows that the ring cluster produces more binaries than the fiducial model, but also that fewer triples are produced.

Table 9.13: Average number of multiple systems produced per core.

Ring	Binaries	Triples	Hierarchical Quadruples	Double Quadruples
Fiducial	0.6799	0.3055	0.0037	0.0185
$M_d = 0.0\ M_*$	0.9314	0.1110	0.0031	0.0193
$M_d = 0.5\ M_*$	0.9289	0.1112	0.0022	0.0169

With the requirement that the KS test must be rejected at the 1% level for both the Ring cluster and Ring cluster with disks for a given property, we can say that the eccentricities for the binaries, inner triples and double quadruples (inner and outer), the mass ratio distributions for the binaries and triples (inner and outer), and period distributions for the binaries, triples (inner and outer), inner hierarchical quadruples and double quadruples (inner and outer) change with the ring cluster with reasonable confidence (See Table 9.14). The period of the binaries and possibly the mass ratio distributions could be detected observationally.

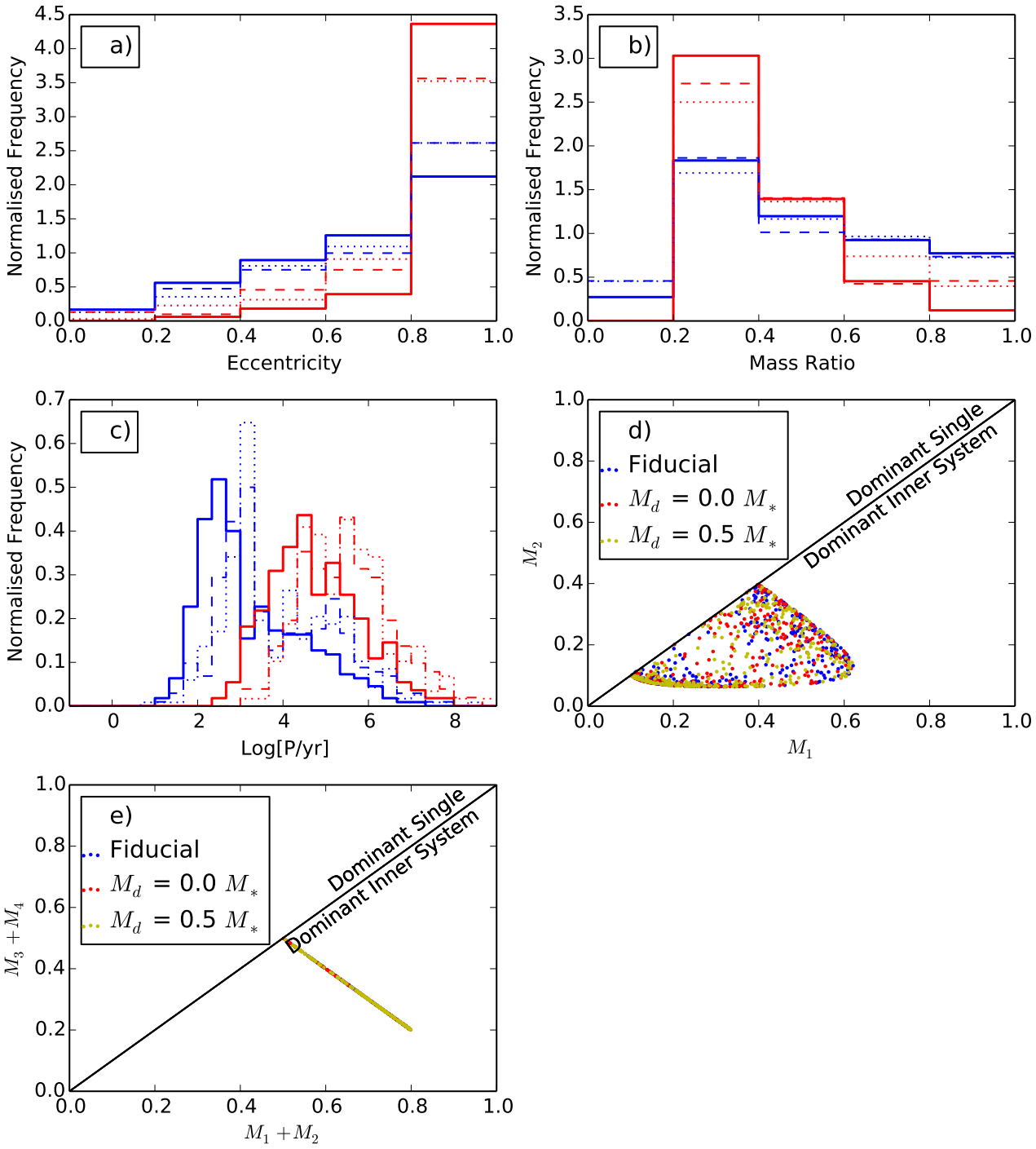

Figure 9.18: The variation of properties of double quadruples formed in ring clusters. The solid/dotted/dashed lines in each of the Frames describes the distributions attained for the fiducial model, ring cluster, and ring cluster with disks respectively. The blue lines show the inner periods, whilst the red lines show the outer periods. Frame a) shows the normalised distribution of eccentricities, Frame b) shows the normalised distribution of mass ratios and Frame c) shows the normalised distribution of periods [yr]. Frame d) plots M_2 against M_1 and M_4 against M_3, and Frame e) plots $M_4 + M_3$ against $M_2 + M_1$. 165, 176, 153 double quadruple systems are plotted for the fiducial model, ring cluster and ring cluster with disks respectively.

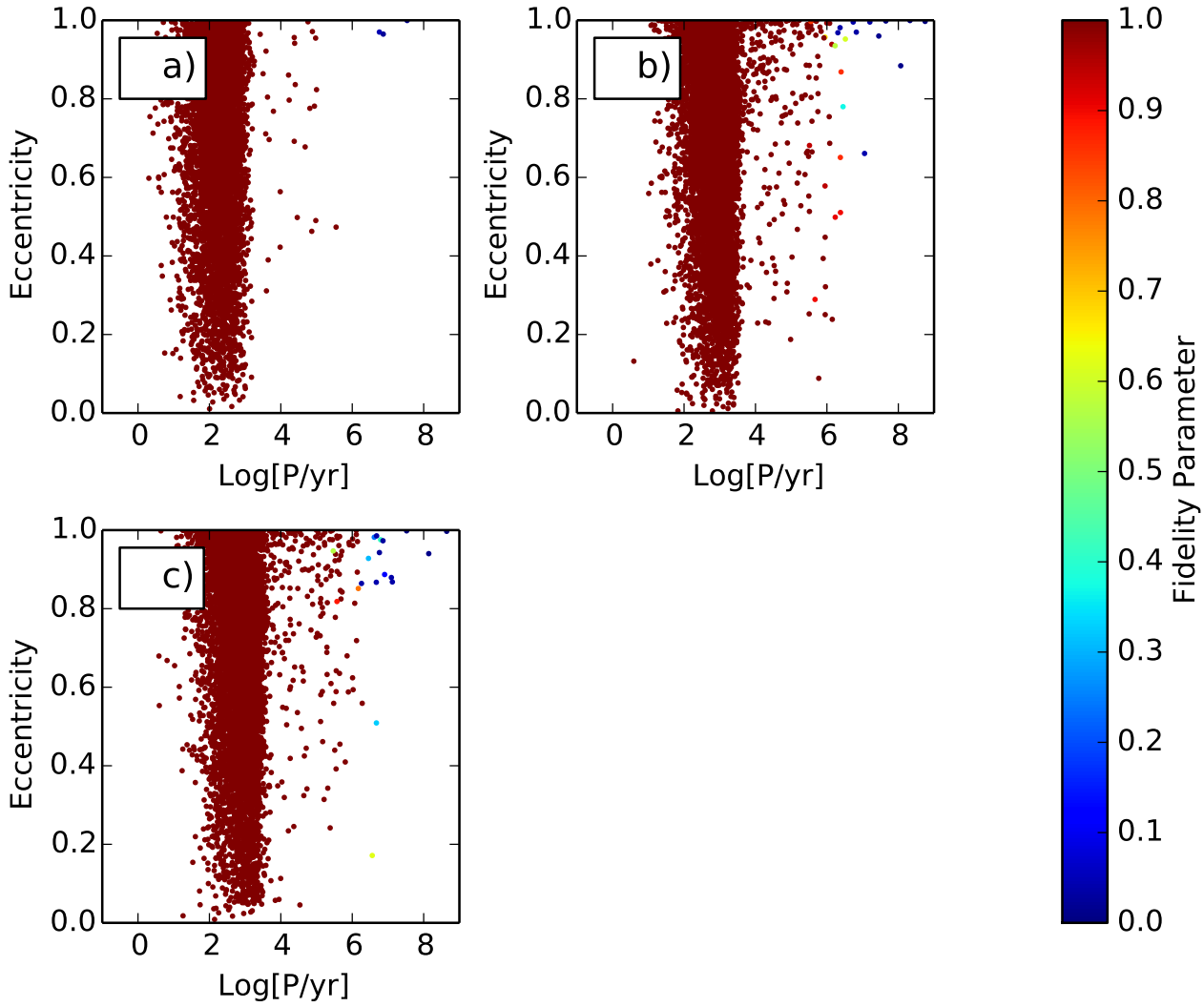

Figure 9.19: The distribution of binary systems in the $(\log_{10}(P/\mathrm{yr}), \mathrm{e})$-plane. The colour of the points encodes the fidelity parameter. Frame a) corresponds to the fiducial model, b) ring cluster, and c) ring cluster with disks. 6065, 8491, 8412 binary systems are plotted for the fiducial model, ring cluster and ring cluster with disks respectively.

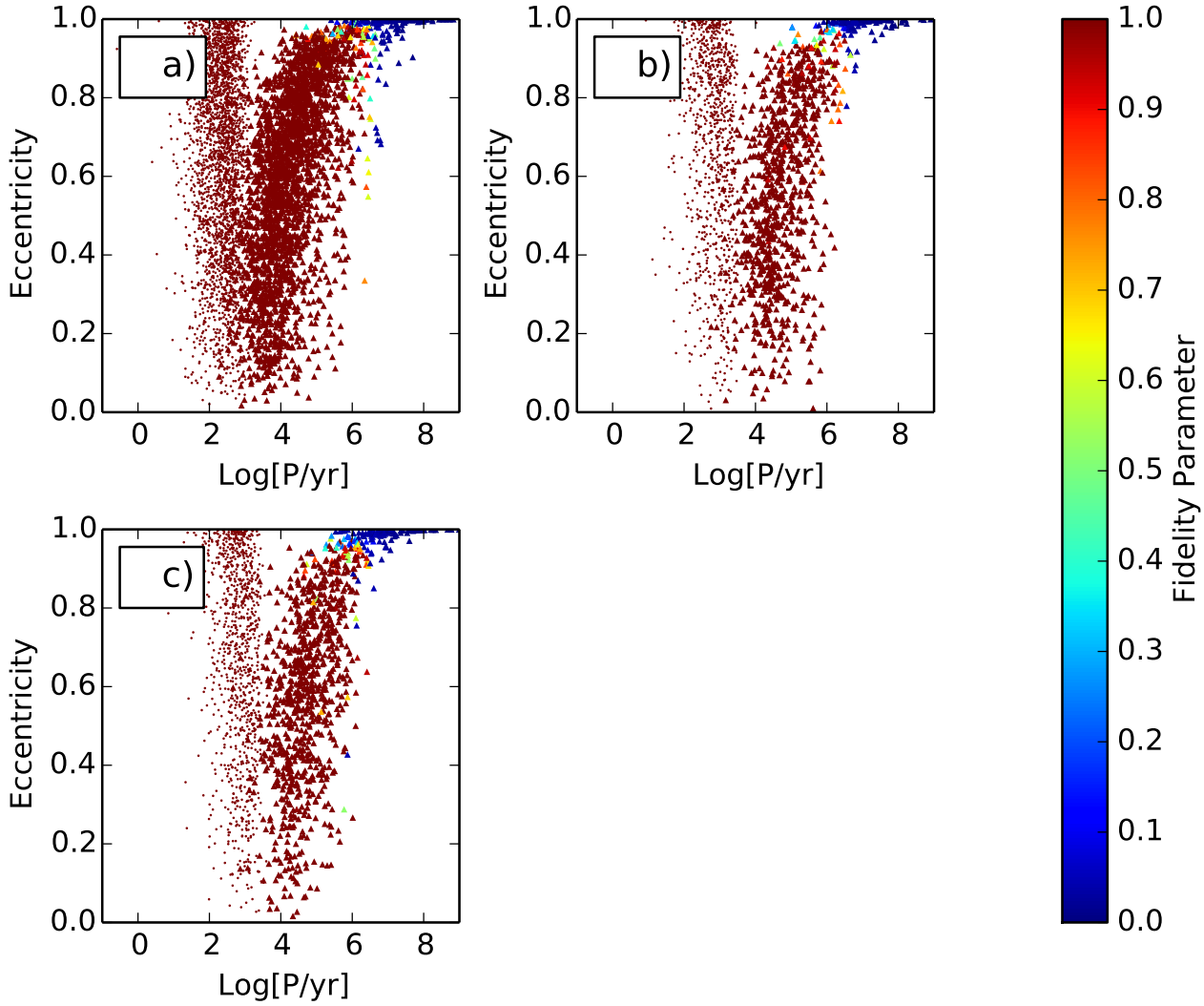

Figure 9.20: The distribution of triple systems in the $(\log_{10}(P/\mathrm{yr}), \mathrm{e})$-plane. Small circles represent inner orbits, and triangles represent outer orbits. The colour of the points encodes the fidelity parameter. Frame a) corresponds to the fiducial model, b) ring cluster, and c) ring cluster with disks. 2725, 1012, 1007 triple systems are plotted for the fiducial model, ring cluster and ring cluster with disks respectively.

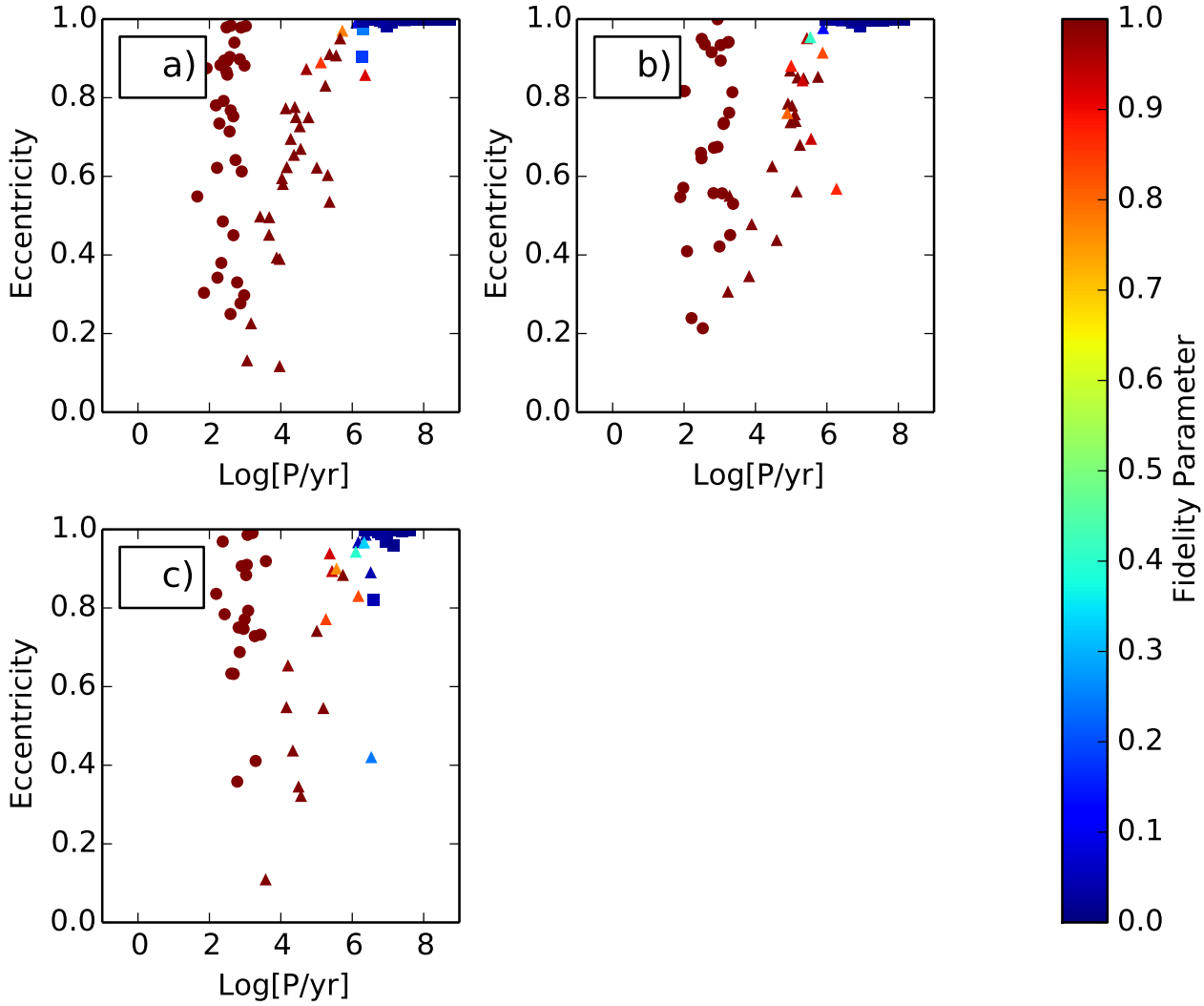

Figure 9.21: The distribution of hierarchical quadruple systems in the $(\log_{10}(P/\mathrm{yr}), \mathrm{e})$-plane. Circles represent inner orbits, triangles represent mid orbits and squares represent outer orbits. The colour of the points encodes the fidelity parameter. Frame a) corresponds to the fiducial model, b) ring cluster, and c) ring cluster with disks. 33, 28, 20 hierarchical quadruple systems are plotted for the fiducial model, ring cluster and ring cluster with disks respectively.

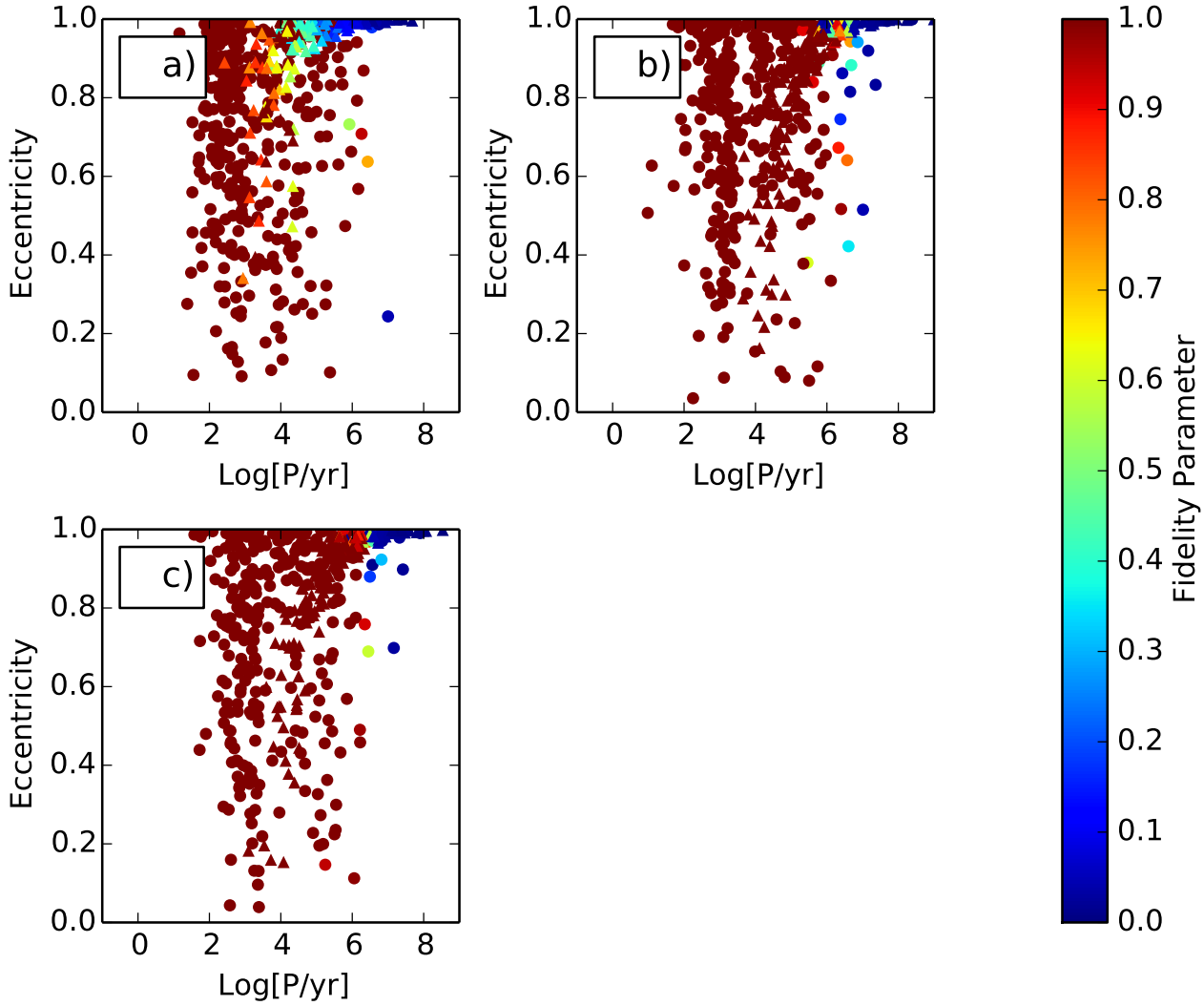

Figure 9.22: The distribution of double quadruple systems in the $(\log_{10}(P/\mathrm{yr}), \mathrm{e})$-plane. Circles represent inner orbits and triangles represent outer orbits. The colour of the points encodes the fidelity parameter. Frame a) corresponds to the fiducial model, b) ring cluster, and c) ring cluster with disks. 165, 176, 153 double quadruples are plotted for the fiducial model, ring cluster and ring cluster with disks respectively.

Table 9.14: This table shows the eccentricity, mass ratio and period distributions that for which the null hypothesis can be rejected at the 1% level, as determined by the K-S test for the Ring cluster.

Ring	System Type	Eccentricity	Mass Ratio	Period
Ring	Binaries	✓	✓	✓
Ring + Disks	Binaries	✓	✓	✓
Ring	Triples inner	✓	✓	✓
Ring + Disks	Triples inner	✓	✓	✓
Ring	Triples outer		✓	✓
Ring + Disks	Triples outer		✓	✓
Ring	Hierarchical Quadruples inner			✓
Ring + Disks	Hierarchical Quadruples inner			✓
Ring	Hierarchical Quadruples mid		✓	
Ring + Disks	Hierarchical Quadruples mid			
Ring	Hierarchical Quadruples outer			
Ring + Disks	Hierarchical Quadruples outer	✓		
Ring	Double Quadruples inner	✓		✓
Ring + Disks	Double Quadruples inner	✓		✓
Ring	Double Quadruples outer	✓		✓
Ring + Disks	Double Quadruples outer	✓		✓

9.4 Line Cluster with Disks

In this section I present the results of setting the initial positions of stars along a line, and then adding disks. I run 8920, 9642, 5911 simulations for the fiducial model, a line cluster and a line cluster with disks of mass $d_m = 0.5$ respectively. Fewer simulations for the line cluster with disks are run due to the increased computational time required. These sets of simulations produce 6065, 8293, 5248 binaries, and 2725, 1485, 928 triples, 33, 11, 7 hierarchical quadruples and 165, 123, 69 double quadruples for the fiducial model, the line cluster and the line cluster with disks respectively.

The properties of binaries produced are given in Figure 9.23. There are fewer high-eccentricity binaries for the line cluster than the fiducial model (see Sub-figure 9.23a). The line cluster configuration increases the fraction of low mass-ratio binaries, and adding disks increases it further (see Sub-figure 9.23b). The mean of the period as seen in Sub-figure 9.23c and Table 9.15 decreases very slightly with the line cluster, and again when adding disks, whilst the multiplicity frequency as seen in Sub-figure 9.23d shows that the smaller stars are more likely to be primaries, and larger stars are more likely to be singles in the line cluster. These effects can be explained by considering the initial configuration of the system. The stars are placed along a line, taking up a length proportional to its mass. Smaller stars take up only a short length, so lie closer to its neighbours than more massive stars. This proximity, especially between two smaller mass stars, means that they are more likely to form a binary system than in the fiducial model. The more random choice of component means that there is a higher fraction of binaries with a low mass ratio. As the stars start off closer, the binary systems are also more likely to have a smaller period as well. The eccentricities of the binaries tend to be more circular than the fiducial model because the stars are assigned initial velocities that are perpendicular to the position-vector between the two stars. The cross product, and therefore the angular momentum is then very high. From Equation 6.11, we can see that this would lead to a small eccentricity of the system. The graph of M_1 against M_2 is plotted in Sub-figure 8.5e. There is no change in the distributions with the lines cluster. The effect of disks on the distributions are the same as discussed in Section 9.2.

Table 9.15: Mean and standard deviation of $\log_{10}(P/\mathrm{yr})$

Line			
	Binaries	Triples	
		Inner	Outer
Fiducial	2.236±0.487	2.292±0.434	4.479±1.040
$M_d = 0.0M_*$	2.172±0.514	2.169±0.397	4.253±0.987
$M_d = 0.5M_*$	2.118±0.528	2.070±0.448	4.103±0.957

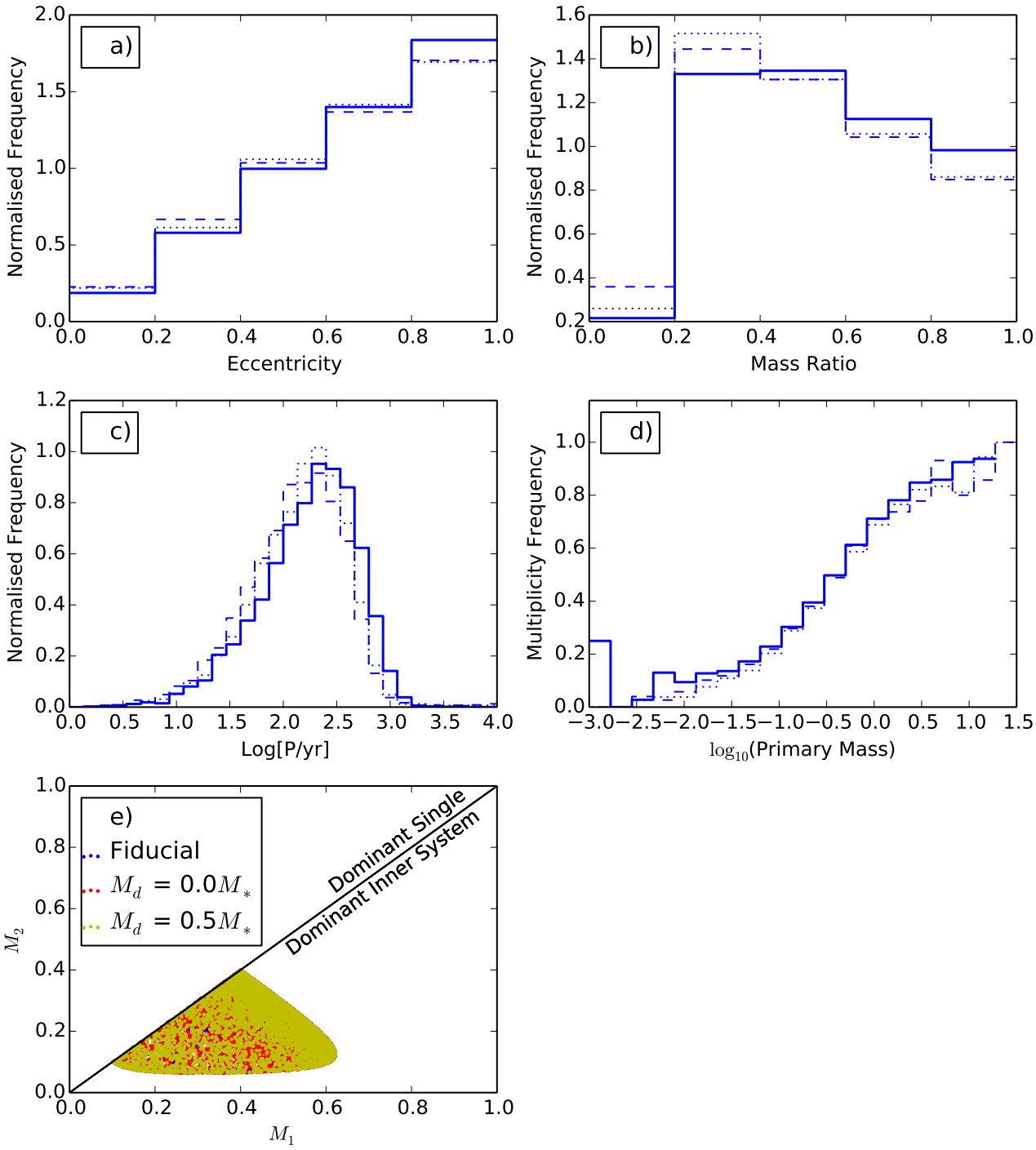

Figure 9.23: The variation of binary properties formed in line clusters. The solid/dotted/dashed lines in each of the Frames describes the distributions attained for the fiducial model, line cluster, and line cluster with disks respectively. Frame a) shows the normalised distribution of eccentricities, Frame b) shows the normalised distribution of mass ratios, Frame c) shows the normalised distribution of periods [yr] and Frame d) shows the multiplicity frequency as a function of primary mass, and Frame e) plots M_2 against M_1. 6065, 8293, 5248 binary systems are plotted for the fiducial model, the line cluster and the line cluster with disks respectively.

Table 9.16: Mean and standard deviation of $\log_{10}(P/\mathrm{yr})$

Line					
	Quad, Hierarchical			Quad, Double	
	Inner	Mid	Outer	Inner	Outer
Fiducial	2.491±0.299	4.713±0.877	7.316±0.780	3.231±1.226	4.715±1.065
$M_d = 0.0M_*$	2.112±0.499	4.280±1.006	6.943±0.516	3.025±1.281	4.452±1.143
$M_d = 0.5M_*$	1.913±0.567	4.015±0.740	7.542±1.115	2.994±1.314	4.463±1.142

The properties of triple systems are shown in Figure 9.24. The eccentricity distribution as seen in Sub-figure 9.24a is flatter for the outer orbits of the triple systems formed in the line cluster than those in the fiducial model. The mass ratio distribution in Sub-figure 9.24b has a much lower fraction of low mass ratios for outer orbits, and has a high mass ratio tail, where the outer star is larger than the mass of the inner pair. This occurs when two low mass stars are placed side by side in the line. Because they take up a length proportional to their mass, they are placed very close to one another and form a tight binary. This binary can then be bound to a larger star nearby. The mean of the period decreases with the line cluster (Sub-figure 9.24c and Table 9.15) for both inner and outer orbits. In Sub-figure 8.6d M_2 is plotted against M_1, and in Sub-figure 8.6d M_3 is plotted against $M_2 + M_1$.

Due to low number statistics, it is difficult to discern any trend for how any of the properties of hierarchical quadruples change with the line cluster.

The properties of double quadruples are shown in Figure 9.25. Sub-figure 9.25a shows that the line cluster produces fewer high-eccentricity systems, both for inner and outer orbits. The inner mass ratio distribution as shown in Sub-figure 9.25b becomes flatter, whilst there are fewer low mass ratio outer orbits. Double quadruples tend to be created in the line cluster when the two larger stars each pair up with a smaller star to form two binaries that are then similar in mass. This occurs when the two smaller stars are placed on the ends of the line cluster, and the two larger stars in the middle. Sub-figure 9.25c and Table 9.16 show that the means of the periods decrease with the line cluster, and the standard deviation increases. In Sub-figure 8.8d, M_2 is plotted against M_1 and M_4 is plotted against M_3. In Sub-figure 8.8e $M_4 + M_3$ is plotted against $M_2 + M_1$.

Figures 9.26, 9.27, 9.28 and 9.29 shows the period against eccentricity plot for binaries, triples, hierarchical quadruples and double quadruples respectively. There is little difference between the distributions of any of the system types.

The average number of binaries produced per core increases for the line cluster, whilst the number of higher-order multiples decreases.

With the requirement that the KS test must be rejected at the 1% level for both the Ring

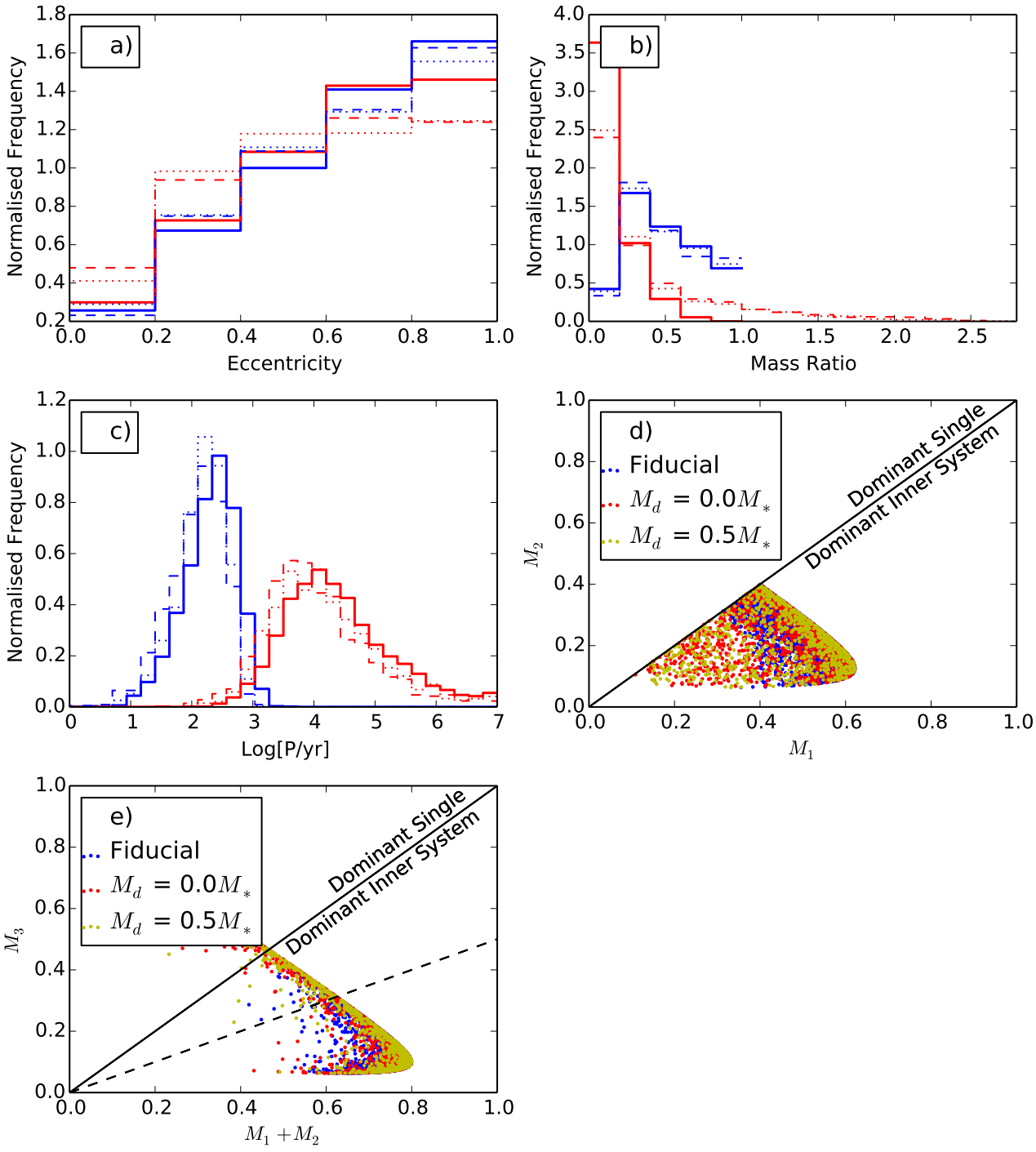

Figure 9.24: The variation of properties of triples formed in line clusters. The solid/dotted/dashed lines in each of the Frames describes the distributions attained for the fiducial model, line cluster, and line cluster with disks respectively. The blue lines show the inner periods, whilst the red lines show the outer periods. Frame a) shows the normalised distribution of eccentricities, Frame b) shows the normalised distribution of mass ratios and Frame c) shows the normalised distribution of periods [yr]. Frame d) plots M_2 against M_1, whilst Frame e) plots M_3 against $M_2 + M_1$. 2725, 1485, 928 triple systems are plotted for the fiducial model, the line cluster and the line cluster with disks respectively.

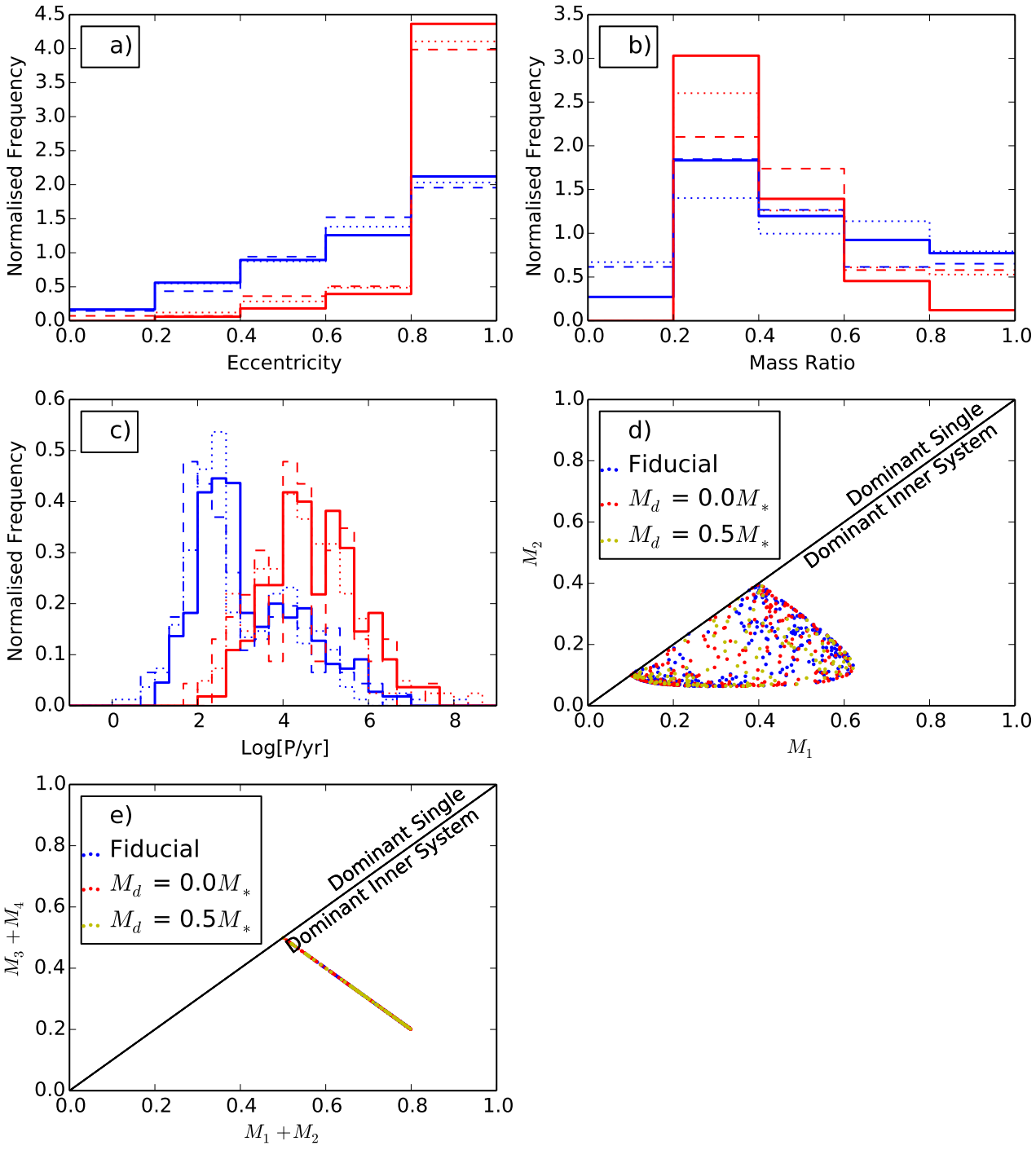

Figure 9.25: The variation of properties of double quadruples formed in line clusters. The solid/dotted/dashed lines in each of the Frames describes the distributions attained for the fiducial model, line cluster, and line cluster with disks respectively. The blue lines show the inner periods, whilst the red lines show the outer periods. Frame a) shows the normalised distribution of eccentricities, Frame b) shows the normalised distribution of mass ratios and Frame c) shows the normalised distribution of periods [yr]. Frame d) plots M_2 against M_1 and M_4 against M_3, and Frame e) plots $M_4 + M_3$ against $M_2 + M_1$. 165, 123, 69 double quadruples are plotted for the fiducial model, the line cluster and the line cluster with disks respectively.

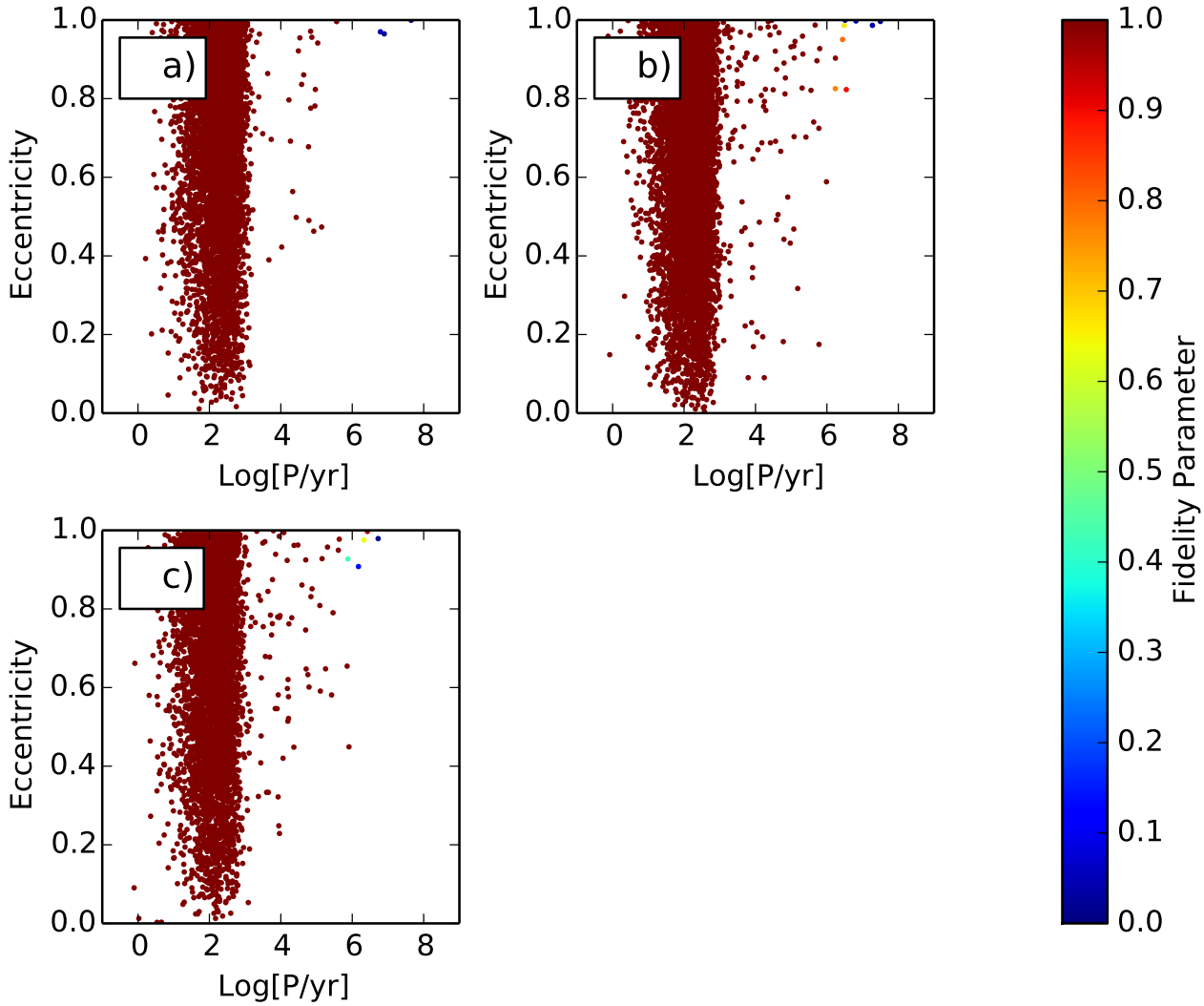

Figure 9.26: The distribution of binary systems in the $(\log_{10}(P/\mathrm{yr}), \mathrm{e})$-plane. The colour of the points encodes the fidelity parameter. Frame a) corresponds to the fiducial model, b) line cluster, and c) line cluster with disks. 6065, 8293, 5248 binary systems are plotted for the fiducial model, the line cluster and the line cluster with disks respectively.

Table 9.17: Average number of multiple systems produced per core.

Line	Binaries	Triples	Hierarchical Quadruples	Double Quadruples
Fiducial	0.6799	0.3055	0.0037	0.0185
$M_d = 0.0 M_*$	0.8601	0.1540	0.0011	0.0128
$M_d = 0.5 M_*$	0.8878	0.1570	0.0012	0.0117

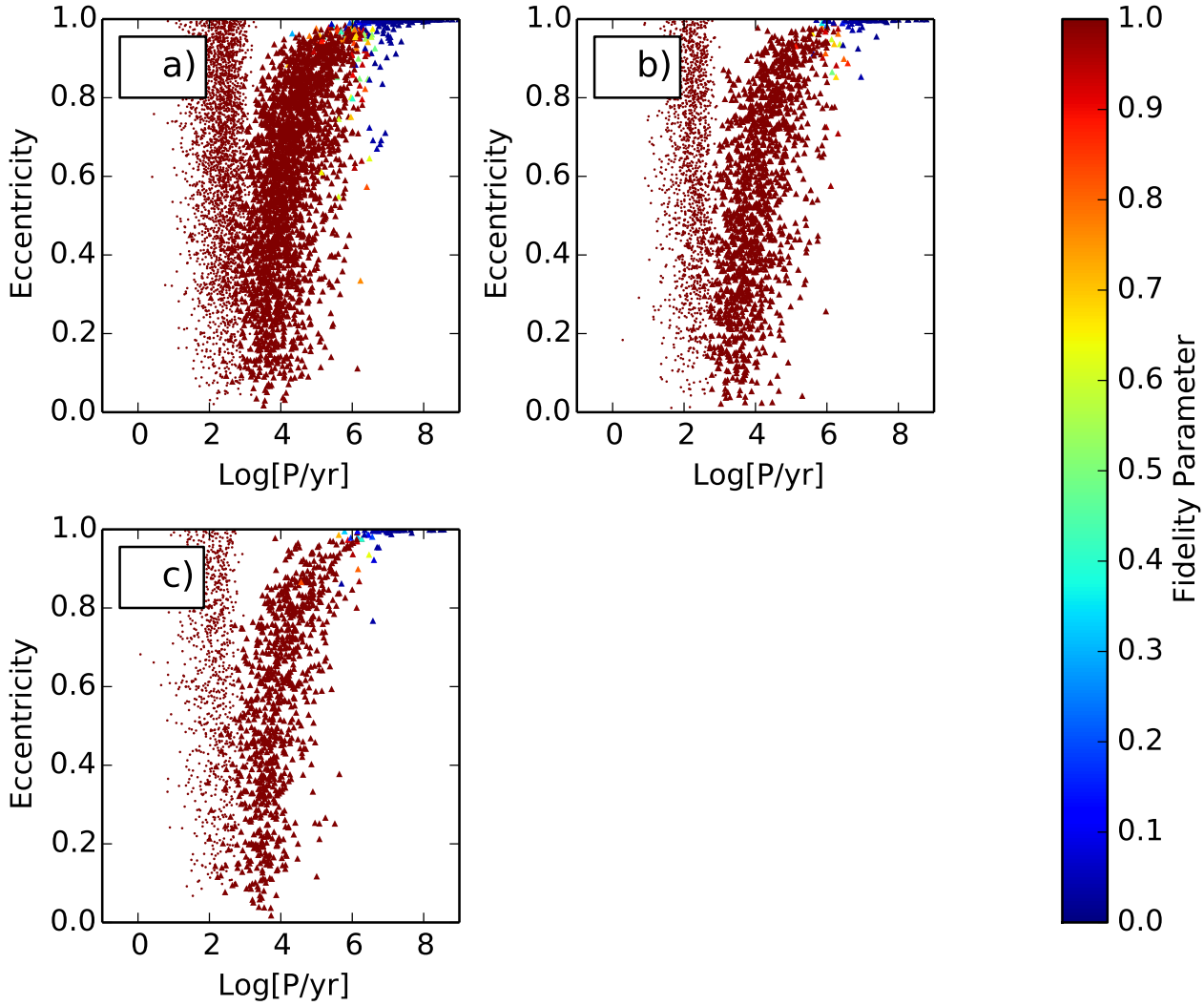

Figure 9.27: The distribution of triple systems in the $(\log_{10}(P/\mathrm{yr}), \mathrm{e})$-plane. Small circles represent inner orbits and triangles represent outer orbits. The colour of the points encodes the fidelity parameter. Frame a) corresponds to the fiducial model, b) line cluster, and c) line cluster with disks. 2725, 1485, 928 triple systems are plotted for the fiducial model, the line cluster and the line cluster with disks respectively.

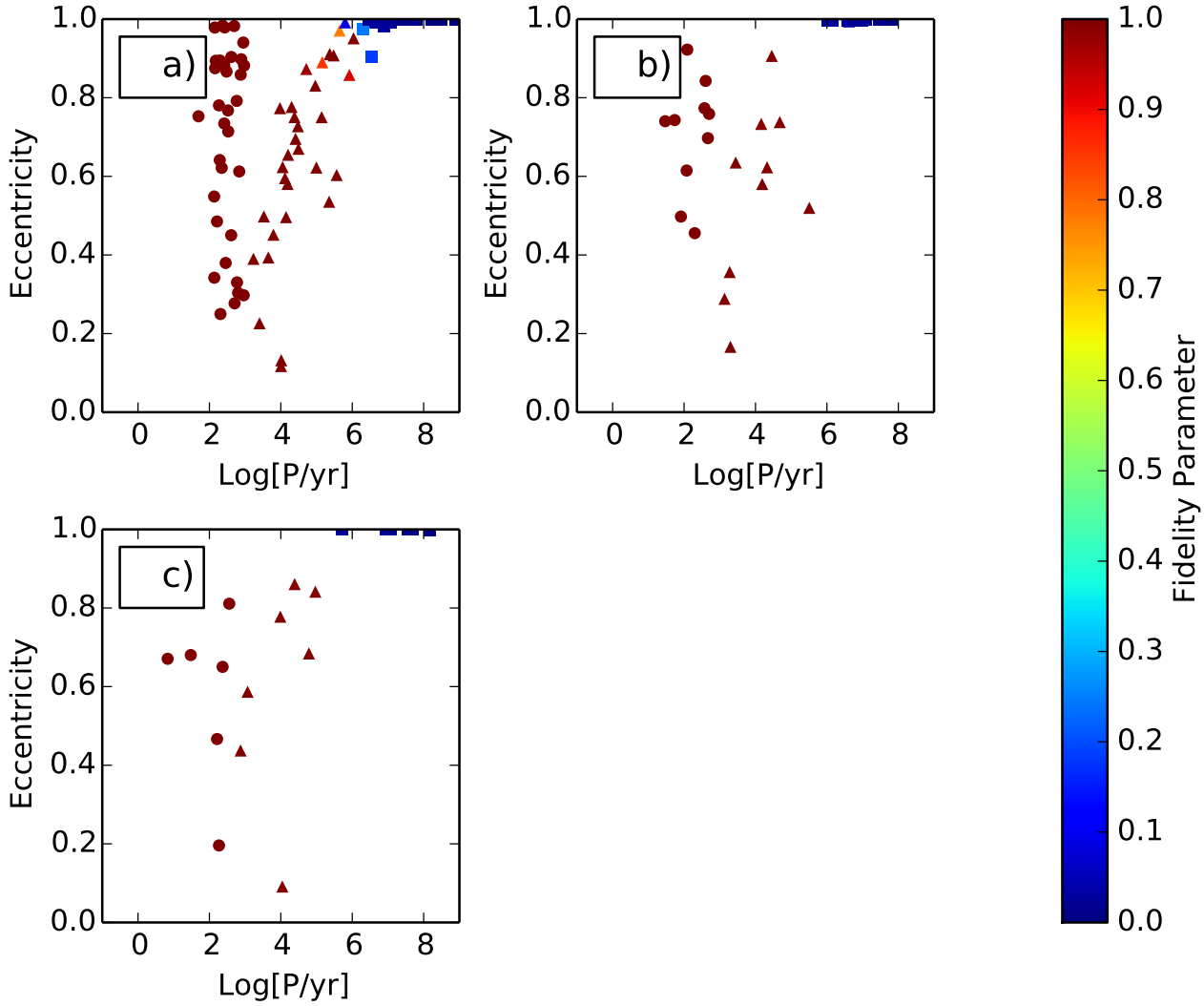

Figure 9.28: The distribution of hierarchical quadruple systems in the $(\log_{10}(P/\mathrm{yr}), \mathrm{e})$-plane. Circles represent inner orbits, triangles represent mid orbits and squares represent outer orbits. The colour of the points encodes the fidelity parameter. Frame a) corresponds to the fiducial model, b) line cluster, and c) line cluster with disks. 33, 11, 7 hierarchical quadruple systems are plotted for the fiducial model, the line cluster and the line cluster with disks respectively.

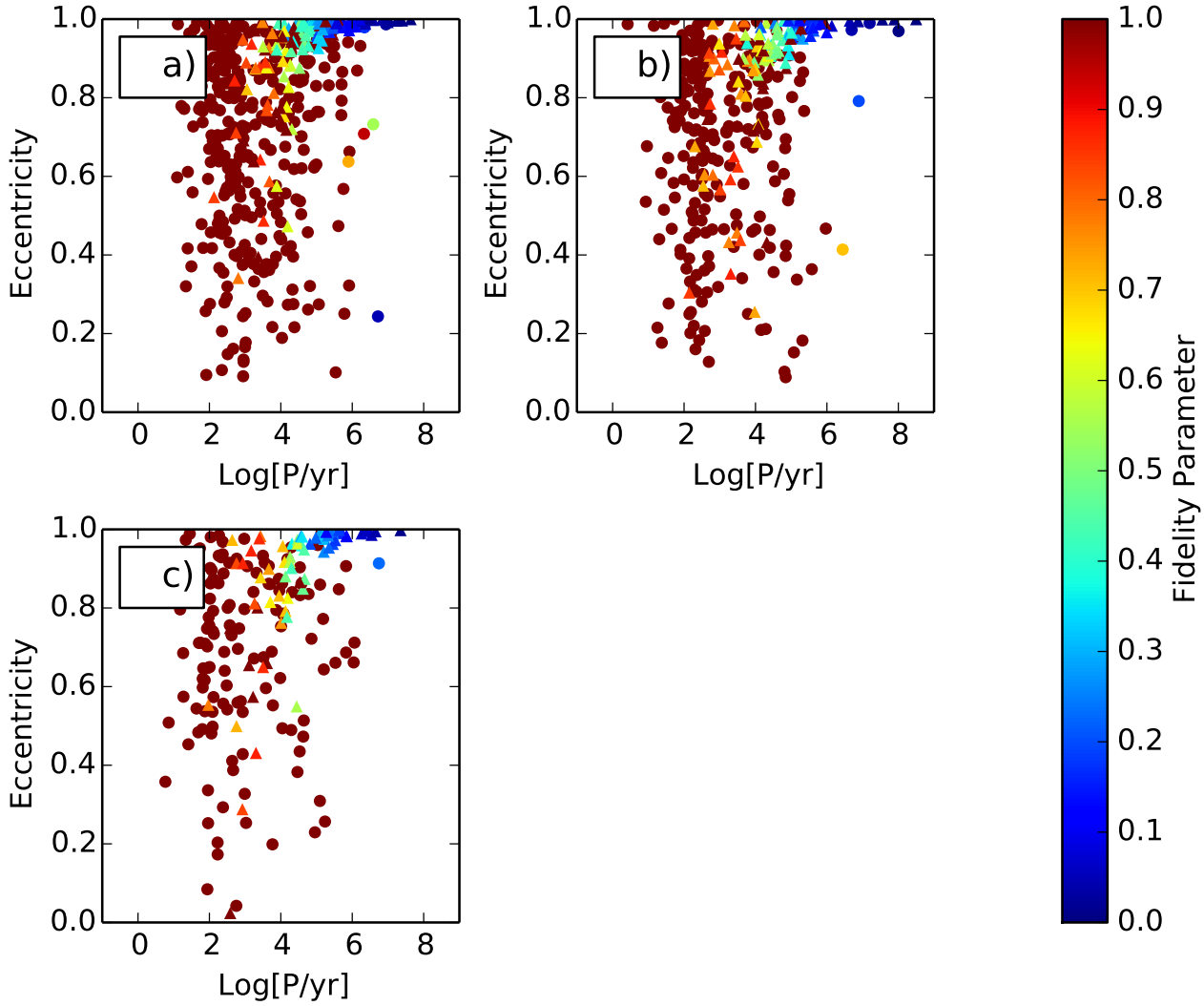

Figure 9.29: The distribution of double quadruple systems in the $(\log_{10}(P/\mathrm{yr}), \mathrm{e})$-plane. Circles represent inner orbits, and triangles represent outer orbits. The colour of the points encodes the fidelity parameter. Frame a) corresponds to the fiducial model, b) line cluster, and c) line cluster with disks. 165, 123, 69 double quadruple systems are plotted for the fiducial model, the line cluster and the line cluster with disks respectively.

Table 9.18: This table shows the eccentricity, mass ratio and period distributions that for which the null hypothesis can be rejected at the 1% level, as determined by the K-S test for the line cluster.

Line	System Type	Eccentricity	Mass Ratio	Period
Line	Binaries	✓	✓	✓
Line + Disks	Binaries	✓	✓	✓
Line	Triples inner			✓
Line + Disks	Triples inner			✓
Line	Triples outer	✓	✓	✓
Line + Disks	Triples outer	✓	✓	✓
Line	Hierarchical Quadruples inner			
Line + Disks	Hierarchical Quadruples inner			✓
Line	Hierarchical Quadruples mid			
Line + Disks	Hierarchical Quadruples mid			
Line	Hierarchical Quadruples outer			
Line + Disks	Hierarchical Quadruples outer			
Line	Double Quadruples inner			✓
Line + Disks	Double Quadruples inner			✓
Line	Double Quadruples outer	✓		
Line + Disks	Double Quadruples outer			

cluster and Ring cluster with disks for a given property, we can say that the eccentricities for the binaries and outer triples, mass ratios for the binaries and outer triples, and periods for the binaries, triples (inner and outer) and inner period of the double quadruples change with the Ring cluster with reasonable confidence (See Table 9.14). However, these distributions are unlikely to be distinguished between observationally.

9.5 Background Potential

In this section I present the results of introducing a background potential (See Table 5.2). I present the results of changing t_p. I run 8920, 7608, 9300, 9663, 3481 simulations for $t_p = 0$, 10, 30, 100, and 300 respectively. These sets of simulations produce 6065, 4014, 5416, 7176, 3071 binaries, 2725, 3131, 3353, 2042, 247 triples, 33, 85, 91, 10, 0 hierarchical quadruples and 165, 23, 3, 3, 0 double quadruples for $t_p = 0$, 10, 30, 100 and 300 respectively.

The properties of the binaries are shown in Figure 9.30. The eccentricity distributions of the binaries in all cases are approximately thermal (see Sub-figure 9.30a). There are more equal-mass binaries as t_p is increased, as can be seen in Sub-figure 9.30b. The Plummer background potential serves to compact the binary systems, reducing the mean of the periods further as the longevity of the Plummer background potential increases. The standard deviation of the periods also decrease, as long period binaries are suppressed (see Sub-figure 9.30c and Table 9.20). The multiplicity frequency in Sub-figure 9.30d becomes a little steeper as t_p increases because the core-cluster is kept from dissolving for a time by the prolonged Plummer background potential. This extra time allows the two most massive stars a greater opportunity to form the basis of a multiple system. These two stars will be more equal in mass than a more random pairing, explaining the increase in the proportion of high mass ratio binaries (see Sub-figure 9.30b). The graph of M_1 against M_2 is plotted in Sub-figure 8.5 e, again there is no change with t_p.

Table 9.19: Percentage of cores producing systems involving the most massive stars

Time	Most massive star	Two most massive stars
Fiducial	0.96	0.77
$t_p = 10$	0.91	0.77
$t_p = 30$	0.91	0.77
$t_p = 100$	0.92	0.78
$t_p = 300$	0.92	0.76

The properties of the triple systems produced are shown in Figure 9.31. t_p has a strong affect on the eccentricities of the triple systems (Sub-figure 9.31a). As t_p increases, the peak of the eccentricity distribution of the outer orbits moves towards smaller eccentricities. This is because as t_p increases, the Plummer background potential has time to compact the outer orbits further. As the outer star of a system with an eccentric orbit passes close to the inner pair, and is likely to be disrupted, meaning that the high eccentricity systems are more unstable. The eccentricities of the inner orbits however remain roughly thermal, as for the pure binaries. There are fewer low mass ratio outer orbits as seen in Sub-figure 9.31b as t_p increases, i.e. the binary is orbited by a larger star in comparison to the inner pair. The inner mass ratios are less affected by the presence of the Plummer background potential. The means of the period

Table 9.20: Mean and standard deviation of $\log_{10}(P/\mathrm{yr})$

Time			
	Binaries	Triples	
		Inner	Outer
Fiducial	2.254±0.476	2.287±0.443	4.474±1.038
$t_p = 10$	2.045±0.477	2.080±0.411	4.595±0.877
$t_p = 30$	1.976±0.472	2.045±0.405	4.383±0.729
$t_p = 100$	1.916±0.459	2.022±0.412	3.953±0.533
$t_p = 300$	1.861±0.461	2.005±0.461	3.632±0.467

Table 9.21: Mean and standard deviation of $\log_{10}(P/\mathrm{yr})$

Time					
	Quad, Hierarchical			Quad, Double	
	Inner	Mid	Outer	Inner	Outer
Fiducial	2.447±0.384	4.669±1.039	7.272±0.777	3.224±1.211	4.708±1.029
$t_p = 10$	2.091±0.400	4.341±0.910	5.931±0.841	3.486±1.609	5.405±1.134
$t_p = 30$	2.055±0.436	3.908±0.758	5.399±0.755	2.902±1.361	4.605±0.371
$t_p = 100$	2.161±0.361	3.604±0.383	4.795±0.495	4.059±2.056	6.553±0.562
$t_p = 300$	—±nan	—±nan	—±nan	—±nan	—±nan

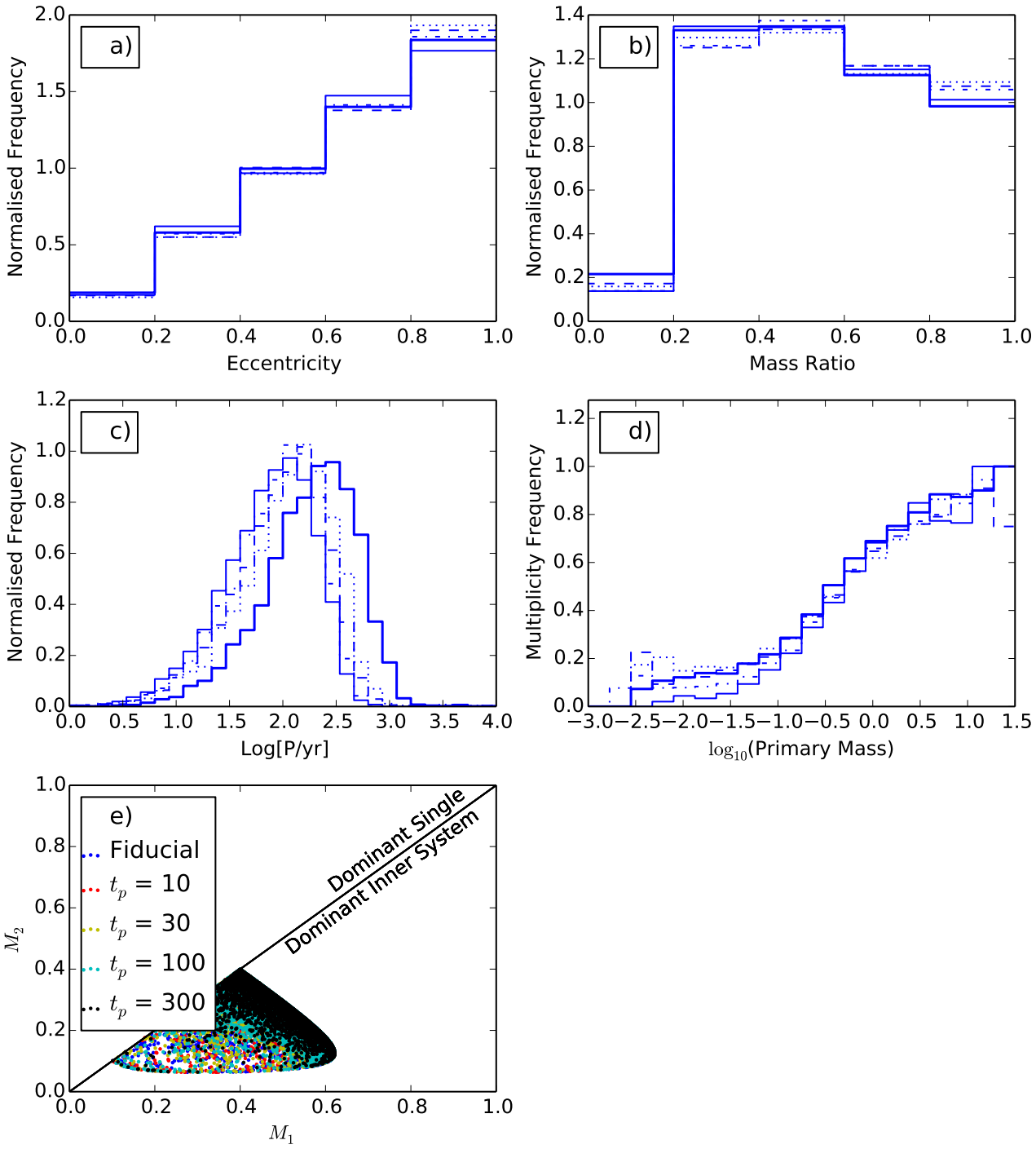

Figure 9.30: The variation of binary properties with t_p. The thick solid/dotted/dashed/dot-dashed/thin solid lines in each of the Frames describes the distributions attained when $t_p = 0$, 10, 30, 100 and 300 respectively. Frame a) shows the normalised distribution of eccentricities, Frame b) shows the normalised distribution of mass ratios, Frame c) shows the normalised distribution of periods [yr] and d) shows the multiplicity frequency as a function of primary mass, and Frame e) plots M_2 against M_1. 6065, 4014, 5416, 7176, 3071 binary systems are plotted for $t_p = 0$, 10, 30, 100 and 300 respectively.

distributions as shown in Sub-figure 9.31c and Table 9.20 decrease as t_p increases. The standard deviations also decrease, because the presence of the Plummer potential prevents long period systems forming, decreasing the possible spread of periods that systems can have. In Sub-figure 8.6d M_2 is plotted against M_1, and in Sub-figure 8.6d M_3 is plotted against $M_2 + M_1$.

The properties of hierarchical quadruples are shown in Sub-figure 9.32. The peak of the eccentricity distributions of both the mid and outer orbits moves to lower eccentricities as t_p increases (Sub-figure 9.32a). The distribution of mass ratios of each orbit as seen in Sub-figure 9.32b tends towards higher mass ratios as t_p increases. As with the triples and binaries, the mean of the period decreases as t_p increases (see Sub-figure 9.32 c and Table 9.21). In Sub-figure 8.7d M_2 is plotted against M_1, in Sub-figure 8.7e M_3 is plotted against $M_2 + M_1$ and in Sub-figure 8.7f M_4 is plotted against $M_3 + M_2 + M_1$.

The properties of double quadruples are shown in Figure 9.33. I will not discuss the results of $t_p > 10$, as the number statistics are too low to draw any firm conclusions. However, when a short-lived Plummer background potential is added, the outer orbits become more circularised (see Sub-figure 9.33 a, solid and dotted lines). A higher fraction of outer orbits have an equal mass ratio than for the fiducial model, whilst the mass ratios of the inner periods are unaffected (see Sub-figure 9.33b). Unlike the other multiple systems, the mean of both the inner and outer periods as shown in Sub-figure 9.33c and Table 9.21 increases when a Plummer sphere is added, however this result may be due to low number statistics. A lower fraction of double quadruples are produced when a Plummer background potential is used, compared to the fiducial model. In Sub-figure 8.8d, M_2 is plotted against M_1 and M_4 is plotted against M_3. In Sub-figure 8.8e $M_4 + M_3$ is plotted against $M_2 + M_1$.

The distribution of systems in the $(\log_{10}(P/\mathrm{yr}), \mathrm{e})$-plane are given in Figures 9.34, 9.35, 9.36 and 9.37 for binaries, triples, hierarchical quadruples and double quadruples respectively. The diagram does not change with t_p for the binary systems (Figure 9.34). But for the triple systems (Figure 9.35), as t_p increases, the period of the widest system decreases, the overall eccentricity decreases, and the average fidelity increases. There are no low-fidelity triples produced when t_p is large. The outer orbit of the hierarchical quadruples (Figure 9.36) has a lower eccentricity on average as t_p increases. Due to low number statistics, no conclusions can be drawn from (Figure 9.37).

When a short-lived Plummer background potential, (t_p=10,30) is included in the model, the number of binaries formed decreases in favour of triples and hierarchical quadruples (See Table 9.22). The background potential keeps the cluster from ejecting members too quickly, allowing time for higher-order multiple systems to form. But as t_p is increased, further, (t_p=100,300), i.e. the longer the time for which the Plummer sphere is influential, the more compact the systems become, the effect being greatest for the outermost orbits. In order for a higher-order multiple system to be stable, the semi-major axis of the outer orbit must be significantly greater than

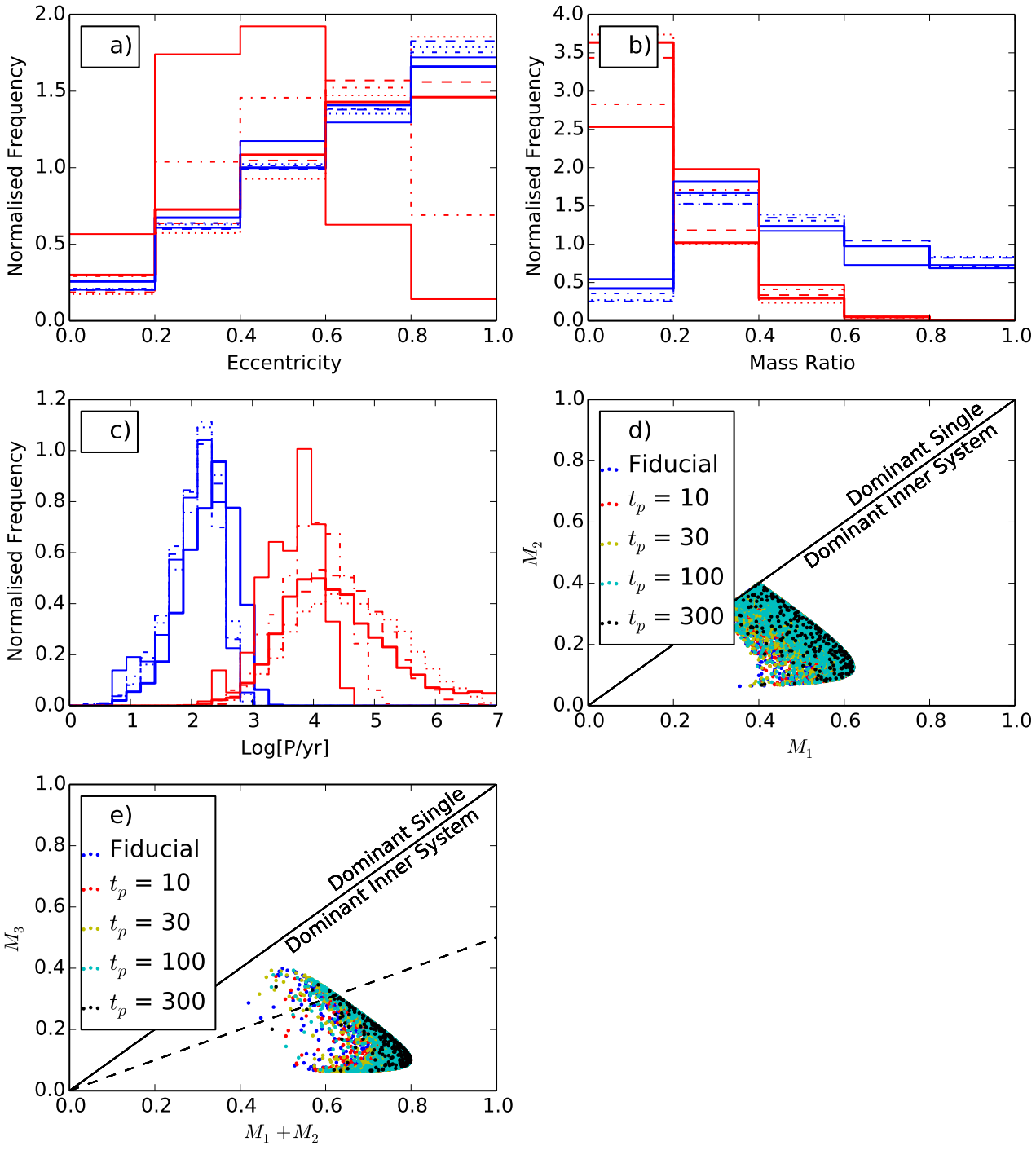

Figure 9.31: The variation of properties of triples formed with t_p. The thick solid/dotted/dashed/dot-dashed/thin solid lines in each of the Frames describes the distributions attained when t_p = 0, 10, 30, 100 and 300 respectively. The blue lines show the inner periods, whilst the red lines show the outer periods. Frame a) shows the normalised distribution of eccentricities, Frame b) shows the normalised distribution of mass ratios and Frame c) shows the normalised distribution of periods [yr]. Frame d) plots M_2 against M_1, whilst Frame e) plots M_3 against $M_2 + M_1$. 2725, 3131, 3353, 2042, 247 triple systems are plotted for t_p = 0, 10, 30, 100 and 300 respectively.

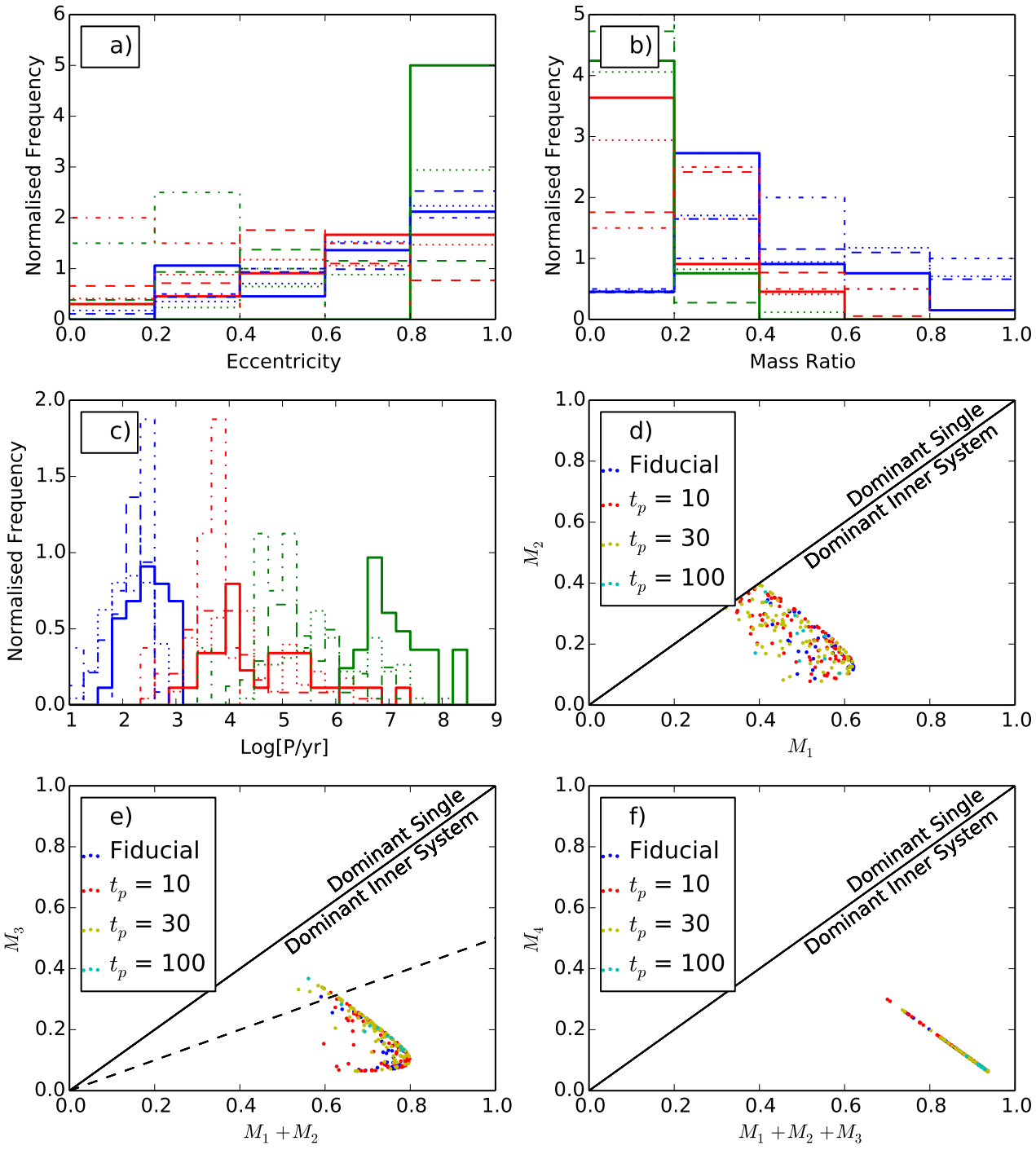

Figure 9.32: The variation of properties of hierarchical quadruples formed with t_p. The thick solid/dotted/dashed/dot-dashed/thin solid lines in each of the Frames describes the distributions attained when t_p = 0, 10, 30, 100 and 300 respectively. The blue lines show the inner periods, the red lines show the middle periods and the green lines show the outer periods. Frame a) shows the normalised distribution of eccentricities, Frame b) shows the normalised distribution of mass ratios and Frame c) shows the normalised distribution of periods [yr]. Frame d) plots M_2 against M_1, whilst Frame e) plots M_3 against $M_2 + M_1$, and Frame f) plots M_4 against $M_3 + M_2 + M_1$. 33, 85, 91, 10, 0 hierarchical quadruple systems are plotted for t_p = 0, 10, 30, 100 and 300 respectively.

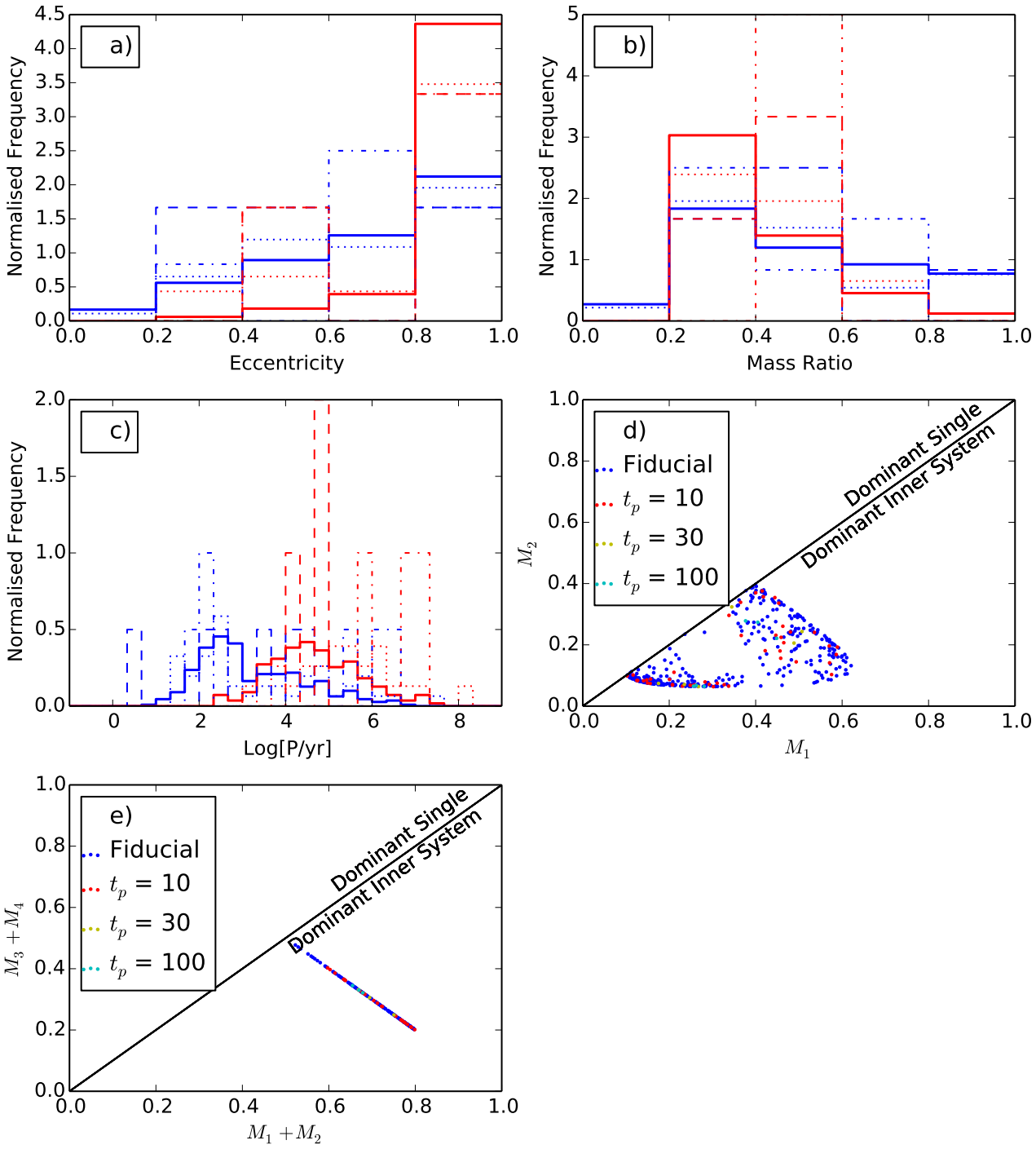

Figure 9.33: The variation of properties of double quadruples formed with t_p. The thick solid/dotted/dashed/dot-dashed/thin solid lines in each of the Frames describes the distributions attained when t_p = 0, 10, 30, 100 and 300 respectively. The blue lines show the inner periods, whilst the red lines show the outer periods. Frame a) shows the normalised distribution of eccentricities, Frame b) shows the normalised distribution of mass ratios and Frame c) shows the normalised distribution of periods [yr]. Frame d) plots M_2 against M_1 and M_4 against M_3, and Frame e) plots $M_4 + M_3$ against $M_2 + M_1$. 165, 23, 3, 3, 0 double quadruple systems are plotted for t_p = 0, 10, 30, 100 and 300 respectively.

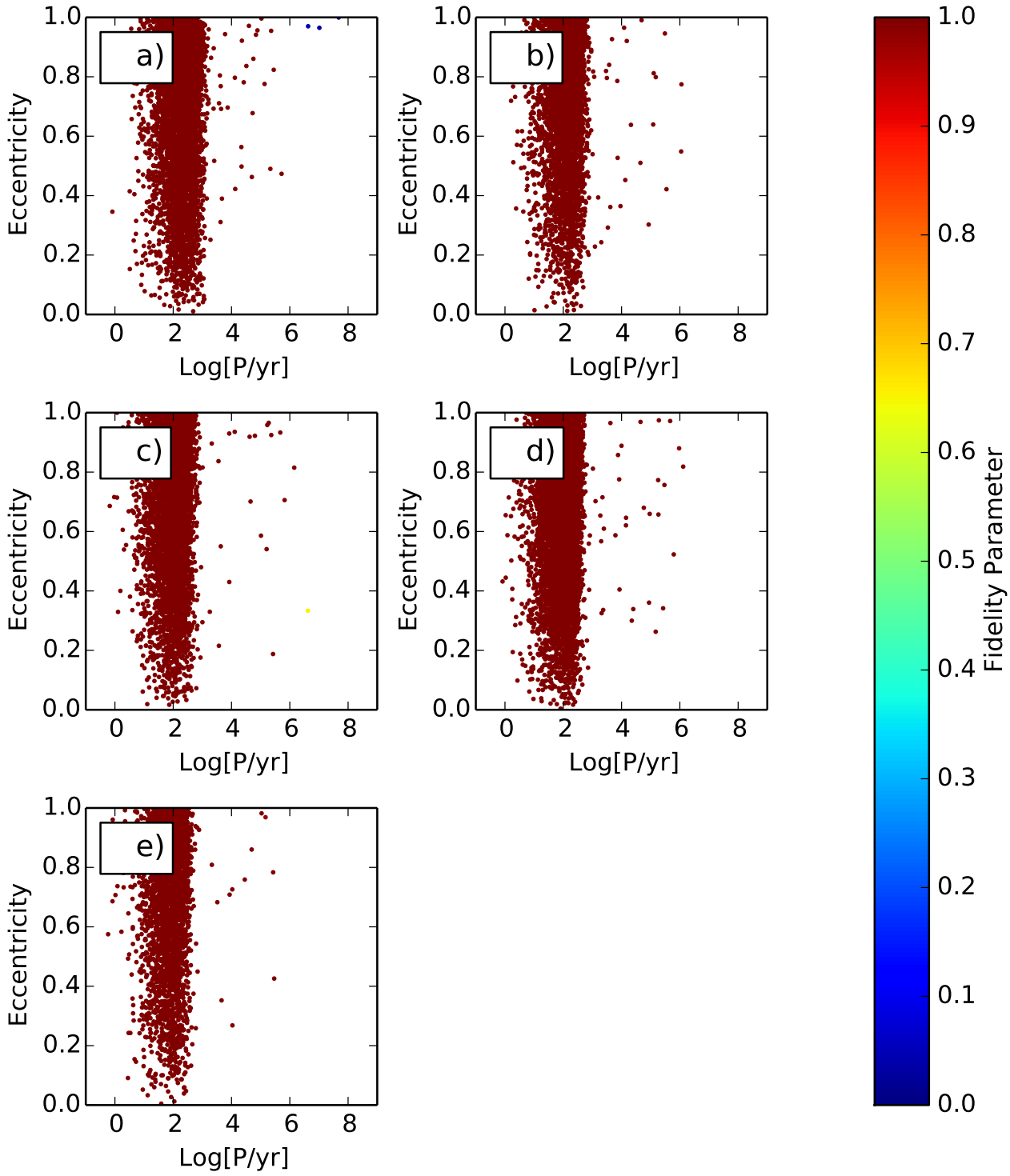

Figure 9.34: The distribution of binary systems in the $(\log_{10}(P/\mathrm{yr}), \mathrm{e})$-plane. The colour of the points encodes the fidelity parameter. Frame a) corresponds to $t_p = 0$, b) 10, c) 30, d) 100, and e) 300. 6065, 4014, 5416, 7176, 3071 binary systems are plotted for $t_p = 0$, 10, 30, 100 and 300 respectively.

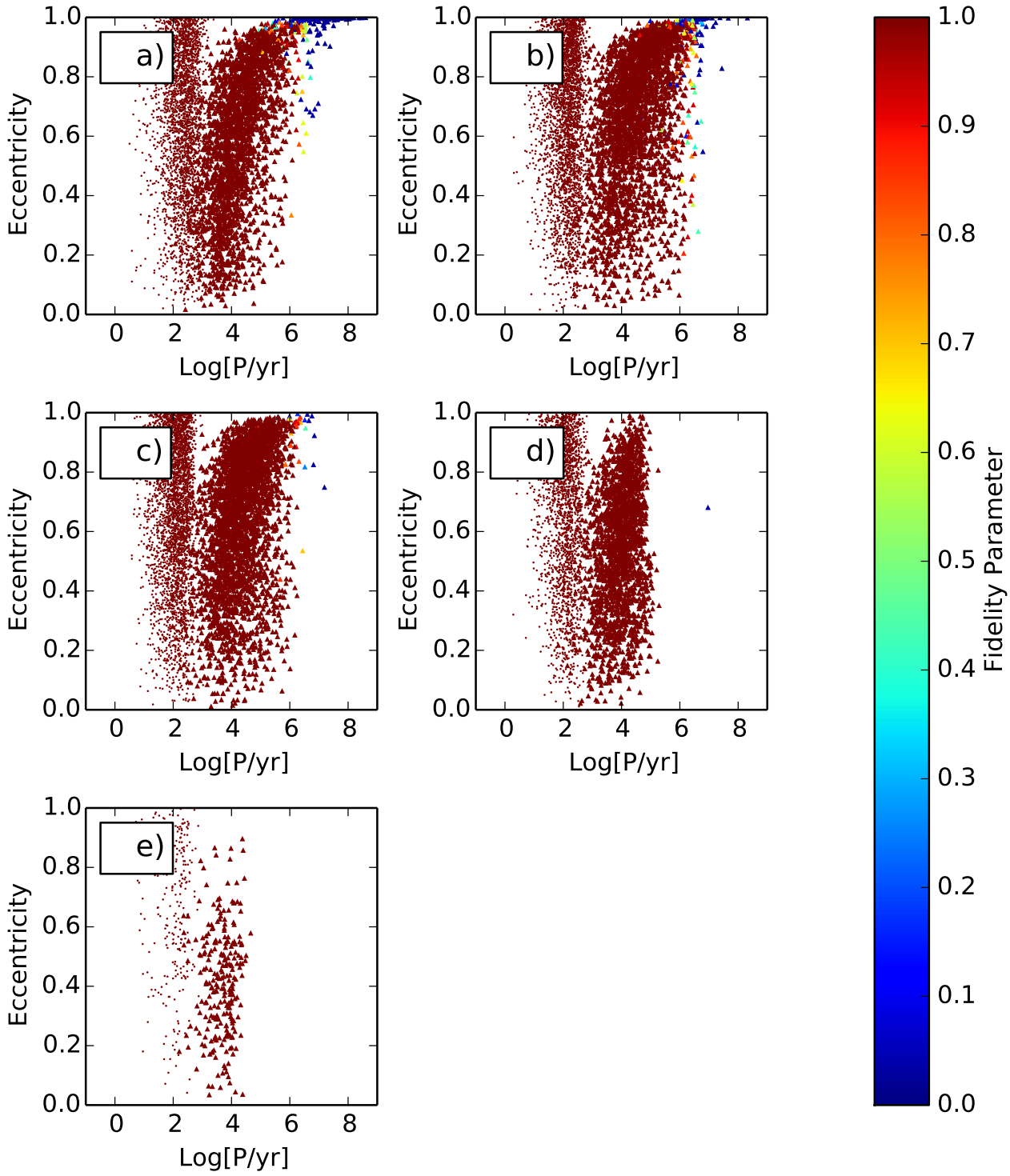

Figure 9.35: The distribution of triple systems in the $(\log_{10}(P/\mathrm{yr}), \mathrm{e})$-plane. Small circles represent inner orbits and triangles represent outer orbits. The colour of the points encodes the fidelity parameter. Frame a) corresponds to $t_p = 0$, b) 10, c) 30, d) 100, and e) 300. 2725, 3131, 3353, 2042, 247 triple systems are plotted for $t_p = 0$, 10, 30, 100 and 300 respectively.

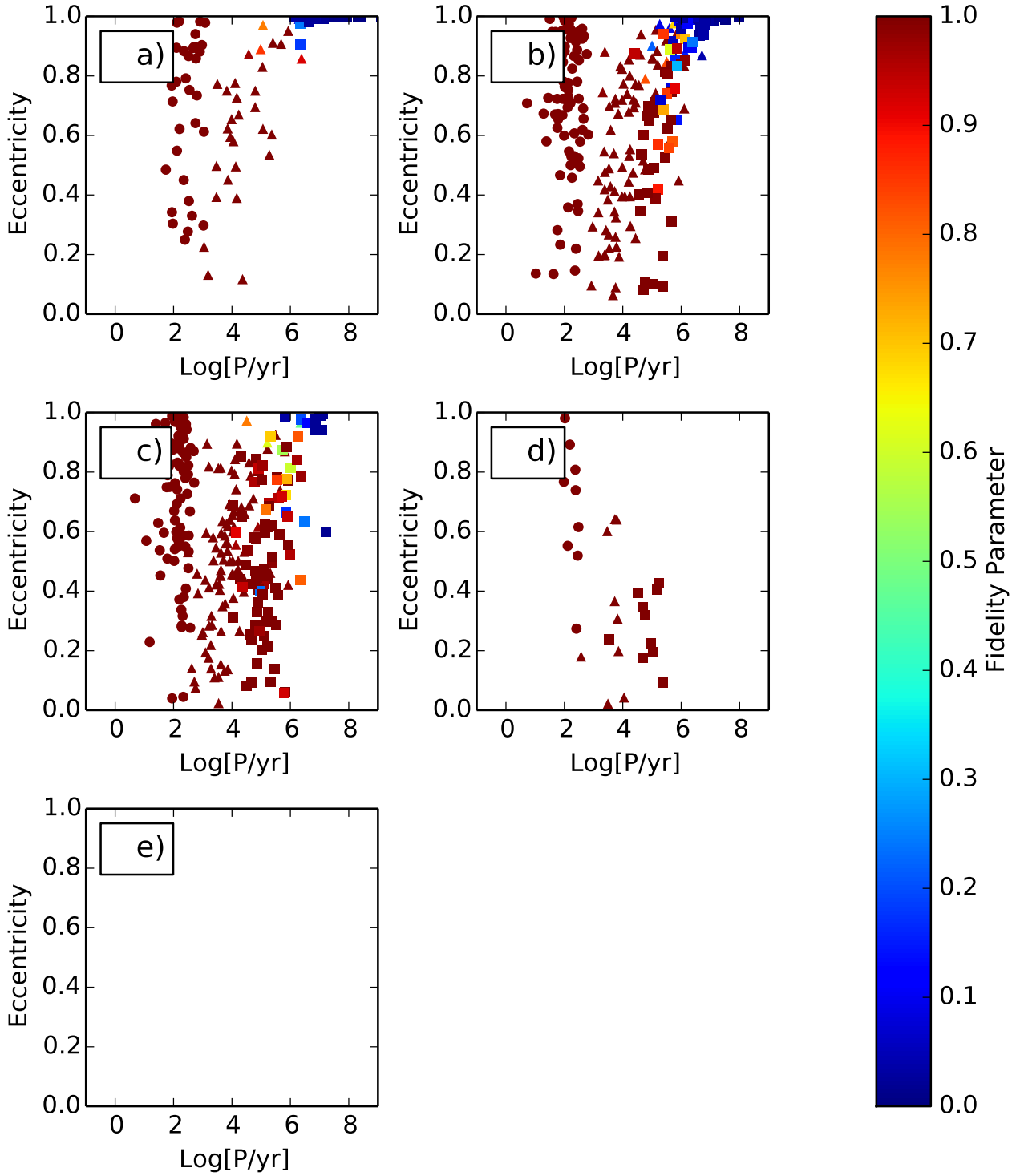

Figure 9.36: The distribution of hierarchical quadruple systems in the $(\log_{10}(P/\mathrm{yr}), \mathrm{e})$-plane. Circles represent inner orbits, triangles represent middle orbits and squares represent outer orbits. The colour of the points encodes the fidelity parameter. Frame a) corresponds to $t_p =$ 0, b) 10, c) 30, d) 100, and e) 300. 33, 85, 91, 10, 0 hierarchical quadruple systems are plotted for $t_p = 0$, 10, 30, 100 and 300 respectively.

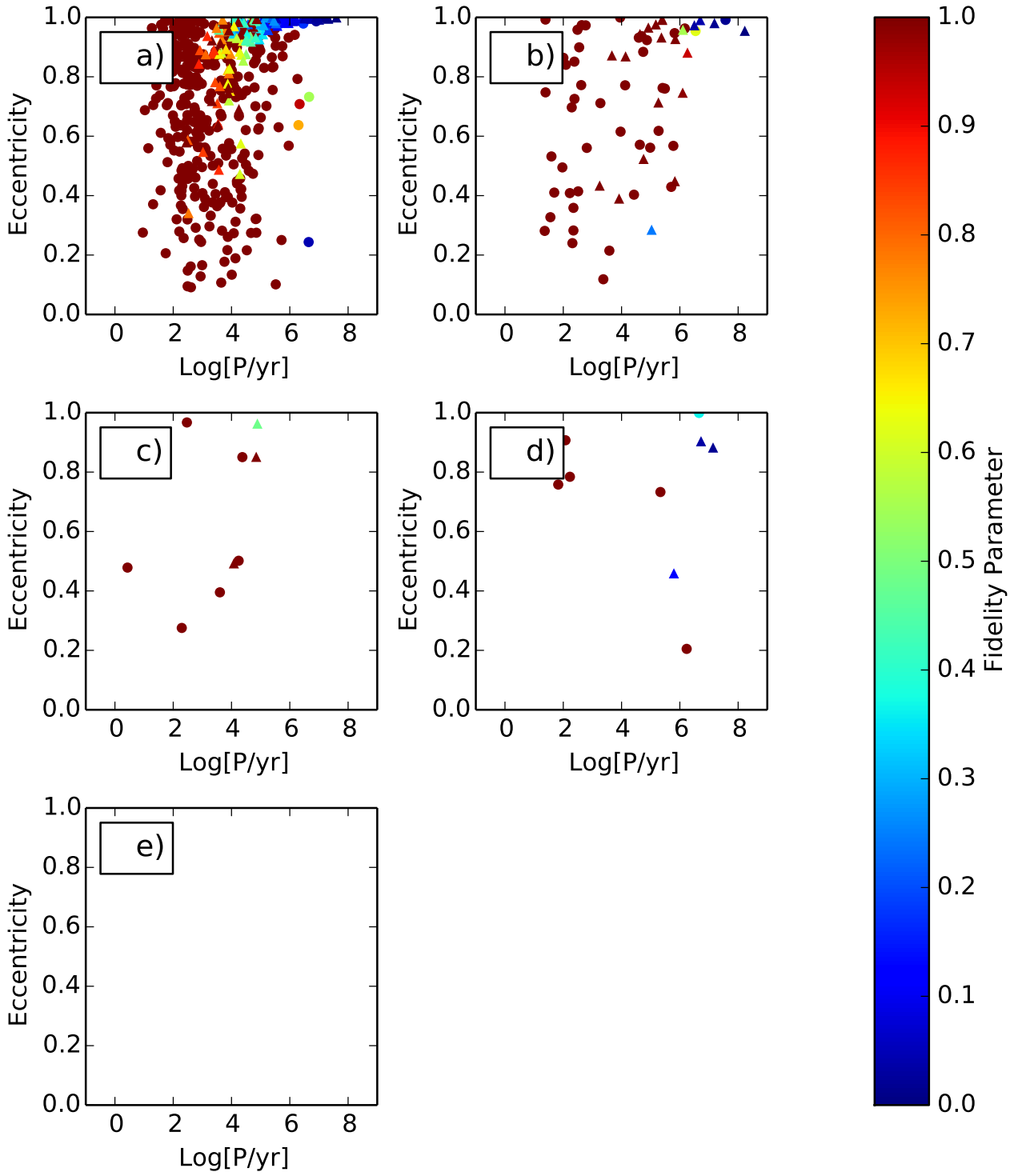

Figure 9.37: The distribution of double quadruple systems in the $(\log_{10}(P/\mathrm{yr}), \mathrm{e})$-plane. Circles represent inner orbits and triangles represent outer orbits. The colour of the points encodes the fidelity parameter. Frame a) corresponds to $t_p = 0$, b) 10, c) 30, d) 100, and e) 300. 165, 23, 3, 3, 0 double quadruple systems are plotted for $t_p = 0$, 10, 30, 100 and 300 respectively.

the semi-major axis of the inner orbit. As the system is compacted, the semi-major axis of the outer orbits of some of the higher order multiples become too small compared to the semi-major axis of the inner orbits, and the multiple system is no longer stable. The higher-order multiples therefore degrade to pure binaries.

Table 9.22: Average number of multiple systems produced per core.

Time	Binaries	Triples	Hierarchical Quadruples	Double Quadruples
Fiducial	0.6799	0.3055	0.0037	0.0185
$t_p = 10$	0.5276	0.4115	0.0112	0.0030
$t_p = 30$	0.5824	0.3605	0.0098	0.0003
$t_p = 100$	0.7426	0.2113	0.0010	0.0003
$t_p = 300$	0.8822	0.0710	0.0000	0.0000

With the requirement that the KS test must be rejected at the 1% level for all values of t_p for a given property, we can say that the outer eccentricities of the triples, and the periods of the binaries, triples (inner and outer) and the hierarchical quadruples (inner and outer) change with t_p with reasonable confidence (See Table 9.23). The different eccentricities could be detected observationally, however, the peak of the period does not change sufficiently to be detected easily observationally.

Table 9.23: This table shows the eccentricity, mass ratio and period distributions that for which the null hypothesis can be rejected at the 1% level, as determined by the K-S test for the different values of t_p.

t_p	System Type	Eccentricity	Mass Ratio	Period
10	Binaries			✓
30	Binaries			✓
100	Binaries		✓	✓
300	Binaries			✓
10	Triples inner		✓	✓
30	Triples inner		✓	✓
100	Triples inner			✓
300	Triples inner			✓
10	Triples outer	✓		✓
30	Triples outer	✓	✓	✓
100	Triples outer	✓	✓	✓
300	Triples outer	✓	✓	✓
10	Hierarchical Quadruples inner			✓
30	Hierarchical Quadruples inner			✓
100	Hierarchical Quadruples inner			✓
10	Hierarchical Quadruples mid			
30	Hierarchical Quadruples mid		✓	✓
100	Hierarchical Quadruples mid	✓	✓	✓
10	Hierarchical Quadruples outer	✓		✓
30	Hierarchical Quadruples outer	✓	✓	✓
100	Hierarchical Quadruples outer	✓	✓	✓
10	Double Quadruples inner			
30	Double Quadruples inner			
100	Double Quadruples inner			
300	Double Quadruples inner			
10	Double Quadruples outer			
30	Double Quadruples outer			
100	Double Quadruples outer			
300	Double Quadruples outer			

Chapter 10

Discussion and Conclusions

In this chapter, I summarise the work done in my thesis, and discuss further work that might be done to extend these investigations.

10.1 Mapping from the CMF to the StIMF

I have found during the course of this project that a self similar mapping from the CMF to the StIMF can be achieved, so long as Equations (4.1) and (4.3) are satisfied. This leads to a degeneracy. I can further constrain the parameters by invoking the binary frequency and mass ratios, which allows us to constrain the parameters to those found in Table 4.1. It is a combination of fitting both the StIMF and the binary frequency that constrains the parameter space most critically. This model is unique in that it fits the StIMF, binary frequency and mass ratios.

Self-similar mapping fits the observational constraints for the StIMF, binary frequency and mass ratios for sun-like and M-dwarf primaries, so long as the efficiency is high, approximately 100%. This is higher than previously proposed (e.g. $\eta_0 \sim 0.3$, Alves et al. 2007). We would therefore expect that most of the mass of the core would end up in the mass of the stars. Additional accretion would counteract any mass loss via outflows. Each core needs to fragment into about 4 or 5 stars, and so most stars would not form in isolation. Higher values of N_0 may be possible, but the efficiency would have to be increased even further and each core would have to produce more than one binary. The dynamical biasing parameter, β, is somewhat small in the best fit, suggesting that there is some form of dissipation between the stars, allowing the lower mass stars an opportunity to be part of a long lived binary.

Four secondary parameters are investigated, χ_t, χ_{η_0}, χ_{N_0} and χ_{σ_0}. These parameters allow N_0, σ_0, η_0 and the lifetime of cores to vary with $M_{\rm c}$. However, these parameters do not improve the fit enough to warrant being included.

N_0, η_0, and μ_c all have a high influence on μ_{St}, whilst $\sigma_{\rm C}$ and σ_0 have a high influence on

the standard deviation of the final StIMF distribution. As σ_{St} and σ_{C} are similar in size, σ_{0} cannot be too large (see Equation 4.3).

The slope of the binary frequency graph against primary mass gets steeper as either N_0 increases, β increases or σ_{0} increases.

$\beta \gg 1$ produces binaries with mass ratios approximately equal to 1. For $\sigma_{0} = 0$, we would expect all the mass ratios to be equal to 1. Intermediate values of σ_{0} will reproduce a flat mass ratio distribution, whilst small values of σ_{0} will reproduce a mass ratio distribution that peaks towards $q = 1$.

Note that I do not claim, nor have I claimed at any point, that self-similar mapping is the one and only answer. I do however say that at this point in time it cannot be ruled out, and may turn out to be useful as a rough and ready guideline.

10.2 Core Cluster Simulations

Using the best-fit results of the project described in Chapters 3 and 4 as a fiducial model, I perform N-body calculations of small core-clusters to follow the production of multiple systems. Using a fidelity parameter defined in this thesis, I investigate the dependence of the structure and stability of these multiple systems on certain initial conditions, including the number of stars in a core-cluster, the variance in masses in those stars, the virial ratio and radial dependence of stellar density. I expand on those results by including a prescription for the influence of disks during stellar flybys, the influence of different initial spatial configurations of the stars (i.e. line and ring clusters) and the presence of a background potential due to residual gas in the core-cluster.

The period distribution for the binaries formed in these simulations is always very narrow, with a logarithmic standard deviation of approximately 0.6 to 0.7. The range of periods observed in the field is much larger, with a logarithmic standard deviation of approximately 2.3 for solar-mass binaries (Raghavan et al. 2010, mean $P \approx 250$ yr). However, the spread of periods observed in the field can be partly explained by these simulations if some of the wider periods observed are in fact the mid or outer orbits of higher-order multiples with unresolved companions, the longest period systems being the outer orbits of hierarchical quadruples. Due to the overlap in the period distributions of the inner, mid and outer orbits of multiple systems (see Figures 8.2, 8.3 and 8.2), when observing in the field, it would not be possible to distinguish between pairwise orbits of higher order multiples and very wide binaries by separation alone. The combined distribution of all the possible pairwise orbits (including binaries) for the fiducial model is given in Figure 10.1. The distribution consists of a log normal similar in spread and mean to the distribution for pure binaries, with a high period tail. The spread of the periods could be increased further by increasing the range of sizes of the cores, but also by allowing $\mathcal{V}$

to vary between cores. The peak of the period distribution moves from $10^{2.0}$ to $10^{2.4}$ for virial parameters between 0.3 and 0.8.

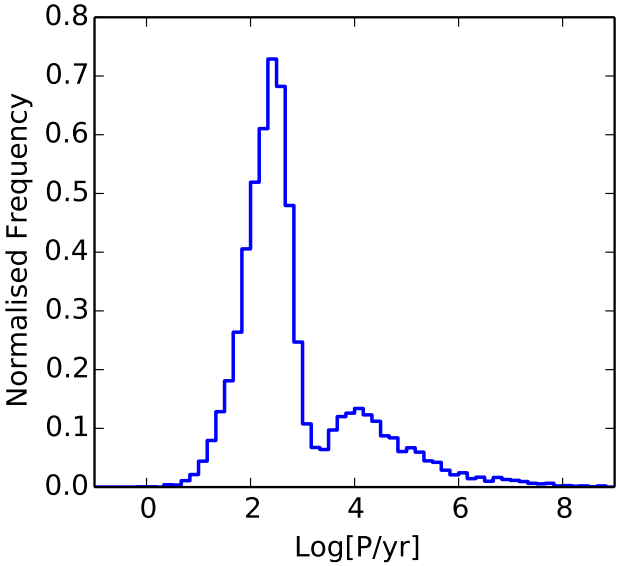

Figure 10.1: The combined period distribution of all the pair-wise orbits produced in the fiducial model. The distribution consists of a log normal similar in spread and mean to the distribution for pure binaries, with a high period tail.

Although long period systems are produced using this model, tight, spectroscopic-like binaries are not reproduced. This is possibly a result of our models not incorporating protostellar accretion, which has been shown to significantly harden binary systems (Umbreit et al. 2005).

The mass ratio distribution as found by Raghavan et al. (2010) is consistent with being flat for $q > 0.2$, with a possible peak at $q = 1$. Duchêne & Kraus (2013) find a similar mass ratio distribution for solar-mass short-period subsystems. Too few high mass ratio binaries are produced in the majority of these simulations for the distribution to be consistent with being flat, and a peak of the mass ratio at $q = 1$ is only possible if all the systems are double quadruple and σ_0 is large.

$\sigma_0 = 0.1$ comes closest to reproducing the correct mass ratio distributions for triple systems as observed by Tokovinin (2008). Duchêne & Kraus (2013) summarise that long period subsystems have a mass ratio preferentially less than 0.5, a result that is reproduced in these simulations.

These simulations produce a large fraction of systems with high eccentricity, the distribution being thermal in most cases, or having a strong peak at e = 1 for the outermost orbits if no stars are ejected. The peak of the eccentricity distribution of the outer orbits of triples and hierarchical quadruples can be shifted to smaller eccentricities if a Plummer sphere is influential for a significant length of time, possibly reproducing the flat or falling eccentricity distribution

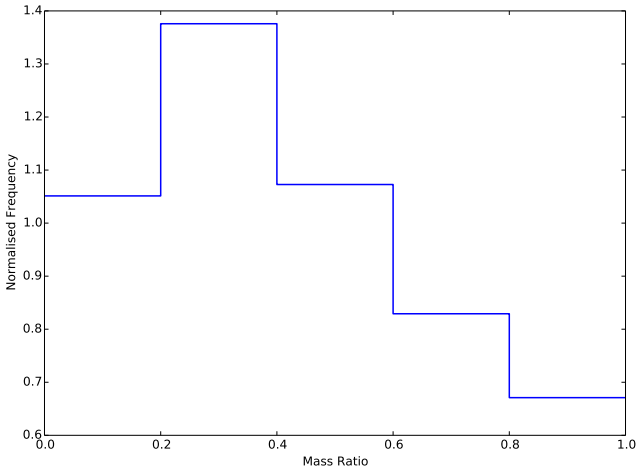

Figure 10.2: The combined mass ratio distribution of all the pairwise orbits produced in the fiducial model.

observed in the field, (see Figure 15 of Raghavan et al. 2010). But note that the eccentricity distributions of binaries and double quadruples are less affected. We never get circularization of short period binaries, unlike that observed in the field (see Figure 14 of Raghavan et al. 2010), because we do not include tidal interactions between stars.

Duchêne & Kraus (2013) state that for solar-mass and subsolar-mass systems, approximately 20 to 25% of multiple systems have 3 or more components. Most of the cases investigated in this thesis produce higher order multiple fractions of at least 20%, but the line cluster, ring cluster and $N_0 = 2$ and 3 produce too many binary systems. The fraction of higher order multiple systems can be increased either by increasing the number of stars per core, or implementing a small value of σ_0. Increasing N_0 increases the fraction of higher order multiple systems because there are more excess stars that can be ejected, carrying away energy, leaving behind a hardened system. A small value of σ_0 will produce a higher fraction of higher order multiples because multiple systems are more stable if their components are of roughly equal masses.

The best way to increase the fraction of hierarchical quadruples is to increase N_0, whilst the fraction of double quadruples can be increased by either increasing N_0, and/or decreasing σ_0. As the fraction of hierarchical quadruples rises more quickly than the fraction of double quadruples as N_0 increases, in order to reproduce the observation that more double quadruples are found than hierarchical quadruples (see Figure 23 of Raghavan et al. 2010, who find 9 double quadruples, and 2 hierarchical quadruple systems), N_0 must be equal to about 4 or 5. This range however could be larger, when considering that the average fidelity of the hierarchical quadruples is lower than that of the double quadruples, meaning that the ratio of hierarchical quadruples to double quadruples will decrease with time.

The sample analysed by Tokovinin (2008) has a triple system to double quadruple system

ratio of approximately 9. Most of the cases investigated in this thesis produce too large a fraction of triples, however, both the ring cluster and small σ_0 reproduce the correct ratio.

Most hierarchical multiples found in these simulations consist of a subsystem of stars orbited by a star on average smaller than the components of the subsystem. This is reflected in the low mass ratios of the outer orbits. However, on occasion a subsystem can be orbited by a star larger than the total mass of the subsystem's components. This occurs for the line cluster, ring cluster and large values of N_0. This occurs for the non-spherical clusters because small stars are placed preferentially closer together, and so they are more likely to form a binary system, which can then be 'captured' by a larger star. Compare with close brown dwarf/brown dwarf binaries in orbit around solar-mass stars.

Tokovinin (2008) finds that double quadruples tend to comprise two pairs of stars that have similar periods, with mass ratios tending towards 1. In these simulations, double quadruples tend to consist of two dissimilar pairs. One pair has a short period, and is comparable to the periods of pure binaries, and the second pair will have a period that is much larger than the first. Had we taken into account the results of Hennebelle et al. (2004), who concluded that stars formed in a ring tend to have similar masses, the properties of these quadruple systems may have more closely matched those of the field. Taking into account the Bonnell & Bate (1994) results that the initial separations of the stars are of the order a few solar radii would produce tighter quadruple systems. Tokovinin (2008) also finds that the inner pairs of triples tends to have a period distribution that is tighter than for binaries. This result is reproduced with $N_0 = 5$ and 6, $\sigma_0 = 0.4$ and 0.5, the line cluster, and line cluster with disks, the ring cluster, and ring cluster with disks, but not the spherical cluster with disks for some reason. However, the difference is not very significant. In the remainder of the simulations, the inner pairs have a period the pure binaries. This result may be explained in remembering that one way a binary can be hardened is to throw out the third member of the system. 50% of triple systems in the fiducial model have outer to inner period ratios of between 30 and 446. The majority of triple systems over all the simulations have period ratios that range between about 22 to 812.

Several properties of the multiple systems are significantly different from the fiducial model according to the KS test. However, for the majority of cases, the differences between the distributions are too small to be distinguished between observationally. The exceptions are the eccentricity distributions when t_p is altered, the mass ratio distributions when σ_0 is varied, and the mass ratio distribution of $N_0 = 2$ as compared to $N > 2$. The ring cluster produces distributions of binary mass ratios and binary periods that could be distinguishable from those produced by a spherical cluster.

The multiplicity frequency for solar mass stars is correct if either $N_0 = 5$ or 6, or $\sigma_0 = 0.1$, $N_0 = 6$ appears to produce also roughly the correct slope, but $\sigma_0 = 0.1$ produces a slope that is

too shallow. Otherwise, the slope of multiplicity against primary mass is too steep. This is as a result of most multiple systems being formed from the most massive stars in the core-cluster. This dynamical biasing is reduced for larger N_0, larger $\mathcal{V}$, larger σ_0, and decreasing t_p.

The ring cluster produces double quadruple systems that have outer orbits that not only populate the low eccentricities more than the fiducial, but their fidelity is also much higher, meaning that these quadruples would be more likely to reach the field intact. For double quadruples in general, the outer orbits have a lower fidelity than the inner orbits, with the fidelity decreasing as both the eccentricity and period increases, i.e. the more compact, circular systems are the most stable. This may be due to, in part, the fact that the widest systems have not yet unfolded, i.e. the simulation was terminated before the outer system had completed a full orbit.

No one set of initial conditions reproduced all the properties of multiple systems as observed in the field. For the binaries in particular, the properties of multiple systems don't appear to provide a clear test of formation history. However, it was found that the structure of higher-order multiples had a dependence on the initial configuration of the cluster, i.e. ring, line or spherical. More observational data on higher-order multiples may lead to a determination of the dominant mode of formation. For example, a large fraction of double quadruples compared to hierarchical quadruples would indicate an initial ring configuration in the core.

10.3 Future Work

The models could be expanded to include additional parameters such as adding radial velocities to the ring clusters, or adding velocities parallel to the filament in the line cluster. A rotation parameter could also be included in the spherical models, and an initial disk cluster could be investigated, to simulate the formation of stars in a 'circumstellar accretion region' (Boss 1996). The inclusion of the rotation of the core may help to produce a flatter eccentricity distribution of the multiple systems.

Accretion affects need to be investigated more thoroughly, as well as a more in-depth treatment of disks. These may help to produce more spectroscopic binaries by hardening the systems formed. Accretion will increase the mass of the protostars with time, and as a result the system will shrink (Umbreit et al. 2005), and become more circular. Accretion can also lead to equalisation of masses (Bate et al. 2002b). These effects could be included using analytical arguments, as for these simulations, or by using a hybrid SPH and N-body code such as Gandalf (Hubber etal. in prep.), to determine the influence of the embedded gas on the multiple systems formed.

Other forms of dissipation can also play a role in N-body dynamics, including Kozai oscillations and magnetic braking with disks (see Kroupa 1995, and references therein)

Bibliography

Allen, P. R. 2007, ApJ, 668, 492

Alves, J., Lombardi, M., & Lada, C. J. 2007, A&A, 462, L17

Andre, P., Ward-Thompson, D., & Barsony, M. 1993, ApJ, 406, 122

Anosova, J. P. 1986, Ap&SS, 124, 217

Balega, Y. Y., Dyachenko, V. V., Maksimov, A. F., et al. 2011, Astronomische Nachrichten, 332, 978

Basri, G. & Reiners, A. 2006, AJ, 132, 663

Bate, M. R. & Bonnell, I. A. 1997, MNRAS, 285, 33

Bate, M. R., Bonnell, I. A., & Bromm, V. 2002a, MNRAS, 332, L65

Bate, M. R., Bonnell, I. A., & Bromm, V. 2002b, MNRAS, 336, 705

Bate, M. R., Bonnell, I. A., & Bromm, V. 2003, MNRAS, 339, 577

Blake, C. H., Charbonneau, D., & White, R. J. 2010, ApJ, 723, 684

Bonnell, I. A. & Bate, M. R. 1994, MNRAS, 271, 999

Bonnell, I. A., Clark, P., & Bate, M. R. 2008, MNRAS, 389, 1556

Boss, A. P. 1996, ApJ, 468, 231

Bouy, H., Brandner, W., Martín, E. L., et al. 2003, AJ, 126, 1526

Branch, D. 1976, ApJ, 210, 392

Burgasser, A. J., Reid, I. N., Siegler, N., et al. 2007, Protostars and Planets V, 427

Carquillat, J.-M. & Prieur, J.-L. 2007, MNRAS, 380, 1064

Carrier, F., North, P., Udry, S., & Babel, J. 2002, A&A, 394, 151

Cha, S.-H. & Whitworth, A. P. 2003, MNRAS, 340, 91

Chabrier, G. 2003, ApJ, 586, L133

Chabrier, G. 2005, in Astrophysics and Space Science Library, Vol. 327, The Initial Mass Function 50 Years Later, ed. E. Corbelli, F. Palla, & H. Zinnecker, 41–50

Chabrier, G. & Hennebelle, P. 2010, ApJ, 725, L79

Chen, X., Arce, H. G., Zhang, Q., et al. 2013, ApJ, 768, 110

Chini, R., Hoffmeister, V. H., Nasseri, A., Stahl, O., & Zinnecker, H. 2012, MNRAS, 424, 1925

Clark, P. C., Klessen, R. S., & Bonnell, I. A. 2007, MNRAS, 379, 57

Clarke, C. J. 1996, MNRAS, 283, 353

Clarke, C. J. & Pringle, J. E. 1993, MNRAS, 261, 190

Close, L. M., Siegler, N., Freed, M., & Biller, B. 2003, ApJ, 587, 407

Connelley, M. S., Reipurth, B., & Tokunaga, A. T. 2008, AJ, 135, 2526

De Rosa, R. J., Patience, J., Vigan, A., et al. 2012, MNRAS, 422, 2765

Delfosse, X., Beuzit, J.-L., Marchal, L., et al. 2004, in Astronomical Society of the Pacific Conference Series, Vol. 318, Spectroscopically and Spatially Resolving the Components of the Close Binary Stars, ed. R. W. Hilditch, H. Hensberge, & K. Pavlovski, 166–174

Delgado-Donate, E. J., Clarke, C. J., Bate, M. R., & Hodgkin, S. T. 2004, MNRAS, 351, 617

Dieterich, S. B., Henry, T. J., Golimowski, D. A., Krist, J. E., & Tanner, A. M. 2012, AJ, 144, 64

Duchêne, G. 1999, A&A, 341, 547

Duchêne, G. & Kraus, A. 2013, ARA&A, 51, 269

Duchêne, G., Simon, T., Eislöffel, J., & Bouvier, J. 2001, A&A, 379, 147

Dupuy, T. J. & Liu, M. C. 2011, ApJ, 733, 122

Duquennoy, A. & Mayor, M. 1991, A&A, 248, 485

Eggleton, P. & Kiseleva, L. 1995, ApJ, 455, 640

Elmegreen, B. G., Klessen, R. S., & Wilson, C. D. 2008, ApJ, 681, 365

Enoch, M. L., Evans, II, N. J., Sargent, A. I., et al. 2008, ApJ, 684, 1240

Enoch, M. L., Young, K. E., Glenn, J., et al. 2006, ApJ, 638, 293

Fischer, D. A. & Marcy, G. W. 1992, ApJ, 396, 178

Goodman, J. & Hut, P. 1993, ApJ, 403, 271

Goodwin, S. P. 2010, Royal Society of London Philosophical Transactions Series A, 368, 851

Goodwin, S. P. & Kouwenhoven, M. B. N. 2009, MNRAS, 397, L36

Goodwin, S. P. & Kroupa, P. 2005, A&A, 439, 565

Goodwin, S. P., Nutter, D., Kroupa, P., Ward-Thompson, D., & Whitworth, A. P. 2008, A&A, 477, 823

Gould, A., Bahcall, J. N., & Flynn, C. 1997, ApJ, 482, 913

Guenther, E. W. & Wuchterl, G. 2003, A&A, 401, 677

Hartigan, P. & Kenyon, S. 2001, in IAU Symposium, Vol. 200, The Formation of Binary Stars, ed. H. Zinnecker & R. Mathieu, 496

Hatchell, J. & Fuller, G. A. 2008, A&A, 482, 855

Heller, C. H. 1993, ApJ, 408, 337

Hennebelle, P. & Chabrier, G. 2009, ApJ, 702, 1428

Hennebelle, P., Whitworth, A. P., Cha, S.-H., & Goodwin, S. P. 2004, MNRAS, 348, 687

Henry, T. J. & McCarthy, Jr., D. W. 1990, ApJ, 350, 334

Hillenbrand, L. A. & White, R. J. 2004, ApJ, 604, 741

Holman, K., Walch, S. K., Goodwin, S. P., & Whitworth, A. P. 2013, Monthly Notices of the Royal Astronomical Society, 432, 3534

Hubber, D. A., Allison, R. J., Smith, R., & Goodwin, S. P. 2013, MNRAS, 430, 1599

Hubber, D. A., Batty, C. P., McLeod, A., & Whitworth, A. P. 2011, A&A, 529, A27

Hubber, D. A. & Whitworth, A. P. 2005, A&A, 437, 113

Ivanov, V. D., Chauvin, G., Foellmi, C., et al. 2006, Ap&SS, 304, 247

Janson, M., Hormuth, F., Bergfors, C., et al. 2012, ApJ, 754, 44

Johnstone, D. & Bally, J. 2006, ApJ, 653, 383

Johnstone, D., Fich, M., Mitchell, G. F., & Moriarty-Schieven, G. 2001, ApJ, 559, 307

Johnstone, D., Wilson, C. D., Moriarty-Schieven, G., et al. 2000, ApJ, 545, 327

Kauffmann, J., Bertoldi, F., Bourke, T. L., Evans, II, N. J., & Lee, C. W. 2008, A&A, 487, 993

Kiminki, D. C. & Kobulnicky, H. A. 2012, ApJ, 751, 4

Kiminki, D. C., Kobulnicky, H. A., Ewing, I., et al. 2012, ApJ, 747, 41

Könyves, V., André, P., Men'shchikov, A., et al. 2010, A&A, 518, L106+

Kouwenhoven, M. B. N., Brown, A. G. A., Portegies Zwart, S. F., & Kaper, L. 2007, A&A, 474, 77

Kraus, A. L., Ireland, M. J., Martinache, F., & Hillenbrand, L. A. 2011, ApJ, 731, 8

Kraus, A. L., Ireland, M. J., Martinache, F., & Lloyd, J. P. 2008, ApJ, 679, 762

Kroupa, P. 1995, MNRAS, 277, 1491

Kroupa, P. 2001, MNRAS, 322, 231

Kroupa, P. & Bouvier, J. 2003, MNRAS, 346, 369

Krumholz, M. R., Klein, R. I., & McKee, C. F. 2007, ApJ, 656, 959

Lada, C. J. 1987, in IAU Symposium, Vol. 115, Star Forming Regions, ed. M. Peimbert & J. Jugaku, 1–17

Lafrenière, D., Jayawardhana, R., Brandeker, A., Ahmic, M., & van Kerkwijk, M. H. 2008, ApJ, 683, 844

Larson, R. B. 1981, MNRAS, 194, 809

Launhardt, R., Nutter, D., Ward-Thompson, D., et al. 2010, ApJS, 188, 139

Li, P. S., Norman, M. L., Mac Low, M.-M., & Heitsch, F. 2004, ApJ, 605, 800

Lomax, O., Whitworth, A. P., & Cartwright, A. 2013, MNRAS, 436, 2680

Machida, M. N., Matsumoto, T., Hanawa, T., & Tomisaka, K. 2005, MNRAS, 362, 382

Machida, M. N., Tomisaka, K., Matsumoto, T., & Inutsuka, S.-i. 2008, ApJ, 677, 327

Makino, J. & Aarseth, S. J. 1992, PASJ, 44, 141

Mason, B. D., Gies, D. R., Hartkopf, W. I., et al. 1998, AJ, 115, 821

Mason, B. D., Hartkopf, W. I., Gies, D. R., Henry, T. J., & Helsel, J. W. 2009, AJ, 137, 3358

Matzner, C. D. & McKee, C. F. 2000, ApJ, 545, 364

Maxted, P. F. L. & Jeffries, R. D. 2005, MNRAS, 362, L45

McDonald, J. M. & Clarke, C. J. 1995, MNRAS, 275, 671

Motte, F., Andre, P., & Neri, R. 1998, A&A, 336, 150

Motte, F., André, P., Ward-Thompson, D., & Bontemps, S. 2001, A&A, 372, L41

Myers, P. C. 1983, ApJ, 270, 105

Myers, P. C. 2013, ApJ, 764, 140

Nakano, T., Hasegawa, T., & Norman, C. 1995, ApJ, 450, 183

Nutter, D. & Ward-Thompson, D. 2007, MNRAS, 374, 1413

Öpik, E. 1924, Publications of the Tartu Astrofizica Observatory, 25, 1

Padoan, P. & Nordlund, Å. 2002, ApJ, 576, 870

Padoan, P., Nordlund, Å., Kritsuk, A. G., Norman, M. L., & Li, P. S. 2007, ApJ, 661, 972

Peter, D., Feldt, M., Henning, T., & Hormuth, F. 2012, A&A, 538, A74

Peters, T., Schleicher, D. R. G., Klessen, R. S., et al. 2012, ApJ, 760, L28

Preibisch, T., Balega, Y., Hofmann, K., Weigelt, G., & Zinnecker, H. 1999, New A, 4, 531

Raghavan, D., McAlister, H. A., Henry, T. J., et al. 2010, ApJS, 190, 1

Rathborne, J. M., Lada, C. J., Muench, A. A., et al. 2009, ApJ, 699, 742

Reid, I. N. & Gizis, J. E. 1997, AJ, 113, 2246

Reid, I. N., Kirkpatrick, J. D., Liebert, J., et al. 2002, AJ, 124, 519

Reid, M., Wadsley, J., Petitclerc, N., & Sills, A. 2010, ApJ, 719, 561

Reipurth, B. & Clarke, C. 2001, AJ, 122, 432

Reipurth, B. & Mikkola, S. 2012, Nature, 492, 221

Reipurth, B. & Zinnecker, H. 1993, A&A, 278, 81

Salpeter, E. E. 1955, ApJ, 121, 161

Sana, H., de Koter, A., de Mink, S. E., et al. 2013, A&A, 550, A107

Sana, H., de Mink, S. E., de Koter, A., et al. 2012, Science, 337, 444

Sana, H. & Evans, C. J. 2011, in IAU Symposium, Vol. 272, IAU Symposium, ed. C. Neiner, G. Wade, G. Meynet, & G. Peters, 474–485

Sana, H., Gosset, E., & Evans, C. J. 2009, MNRAS, 400, 1479

Shatsky, N. & Tokovinin, A. 2002, A&A, 382, 92

Sicilia-Aguilar, A., Henning, T., Linz, H., et al. 2013, A&A, 551, A34

Simpson, R. J., Nutter, D., & Ward-Thompson, D. 2008, MNRAS, 391, 205

Smith, R. J., Clark, P. C., & Bonnell, I. A. 2009, MNRAS, 396, 830

Southworth, J. 2012, in Orbital Couples: Pas de Deux in the Solar System and the Milky Way, ed. F. Arenou & D. Hestroffer, 51–58

Stanke, T., Smith, M. D., Gredel, R., & Khanzadyan, T. 2006, A&A, 447, 609

Sterzik, M. F. & Durisen, R. H. 1998, A&A, 339, 95

Sterzik, M. F. & Durisen, R. H. 2003, A&A, 400, 1031

Sterzik, M. F., Durisen, R. H., & Pickett, B. K. 2001, in Astronomical Society of the Pacific Conference Series, Vol. 244, Young Stars Near Earth: Progress and Prospects, ed. R. Jayawardhana & T. Greene, 116

Sterzik, M. F., Durisen, R. H., & Zinnecker, H. 2003, A&A, 411, 91

Stutzki, J. & Guesten, R. 1990, ApJ, 356, 513

Swift, J. J. & Williams, J. P. 2008, ApJ, 679, 552

Tanner, A., White, R., Bailey, J., et al. 2012, ApJS, 203, 10

Testi, L. & Sargent, A. I. 1998, ApJ, 508, L91

Tohline, J. E. 2002, ARA&A, 40, 349

Tokovinin, A. 2008, MNRAS, 389, 925

Tothill, N. F. H., White, G. J., Matthews, H. E., et al. 2002, ApJ, 580, 285

Umbreit, S., Burkert, A., Henning, T., Mikkola, S., & Spurzem, R. 2005, ApJ, 623, 940

van Albada, T. S. 1968a, Bull. Astron. Inst. Netherlands, 19, 479

van Albada, T. S. 1968b, Bull. Astron. Inst. Netherlands, 20, 47

van der Tak, F. 2012, Advances in Space Research, 49, 1395

Vesperini, E. 2010, Royal Society of London Philosophical Transactions Series A, 368, 829

Ward-Thompson, D., Scott, P. F., Hills, R. E., & Andre, P. 1994, MNRAS, 268, 276

Ward-Thompson, D., Zylka, R., Mezger, P. G., & Sievers, A. W. 2000, A&A, 355, 1122

Whitworth, A., Stamatellos, D., Walch, S., et al. 2010, in IAU Symposium, Vol. 266, IAU Symposium, ed. R. de Grijs & J. R. D. Lépine, 264–271

Williams, J. P. & Cieza, L. A. 2011, ARA&A, 49, 67

Williams, J. P., de Geus, E. J., & Blitz, L. 1994, ApJ, 428, 693

Young, K. E., Enoch, M. L., Evans, II, N. J., et al. 2006, ApJ, 644, 326